

DISS. ETH Nr. 16782

Rydberg states in atom and molecule optics

A dissertation submitted to

ETH ZURICH

for the degree of

Doctor of Natural Sciences

presented by

Edward Vliegen

Master of science

Utrecht University

born 4th of November 1976

citizen of The Netherlands

Accepted on the recommendation of:

Prof. Dr. F. Merkt, examiner

Prof. Dr. T. Esslinger, co-examiner

2007

If the miles behind me could be put into words before you,
you would feel my efforts, my struggles, my desires.
Most of all you would see my joy.
Watch me from afar run the trails and hills and miles upon miles and you will see...
Anonymous

en gaat het niet zoals ik wil,
dan doe ik dit... en alles staat stil.
Ti-Ta tovenaars openingslied

Abstract

In this thesis a new method of controlling the motion of particles is described which is in principle applicable to all atoms and molecules in the gas phase. With this method, which relies on the large Stark effect exhibited by Rydberg states, samples of slow and cold atoms and molecules can be produced, which have potential applications in, for instance, high-resolution spectroscopic experiments, in studies of cold collisions, and in quantum computation or quantum information processing.

This new method, which has been developed and tested in deceleration experiments on argon and hydrogen atoms in supersonic beams, is based on the large dipole moments that atoms and molecules exhibit when they are excited to Rydberg Stark states in electric fields. As a result of these dipole moments, which can exceed 1000 Debye, large forces can be exerted on the particles when they fly through inhomogeneous electric fields. The forces are so large that efficient control of the translational motion can be achieved by applying only moderate voltages on the electrodes of deceleration devices which can be only a few mm large.

The behaviour of hydrogenic and nonhydrogenic Rydberg atoms in inhomogeneous electric fields in the vicinity of crossings of Stark energy levels and the influence of these crossings on the deceleration process have been studied using high-resolution VUV laser spectroscopy and time-of-flight measurements. In the case of hydrogen, the crossings are exact and are traversed diabatically during the deceleration process, i.e. the hydrogen atoms do not change their quantum state when the crossings are traversed. In the case of nonhydrogenic systems, argon in this study, the crossings are avoided and are traversed adiabatically during the deceleration process. The adiabatic traversal of the crossings leads to changes of the quantum states of the Rydberg atoms and thus to changes in the deceleration/acceleration behaviour. Therefore the maximum electric field strength that can be used in the deceleration of nonhydrogenic atoms and molecules must be kept below the so-called Inglis-Teller field, i.e. the field at which Stark manifolds of adjacent Rydberg states start to overlap. Above the Inglis-Teller field the large number of avoided crossings leads to rapid changes of quantum states which inhibits the deceleration. The characterization of the effects of avoided crossings on the deceleration behaviour necessitated the recording of high-resolution Stark spectra of the Rydberg states of argon and their simulation by multi-channel quantum defect theory.

The deceleration process could be optimized using time-dependent inhomogeneous electric fields. In this case, the electric fields are modified so that the gradients, and therefore also the forces, are always maximal at the instantaneous positions of the Rydberg atoms. Using time-of-flight and imaging techniques, changes in the three-dimensional spatial and velocity distributions after deceleration could be

monitored. The interpretation of the data was aided by simulations of the trajectories of the Rydberg atoms during the deceleration process. For an argon beam with an initial velocity of 580 m/s, the kinetic energy of the particles could be reduced by 10% or $\Delta E_{\text{kin}}/hc = 60 \text{ cm}^{-1}$. This result implies that atoms and molecules with mass $m \leq 14 \text{ u}$ moving in a supersonic beam of xenon can be decelerated from an initial velocity of 320 m/s to zero velocity.

Using this deceleration method it was possible to completely control the spatial and velocity distributions in two dimensions of a cloud of hydrogen atoms. Because the curve crossings are traversed diabatically, large electric field strengths can be used. Moreover, since the mass of hydrogen is small, accelerations of up to $2 \cdot 10^8 \text{ m/s}^2$ could be reached. Depending on the voltage sequences that were applied to the electrodes, the deceleration device also functioned as a normal-incidence mirror, a cylindrical lense, or a two-dimensional trap for the Rydberg atoms. The distributions of positions and velocities of the cloud of atoms in these Rydberg atom optics experiments were monitored by pulsed field ionization.

In the mirroring experiments a supersonic beam of hydrogen atoms was decelerated from 720 m/s to 0 after only 1.9 mm and 4.8 μs of flight, and the Rydberg atoms were brought back to their original position after 9.8 μs .

In the trapping experiments, the hydrogen atoms could be trapped in two dimensions. The temperature of the trapped cloud of Rydberg atoms was determined to be approximately 300 mK and the trapping time was measured to be 50 μs . The initial density of Rydberg hydrogen atoms in the trap could be increased to more than 10^7 cm^{-3} by using a two-photon excitation sequence to prepare the Rydberg Stark states and optimizing the polarization vectors of the laser beams relative to the direction of the electric field vector in the photoexcitation region. It was possible to trap hydrogen atoms in a wide range of quantum states without changing the potentials of the electrodes significantly, demonstrating that the trapping procedure is very versatile. The dynamics of a cloud of hydrogen atoms in the electrostatic trap was studied by pulsed field ionization supported by trajectory calculations of the neutral Rydberg atoms in the trap and of the positive ions after field ionization. The factors limiting the trapping time are discussed.

Zusammenfassung

In dieser Dissertation wird eine auf dem Starkeffekt basierende Methode vorgestellt, die es ermöglicht, die translatorische Bewegung von Atomen und Molekülen in drei Dimensionen zu beeinflussen, und die prinzipiell auf alle Atome und Moleküle in der Gasphase anwendbar ist. Mit dieser Methode können Atom- und Molekülstrahlen abgebremst werden und Proben sowohl kalter als auch langsamer Gasphasenteilchen erzeugt werden, die in hochauflösenden spektroskopischen Experimenten, in Untersuchungen von kalten Kollisionen sowie in der Verarbeitung von Quanteninformation Anwendungen finden können.

Diese neue Methode wurde in Abbremsexperimenten an Argon- und Wasserstoffatomproben in Überschallstrahlen entwickelt und charakterisiert. Sie beruht auf den sehr grossen Dipolmomenten, welche Atome und Moleküle in Rydbergzuständen in Anwesenheit von elektrischen Feldern aufweisen. Wegen dieser Dipolmomente, die 1000 Debye überschreiten können, wirken grosse Kräfte auf die Teilchen, wenn diese sich durch ein inhomogenes elektrisches Feld bewegen. Die Kräfte sind so gross, dass selbst das Anlegen niedriger Spannungen an die Elektroden von Abbremsvorrichtungen mit Abmessungen von wenigen Millimetern genügt, um die translatorische Bewegung der Teilchen effizient zu kontrollieren.

Das Verhalten wasserstoffähnlicher und nichtwasserstoffähnlicher Rydbergatome in inhomogenen elektrischen Feldern in der Nähe von Kreuzungen zweier Starkzustände und der Einfluss dieser Kreuzungen auf das Abbremsverfahren wurden anhand hochauflösender VUV-Laserspektroskopie und Flugzeitmessungen untersucht. Im Falle des Wasserstoffatoms sind diese Kreuzungen aus Symmetriegründen exakt und werden daher während des Abbremsvorganges diabatisch durchquert, so dass die Atome beim Durchqueren der Kreuzungen in ihrem ursprünglichen Quantenzustand bleiben. Bei nichtwasserstoffähnlichen Atomen – Argonatomen in den hier beschriebenen Untersuchungen – sind diese Kreuzungen vermieden und werden somit im Bremsprozess adiabatisch durchlaufen. Dies hat zur Folge, dass die Rydbergatome beim Durchqueren der Kreuzungen von dem ursprünglich angeregten Quantenzustand in einen anderen Quantenzustand übergehen, welcher ein anderes Beschleunigungs- beziehungsweise Bremsverhalten aufweist. Um solche adiabatische Übergänge zu vermeiden, darf beim Abbremsen nichtwasserstoffähnlicher Teilchen die elektrische Feldstärke das sogenannte Inglis-Teller-Feld – das Feld, an dem die Mannigfaltigkeiten der Starkzustände von benachbarten Hauptquantenzahlen anfangen zu überlagern – nicht überschreiten. Oberhalb des Inglis-Teller-Feldes verursacht die Häufung dieser vermiedenen Kreuzungen eine schnelle Änderung der Quantenzustände und verhindert eine effiziente Kontrolle der translatorischen Bewegung der Teilchen. Für die Charakterisierung der Auswirkung dieser vermiedenen Kreuzun-

gen auf das Bremsverhalten bedurfte es hochaufgelöster Spektren der Rydbergstarkzustände von Argon und einer theoretischen Analyse dieser Spektren mit Hilfe der Vielkanalquantendefekttheorie.

Das Abbremsverfahren konnte durch das Verwenden zeitabhängiger elektrischer Felder optimiert werden. Hierbei werden die elektrischen Felder zeitlich so verändert, dass die Feldgradienten, und somit auch die ausgeübten Kräfte an dem Ort, an dem sich die Rydbergteilchen befinden, immer maximal sind. Veränderungen in den dreidimensionalen Positions- und Geschwindigkeitsverteilungen während des Abbremsverfahrens konnten anhand von zeit- und orts aufgelösten Messungen untersucht werden. Die Interpretation der Daten wurde durch Simulationen der Trajektorien der Rydbergatome unterstützt. Die kinetische Energie von Argonatomen mit einer Anfangsgeschwindigkeit von 580 m/s in einem Überschallatomstrahl konnte um 10% oder $\Delta E_{\text{kin}}/hc = 60 \text{ cm}^{-1}$ verringert werden. Aus diesem Ergebnis folgt, dass Atome und Moleküle mit einer Masse von $m \leq 14 \text{ u}$, die sich in einem Überschallatomstrahl aus Xenonatomen mit einer Anfangsgeschwindigkeit von 320 m/s bewegen, vollständig abgebremst werden können.

Mit dieser neuen Methode war es möglich, die örtliche Ausdehnung und Geschwindigkeitsverteilung einer Wolke von Wasserstoffatomen in zwei Dimensionen vollständig zu kontrollieren. Wegen der diabatisch durchquerten Kreuzungen konnten in diesem Fall höhere elektrische Felder angelegt werden. Darüber hinaus konnte wegen der geringen Masse von Wasserstoffatomen eine Beschleunigung von $2 \cdot 10^8 \text{ m/s}^2$ erreicht werden. Je nach der Spannungssequenz, die an den Elektroden angelegt wurde, konnte die Abbremsvorrichtung als Spiegel mit senkrechtem Einfallswinkel, als zylindrische Linse oder als zweidimensionale Falle für Rydbergatome dienen. Die Positions- und Geschwindigkeitsverteilungen der Atomwolke in diesen Rydbergatomoptikexperimenten wurden mittels gepulster Feldionisation untersucht.

In den Experimenten mit dem Rydbergatomspiegel wurden Wasserstoffatome in einem Überschallstrahl von einer Anfangsgeschwindigkeit von 720 m/s nach einer nur 1.9 mm und $4.8 \mu\text{s}$ langen Abbremsstrecke vollständig abgebremst und innert insgesamt $9.8 \mu\text{s}$ zu ihrer ursprünglichen Position zurückgeführt.

In den Experimenten mit der elektrostatischen Rydbergatomfalle konnten die Wasserstoffatome in zwei Dimensionen eingefangen werden. Die Temperatur der eingefangenen Rydbergatomwolke wurde auf ungefähr 300 mK bestimmt und die Zerfallszeit der Population eingefangener Atome auf $50 \mu\text{s}$ abgeschätzt. Die Dichte der angeregten Wasserstoffatome konnte durch Verwendung eines Doppelresonanzanregungsschemas und die optimale Wahl der Polarisationsvektoren relativ zur Richtung des elektrischen Feldes in der Anregungsregion auf mehr als 10^7 cm^{-3} optimiert werden. Die Wasserstoffatome konnten in verschiedenen Quantenzuständen eingefangen werden ohne dass das Potenzial an den Elektroden signifikant verändert werden musste, was auf die Vielseitigkeit der Falle schließen lässt. Die Dynamik der Wasserstoffatomwolke in der elektrostatischen Falle wurde durch gepulste Feldionisation verfolgt und mit Hilfe von Trajektorienberechnungen für die neutralen gefan-

genen Rydbergatome vor und für die Kationen nach der Feldionisation, analysiert. Die Faktoren, die die Zerfallszeit der Rydbergatompopulation in der Falle einschränken, werden diskutiert.

Samenvatting

In dit proefschrift wordt een nieuwe methode beschreven waarmee de beweging van atomen en moleculen beheerst kan worden en die in principe toegepast kan worden op alle atomen en moleculen in de gasfase. Met deze methode, die gebaseerd is op het Stark-effect voor Rydberg-toestanden, kunnen monsters van zowel langzame als koude atomen en moleculen geproduceerd worden. Deze monsters kunnen mogelijk worden gebruikt in bijvoorbeeld hoge resolutie spectroscopie, in studies van koude botsingen en in quantumberekeningen.

De nieuwe afremmethode, die werd ontwikkeld en getest in afremexperimenten op argon en atomair waterstof in supersonische gasstralen, is gebaseerd op de grote dipoolmomenten van atomen en moleculen in Rydberg-toestanden in aanwezigheid van elektrische velden. Deze dipoolmomenten, die groter dan 1000 Debye kunnen zijn, resulteren in grote krachten op de deeltjes in inhomogene elektrische velden. De krachten zijn zo groot, dat de beweging van de deeltjes al beheerst kan worden met lage potentialen op de elektroden van de afreminstrumenten die maar een paar millimeter groot zijn.

Het gedrag van waterstofachtige en nietwaterstofachtige Rydberg-atomen in inhomogene elektrische velden in de nabijheid van een kruising van Stark-energietoestanden en het effect van zo'n kruising op de afremvoortgang werd bestudeerd met behulp van hoge resolutie spectroscopie en door het meten van de vluchtduur van de atomen. Voor atomair waterstof zijn de kruisingen exact en worden diabatisch doorlopen tijdens de afremvoortgang. Dit betekent dat de waterstofatomen in dezelfde quantumtoestand blijven tijdens het doorlopen van de kruisingen. Voor nietwaterstofachtige systemen, argon in dit proefschrift, vermijden de Stark-energietoestanden elkaar en worden de vermeden kruisingen adiabatisch doorlopen tijdens de afremvoortgang. Het adiabatisch doorlopen van de kruisingen leidt tot veranderingen in de quantumtoestanden van de Rydberg-atomen en daardoor tot veranderingen in het afrem- danwel versnelproces. Het maximale elektrische veld dat wordt aangelegd in afremexperimenten dient daarom onder het Inglis-Teller veld gehouden te worden. Het Inglis-Teller veld is het veld waarbij de Stark-energietoestanden van verschillende Rydberg-toestanden beginnen te overlappen. Boven het Inglis-Teller veld voert het grote aantal vermeden kruisingen tot snelle veranderingen van quantumtoestand wat de afremvoortgang hindert. Voor de karakterisering van het effect van vermeden kruisingen op de afremvoortgang was het nodig hoge resolutie Stark-spectra van de Rydberg-toestanden van argon op te nemen en de energietoestanden met behulp van multikanaalquantumdefecttheorie te simuleren.

De afremvoortgang kon worden geoptimaliseerd door tijdsafhankelijke elektrische velden te gebruiken. Daarbij werd het elektrische veld zo aangepast dat de gradien-

ten, en dus ook de krachten, altijd maximaal waren op de positie van het Rydberg-atoom. Met behulp van tijd- en positieopgeloste metingen konden veranderingen in de driedimensionale positie- en snelheidsverdelingen na het afremmen worden gemeten. Simulaties van de banen van de Rydberg-atomen tijdens de afremvoortgang droegen bij tot de interpretatie van de data. Voor een straal van argonatomen met een beginsnelheid van 580 m/s kon de kinetische energie om 10% of $\Delta E_{\text{kin}}/hc = 60 \text{ cm}^{-1}$ verminderd worden. Dit resultaat impliceert dat atomen en moleculen met een massa kleiner dan 14 u, bewegend in een supersonische xenonstraal met een beginsnelheid van 320 m/s, gestopt kunnen worden.

Met behulp van deze afremmethode was het mogelijk de positie- en snelheidsverdelingen van een wolk van waterstofatomen in twee dimensies volledig te beheersen. Omdat de kruisingen diabatisch doorlopen worden, kunnen hogere elektrische velden worden aangelegd. Bovendien is de massa van waterstof klein waardoor versnellingen van $2 \cdot 10^8 \text{ m/s}^2$ konden worden bereikt. Afhankelijk van de spanningssequentie die op de elektroden werd aangelegd, kon de afreminstallatie ook dienen als spiegel waarop de atoomstraal loodrecht invalt, als cilindrische lens of als een tweedimensionale val voor Rydberg-atomen. De positie- en snelheidsverdelingen van de wolk van atomen in deze Rydberg-atoomoptica experimenten werden bestudeerd met behulp van gepulste veldionisatie.

In de spiegelexperimenten werd een supersonische straal van waterstofatomen van 720 m/s tot 0 afgeremd binnen slechts 1.9 mm en 4.8 μs vluchtduur. De Rydberg-atomen werden binnen 9.8 μs naar hun beginpositie teruggeleid.

In de experimenten met de elektrostatische val konden de waterstofatomen ingevangen worden in twee dimensies. De temperatuur van de ingevangen wolk van Rydberg-atomen werd bepaald ongeveer 300 mK te zijn. Het aantal ingevangen waterstofatomen vervalt exponentieel met een tijdsconstante van 50 μs . De aanvankelijke dichtheid van Rydberg-atomen in de val kon worden verhoogd tot meer dan 10^7 cm^{-3} door de Rydberg-atomen aan te slaan met twee resonante fotonen en door de polarisatievectoren van de laserstralen ten opzichte van de richting van de elektrische veldvector te optimaliseren. Het was mogelijk waterstofatomen in een groot bereik van quantumtoestanden te vangen zonder de potentialen aangelegd aan de elektroden te veranderen, wat demonstreert dat de invangprocedure zeer veelzijdig is. De dynamica van een wolk van ingevangen waterstofatomen in de elektrostatische val werd bestudeerd met behulp van gepulste veldionisatie ondersteund door berekeningen van de banen van de neutralen Rydberg-atomen in de val en van de positief geladen ionen na veldionisatie. De factoren die de duur die de atomen in de val ingevangen blijven, limiteren, worden bediscussieerd.

Contents

Abstract	i
1 Introduction	1
1.1 Applications of slow and cold molecules	2
1.1.1 High-resolution spectroscopic experiments	2
1.1.2 Cold collisions	3
1.2 Methods for the production of slow and cold molecules	3
1.2.1 Methods starting from a sample of cold atoms	3
1.2.2 Methods starting from a supersonic beam	4
1.2.3 Other methods	5
1.3 Stark deceleration of Rydberg atoms and molecules	6
2 Rydberg atoms and molecules in electric fields	7
2.1 The hydrogen atom in an electric field.	7
2.2 Nonhydrogenic particles in electric fields	11
2.3 Landau-Zener dynamics at avoided crossings	13
2.4 Field ionization of Rydberg atoms and molecules	14
2.5 The lifetimes of Rydberg states	15
2.5.1 Spontaneous emission	16
2.5.2 Black body radiation	17
2.5.3 Predissociation	18
2.6 Deceleration of Rydberg particles in inhomogeneous electric fields . . .	19
2.7 Numerical simulations	22
3 Experimental setup and methods	25
3.1 VUV generation	25
3.1.1 Dye ring laser setup	27
3.1.2 Pulsed dye-laser setup	28
3.2 Gas beam	29
3.3 Detection system	30
3.3.1 Detection modes	30
3.3.2 Microchannel plate with spatial resolution	32
3.4 Measuring neutral Rydberg atoms	32

3.4.1	Time-of-flight measurements	33
3.4.2	Imaging measurements	35
3.5	Conclusions	37
4	Nonhydrogenic effects in the deceleration of Rydberg atoms	39
4.1	Introduction	39
4.2	Experimental setup	40
4.3	Spectroscopic and deceleration results	41
4.3.1	Stark map	41
4.3.2	Deceleration at avoided crossings	44
4.3.3	Optimizing the deceleration	46
4.3.4	Lifetimes of Rydberg states	47
4.4	Multi-channel quantum defect theory	51
4.4.1	General outline of the theory	52
4.4.2	Results of the calculation	57
4.4.3	Discussion of the MQDT calculations	63
4.5	Conclusions	64
5	Stark deceleration of hydrogen atoms	67
5.1	Introduction	67
5.2	The Runge-Lenz vector	68
5.3	Experimental setup	69
5.3.1	A supersonic beam of hydrogen atoms	69
5.3.2	Electrode setup and excitation scheme	70
5.4	Results	71
5.4.1	Zero-field spectroscopy	71
5.4.2	Polarization effects	72
5.4.3	Acceleration after excitation in homogeneous electric fields	74
5.4.4	Acceleration after excitation in inhomogeneous electric fields . .	76
5.5	Conclusions	78
6	Deceleration of argon using time-dependent inhomogeneous electric fields	81
6.1	Introduction	81
6.2	The electrode setup	81
6.3	Deceleration results	85
6.3.1	Experiments using time-independent fields	87
6.3.2	Experiments using time-dependent fields	88
6.4	Imaging results	91
6.4.1	Experimental results	92
6.4.2	Simulations	96
6.5	Conclusions	97

7	Normal-incidence Rydberg atom mirror	99
7.1	Introduction	99
7.2	Mirrors for atoms and molecules	99
7.3	Experimental methods and techniques	100
7.3.1	Detection of Rydberg atoms by pulsed field ionization	101
7.3.2	Atom mirror pulse sequence	102
7.4	Results	102
7.4.1	Ion TOF measurements	102
7.4.2	Calculations of phase-space distributions	105
7.4.3	Imaging measurements	106
7.5	Conclusions	107
8	Trapping Rydberg atoms	109
8.1	Introduction	109
8.2	Trapping atoms and molecules using electromagnetic fields	109
8.3	Experimental methods and techniques	110
8.3.1	Atom trap pulse sequence	110
8.3.2	The Rydberg atom trap	112
8.4	Results	113
8.4.1	Trapping Rydberg hydrogen atoms	113
8.4.2	Dynamics in the trap	117
8.4.3	SFI measurements	122
8.4.4	Factors limiting the trapping time	126
8.5	Conclusions	128
9	Outlook	129
9.1	High-resolution spectroscopic experiments on slow decelerated Rydberg atoms and molecules	129
9.2	Three-dimensional trapping of Rydberg atoms	131
9.3	Deceleration and trapping of molecules in Rydberg Stark states	132
A	Units and Constant	135
B	s-d and p-p interaction elements for argon	137
	List of figures	139
	List of tables	141
	Bibliography	145
	Curriculum Vitae	157
	Publications	158

Chapter 1

Introduction

Over the last two decades increasing effort has been made to develop general methods to create samples of cold and slow molecules [14, 31]. These studies have partly been motivated by experiments performed on trapped, laser-cooled clouds of atoms. In these experiments the particle-wave duality of matter and the collective nature of the atoms at low temperature was studied in unprecedented detail and variety [2, 3, 16, 20, 28, 51, 78]. Laser cooling experiments rely on many ($\sim 10\,000$) absorption-emission cycles in closed two-level systems. In general, such closed two-level systems do not occur in molecular systems because of the many rotational and vibrational levels. Although a list of molecules which might be laser cooled, including CaH, BeH, and AlCl, is given in reference [30], no molecular sample has been laser cooled so far.

The extension of these experiments to molecular samples is a tantalizing prospect but represents a considerable challenge. Two main difficulties need to be overcome. First, an alternative method to laser cooling must be developed to generate samples of molecules in the (sub)mk temperature range. Second, ways to further reduce the temperature by evaporative cooling must be established. Evaporative cooling can be expected to be particularly difficult in molecular samples because inelastic scattering cross sections are in general larger than elastic scattering cross sections. Whereas no immediate solutions to the second difficulty can be expected in the near future, rapid progress is currently being made to overcome the first difficulty and this thesis describes a possible strategy to generate cold molecular samples.

Samples of cold molecules offer the advantages of a long interaction time with other molecules or with a light source and very low collision energy. The molecules can thus in principle be studied for longer times and with more detail than in a standard molecular beam experiment. Moreover, if the velocity distribution of a sample of molecules can be fully controlled, molecular beams with an adjustable velocity can be produced which can be used in scattering experiments.

Several of the experiments that become feasible with cold and slow molecules are described in section 1.1. An overview of the current methods of decelerating and/or cooling molecules is given in section 1.2.

1.1 Applications of slow and cold molecules

1.1.1 High-resolution spectroscopic experiments

It was shown in reference [87] that the resolution in spectra of transitions between highly excited Rydberg states of krypton was limited by the interaction time of the particles with the millimeter wave (mmw) radiation. In a beam experiment, the measurement time is limited by the transit time of the particle through the interaction region. The transit time can be increased if the beam velocity is reduced. Slow beams and thus long interactions can be reached by seeding the sample gas with a heavy atom, typically xenon. If the velocity of the Rydberg particles can be reduced further such that the particles remain in the mmw field longer, the resolution can be improved so that ultimately the Lorentzian line profile, given by the natural lifetime of the excited states, can be measured.

In reference [123] the resolution of a spectroscopic measurement of the inversion tunneling doubling of ND₃ in the $|JK\rangle = |11\rangle$ state was improved by decelerating part of the supersonic beam of ND₃ molecules from 280 m/s to 52 m/s using the Stark deceleration method described in section 1.2.2. At 280 m/s the full width at half maximum (FWHM) of the transition amounts to 8.7 kHz, limited by the transition time, whereas for the decelerated part of the beam the linewidth could be reduced to 1 kHz. The smaller linewidth enabled the resolution of all allowed hyperfine components of the transition in this part of the spectrum.

In reference [122] the lifetime of the upper component of the Λ doublet of the X $^2\Pi_{3/2}$ $v = 1$, $J = 3/2$ state in OH was measured after decelerating and trapping the OH molecules using the Stark deceleration method. Because this lifetime is large, 59.0 ± 2.0 ms, long interaction times are needed in this measurement, which cannot be performed in a standard molecular beam experiment where the typical interaction times are 2 to 3 orders of magnitude smaller.

The improvement in resolution also opens up the possibility to measure fundamental properties of matter with cold molecules. For instance, references [65] and [119] describe how the electron dipole moment (edm) could be measured using Stark decelerated molecules if it is larger than $\sim 10^{-28}$ e cm. The standard model predicts a much smaller value for the edm but theories which go beyond the standard model predict an edm of 10^{-26} to 10^{-28} e cm. With the aid of cold molecules the predictions of theories beyond the standard model can be tested. Ultra-cold molecular samples may also help in measuring the small frequency shifts caused by the parity-violating weak interaction [96, 97]. Recent calculations [10, 50] predict such shifts to be of the order of a 0.01 Hz and measurement times of several ms will be needed in realistic experiments.

1.1.2 Cold collisions

A second line of research which will undoubtedly benefit from the possibility of generating samples of ultra-cold molecules is the study of chemical reactions at very low collisional energies where the effect of tunneling through the reaction barrier or scattering resonances may be studied in detail. The observation of scattering resonances will in addition require the collisional energy to be tunable. In reference [6] calculations of the reaction probability of the $F + H_2 \rightarrow FH + H$ reaction is given as a function of the total energy. The reaction probability shows large oscillations just above threshold because of bound states in the van der Waals well in the product channel. These resonances might be tuned using electric and magnetic fields [73]. Similar calculations have been reported for the $Cl + HD$ reaction [5] and the $OH + H_2CO$ hydrogen abstraction reaction [64]. Both OH and H_2CO can be decelerated using the Stark deceleration method and therefore the collisional energy can be fully controlled in this reaction.

1.2 Methods for the production of slow and cold molecules

1.2.1 Methods starting from a sample of cold atoms

The coldest molecular samples that have been produced experimentally, were generated by starting from a ultracold sample of atoms in a MOT or a BEC and forming molecules in vibrational levels close to the dissociation limit by photoassociation or by the use of a Feshbach resonance. In the latter case, temperatures of the resulting molecules (6Li_2 [19, 68, 150], or $^{40}K_2$ [53]) well below $1\ \mu K$ could be reached, leading to the first observation of a molecular BEC.

Although many different electronically excited homonuclear and heteronuclear molecules have been formed using the technique of photoassociation, only a few species have been subsequently trapped. The main problem is that the photoassociated molecules rapidly fluoresce back to the ground state. Because in most alkali dimer systems the width of the potential well is much smaller in the ground state than in the excited state, the two atoms are not bound anymore after de-excitation. This problem can be circumvented by exciting a purely long-range state which has a non-negligible Frank-Condon overlap with a vibrationally excited state in the electronic ground state of the molecule. In this way Cs_2 [118, 125], Rb_2 [39] and KRb [132] were trapped in their electronic ground state. The trapping times were on the order of 100 ms and the temperature on the order of $100\ \mu K$.

The disadvantage of both these methods is that they can only be applied to atoms which can be laser cooled and were only proven successful for homo- and heteronuclear alkali dimers. At present, these methods are however best suited to study fundamental physics of cold quantum degenerate molecular gasses such as, for instance, Bose-Einstein condensation (BEC) and BEC-BCS crossover. With the use of dipolar het-

eronuclear alkali dimers also the condensation of dipolar molecules may be studied.

1.2.2 Methods starting from a supersonic beam

The rotating nozzle method

The most direct method to slow down molecules from a supersonic expansion is by directly compensating the high velocity of the particles in the beam through retraction of the nozzle during the expansion phase. Technically this can be achieved by counter-rotating the nozzle with a high rotational frequency. In this way particles can be decelerated and can also be accelerated by reversing the direction of rotation. The advantages of this method are that it can be applied to any molecule in the gas phase and has been successfully used to produce slow CH_3F , O_2 , and SF_6 molecules [55, 56] and that the molecules in the supersonic beam are internally cold, i.e. only the lowest rotational levels are significantly populated. The main disadvantages are that at high rotational frequencies, the intensity of the slow molecular beam drops by a few orders of magnitude and that the lowest attainable velocity is limited by the nozzle rotation period. Another problem is that the beam is always on, necessitating very high pumping capacities.

Stark deceleration of polar molecules

Stark deceleration [14] is based on the shifts, ΔE_{Stark} , of the energy levels of a polar particle induced by an applied electric field. Using inhomogeneous electric fields this energy shift can be converted into a kinetic energy difference and therefore used to slow down dipolar molecules. The highest electric field strength that can be applied in the lab routinely is approximately 200 kV/cm. At such an electric field strength, the Stark shift for a molecule with a dipole of 1 Debye amounts to $\Delta E_{\text{Stark}}/hc \approx 1 \text{ cm}^{-1}$. Because the initial kinetic energy in a molecular beam is typically two orders of magnitude larger, long arrays (50 to 300 stages) of sets of electrodes are needed to decelerate molecules to zero velocity. In the case of ND_3 [13] and OH [121] the slowed down molecular cloud could subsequently be trapped for over 1 second at a density of 10^7 cm^{-3} and a temperature of 50 mK. In other experiments, OH [17], CO [12], and YbF [119] could be decelerated but were not trapped. Molecular optics experiments were also realized, based on the same principles and the successful operations of a molecular storage ring [27], a lens [70], and a mirror [109] has been described.

Optical Stark deceleration

A method applicable to a larger class of molecules is the method of optical Stark deceleration. The electric field in this method is generated by one or more strongly focussed laser beams which are far off resonance from any transition. In these systems the electric field strength is much larger than the static fields generated by

electrodes. The polarizability of the molecule gives rise to much larger forces and more efficient deceleration. In the case of benzene [41] the acceleration in a tightly focussed Nd:YAG beam with a peak intensity of $1.6 \cdot 10^{12} \text{ W/cm}^2$ was measured to be 10^9 m/s^2 leading to a kinetic energy loss of $\Delta E_{\text{kin}}/hc = 51 \text{ cm}^{-1}$ in a time of only 15 ns. This deceleration method poses large demands on the stability of the laser sources and has not been used yet to stop molecules in a supersonic beam.

Billiard-like collisions

Allowing a beam of molecules to collide with an atomic beam at a specific angle is a very general way of producing slow molecules. In a collision experiment of NO with argon, a sample of NO molecules was observed with a velocity distribution centered around zero and a temperature of 400 mK [34]. The density of particles was found to be 10^8 to 10^9 cm^{-3} but these molecules were not trapped.

1.2.3 Other methods

Buffer-gas cooling

The technique of buffer-gas cooling stands out in the sense that it is a true cooling technique, i.e. it is energy dissipative, and not only a slowing technique. It relies on the fact that helium still has a reasonable vapour pressure at temperatures well below 1 K. The cold He vapour can then sympathetically cool any atom or molecule in a beam that is injected into it. In [135] such a cryogenic setup was combined with a magnet producing a quadrupolar field such that paramagnetic particles could be trapped in its minimum. Only particles in low-field seeking states can be trapped. The requirement for efficient cooling and long trapping times is that the elastic cross section (σ_e) is much larger than the spin-flip cross section (σ_s). In CaH $\sigma_e/\sigma_s > 10^4$ where only 100 collisions are needed for rethermalization. In the experiment 10^8 ground state CaH molecules could be trapped with a temperature of $400 \pm 50 \text{ mK}$ and a density of $8 \cdot 10^7 \text{ cm}^{-3}$. The trapping time was 0.5 s. In a similar experiment, 10^{12} NH molecules were cooled to a temperature below 6 K but they were not trapped and diffused out of the detection region in 3.1 ms [33].

Velocity filtering from an effusive beam

The problem of slowing down a beam of cold but fast molecules can be circumvented completely by using an effusive beam and selecting a small part of the low-velocity tail of the Maxwell-Boltzmann distribution. The selection can be achieved by guiding slow polar molecules through a bend electrode setup exploiting the first order Stark effect. Molecules that are too fast will not be deflected enough to follow the curvature of the electrodes and will be lost [99]. After the guide, the slow molecules enter an electrostatic trap similar to the one used in [13] and [121]. In this manner ND_3 , CH_2

and CH_3Cl with a temperature of 300 mK at a density of 10^8 cm^{-3} could be trapped for 130 ms [71, 101]. The disadvantages of this method are that it is only applicable to polar molecules and more importantly that the molecules are not internally cold, although a certain degree of state selectivity has been achieved.

1.3 Stark deceleration of Rydberg atoms and molecules

In this thesis the method of Stark deceleration of Rydberg atoms and molecules is presented and the experimental results using argon and atomic hydrogen are discussed. The deceleration method is based on the large dipoles that Rydberg Stark states exhibit in an electric field. These dipoles result in large forces on the particles when they travel through an inhomogeneous electric field. Because all atoms and molecules can be excited to Rydberg Stark state, this method is applicable to any atom or molecule in the gas phase.

In chapter 2 the behaviour of Rydberg atoms and molecules in electric fields is reviewed and the deceleration method is presented in detail. The experimental setup is described in chapter 3. In chapters 4 and 5 the differences in the deceleration behaviour between nonhydrogenic and hydrogenic systems are illustrated with the example of argon, a nonhydrogenic system, and atomic hydrogen. The deceleration efficiency was optimized using time-dependent electric fields, as described in chapter 6, and the deceleration was studied for a wide range of n values using time-of-flight and imaging measurements, aided by simulations of the trajectories of the Rydberg atoms in the inhomogeneous electric field.

The small mass of the hydrogen atom makes it possible to apply accelerations large enough to fully control the motion of the atoms with inhomogeneous electric fields. Using the deceleration device it was not only possible to stop the hydrogen atoms excited to Rydberg Stark states but also to retro-reflect a beam of hydrogen atoms (see chapter 7) and to trap the decelerated atoms in two dimensions for more than 100 μs (see chapter 8). In these experiments the spatial and velocity distributions of the cloud of Rydberg atoms were studied by pulsed field ionization of the Rydberg atoms and time-of-flight and imaging measurements of the resulting ions.

In the last chapter the extension of the deceleration method to molecular systems such as, for instance, H_2 and D_2 , are discussed. The possibility of trapping atoms and molecules in a three dimensional trap is also considered. Finally the prospects of doing high resolution spectroscopy on such trapped samples are discussed.

Chapter 2

Rydberg atoms and molecules in electric fields

In this chapter the behaviour of Rydberg atoms and molecules in electric fields is described. Expressions for the quantities on which the deceleration of particles excited to Rydberg Stark states is based, such as the energies, the lifetimes, and the field-ionization thresholds of the Stark states, are derived. In the second part the Rydberg Stark deceleration method is presented. All equations are given in atomic units (see appendix A) unless explicitly stated otherwise. Excellent descriptions of the physical properties of atomic Rydberg states are given in [11, 32, 44]. The properties of molecular Rydberg states are discussed in [80, 112].

2.1 The hydrogen atom in an electric field.

The Schrödinger equation describing the relative motion of a proton and an electron interacting with each other electrostatically is given by

$$\left(-\frac{\nabla_e^2}{2} + V\right)\Psi = E\Psi, \quad (2.1)$$

where interactions arising from the electron and proton spins are ignored and the proton is assumed to be infinitely heavy. The Coulomb potential is given by $V = -\frac{1}{r}$ where r is the distance between the two particles. This equation is commonly solved in spherical (polar) coordinates (r, θ, ϕ) and the solutions are the well-known eigenfunctions of the hydrogen atom

$$\Psi_{n\ell m}(r, \theta, \phi) = |n\ell m\rangle = R_{n\ell}(r)Y_{\ell m}(\theta, \phi), \quad (2.2)$$

with eigenenergies corresponding to Balmer's formula [7]

$$E_n = -\frac{1}{2n^2}, \quad (2.3)$$

in which $E = 0$ is chosen to be equal to the field-free ionization threshold. The energy levels only depend on the principal quantum number n and are therefore n^2 fold degenerate.

When an electric field is applied in the z direction the total interaction potential is given by

$$\tilde{V} = -\frac{1}{r} + Fz. \quad (2.4)$$

The symmetry of the potential \tilde{V} is cylindrical and no longer spherical. It is therefore more convenient to use the parabolic coordinates (ξ, η, ϕ) which are related to the regular Cartesian coordinates by the following transformations

$$\xi = r + z \quad (2.5)$$

$$\eta = r - z \quad (2.6)$$

$$\phi = \arctan\left(\frac{y}{x}\right), \quad (2.7)$$

in which $r = \sqrt{x^2 + y^2 + z^2}$. For solutions that can be written as a product

$$\Psi_{nn_1m}(\xi, \eta, \phi) = |nn_1n_2m\rangle = u_1(\xi)u_2(\eta) \exp(im\phi), \quad (2.8)$$

the Schrödinger equation can be separated into two independent equations for $u_1(\xi)$ and $u_2(\eta)$

$$\frac{d}{d\xi} \left(\xi \frac{du_1}{d\xi} \right) + \left(\frac{E\xi}{2} + Z_1 - \frac{m^2}{4\xi} - \frac{F\xi^2}{4} \right) u_1 = 0 \quad (2.9)$$

$$\frac{d}{d\eta} \left(\eta \frac{du_2}{d\eta} \right) + \left(\frac{E\eta}{2} + Z_2 - \frac{m^2}{4\eta} + \frac{F\eta^2}{4} \right) u_2 = 0. \quad (2.10)$$

where Z_1 and Z_2 are two constants which are related to each other by $Z_1 + Z_2 = 1$.

The energy levels of the hydrogen atom in an electric field can be determined by perturbation theory to first order using the zero-field solutions of equations 2.9 and 2.10, see for instance [44]. The zero-field wave functions depend on the principal quantum number n , and also on two quantum numbers n_1 and n_2 , which represent the number of nodes in the u_1 and u_2 wave functions, respectively. They are related to n and $|m|$ by

$$n = n_1 + n_2 + |m| + 1, \quad (2.11)$$

and to Z_1 and Z_2 by

$$Z_1 = \frac{1}{n} \left(n_1 + \frac{|m| + 1}{2} \right) \quad (2.12)$$

$$Z_2 = \frac{1}{n} \left(n_2 + \frac{|m| + 1}{2} \right). \quad (2.13)$$

The parabolic zero-field wave functions $|nn_1n_2m\rangle$ can be expressed using the

spherical $|n\ell m\rangle$ wave functions as basis functions

$$|nn_1n_2m\rangle = \sum_{\ell} |n\ell m\rangle \langle n\ell m|nn_1n_2m\rangle, \quad (2.14)$$

using the expansion coefficients

$$\begin{aligned} \langle nn_1n_2m|n\ell m\rangle &= (-1)^{(1-n+m+n_1-n_2)/2+\ell} \sqrt{2\ell+1} \\ &\times \begin{pmatrix} \frac{n-1}{2} & \frac{n-1}{2} & \ell \\ \frac{m+n_1-n_2}{2} & \frac{m-n_1+n_2}{2} & -m \end{pmatrix} \\ &= \sqrt{\frac{2}{n}} (-1)^{\ell} P_{\ell m}(Z_1 - Z_2), \end{aligned} \quad (2.15)$$

where $P_{n\ell}$ is a normalized associated Legendre polynomial. The parabolic wave functions are therefore a superposition of all ℓ states and ℓ is not a good quantum number anymore and is replaced by the parabolic quantum numbers n_1 and n_2 [44].

Because in a one-photon or a two-photon transition from the ground state only low- ℓ states can be excited, the dilution of low- ℓ character over all Stark states implies that all low- $|m|$ Stark states can be excited but with a reduced intensity compared to the low- ℓ states at zero field.

The (negative) electron charge distributions for $n = 8$, $m = 0$ and $n_1 - n_2 = -7$ to 7 are drawn in figure 2.1. The proton is situated in the middle of the plane for all graphs. From the asymmetric charge distributions along the z axis, one sees that the dipole moment increases with the value of $|n_1 - n_2|$. Therefore, a first-order dependence of the energy on the electric field is expected. Indeed, if the zero-field wave functions are used to calculate the first-order energies one obtains

$$E_{nn_1n_2m} = -\frac{1}{2n^2} + \frac{3}{2}F(n_1 - n_2)n = -\frac{1}{2n^2} + \frac{3}{2}Fkn, \quad (2.16)$$

with $k = n_1 - n_2$. The field thus lifts the degeneracy of the zero-field energy levels partially. For given n and m values there are $n - |m|$ levels which are each $(n - |k|)$ -fold degenerate. The second-order Stark shift can also be calculated and is equal to

$$\Delta E_2 = -\frac{F^2}{16}n^4 \left(17n^2 - 3(n_1 - n_2)^2 - 9m^2 + 19 \right). \quad (2.17)$$

The second-order Stark shift thus lifts the m degeneracy. For low- n states ($n < 30$) in moderate electric field strengths ($F < 500$ V/cm), as is mostly the case in our studies, the first- and second-order corrections suffice to calculate the energy shifts accurately. When the field becomes much higher one has to take into account higher order Stark shifts, see [111, 149] for example.

A plot of the $|m| = 0$ energy levels from $n = 8$ to $n = 14$ as a function of the electric field strength, for field strengths between 0 to 10^5 V/cm is displayed in fig-

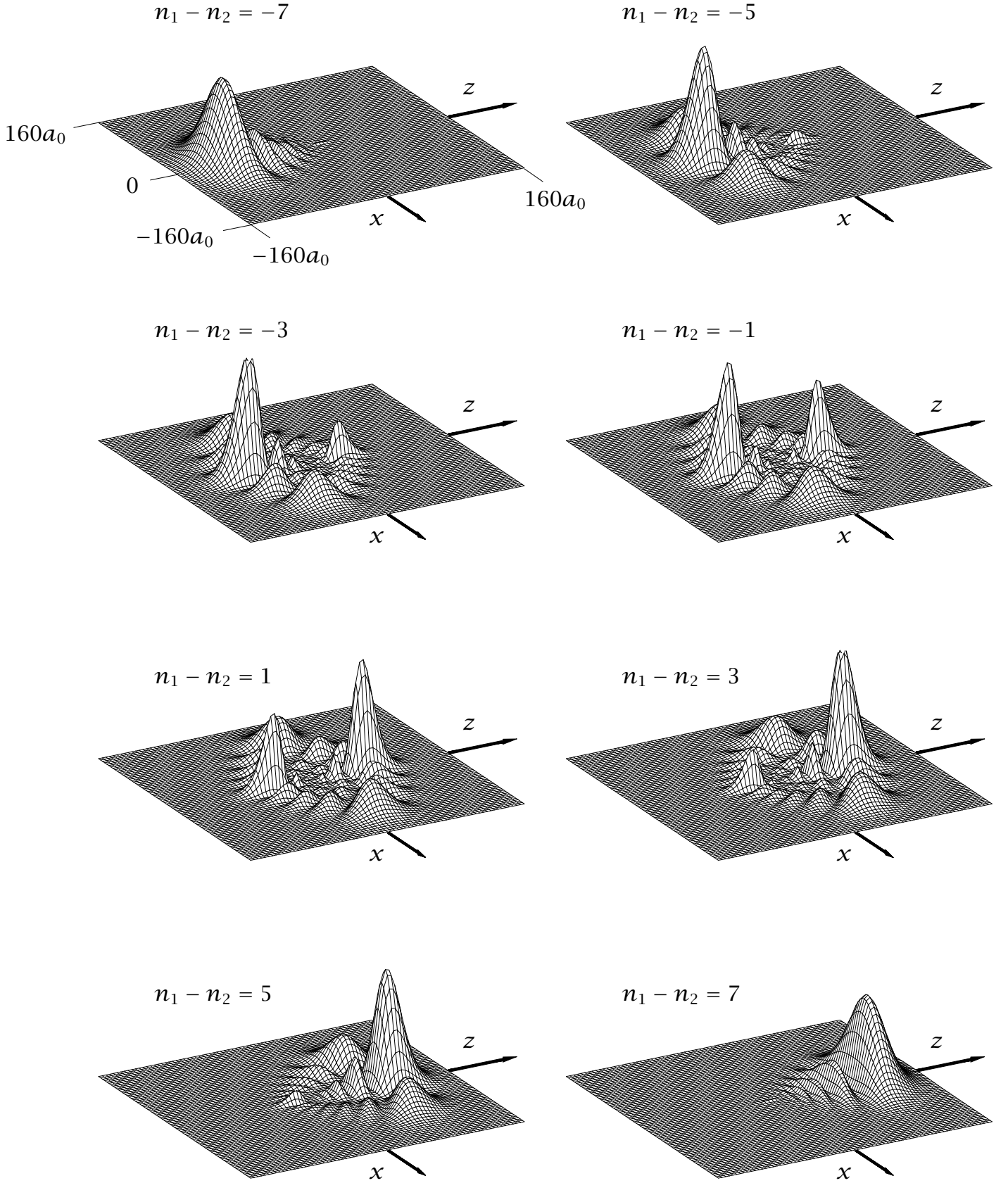


Figure 2.1: Charge density distributions for all $n = 8$, $m = 0$ Stark states. The electric field vector lies parallel to the z axis. The yz plane is $320 a_0 \times 320 a_0$ large.

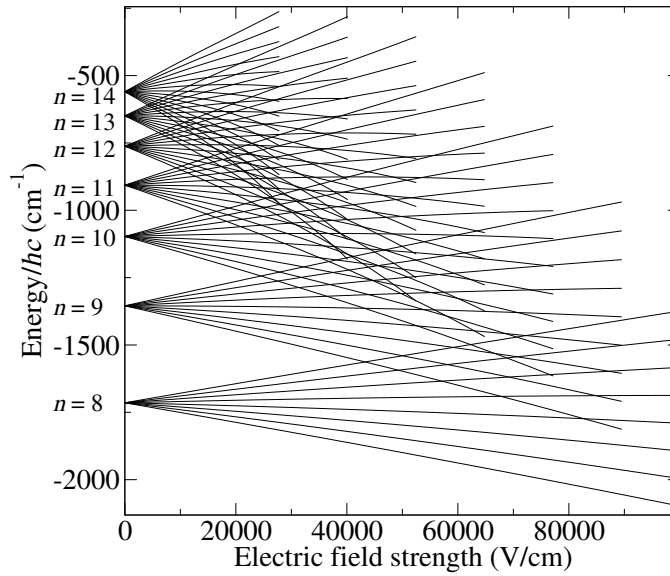


Figure 2.2: Calculated Stark map of the $m = 0$ Stark states of the hydrogen atom with $n = 8$ to 14.

ure 2.2. This type of plots in which the energy of all Stark states in a given range of n -values is drawn as a function of the field is often referred to as a Stark map [117]. As can be seen from this figure, the manifolds of neighbouring n values start to overlap at decreasing electric field strengths when n increases. From the combined Stark shifts of the extreme red and blue shifted states, $-3n^2F/2$ and $3n^2F/2$, respectively, and the spacing between two adjacent zero-field states ($1/n^3$), one can calculate that adjacent manifolds start to overlap at a field

$$F_{IT} = \frac{1}{3n^5}, \quad (2.18)$$

which is called the Inglis-Teller field [66]. In atomic hydrogen, the crossings of the energy levels in the Stark map are exact as will be discussed in more detail in chapter 5.

2.2 Nonhydrogenic particles in electric fields

In all nonhydrogenic atoms and molecules, the potential V in zero electric field is not exactly Coulombic because of the finite size of the positively charged ion core, i.e. the whole atom or molecule with the exception of the Rydberg electron. This deviation from an exact $1/r$ potential has two consequences for the energy-level structure.

First, the degeneracy of the zero-field energy levels is partially lifted as they now also depend on ℓ according to Rydberg's formula [104]

$$E_{n\ell,i} = IE(i) - \frac{1}{2(n - \delta_\ell)^2}, \quad (2.19)$$

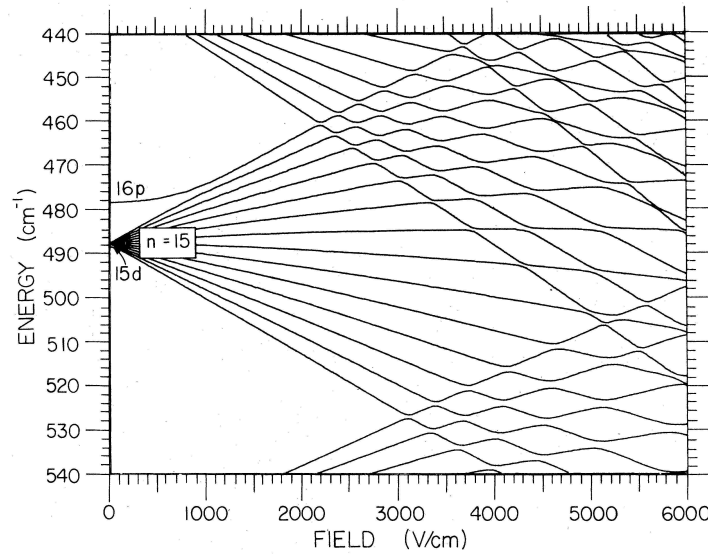


Figure 2.3: $|m| = 1$ Stark map of Na around $n = 15$ taken from [149]. The energy scale corresponds to the binding energy of the Rydberg electron.

in which $IE(i)$ is the energy of the threshold labelled i on which the Rydberg series converges. The quantum defects δ_ℓ for high- ℓ states ($\ell > 3$) are usually smaller than 0.01. In a one-photon transition the resolution is typically at best 0.01 cm^{-1} and these high- ℓ states cannot be resolved from the high- ℓ manifold in zero electric field for $n > 60$. In a Stark map the effect of a small quantum defect is only visible for low electric field strengths [22] because states with a quantum defect of 0.01 or smaller have merged with the high- ℓ manifold within the first 2% of the Inglis-Teller field. Therefore all states with $\ell > 2$ are considered high- ℓ states in this thesis and form the high- ℓ Stark manifold.

At low electric fields, the high- ℓ energy levels start to mix and form a linear Stark manifold in the same manner as in the hydrogenic case. The low- ℓ energy levels, on the other hand, are only subject to a quadratic Stark shift and their energetic positions do not change significantly with increasing electric field, until they start to interact with the hydrogenic Stark manifold of high- ℓ states. As an example, the Na $n = 15$ to $n = 17$, $|m| = 1$ energy levels as determined by Zimmerman et al. [149] are drawn in figure 2.3 which clearly shows the quadratic Stark shift of the 16p state at fields below 1000 V/cm and the interaction with the high- ℓ manifold above this field.

The second deviation from nonhydrogenic behaviour is also visible in figure 2.3: At fields above the Inglis-Teller field the energy levels of adjacent n do not cross exactly, as they do in the hydrogen atom, but most crossings are avoided, leading to an oscillatory behaviour of the energy levels above this field. The magnitude of the energy splittings at the avoided crossings depends on the quantum defects of all ℓ states. Because δ_ℓ is small for high- ℓ states and because $\ell > |m|$, the size of the avoided crossings is strongly reduced at high- $|m|$ values. The $|m|$ values of the

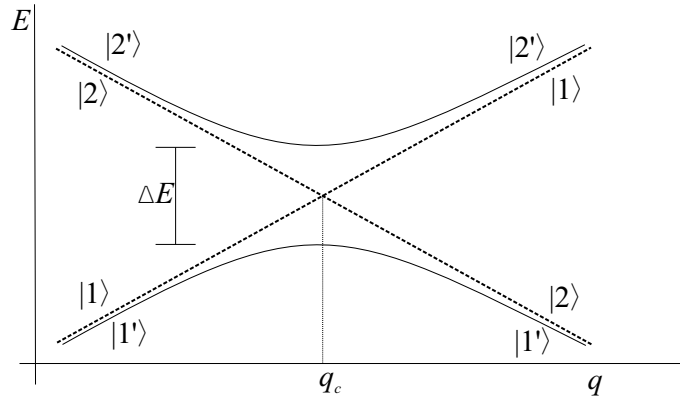


Figure 2.4: Schematic view of an (avoided) crossing in a two level system. The dashed lines represent the evolution of the energy levels as a function of the parameter q , assuming that the levels do not interact (diabatic energy curves $|1\rangle$ and $|2\rangle$). The solid lines represent the energy levels for a nonzero interaction (adiabatic energy curves $|1'\rangle$ and $|2'\rangle$).

states excited in this study always have an absolute value of at most two and thus the avoided crossings between Stark states of neighbouring manifolds need to be considered in detail.

2.3 Landau-Zener dynamics at avoided crossings

As discussed in the previous section, in nonhydrogenic atoms and in molecules the interaction potential of the nucleus with the Rydberg electron is not exactly Coulombic (i.e. $V \neq 1/r$), which causes the crossings between Stark states in a Stark map to be avoided. These crossings occur on the one hand at electric fields and energetic positions where the low- ℓ states start to mix with the high- ℓ manifold of Stark states and on the other hand beyond the Inglis-Teller field where the Stark states of neighbouring n start to interact.

Landau-Zener theory [74, 148] enables one to estimate the probabilities that a quantum mechanical system follows a diabatic (dashed lines in figure 2.4) or an adiabatic path (solid lines in figure 2.4) when a dynamical parameter q is tuned through an avoided crossing. The dynamics at the crossings in a Stark map can be described by Landau-Zener theory as was demonstrated in a study of the behaviour of Stark states in time-dependent fields in [103].

We consider a Hamiltonian \hat{H}_0 which has two eigenstates $|1\rangle$ and $|2\rangle$, the energies, E_1^0 and E_2^0 , of which depend linearly on a tunable parameter q . At a specific value q_c , $E_1^0 = E_2^0$, see the dashed lines in figure 2.4. If the two states interact, the total Hamiltonian is given by $\hat{H}_{\text{tot}} = \hat{H}_0 + \hat{V}$. If \hat{V} is independent of q and is of the form $V_{11} = V_{22} = 0$, $V_{12} = V_{21} \neq 0$, the eigenstates of H_{tot} $|1'\rangle$ and $|2'\rangle$ follow the adiabatic energy curves $E_1'(q)$ and $E_2'(q)$ described by the solid lines in figure 2.4. The adiabatic

energy curves do not cross but have a minimal energy splitting at $q = q_c$ which is equal to

$$\Delta E = 2V_{12} = 2\langle 1|V|2\rangle. \quad (2.20)$$

A particle which is in state $|1'\rangle$ at a value $q_0 \neq q_c$ can now make a diabatic transition to state $|2'\rangle$ when q is changed such that the energies are swept through the crossing. The probability that such a transition takes place is equal to:

$$P_{|1'\rangle \rightarrow |2'\rangle} = \exp\left(-2\pi \frac{|V_{12}|^2}{\hbar(dE/dt)}\right), \quad (2.21)$$

where $(dE/dt) = (d(E_1^0 - E_2^0)/dt)$ is the slew rate. If such a transition occurs the crossing is said to be traversed diabatically whereas if the particle remains in state $|1'\rangle$ the crossing is said to be traversed adiabatically. In electric fields the slew rate is determined by the rate with which the electric field changes (dF/dt) and by the dependence of the Stark states on the electric field (dE/dF) . This last term is to first order equal to $\frac{3}{2}nk - \frac{3}{2}n'k'$ for states within the hydrogenic manifold.

2.4 Field ionization of Rydberg atoms and molecules

One of the most important tools to study Rydberg states is selective field ionization [32, 44] which utilizes the property that the field needed to ionize a Rydberg state decreases rapidly with increasing n and reaches values easily applicable in the laboratory (i.e. < 5000 V/cm around $n = 20$).

For an extreme red-shifted Stark state the electric field required to ionize the particle can be estimated by considering that the potential \tilde{V} (see equation 2.4) has a saddle point on the z axis at $z = -1/\sqrt{F}$ with a value of $\tilde{V} = -2\sqrt{F}$, see figure 2.5. Classically, the electron can escape if the total energy is larger than the potential at the saddle point, a condition that can be expressed for the extreme red-shifted Stark state ($n \approx k$) as

$$E = -\frac{1}{2n^2} - \frac{3n^2F}{2} = -2\sqrt{F}. \quad (2.22)$$

The classical field at which ionization can occur is thus given by

$$F_{\text{ion}}^{\text{red}} = \frac{1}{9n^4}. \quad (2.23)$$

Because the electron density for a blue-shifted Stark state is highest for positive z values (see figure 2.1) and the saddle point is situated on the negative side of the positively charged core, the ionization field for these states is larger by typically a factor of two than the ionization field for red-shifted states with the same n value. Therefore, by applying a field pulse with a variable amplitude one can establish the principal quantum number, and also approximately the k value, of the Rydberg state from the amplitude of the field at which ionization is observed.

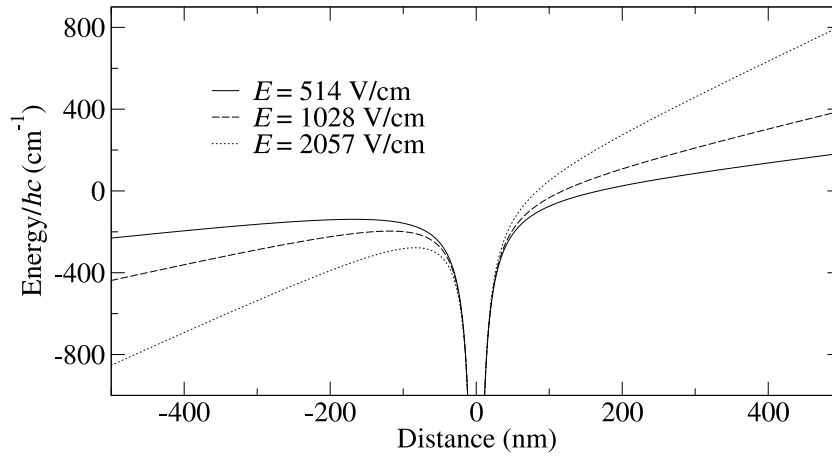


Figure 2.5: Potential energy $\tilde{V}(z)$ felt by a Rydberg electron along the z axis for different electric field strengths.

The condition for (2.22) and thus (2.23) to be valid, is that the crossings between Stark levels are traversed diabatically during the rise of the field-ionization pulse, which tends to be the case for high- n , high- m states and for rapidly rising electric field ionization pulses. If most crossings are traversed adiabatically, the field needed to ionize a Rydberg state is more closely estimated by ignoring the Stark shift in equation 2.22 [67]

$$E = -\frac{1}{2n^2} = -2\sqrt{F}, \quad (2.24)$$

and the ionization field is given by

$$F_{\text{ion}} = \frac{1}{16n^4}, \quad (2.25)$$

irrespective of the k value of the excited state. These two field-ionization limits are called the diabatic and adiabatic field-ionization limits, respectively.

Because the electron is a light particle, it can tunnel through the barrier displayed in figure 2.5 if the field is lower than the classical ionization limit. However, the tunneling rate decreases exponentially at decreasing field strength and the classical ionization limit represents a good approximation as long as short pulses are used.

2.5 The lifetimes of Rydberg states

In a collision-free environment the lifetime of a Rydberg state of a molecule is determined by the spontaneous emission rate, the black body radiation transition rate, the autoionization rate, and the predissociation rate. Predissociation only occurs in molecules and autoionization does not occur below the first ionization limit. The lifetime of atomic Rydberg states below the first ionization limit is thus limited by the

natural lifetime τ and by transitions induced by black body radiation (lifetime τ_{BB}). The total lifetime τ_{total} in this case is given by

$$\frac{1}{\tau_{\text{total}}} = \frac{1}{\tau} + \frac{1}{\tau_{\text{BB}}}. \quad (2.26)$$

The two contributions to τ_{total} are now discussed separately to estimate the lifetime of a Rydberg state below the first ionization limit in an atom. The effect of predissociation on the lifetime of molecular Rydberg states is then discussed in section 2.5.3. The equations in this section are given in S.I. units.

2.5.1 Spontaneous emission

In zero electric field the spontaneous emission lifetime $\tau_{n\ell}$ of Rydberg states is given by

$$\tau_{n\ell} = \left[\sum_{n'\ell'} A_{n'\ell',n\ell} \right]^{-1}, \quad (2.27)$$

where $A_{n'\ell',n\ell}$ is the spontaneous decay rate from a state $n\ell$ to a lower lying state $n'\ell'$ and is given by [11]

$$A_{n'\ell',n\ell} = \frac{4e^2\omega_{n'\ell',n\ell}^3}{3\hbar c^3} \frac{\max(\ell, \ell')}{2\ell + 1} |\langle n'\ell' | r | n\ell \rangle|^2. \quad (2.28)$$

The $A_{n'\ell',n\ell}$ coefficients depend on the third power of the energy difference $\hbar\omega_{n'\ell',n\ell}$ between the two states. The decay rate, and hence the lifetime, of a Rydberg state that is optically accessible from the ground state, $|\text{GS}\rangle$, in a one-photon process, ($|\langle n'\ell' | r | \text{GS} \rangle|^2 \neq 0$) is therefore dominated by transitions back to the ground state provided that the ground state has an energy that is much lower than that of the first excited state. Furthermore, states which can be excited in a one-photon transition from the ground state typically have a shorter radiative lifetime than states that are not optically accessible from the ground state. If, for instance, in the ground state the outer valence electrons have p symmetry, as is the case for the rare gases, the lifetimes of the ns and nd Rydberg states are typically shorter than those of the other $n\ell$ states which can only radiate to excited states.

To determine the scaling of $\tau_{n\ell}$ with n , one has to realize that for increasing n in a Rydberg series, $\omega_{n'\ell',n\ell}$ approaches a constant. The evolution of the lifetime with increasing n is therefore dominated by the change in the Rydberg electron wave function in the immediate vicinity of the ion core. Because the amplitude of the wave function scales as $n^{-3/2}$ [44], the lifetime scales as

$$\tau_{n\ell} \propto n^3, \quad (2.29)$$

typical values for low- ℓ states being $\tau \approx 1 \mu\text{s}$ at n values around 10.

The lifetime of a Stark state can be calculated with the aid of equation 2.15

$$\frac{1}{\tau_{nn_1n_2m}} = \sum_{n\ell} |\langle nn_1n_2m | n\ell m \rangle|^2 \frac{1}{\tau_{n\ell}}. \quad (2.30)$$

The lifetime of a Stark state is thus limited by the $n\ell$ states which have the shortest lifetime. If the valence electron in the ground state is assumed to have p symmetry, the lifetimes of the s and d states are much shorter than for all other ℓ states, and equation 2.30 reduces to

$$\frac{1}{\tau_{nn_1n_20}} = \frac{|\langle nn_1n_20 | n20 \rangle|^2}{\tau_{nd}} + \frac{|\langle nn_1n_20 | n00 \rangle|^2}{\tau_{ns}}, \quad (2.31)$$

for $m = 0$ Stark states. Consequently the lifetime of the Stark state is approximately a factor $n/2$ longer than that of the ns and nd states because the low- ℓ character of the wave function is reduced by the field-induced admixture of high- ℓ components. Moreover, because the number of states over which the low- ℓ character is diluted grows linearly with n , the spontaneous emission lifetime of a Stark state scales as n^4 instead of n^3 for low- ℓ states. Typical radiative lifetimes of Rydberg Stark states with $n \approx 20$ therefore amount to several tens of microseconds.

2.5.2 Black body radiation

The 300 K background radiation coming from the environment can induce transitions between Rydberg states because the spacing between two adjacent Rydberg states for $n > 15$ is much smaller ($< 65 \text{ cm}^{-1}$) than $\frac{kT}{hc} \approx 200 \text{ cm}^{-1}$. The photon occupation number

$$\bar{n} = \frac{1}{e^{h\nu/kT} - 1}, \quad (2.32)$$

is small for energy splittings above $h\nu = kT$ but grows like $\bar{n} = \frac{kT}{h\nu}$ for $h\nu \ll kT$. For levels with $n > 15$, the decay rate $K_{n\ell}^{\text{BB}}$ caused by transitions induced by black body radiation is given at zero electric field to good approximation by [44]

$$K_{n\ell}^{\text{BB}} = \frac{1}{\tau_{n\ell}^{\text{BB}}} = \frac{4\alpha^3 kT}{3\hbar n^2}, \quad (2.33)$$

and is independent of ℓ . The black body decay rates are therefore the same for each Stark state and are given by equation 2.33. It is important to note that $\tau_{n\ell}^{\text{BB}}$ increases slower ($\propto n^2$) than the spontaneous emission lifetime ($\propto n^3$) and the decay induced by black body radiation will always dominate at high n .

For $h\nu \ll kT$ the transition rate between two Stark states i, j induced by black body radiation is given by [44, 49]

$$\Gamma_{ij} = \bar{n} \frac{8\pi h\nu^3}{6\epsilon_0 \hbar^2 c^3} |d_{ki}|^2 = kT \frac{8\pi \nu^2}{6\epsilon_0 \hbar^2 c^3} |d_{ij}|^2, \quad (2.34)$$

where $|d_{ij}|^2$ is the square of the transition moment between states i and j . Contrary to spontaneous emission, which favours transitions to low- n states, black body radiation induces transitions to neighbouring n states because the energy splitting is then small and thus the photon occupation number large according to equation 2.32. Moreover, one can see from figure 2.1 that the transitions will predominantly take place between Rydberg Stark states of similar k values because the wave function overlap is largest for these states. Black body radiation therefore leads to a redistribution among states with similar n and k values on the time scale $\tau_{n\ell}^{\text{BB}}$ [46] which amounts to $19.6 \mu\text{s}$ for $n = 20$

2.5.3 Predissociation

To extend the Rydberg Stark deceleration method to molecules, the effect of predissociation on the lifetimes of the Rydberg states must be considered. For Rydberg states in molecules, predissociation is almost always energetically allowed and can be much faster ($\sim\text{ps}$) than the timescale on which the deceleration process takes place ($\sim\mu\text{s}$). In H_2 , for instance, strong predissociation was measured for isolated Rydberg states belonging to series converging on the lowest ionization thresholds of ortho and para H_2 , and the corresponding Rydberg states were found to decay within the first 7 ns after excitation [89].

Nevertheless, millimeter-wave spectra of transitions between nd and $n'p$ and $n'f$ Rydberg series in H_2 in this energetic region, with n and $n' = 50$ to 60 , have been recorded at a resolution limited by the measuring time of up to $6 \mu\text{s}$ [88, 89], indicating that many Rydberg states do not predissociate on this timescale and are metastable. Predissociation can either be inhibited by symmetry or because the intermediate state is a high- ℓ state ($\ell > 2$), the wave function of which has little overlap with the core. In many other molecular systems pulsed-field-ionization zero-electron-kinetic-energy (PFI-ZEKE) [100] spectra were recorded, for which the high-Rydberg states below the ionization thresholds need to live for more than the typical delay of 1 to $3 \mu\text{s}$ between excitation and ionization. It was suggested in references [26, 79] that the lifetimes of these so-called “ZEKE” states can be prolonged by a factor of n^2 by ℓ and m mixing induced by stray electric fields, in particular by the fields of ions in the excitation region [90].

In an electric field the $m = 0$ Stark states are a superposition of all ℓ states. It therefore suffices that only one of the low- ℓ states predissociates on a ns timescale for Stark states in the range $n = 15$ to 25 to predissociate well within $1 \mu\text{s}$ so that deceleration experiments which require several μs become impossible. On the other hand, Stark states with $|m| > 2$ do not contain any low- ℓ components and can be expected to be long lived.

In references [9, 59] a method is proposed to project the low- $|m|$ states, which are typically excited in a one- or two-photon transition, on higher $|m|$ states by applying a rotating electric field. Because in a homogeneous electric field Stark states with dif-

ferent m values do not interact, the populated low- m components will decay but the higher- m components are free of low- ℓ character and will be very stable. A second method to excite high- m Rydberg states is by using a multi-photon excitation scheme in which all laser beams are polarized perpendicular to the electric-field axis or are circularly polarized. In each step, $\Delta m = \pm 1$ and in a three-photon transition states with $|m| = 3$ can be excited from an $m = 0$ ground state. As mentioned above, these high- $|m|$ Stark states do not possess core penetrating low- ℓ character and are stable against predissociation. Moreover, the suppression of low- ℓ character also increases the spontaneous emission lifetime so that these states are truly long lived, their lifetime only being limited by black body radiation induced transitions. The experiments on the deceleration of atomic Rydberg states described in this thesis can thus also be carried out on molecular systems as long as high- $|m|$ Rydberg Stark states are used.

As already mentioned in section 2.2, the avoided crossings between the Stark states of different n manifolds are strongly reduced for $|m| > 2$ states and the probability that the avoided crossings are traversed diabatically is increased. The diabatic traversal of crossings between different Stark states greatly facilitates the Rydberg Stark deceleration, as will be explained in chapters 4 and 5.

2.6 Deceleration of Rydberg particles in inhomogeneous electric fields

The idea to use Rydberg Stark states in inhomogeneous electric fields to manipulate the velocity of atoms and molecules was proposed more than 20 years ago [21] and is based on the linear dependence of the energy levels of the Stark manifold on the electric field strength, see equation 2.16. The force on a Rydberg particle in an inhomogeneous electric field can be calculated to first order by taking the gradient of equation 2.16

$$\vec{f} = -\nabla E_{\text{Stark}} = -\frac{3}{2}nk\nabla F = |\vec{\mu}_{\text{el}}|\nabla F. \quad (2.35)$$

From this equation one sees that an inhomogeneous electric field ($\nabla F \neq 0$) induces a force on the Rydberg particle because of the large dipoles $|\vec{\mu}_{\text{el}}| = \frac{3}{2}nk$ these particles exhibit: when $n = 20$ and $|k| = 19$, $|\vec{\mu}_{\text{el}}| = 1450$ Debye, which is three orders of magnitude larger than the dipoles typical of polar gas-phase molecules in their ground state; for instance $|\vec{\mu}_{\text{el}}| = 1.47$ Debye for NH_3 . Because all atoms and molecules have Rydberg Stark states with large dipoles, equation 2.35 is valid for all atoms and molecules.

In atomic and molecular beams, the particles predominantly move in one direction, the propagation axis. The mean velocity perpendicular to this axis is zero and the perpendicular temperature lies well below 1 K. In this thesis we call a change in velocity perpendicular to the propagation direction deflection and a change in velocity parallel to the propagation axis deceleration/acceleration. It is easier to deflect

an atomic or molecular beam because the initial velocity is close to zero. This also explains why experiments deflecting an atomic beam using magnetic fields and the Zeeman effect were carried out 75 years ago but the corresponding deceleration experiment has not been performed yet.

If ∇F , and thus \vec{f} , has a component perpendicular to the beam propagation axis, the particles will be deflected, as was shown in [120] for krypton atoms and in [95, 145] for hydrogen molecules. The direction and the magnitude of the deflection in a specific applied potential can be tuned by changing the k value of the excited Stark state.

Rydberg particles can be decelerated or accelerated if \vec{f} has a component in the direction parallel to the beam propagation axis. If $\nabla F < 0$ ($\nabla F > 0$), states with $k < 0$ ($k > 0$) are decelerated and states with $k > 0$ ($k < 0$) are accelerated. If both the particle velocity vector and ∇F lie along the z axis the kinetic energy difference can be calculated by taking the integral of (2.35) along the particle trajectory

$$\Delta E_{\text{kin}} = -\frac{3}{2}nk \int_{z_i}^{z_f} (\nabla F)_z(z, t) dz. \quad (2.36)$$

In equation 2.36 $\nabla F(z, t)$ corresponds to the field gradient at the instantaneous position of the particle, and z_i and z_f represent the initial and final positions of the particle, respectively. For time-independent electric fields the integral reduces to

$$\Delta E_{\text{kin}} = -\frac{3}{2}nk(F(z_f) - F(z_i)) = -\frac{3}{2}nk\Delta F, \quad (2.37)$$

and the kinetic energy difference is proportional to the electric field difference. In this case, the deceleration/acceleration process can thus be understood as a conversion between kinetic energy and the potential energy generated by the inhomogeneous electric field, i.e. the Stark shift. By selectively exciting a specific k value, it is possible to vary the acceleration the particles are subject to.

As will be shown in section 4.3.2 the maximal electric field strength for which the deceleration mechanism is still efficient in nonhydrogenic systems is the Inglis-Teller field, because of the avoided crossings that occur above this field. Thus the maximal kinetic energy difference in time-independent electric fields for particles with $k \approx -n$ becomes

$$\Delta E_{\text{kin}}^{\text{max}} = -\frac{3}{2}nk(0 - F_{\text{IT}}) = \frac{-1}{2n^3}, \quad (2.38)$$

which is equal to half the splitting between two adjacent Rydberg states at zero field. The maximal kinetic energy difference thus becomes smaller when n is increased and the optimal value of n is a compromise between a sufficiently long lifetime, which increases with increasing n , as explained in section 2.5, and a sufficiently large kinetic energy difference.

To illustrate these general principles two possible electrode configurations to decelerate Rydberg particles are displayed in figure 2.6. Figure 2.6 also shows the

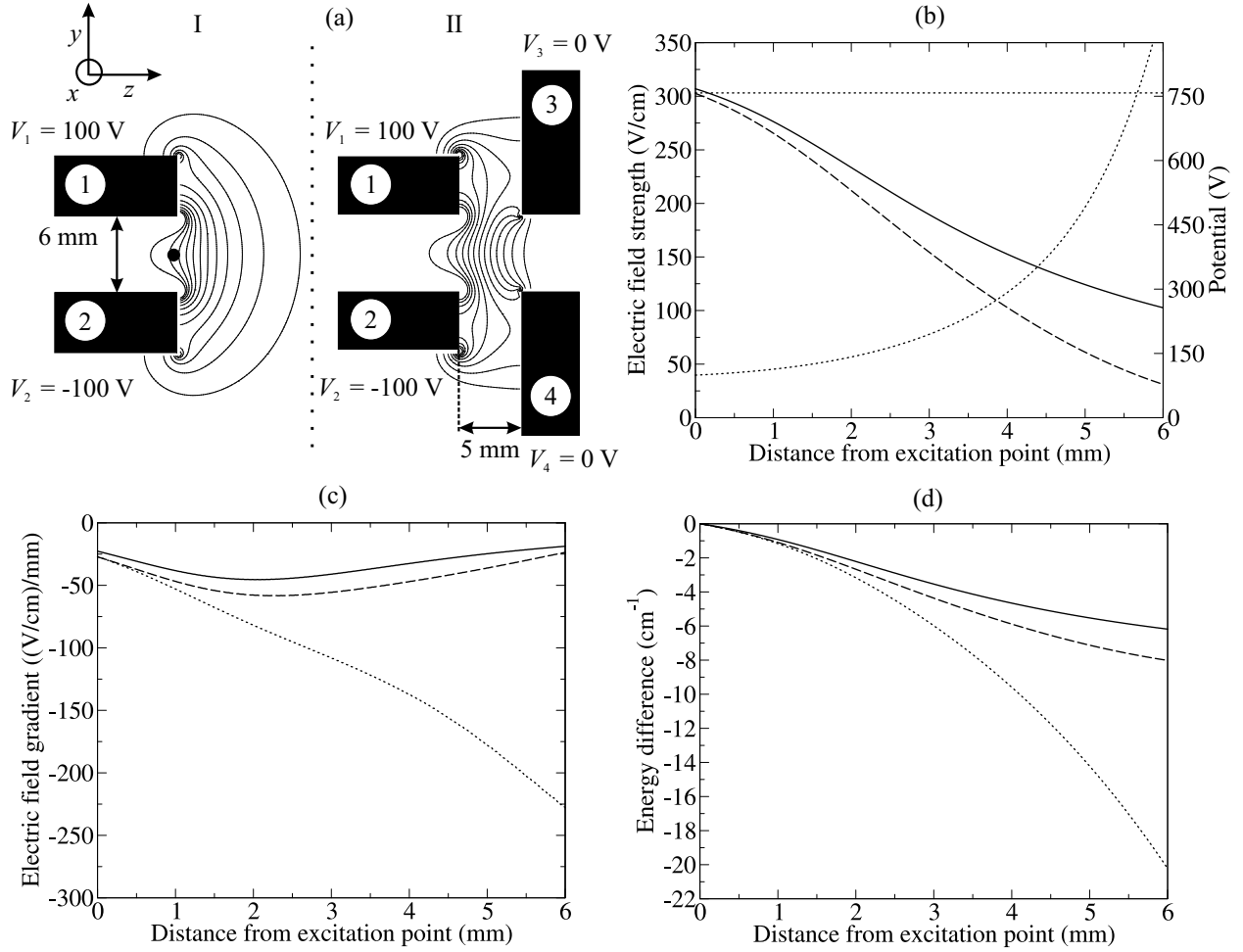


Figure 2.6: Panel a: Two possible electrode configurations to decelerate Rydberg particles. The solid lines represent lines of constant electric field ranging from 50 V/cm to 325 V/cm in steps of 25 V/cm (setup I) and from 25 V/cm to 325 V/cm in steps of 25 V/cm (setup II). Panel b: Electric field strengths on the z axis for setup I with $V_1 = -V_2 = 100$ V (solid line), for setup II with $V_1 = -V_2 = 100$ V and $V_3 = V_4 = 0$ V (dashed line), and for setup II with increasing $V_1 = -V_2$ such that the electric field strength remains constant (constant dotted line). The rising dotted line indicates the increase in potential on electrode 1 and 2 as a function of the position of the Rydberg particle. Panel c: Electric field gradients for the three situations in panel a. Panel d: kinetic energy differences reached as a function of z .

distributions of electric fields (panel (b)) and field gradients (panel (c)) and the kinetic energy loss of a Rydberg particle excited to the $n = 22$, $k = 21$ Stark state at the position indicated by the black dot in setup I. The particles move with an initial velocity v_i through the electrodes in the z direction. In both configurations the potentials on the electrodes 1 and 2 (100 V, -100 V) are such that the particles are excited in a field just below the Inglis-Teller field. In setup II the potentials on electrodes 3 and 4 are zero. The resulting electric field strength as a function of z is shown in panel (b) (solid line: setup I, dashed line: setup II) for z between 0 (the excitation point) and $z = 6$ mm. The two additional electrodes in setup II cause the electric field gradients

to be larger (dashed line in panel (c)) compared to those for setup I (solid line in panel (c)). The kinetic energy difference (panel (d)) over the first 6 mm is therefore also slightly larger for setup II than for setup I, as expected from equation 2.37.

The kinetic energy difference can be optimized by increasing the potentials on the first two electrodes continuously (rising dotted line in panel (b)) such that the electric field strength is always constant ($F = F_{IT}$) at the instantaneous position of the particles (constant dotted line in panel (b)). The gradients at the instantaneous position of the particles (dotted line in panel (c)) are now much larger than in the time-independent case and consequently also the kinetic energy difference as calculated using equation 2.36 (dotted line in panel (d)). After 6 mm, the kinetic energy loss is now 21 cm^{-1} instead of 8 cm^{-1} , and the potentials on the first two electrodes have increased to more than 800 V.

2.7 Numerical simulations

Equations 2.35 to 2.38 give a qualitative and quantitative understanding of the trajectories of individual particles within the deceleration setup. To simulate the functioning of the decelerator for a realistic experimental situation, the velocity and position distributions of the cloud of Rydberg particles has to be considered. For this purpose, a numerical trajectory simulation program was written. The simulation procedure is based on a numerical calculation of the distributions of potentials within the decelerator for a set of specific potentials on the electrodes. The distributions of potentials were calculated using SIMION. From these potential distributions, the electric field and the gradient of the electric field can be calculated at every point for arbitrary values of the potentials applied to the electrodes.

The excitation of the particles is simulated by randomly sampling the spatial overlap between the VUV-laser beam and the gas beam, taking into account the Gaussian shape of the VUV-laser beam. The three components of the velocity vector are also chosen randomly within a Gaussian distribution with a specific central velocity and a specific temperature for each direction.

The actual trajectory calculation is carried out in a stepwise manner with a time-step size of 10 ns. At every time step, the force on the particles is calculated using equations 2.16 and 2.17. If the electric field strength at the position of a nonhydrogenic particle exceeds the Inglis-Teller limit, the force is set to zero. Particles are removed from the trajectory simulation if they enter a region where the electric field strength exceeds the ionization field strength. From the force, the acceleration and the changes in velocity and position are calculated. Because the electric field is homogeneous in the x direction (see figure 2.6a), the electric field gradients, and thus the forces, in this direction are zero.

The particles either fly to the MCP where their times of flight and their impact positions are measured or they are field ionized after a specific delay. In the field-

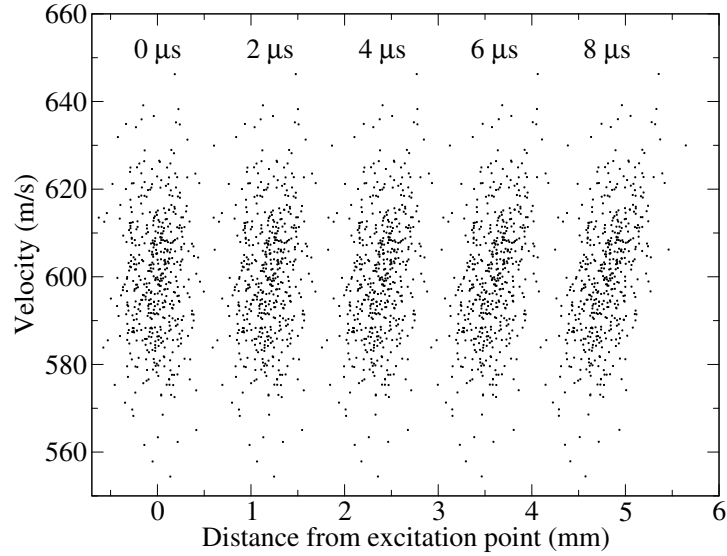


Figure 2.7: Phase-space plot of a cold ($T = 1$ K) cloud of argon atoms moving with a constant mean velocity of 600 m/s. In the simulation 1000 atoms were excited.

ionization experiments, the field pulse is simulated by a time-dependent increase of the ionization potentials using a tangens hyperbolicus function. The rise time is approximately 50 ns and the neutral Rydberg particles are ionized when the local electric field strength exceeds the ionization field strength. After ionization, the force on the ions is given by

$$\vec{f} = q\vec{F}. \quad (2.39)$$

The trajectory of the ion is calculated in a stepwise manner until it reaches the detector where the ion time of flight and the impact position are registered, or until the ion collides with an electrode or with the walls of the chamber in which case the ion is removed from the simulation.

The behaviour of the atom cloud within the electrodes is monitored in the simulation by plotting the position vs. the velocity in one dimension for a large number of particles (~ 1000) at specific times (for instance every μs). From these so-called “phase-space plots” one can assess how the spatial and velocity distributions change within the decelerator over time.

A particularly simple example is the phase-space plot of a cloud of argon atoms moving with a constant velocity shown in figure 2.7. The mean velocity and the translational temperature were chosen to be 600 m/s and 1 K, respectively. The spatial distribution is given by a Gaussian distribution with a Gaussian width of 0.5 mm. Because the fast particles move further than the slow particles in the same amount of time, the spatial distribution stretches as a function of time and the phase-space distribution rotates. Figure 2.7 corresponds to the situation encountered in a pulsed,

skimmed supersonic expansion in free space and illustrates the collision-free nature of the beam.

Experimental setup and methods

3.1 VUV generation

The figure contains two energy level diagrams. The left diagram, labeled 'sum-frequency mixing', shows a ground state at the bottom. A vertical arrow labeled ν_{UV} points to an intermediate level. From this intermediate level, a second vertical arrow labeled ν_2 points to a final level. A dashed horizontal line is shown above the final level. The right diagram, labeled 'difference-frequency mixing', also shows a ground state at the bottom. A vertical arrow labeled ν_{UV} points to an intermediate level. From this intermediate level, a second vertical arrow labeled ν_2 points down to a final level. A dashed horizontal line is shown above the final level. The label 'two-photon resonance' is placed between the two diagrams, indicating the condition where the sum of the two photon frequencies equals the energy difference between the ground and final states.

25

cause no nonlinear crystals exist that can be used to generate VUV radiation below ~ 189 nm, the nonlinear frequency up conversion is achieved in gases such as the rare gases [60] or mercury vapour [61]. The second-order susceptibility, which is used for sum- and difference-frequency mixing in nonlinear crystals, vanishes in isotropic media and the lowest-order nonlinear process in gases is four-wave mixing. The efficiency of a four-wave mixing process is proportional to the square of the third-order susceptibility and the square of the density of the nonlinear gas.

The generation of VUV radiation below 105 nm, a region also called XUV (extreme ultraviolet), is further complicated by the fact that no solid-state material transmits radiation in this region of the electromagnetic spectrum. The nonlinear medium can therefore not be contained in a cell if radiation below 105 nm is generated and the nonlinear gas must be confined in a pulsed gas beam in the same extended vacuum system in which the spectroscopic experiments that use the XUV radiation are performed. By using small orifices between the different parts of the differentially-pumped vacuum system, the background pressure in the photoexcitation region can be kept three orders of magnitude lower than the background pressure of typically 10^{-4} mbar in the part of the vacuum system where the XUV radiation is generated.

In the four-wave-mixing process, the interaction of intense laser beams, which overlap spatially and temporally, with the nonlinear gas gives rise to higher harmonic frequencies when they travel through the nonlinear medium. Because the third-order susceptibility is small compared to the first-order susceptibility but large compared to susceptibilities of higher orders, laser beams of moderate peak intensity ($\sim 10^8$ W/cm²) can be used to generate VUV radiation of sufficient intensity for spectroscopic experiments to be performed.

The intensity of the generated VUV radiation can be enhanced if the combined energy of two input photons corresponds to a two-photon resonance ($2\nu_{UV}$) starting from the ground state of the nonlinear gas, see figure 3.1. The output frequencies are then equal to the third harmonic $\nu_{VUV} = 3\nu_{UV}$, the sum frequency $\nu_{VUV} = 2\nu_{UV} + \nu_2$, and the difference frequency $\nu_{VUV} = 2\nu_{UV} - \nu_2$. All other four-wave mixing frequencies, such as $\nu_{VUV} = 3\nu_2$ for instance, are not resonantly enhanced at the two-photon level and therefore have a much lower intensity.

The experiments described in this thesis all made use of VUV radiation generated by resonance enhanced sum- and difference-frequency mixing in krypton using the two-photon resonance

$$4p^6\ ^1S_0 \longrightarrow 4p^5\ (^2P_{3/2})5p[1/2](J=0), \quad (3.1)$$

at $E/hc = 94092.8678$ cm⁻¹, for which $\nu_{UV}/c = \tilde{\nu}_{UV} = 47046.434$ cm⁻¹. Using frequency-doubling and mixing β Barium-Borate (BBO) crystals this wave number can be reached by doubling the frequency of the laser output at 15682.145 cm⁻¹ and mixing the doubled output with the fundamental beam. The VUV frequency was tuned by changing the frequency of the second laser, ν_2 .

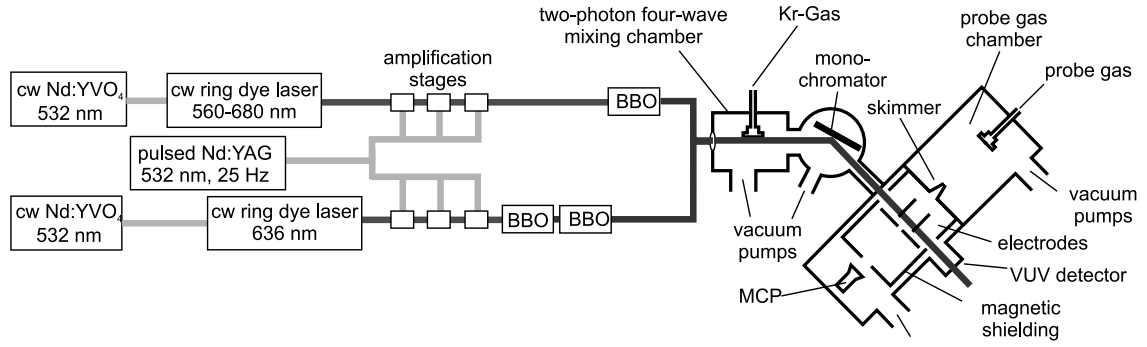


Figure 3.2: Experimental setup used in the experiments on argon. The setup is discussed in detail in section 3.1.1.

In the argon experiments it was essential to spectroscopically resolve the fine structure of the Rydberg Stark states in order to fully interpret the Rydberg Stark deceleration experiments. The experiments were therefore carried out with the narrow-band VUV laser system described in section 3.1.1. The energy-level structure of atomic hydrogen is sufficiently well known that a low resolution laser suffices in the experiments, and the simpler and more versatile VUV laser system described in section 3.1.2 was used to excite the atoms.

3.1.1 Dye ring laser setup

The laser system described in reference [63] and depicted in figure 3.2, was used to generate the XUV radiation with a wave number between $\tilde{\nu}_{\text{XUV}} \approx 126600 \text{ cm}^{-1}$ and $\tilde{\nu}_{\text{XUV}} \approx 127000 \text{ cm}^{-1}$ needed to excite argon from the $(3p)^6 {}^1S_0$ ground state to $n = 15$ to 30 Rydberg states belonging to series converging on the ${}^2P_{3/2}$ ionic ground state. These wave numbers were reached by sum-frequency mixing using the two-photon resonance 3.1 and $\tilde{\nu}_2 = 32500$ to 32900 cm^{-1} .

The single-mode outputs of two continuous-wave dye ring lasers were pulsed amplified in three successive dye cells pumped by the doubled output of a Nd:YAG laser. The wave number of the first ring laser was locked to an iodine line such that $6\tilde{\nu}_1 = 2\tilde{\nu}_{\text{UV}} = 94092.906 \text{ cm}^{-1}$. To generate $\tilde{\nu}_{\text{UV}} = 3\tilde{\nu}_1$, the pulse-amplified output was doubled in a BBO crystal and the doubled beam subsequently mixed with the fundamental beam in a second BBO crystal. The resulting VUV beam was then spatially and temporally overlapped with the doubled, pulse-amplified output of the second ring laser.

The four-wave mixing process took place in a pulsed, supersonic krypton beam and the sum-frequency radiation was separated from the other light beams using the first diffraction order of a grating monochromator. The number of photons per pulse of the resulting XUV radiation amounts to 10^8 to 10^9 after the monochromator at a

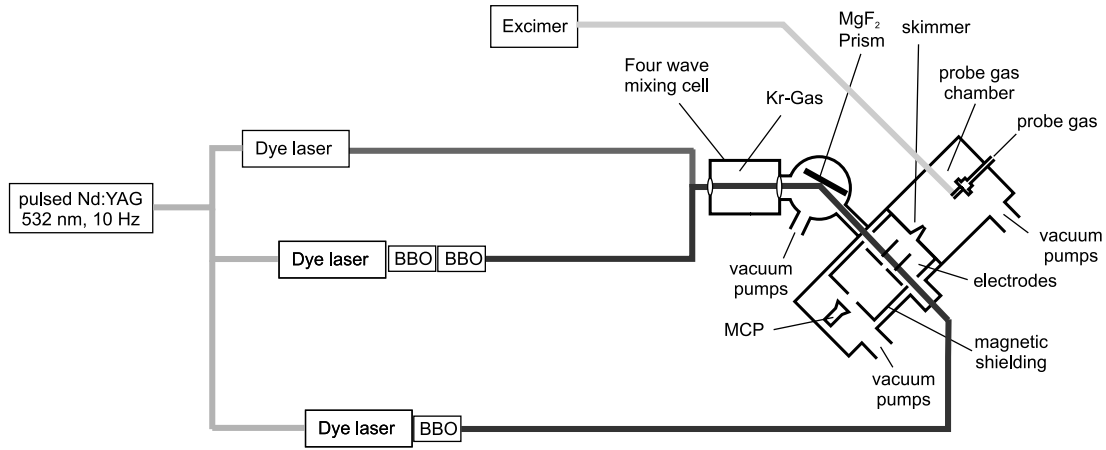


Figure 3.3: Experimental setup used in the experiments on atomic hydrogen. The setup is discussed in detail in section 3.1.2.

repetition rate of 25 Hz. The bandwidth of the XUV laser is approximately 0.008 cm^{-1} . The pulse length is $\sim 2 \text{ ns}$ and the XUV radiation is therefore nearly Fourier-transform limited as expected for the amplification and frequency up conversion of a single-mode cw laser beam. With this laser system it is possible to record Stark maps of Rydberg states with n in the range 20 to 30 at a resolution sufficient to observe all Stark states individually and even to distinguish between different fine-structure components of a given Stark state.

3.1.2 Pulsed dye-laser setup

In the experiments on atomic hydrogen described in chapters 5, 7, and 8, VUV radiation at Lyman α was used to excite the hydrogen atoms from the $^2S_{1/2}$ ground state to the 2P_J intermediate states in the experimental setup depicted in figure 3.3. The VUV radiation was generated by difference-frequency mixing, using the two-photon resonance 3.1 and $\tilde{\nu}_2 = 11834 \text{ cm}^{-1}$, in a gold-coated cell with a constant flow of krypton such that the background pressure was $\sim 10 \text{ mbar}$, as described in references [139, 140]. The radiation of the input beams to the four-wave mixing process was generated by commercial dye lasers pumped by a pulsed Nd:YAG laser. The resulting VUV radiation had a bandwidth of 0.7 cm^{-1} at a repetition rate of 10 Hz. The difference-frequency radiation was separated from the other light beams using a MgF_2 prism which has a higher transmission efficiency than the grating monochromator described in section 3.2.

The hydrogen atoms were excited in a second step from the 2P_J intermediate state to Rydberg states using the doubled output of a third dye laser of wave number $\tilde{\nu}_3 = 27144$ to 27418 cm^{-1} . Also shown in figure 3.3 is the excimer laser beam needed to generate the H atoms by photolysis of NH_3 , as will be discussed in detail in chapter 5.

3.2 Gas beam

The supersonic gas beam was generated by expanding the sample gas at a stagnation pressure of ~ 2 bar through a pulsed solenoid valve (General Valves, Series 9) into vacuum. The valve has a diameter of 0.5 mm and is open for approximately 250 μs . The beam passes through a 0.5 mm diameter skimmer located at an adjustable distance downstream of the nozzle orifice. In this manner a gas sample is generated which is internally and translationally cold; both temperatures are on the order of 1 K. Moreover, supersonic beams provide a collision free environment ideally suited for high-resolution spectroscopy experiments and for the deceleration experiments described in this thesis.

The skimmer (Beam dynamics, Inc) is shaped so as to minimize interference of the molecular beam with the skimmer. The two main sources of skimmer-molecular beam interference are (1) the scattering of molecules in the molecular beam off the exterior of the skimmer, and (2) the pressure build up inside the skimmer through collisions with the interior walls of the skimmer. The former interference can be avoided by using a skimmer with a small exterior opening angle whereas the elimination of the latter interference necessitates a large interior angle. The trumpet-like shape of the skimmers used in the experiments described in this thesis is a compromise between these two requirements. The orifice of the skimmer is small enough to maintain more than two orders of magnitude pressure difference between the nozzle chamber (background pressure 10^{-7} mbar, operating pressure 10^{-4} mbar) and the magnetically shielded photoexcitation region and flight tube (background pressure $5 \cdot 10^{-8}$ mbar, operating pressure $3 \cdot 10^{-7}$ mbar).

The skimmed molecular beam intersects the VUV-laser beam at right angles ~ 7 cm away from the tip of the skimmer, and the excited atoms fly an additional ~ 20 cm or ~ 25 cm to the detector, depending on which detector was used, see section 3.3.

The mean longitudinal velocity and temperature of the gas beam can be inferred from the neutral Rydberg atom time-of-flight measurements. The longitudinal temperature was determined to be ~ 1 K or less. The density, the temperature, and the mean velocity of the gas beam all depend on the time delay between the opening of the nozzle and the excitation of the particles by the VUV laser. This delay can be controlled in our setup with ns accuracy and was optimized before each experiment. Which quantity was used as the optimization criterion depended on the type of experiment.

The transverse velocity distribution is centred around zero and is typically narrower than the longitudinal velocity distribution. The transverse temperature is determined by: (1) the collimation of the beam when it passes through the skimmer, (2) the spot size of the VUV laser beam, and (3) the interaction of the beam with the skimmer, as will be discussed in more detail in chapter 6.

3.3 Detection system

In all the experiments described in this thesis microchannel plate (MCP) assemblies in chevron configuration were used. The MCP detectors consist of two parts: two plates with microchannel electron multipliers imbedded in them (we call the first plate the front plate and the second plate the back plate), and a metal anode or a phosphor screen to collect the resulting electrons. For the experiments described in chapter 4 and in the first half of chapter 6, the MCP detector was used with a metal anode (3025 MA Chevron assembly, Galileo electro-optics Corp.). For the experiments described in the second half of chapter 6 and in chapters 5, 7, and 8, an MCP detector was used in which the metal anode was replaced by a phosphor screen (3040 PS Chevron assembly, Burle). The latter MCP detector was larger (diameter 40 mm vs. 25 mm) and located closer to the excitation region (205 mm vs. 250 mm) than the former. Because of these differences and of several other modifications in the electrode setup, a direct quantitative comparison between the different time-of-flight profiles shown in this section and in the next chapters is not possible without extensive numerical simulations. This section provides a general overview of the different detection modes and methods used in the experiments.

3.3.1 Detection modes

The MCP detectors have two leads which are connected to the front and back plate and can be set individually to any potential up to 2.3 kV. The MCP detector with the phosphor screen has an additional connection to apply voltages to the phosphor screen. The front and back plate are connected as displayed in figure 3.4 so that

Panel (a)	Panel (b)	
$\Delta V = V_{\text{MCP}^+} - V_{\text{MCP}^-} > 0$	$\Delta V = V_{\text{MCP}^+} - V_{\text{MCP}^-} > 0$	(3.2)

$V_{\text{FP}} = V_{\text{MCP}^-} + \frac{1}{12}\Delta V$	$V_{\text{FP}} = V_{\text{MCP}^-} + \frac{1}{11}\Delta V$	(3.3)
---	---	-------

$V_{\text{BP}} = V_{\text{MCP}^+} - \frac{1}{12}\Delta V$	$V_{\text{BP}} = V_{\text{MCP}^+} - \frac{1}{11}\Delta V,$	(3.4)
---	--	-------

where V_{MCP^+} and V_{MCP^-} indicate the potentials supplied to the MCP connections and V_{FP} and V_{BP} are the actual potentials on the front plate and the back plate of the MCP assembly, respectively. The metal anode has approximately the same potential as the MCP^+ connection, whereas the phosphor screen is typically held at 4000 V. In both cases the secondary electrons are accelerated toward the metal anode or the phosphor screen. The resistor and the capacitor attached to the positive MCP connection and to the phosphor screen connection act as a filter for the high-frequency noise coming from the high-power voltage supplies. The resistors, coloured black in figure 3.4, with a resistance of 10 k Ω (panel (a)) and 3.9 k Ω (panel (b)) decouple the output connection from the positive MCP connection. By varying V_{MCP^-} and V_{MCP^+} , keeping

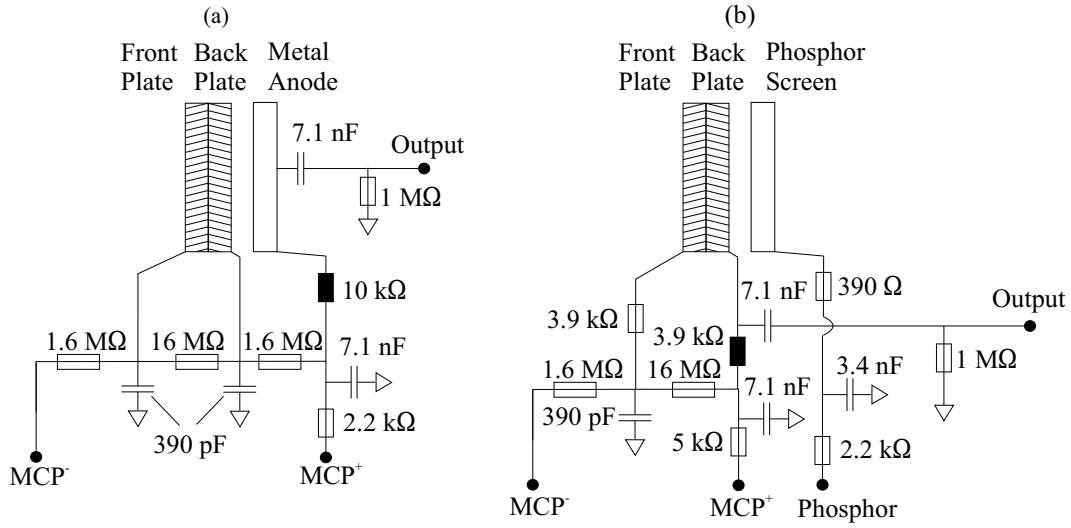


Figure 3.4: Schematic drawing of the electronic circuit used to apply potentials to the MCP detector. Panel (a): Electronic circuit for the MCP assembly with a metal anode. Panel (b): Electronic circuit for the MCP assembly with a phosphor screen.

ΔV constant, one can change the potential on the front plate from positive values via zero to negative values, without changing the overall amplification of the MCP detector.

By applying suitable voltage combinations to the MCP detector, VUV photons, electrons, ions, and neutral Rydberg particles can be detected. Rydberg particles create a signal at the MCP either because their internal energy is larger than the work function (~ 5 eV) of the lead glass the MCP consists of, or because the particles can ionize within the channels of the MCP detector where the field is extremely high. We cannot distinguish between these two processes, but in both cases the particles ionize when they impinge on the surface of the MCP detector. Therefore, the distance the particles have travelled between photoexcitation and the moment they ionize at the MCP detector is to an excellent approximation equal to the distance between the photoexcitation point and the surface of the front plate of the MCP detector.

Neutral particles in their electronic ground state cannot be detected because the field needed to ionize them is too high and their internal energy lies below the work function of the lead glass from which the MCP is made.

In our experiments three different detection modes were used:

- **Electron detection.** In this mode of detection the front plate of the MCP detector is held at a positive voltage ($V_{FP} \approx +200$ V) and electrons, photons, negative ions, and neutral Rydberg particles can be measured.
- **Ion detection.** In this mode of detection the front plate of the MCP detector is held at a negative voltage ($V_{FP} \approx -2000$ V) and positive ions, photons, and neutral Rydberg particles can be measured. This mode of detection was used

for the fluorescence lifetime measurements described in chapter 4 because electrons, which arrive at the same time on the detector as the fluorescence photons, are repelled from the MCP detector.

- Neutral detection. In this mode of detection the front plate of the MCP detector is held at approximately zero volt or at a low negative potential and electrons, photons, and neutral Rydberg particles can be measured. Positive ions cannot be measured in this detection mode because both the gain of the MCP detector and the absolute detection efficiency decrease rapidly with decreasing ion kinetic energy [85]. As a result of the nearly zero potential on the front plate some electrons arrive at the detector but the intensity of the signal is at least an order of magnitude lower than in the electron detection mode.

3.3.2 Microchannel plate with spatial resolution

When an ion, electron, VUV photon, or a Rydberg atom impinges on the surface of the MCP detector, the secondary electrons induce a fluorescence signal on the phosphor screen (P47) at the point of impact on the MCP detector. With the use of a CCD camera (XC-HR50, Sony), which can be mounted from the outside on a window on the vacuum flange, the fluorescence coming from the phosphor screen can be monitored. In this manner the MCP detector signals can be measured with two-dimensional spatial resolution. The CCD camera has an active area of 648×494 pixels, corresponding to a spatial resolution at the MCP detector of 15 pixels/mm. The individual images can be averaged over a large number of laser shots to improve the signal-to-noise ratio. The MCP detector was modified in such a way that the time-resolved signal, integrated across the surface of the MCP detector, and the spatially-resolved images can be measured simultaneously, see figure 3.4b. The time resolution of this MCP detector is reduced compared to that of the MCP detector with a metal anode. In the former case the $1/e$ decay time of an individual signal is ~ 22 ns whereas it is ~ 4 ns in the latter.

The CCD camera can be triggered externally and the minimal opening time is $8 \mu\text{s}$. Therefore, images of particles with different times of flight, for instance a fluorescence image and the image of an ion of specific mass, can be measured selectively, as long as the corresponding TOF peaks are separated by more than $8 \mu\text{s}$.

3.4 Measuring neutral Rydberg atoms

To illustrate the principles of the detection systems described above, this section presents and discusses several selected examples of measurements that are representative of the measurements carried out in the realm of this dissertation.

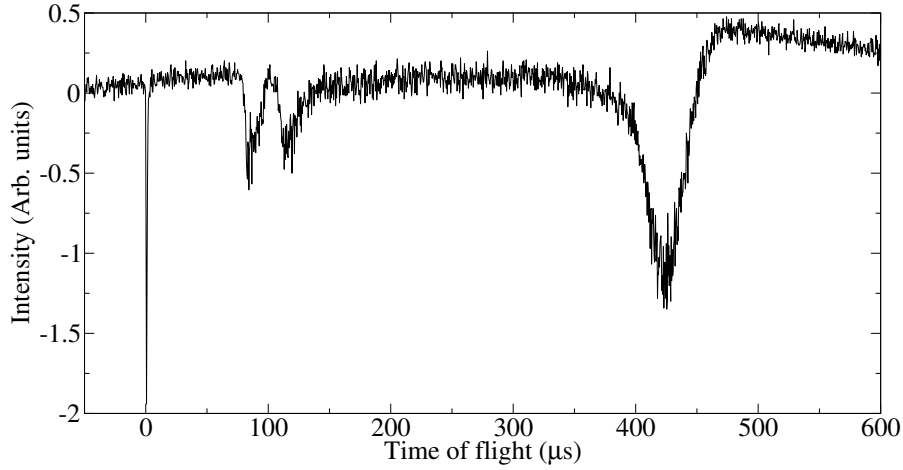


Figure 3.5: TOF spectrum recorded after exciting argon atoms to the $24d[3/2]_1$ state in zero electric field.

3.4.1 Time-of-flight measurements

The time-of-flight spectrum obtained after exciting a $24d[3/2]_1$ state in argon is displayed in figure 3.5. The MCP detector was in ion-detection mode and the fluorescence signal at $t \approx 0$ and the neutral Rydberg atom signal at $t \approx 420 \mu\text{s}$ are clearly visible. In addition, two early peaks are seen around $t = 85 \mu\text{s}$ and $t = 115 \mu\text{s}$. Similar TOF spectra were obtained for different n values in the range $n = 9$ to 40. The overshoot that can be seen most clearly after the neutral argon peak results from the addition of many individual signals which all exhibit an overshoot caused by the RC loops in the output part of the electronic circuit.

Early signals such as those seen between $100 \mu\text{s}$ and $200 \mu\text{s}$ in figure 3.5 were also seen in the deceleration experiments on H_2 [145], where it was argued that these signals probably come from the ionization of excited hydrogen molecules on their way to the detector. In the left panel of figure 3.6 the TOF spectra, recorded in our lab, of a $n = 29$ state belonging to a series converging on the $\text{X}^+ \ ^2\Sigma_g^+ \ v^+ = 0, N^+ = 1$ ground state of ortho H_2^+ are shown for different values of $(V_{\text{MCP}^+}, V_{\text{MCP}^-})$. The times of flight of particles contributing to the late signal around $t = 95 \mu\text{s}$ are independent of $(V_{\text{MCP}^+}, V_{\text{MCP}^-})$ as is expected for neutral particles. A time of flight of $t = 95 \mu\text{s}$ corresponds to a velocity of 2580 m/s, which is the expected velocity for a supersonic beam of hydrogen molecules. The times of flight of the particles contributing to the early peak, however, shift toward later times when V_{MCP^+} is increased and V_{MCP^-} decreased, indicating that the particles are positively charged.

In the right panel of figure 3.6 a similar measurement is shown, recorded after exciting argon atoms to a blue-shifted Stark state of the $n = 18$ manifold in a field of 1067 V/cm. The top trace shows that, for a suitable combination of $(V_{\text{MCP}^+}, V_{\text{MCP}^-})$, $(+1900 \text{ V}, -300 \text{ V})$, the early signal attributed to the positive ions can be completely suppressed. The potential on the front plate amounts to $V_{\text{FP}} = -100 \text{ V}$ so that most

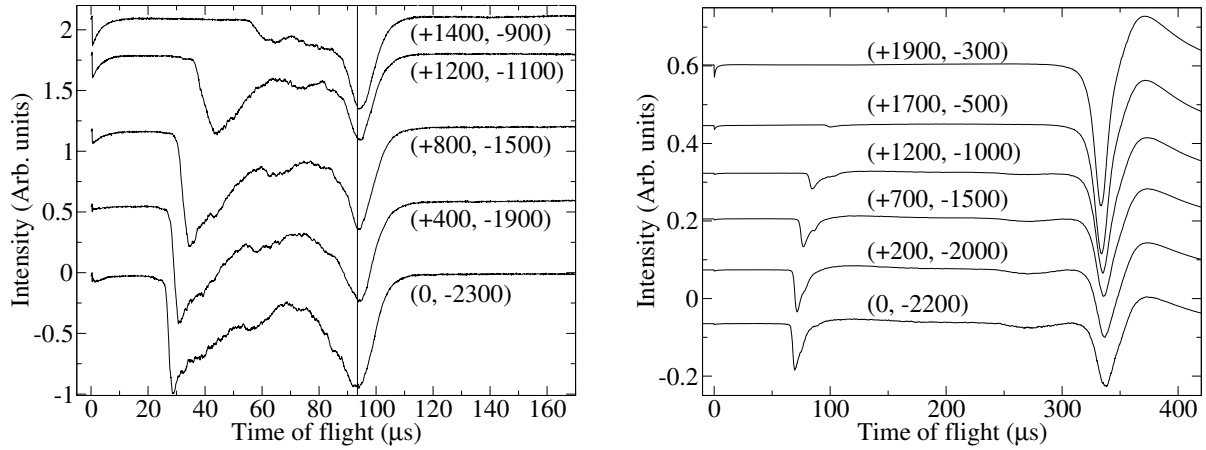


Figure 3.6: Left panel: TOF trace of H_2 molecules excited to a $n = 29$ p state belonging to a series converging on the $N^+ = 1$ threshold. Right panel: TOF trace of argon atoms excited to a blue-shifted Stark state of the $n = 18$ manifold in a field of 1067 V/cm. In both images the numbers in brackets are equal to $(V_{\text{MCP}^+}/V, V_{\text{MCP}^-}/V)$.

electrons are repelled from the MCP detector and cannot be detected. From the data presented in reference [92] one can conclude that the argon ion detection efficiency drops by two orders of magnitude going from the bottom trace to the top trace in the right panel of figure 3.6.

Although we do not know the exact origin of the ions arriving at the detector before the neutral particles, we did make the following observations:

- The ion signals are only seen if the laser frequency is resonant with a transition frequency from the ground state, indicating that the ions are generated by the ionization of Rydberg atoms or molecules.
- The ion signals are also seen at low- n values (<15), indicating that it is unlikely that these ions arise from field ionization of excited particles within the setup because the ionization field for states with such low principal quantum numbers is higher than the electric field in any region of the spectrometer.
- The ions are generated over an extended period of time, that is, not only at $t = 0$. If the ions were only produced at $t = 0$, they would be deflected by the electric field that is applied to excite the Rydberg Stark states, and not reach the detector. This observation rules out the possibility that the ions are generated during the VUV pulse by the absorption of a second photon by a Rydberg particle.
- The ions first fly with the neutral beam velocity until they are all accelerated by the potential of the MCP detector.

Possible mechanisms for the production of ions could be ionization caused by collisions with the background gas, ionization caused by Rydberg-Rydberg interactions,

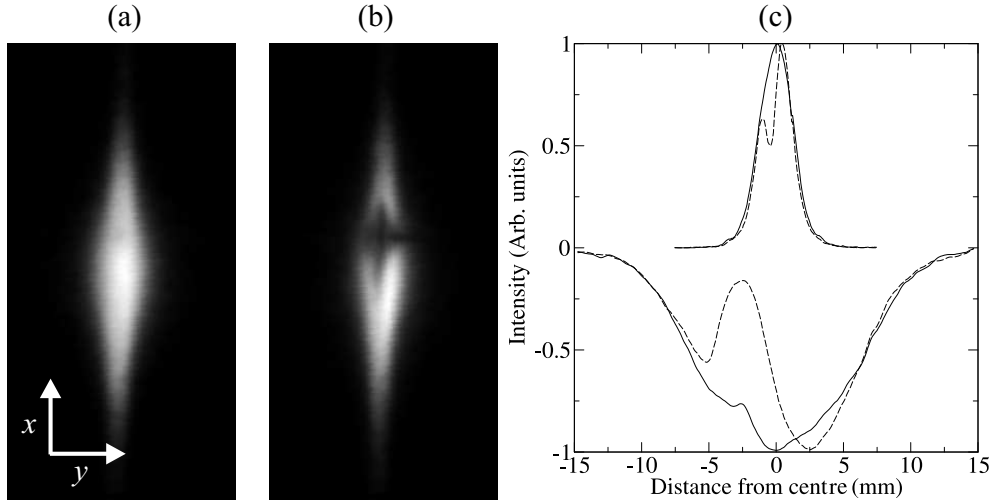


Figure 3.7: Images on the MCP detector of the argon atomic beam recorded after exciting the particles to the same state as in the right panel of figure 3.6. Both images are 15 mm wide (y dimension) and 30 mm high (x dimension). Panel (a): $(V_{\text{MCP}^+}, V_{\text{MCP}^-}) = (+1900 \text{ V}, -300 \text{ V})$. Panel (b): $(V_{\text{MCP}^+}, V_{\text{MCP}^-}) = (0, -2200 \text{ V})$. Panel (c): Intensity profiles for the image in panel (a) (solid lines) and for the image in panel (b) (dashed lines) for lines going through the centre of the images parallel to the y axis (traces pointing up) and parallel to the x axis (inverted traces).

black body radiation induced ionization or electron impact ionization caused by electrons emitted from the walls of the vacuum chamber by VUV radiation.

3.4.2 Imaging measurements

In the time-of-flight measurements following Rydberg deceleration/acceleration the early ion signal only interferes with the detection of the neutral atoms if the atoms are accelerated strongly, and the neutral Rydberg signal and the ion signals start to overlap. In the imaging measurement on the contrary, it is imperative to suppress the ion signals to obtain reliable information on the spatial distribution of the Rydberg atoms. In panels (a) and (b) of figure 3.7 images are displayed of the argon atomic beam after exciting the particles to the same Stark state as in the measurements displayed in the right panel of figure 3.6. For the images in panel (a) the MCP detector potentials were equal to $(V_{\text{MCP}^+}, V_{\text{MCP}^-}) = (+1900 \text{ V}, -300 \text{ V})$, whereas for the images in panel (b) they were equal to $(V_{\text{MCP}^+}, V_{\text{MCP}^-}) = (0, -2200 \text{ V})$. In the latter image a clear reduction in the intensity is seen just above the centre of the image. The fact that this reduction is not seen for $(V_{\text{MCP}^+}, V_{\text{MCP}^-}) = (+1900 \text{ V}, -300 \text{ V})$, when the ion signals are suppressed, is an indication that the reduction in intensity is caused by saturation of the detector by the early ion signals. Panel (c) shows the intensity profiles for both images (solid lines: from the image in panel (a), dashed lines: from the image in panel (b)) for lines going through the centre of the images parallel to the y axis (traces pointing up) and parallel to the x axis (inverted traces).

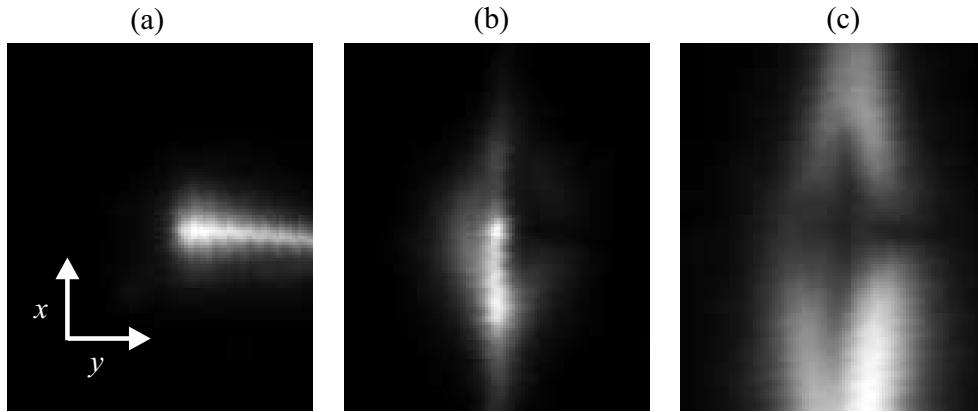


Figure 3.8: Magnified view of the images obtained at the MCP detector for particles arriving $75 \mu\text{s}$ (panel (a)), $270 \mu\text{s}$ (panel (b)), and $320 \mu\text{s}$ (panel (c)) after excitation. All three images are 6.8 mm wide (y direction) and 8.1 mm high (x direction). The potentials on the MCP detector were equal to $(V_{\text{MCP}^+}, V_{\text{MCP}^-}) = (0, -2200 \text{ V})$.

A further indication that the reduction in intensity is caused by the ion signals is presented in figure 3.8. Panels (a), (b), and (c) show an enlarged part of the images recorded with the potentials on the MCP equal to $(V_{\text{MCP}^+}, V_{\text{MCP}^-}) = (0, -2200 \text{ V})$. The image in panel (a) was recorded by opening the camera $75 \mu\text{s}$ after excitation, corresponding to the arrival time of the early Ar^+ ions, the image in panel (b) $270 \mu\text{s}$ after excitation, corresponding to the late Ar^+ ions, and the image in panel (c) $320 \mu\text{s}$ after excitation, corresponding to the Rydberg atom signal. In each case the opening time was chosen such that all particles contributing to the respective signals were measured. In these three images, the two-dimensional spread on the MCP detector of the early ion signal (a), the late ion signal (b), and the neutral atoms (c) were thus recorded selectively. The ions causing the signal in both panels (a) and (b) are seen to arrive at the same spatial position where the reduction in signal is seen for the neutral atoms in panel (c). The ions form tighter images on the MCP detector as a result of the field distribution around the MCP detector. Because the individual channels remain saturated for over 20 ms after an ionization event has been amplified, a signal reduction results at later times at the position of these channels. This explains the complementarity of the images in the three panels of figure 3.8.

A similar effect is observed in images recorded with the MCP detector in electron detection mode, i.e. $(V_{\text{MCP}^+}, V_{\text{MCP}^-}) = (+2200, 0 \text{ V})$; the electron signal at $t = 0$ saturates the central part of the MCP detector and a reduction in neutral Rydberg signal is seen in this region. The fluorescence photons, on the contrary, arrive evenly distributed on the whole active area of the MCP detector and do not cause any measurable reduction of late signals.

3.5 Conclusions

The combination of TOF and imaging measurements is a powerful way of obtaining information on the velocity and spatial distributions of Rydberg particles and ions in experiments using supersonic beams. A careful analysis of the different sources of signals is necessary for the correct interpretation of the experimental data. The analysis is facilitated by exploiting different detection modes for neutral and charged particles.

Neutral argon Rydberg atom time-of flight signals were measured after exciting the atoms to states with principal quantum number as low as 9. The electric field strength needed to ionize such states is equal 87 kV/cm, which cannot be reached in our setup. Measuring the neutral, excited atoms arriving at the detector is therefore an easily applicable method to measure the spectral positions of low lying Rydberg states. No additional laser beam is needed, as in resonance-enhance multi-photon ionization (REMPI) measurements, and it is technically less involved than VUV-absorption measurements [114].

In different setups and for both molecular hydrogen and for argon, we observed ion signals arriving at the detector before the neutral particles. To record reliable two-dimensional images of the Rydberg atom cloud at the MCP detector it is necessary to suppress the detection of these ion signals, without inducing the unwanted detection of stray electrons. When the ion signals and the atomic cloud distribution overlap spatially, suppressing the ion signal by applying appropriate voltages to the MCP detector enables one to avoid the unwanted depletion of the Rydberg TOF signal by saturation of the MCP detector.

Chapter 4

Nonhydrogenic effects in the deceleration of Rydberg atoms

4.1 Introduction

In the first experiments on the manipulation of the velocity of Rydberg particles using inhomogeneous electric fields, krypton atoms [120] were deflected and hydrogen molecules [95, 145] were decelerated in the field of two dipolar rods. The kinetic energy differences reached in these experiments ($\Delta E_{\text{kin}}/hc \leq 10 \text{ cm}^{-1}$) were small compared to the initial kinetic energy ($E_{\text{kin}}/hc = 570 \text{ cm}^{-1}$) because of the limited applied electric field strength, but the possibility to use Rydberg Stark states to change the velocity of particles was shown to be experimentally viable for the first time. The experimental results were interpreted in the realm of a purely hydrogenic model of the Stark effect in Rydberg states.

In this chapter, which is based on reference [131], experiments are described in which the deceleration of argon Rydberg atoms in inhomogeneous electric fields was combined with high-resolution Stark spectroscopy to investigate the role of nonhydrogenic effects in the deceleration of Rydberg atoms and molecules. The deviation from a Coulombic potential causes avoided crossings between different Stark states and causes the penetrating low- ℓ states to be displaced at zero field from the manifold of degenerate high- ℓ states and thus to undergo a quadratic Stark effect at low fields as explained in chapter 2. These nonhydrogenic effects were found to inhibit the acceleration/deceleration mechanism. Another limitation to Rydberg Stark deceleration, that also affects hydrogenic systems, is related to the limited lifetimes of the Rydberg states. The limited lifetimes of the excited Stark states force one to use short deceleration times and thus also short deceleration path lengths.

A possible way to overcome both limitations by using time-dependent fields is outlined: The kinetic energy loss/gain can be enhanced by increasing the potential on the electrodes as the Rydberg particles move through the decelerator so that the particles experience an almost constant, and optimal, field gradient throughout the

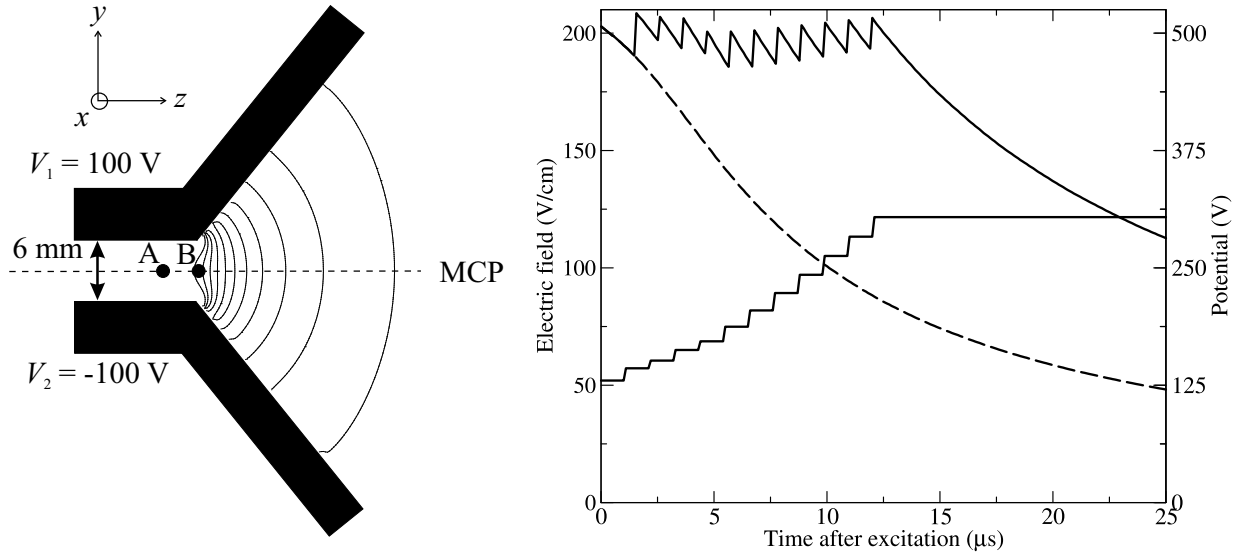


Figure 4.1: Left panel: Schematic view of the Rydberg Stark decelerator. The skimmed supersonic beam propagated in the z direction, halfway between the two electrodes. The VUV laser beam propagated parallel to the plate surfaces and perpendicular to the atomic beam. Photoexcitation was carried out in either homogeneous (point A) or inhomogeneous (point B) electric fields. The solid lines represent lines of constant electric field ranging from 300 V/cm to 50 V/cm in steps of 25 V/cm. Right panel: Time dependence of the potential applied to the electrodes (lower solid line) and of the electric field strength felt by a particle moving with a velocity of 590 m/s for constant potentials (dashed line) and for stepwise increasing potentials (upper solid line).

deceleration path and an electric field strength which never exceeds the Inglis-Teller field where avoided crossings between different n manifolds start to occur.

The energy levels of the Stark states as a function of the electric field can be calculated using a multi-channel quantum defect theory (MQDT) which incorporates the interactions caused by the electric field. In the second part of this chapter a short outline is given of the MQDT formalism that is used to calculate the energies of Rydberg states in electric fields and the results of the calculations for argon are compared with the experimental spectra.

4.2 Experimental setup

In the experiments, argon atoms were excited from the $(3p)^6 \ ^1S_0$ ground state to $n = 15$ to 30 Rydberg states belonging to series converging on the $^2P_{3/2}$ ionization threshold ($E_{\text{IE}}/hc = 127109.842 \text{ cm}^{-1}$ [18]) in a one-photon transition using the narrow-bandwidth VUV-laser system described in section 3.1.1. Excitation took place between two metallic electrodes with polished inner surfaces, depicted in the left panel of figure 4.1. The electrodes were 2 cm long in the x direction and their potential could be set independently to any voltage between 0 and 5000 V. The solid lines represent lines of constant electric field ranging from 300 V/cm to 50 V/cm in steps of 25 V/cm for $V_1 = -V_2 = 100$ V. The argon gas beam (purity grade >99.995%) and the

laser beam crossed at right angles either in a region where the electric field was highly homogeneous (point A) or in a region where the field was inhomogeneous (point B). A particle excited at point B and moving with a constant velocity of 590 m/s experienced a gradually decreasing field along its trajectory if the potential applied to the electrodes was kept constant. For a potential difference $\Delta V = |V_1 - V_2| = 130$ V between the two electrodes, the field felt by the Rydberg atoms decreased from 200 V/cm to 50 V/cm during the first 24 μs of the trajectory, see dashed line in the right panel of figure 4.1. This decrease of the electric field could be avoided if the potential difference was adjusted in a stepwise fashion. Increasing the potential difference from 125 V to 300 V over the first 12.5 μs resulted in a nearly constant field at the instantaneous position of the Rydberg atoms, see solid lines in the right panel of figure 4.1.

The polarization of the VUV laser could be set parallel or perpendicular to the electric field vector so that states with $M_J = 0$ or $M_J = 1$ could be excited selectively. The MCP detector was situated 250 mm away from the excitation point and the excited particles flew for ~ 430 μs before reaching the detector.

By applying suitable voltage pulses to the electrodes the Rydberg particles could be selectively field ionized and the principal quantum number n could be determined. Because the electric field pointed in the direction perpendicular to the detection axis, the resulting ions accelerated toward the electrodes and could not be detected at the MCP detector. Field ionization of the Rydberg particles could thus only be monitored as a reduction of the neutral particle signal but not as a background-free ion signal.

4.3 Spectroscopic and deceleration results

Rydberg states in noble gases are generally described by the $j_c K$ coupling scheme. In this coupling scheme the total angular momentum of the core, $\vec{j}_c = \vec{l}_c + \vec{s}_c$, is first coupled to the orbital angular momentum $\vec{\ell}$ of the Rydberg electron to yield $\vec{K} = \vec{j}_c + \vec{\ell}$. Subsequently \vec{K} is coupled to the Rydberg electron spin \vec{s} , giving $\vec{J} = \vec{K} + \vec{s}$. Rydberg states belonging to series converging on the lower lying $^2\text{P}_{3/2}$ ionic state, for which $j_c = \frac{3}{2}$, are labelled $n\ell[K]_J$ where K and J are the quantum numbers associated with \vec{K} and \vec{J} , respectively. Rydberg states belonging to series converging on the higher lying $^2\text{P}_{1/2}$ ionic state, for which $j_c = \frac{1}{2}$, are labelled $n\ell'[K]_J$.

The projections of \vec{J} , \vec{j}_c , $\vec{\ell}$, and \vec{s} on the z axis are denoted by M_J , m_{j_c} , m_ℓ , and m_s , respectively, with $M_J = m_{j_c} + m_\ell + m_s$.

4.3.1 Stark map

Figure 4.2 shows a Stark map of the $M_J = 0$ Rydberg states of argon in the range around the zero-field position of the high- ℓ states of $n = 22$, measured following photoexcitation at position A in figure 4.1. The origin of the intensity scale of each spectrum has been shifted along the vertical axis by the corresponding field strength

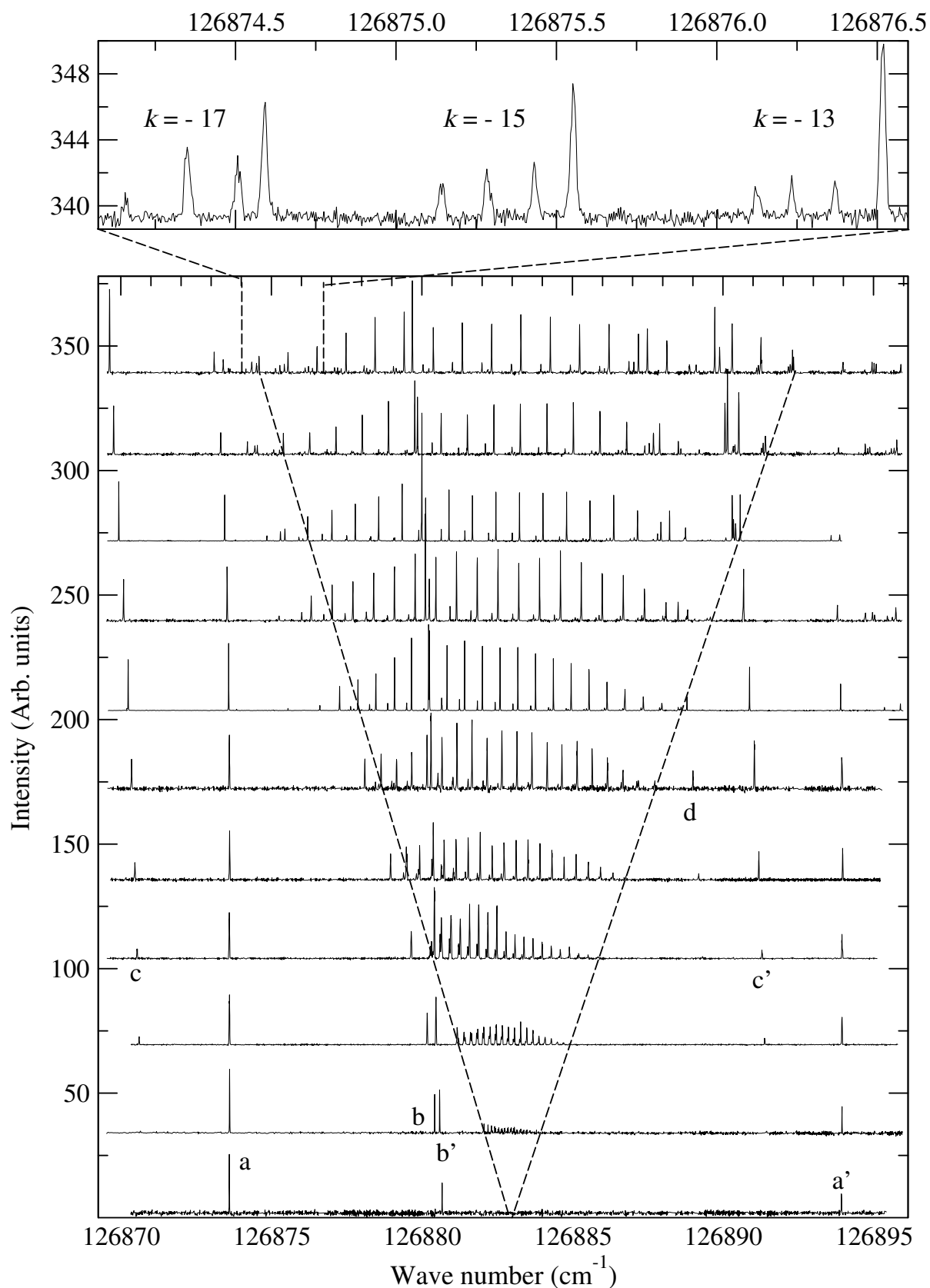


Figure 4.2: Stark map of the $M_J = 0$ Rydberg states of argon in the region around $n = 22$. The upper panel shows a detailed view of part of the spectrum recorded at 340 V/cm. The spectra have been shifted along the y axis so that the origin of the intensity scale corresponds to the electric field strength in V/cm.

in V/cm. In this Stark map four features stand out:

- The linear H-like Stark manifold of high- ℓ states. The outer states of this manifold are highlighted by the dashed lines and these are the states that were used in the acceleration/deceleration experiments.
- The low- ℓ states indicated by the letters a-d. These states are not degenerate at zero field and undergo a quadratic Stark shift at low fields.
- The fine structure components of each Stark state. In the upper panel this fine structure is shown in detail for three k values.
- The states of the $n = 23$ manifold starting to overlap and mix in with the $n = 22$ manifold on the high energy side of the spectrum recorded at a field of 340 V/cm.

At zero field only s and d states can be excited because of the $\Delta\ell = \pm 1$ Laporte selection rule. The zero-field positions of these states are well known [146] and therefore the assignments $22d[1/2]_1$, $23d[1/2]_1$, $22d[3/2]_1$, and $24s[3/2]_1$ can readily be made for the features labelled (a), (a'), (b), and (b'), respectively. At higher electric fields the p states start to mix with the s and d states and transitions to the states $23p[1/2]_0$ (c), $24p[1/2]_0$ (c') and $24p[5/2]_2$ (d) are observed [93, 83]. These states cross the linear Stark manifold above ~ 200 V/cm and how the crossings are traversed in an acceleration/deceleration experiment will be discussed in detail in section 4.3.2.

The fine-structure components highlighted in the upper panel of figure 4.2 arise because the optically accessible $M_J = 0$ states can be formed in 8 different ways by adding the possible values of m_s , m_ℓ , and m_{jc} :

M_J	m_s	m_{jc}	m_ℓ
0	$\frac{1}{2}$	$\frac{3}{2}$	-2
0	$\frac{1}{2}$	$\frac{1}{2}$	-1
0	$\frac{1}{2}$	$-\frac{1}{2}$	0
0	$\frac{1}{2}$	$-\frac{3}{2}$	1
0	$-\frac{1}{2}$	$\frac{3}{2}$	-1
0	$-\frac{1}{2}$	$\frac{1}{2}$	0
0	$-\frac{1}{2}$	$-\frac{1}{2}$	1
0	$-\frac{1}{2}$	$-\frac{3}{2}$	2

Of these 8 combinations only four carry most of the intensity as explained in section 4.4. The detailed structure of the Stark map of argon will be discussed in more detail in section 4.4 where it is compared with the results of the multi-channel quantum defect theory calculation.

It is important to note that at different n values the Stark map of argon looks qualitatively the same. The avoided crossings that occur are universal and the distances between the adiabatic curves scale as n^{-4} . Therefore this Stark map can be

used to identify or predict similar features in spectra recorded at different n using well-known scaling laws, see chapter 2. Such spectra, and spectra recorded in inhomogeneous fields where the lines are inhomogeneously broadened, can thus be accurately predicted without having to measure a whole new Stark map.

4.3.2 Deceleration at avoided crossings

A detailed Stark map in the region of the avoided crossings between the $24p[1/2]_0$ and the two most blue-shifted Stark states is displayed in figure 4.3. The spectra pointing up were recorded in a homogeneous electric field (point A in figure 4.1). In these spectra each Stark state consists of four components, the upper three of which are closely spaced. The first set of avoided crossings involving the $24p[1/2]_0$ state occurs with the four components of the $k = 19$ Stark state at $F \approx 275$ V/cm. Going from low to high field through this set of avoided crossings, one observes that the $24p[1/2]_0$ state (X) correlates adiabatically with the *highest* component of the $k = 19$ Stark state (Y'), whereas it is the *lowest* component of the $k = 19$ Stark state which correlates with the $24p[1/2]_0$ state. The situation repeats itself when the $24p[1/2]_0$ state encounters the four components of the next Stark state with $k = 17$ at a field of ~ 300 V/cm.

The inverted traces in figure 4.3 correspond to measurements carried out following photoexcitation at position B in figure 4.1. Transitions to states with energies that vary rapidly with electric field strength are inhomogeneously broadened according to the behaviour described in [87], and have a smaller peak intensity. States with a small field dependence, i.e. the p states that only undergo a quadratic Stark effect and the Stark states at avoided crossings, are hardly broadened with no significant decrease in peak intensity.

To quantify the role of the avoided crossings on the acceleration of Rydberg particles, the TOF distribution of the Rydberg atoms following photoexcitation at point B in figure 4.1 have been measured at the spectral positions and fields marked X, X' and Y, Y' in figure 4.3. These positions correspond to excitation to the $24p[1/2]_0$ state (X and X') and to the most blue-shifted Stark state (Y and Y') below and above the avoided crossing, respectively. No substantial acceleration is anticipated for the p state because of the small deviation from its zero-field position, whereas an acceleration is expected for the most blue-shifted Stark state. This is indeed observed when excitation takes place at fields below the avoided crossing (X and Y) as illustrated in the lower right panel of figure 4.3: the solid and dashed lines correspond to the TOF spectra measured following excitation to the $24p[1/2]_0$ state (X), and the highest component of the most blue-shifted Stark state (Y), respectively. In the latter case the decrease in the average TOF amounts to $1.3 \mu\text{s}$, corresponding to an increase in velocity of 1.8 m/s (i.e. 0.3%) and in kinetic energy of 3.4 cm^{-1} (i.e. 0.6%). For reasons to be explained below, this acceleration amounts to only 47% of the Stark shift of the excited state. Exactly the opposite behaviour is observed when excitation occurs

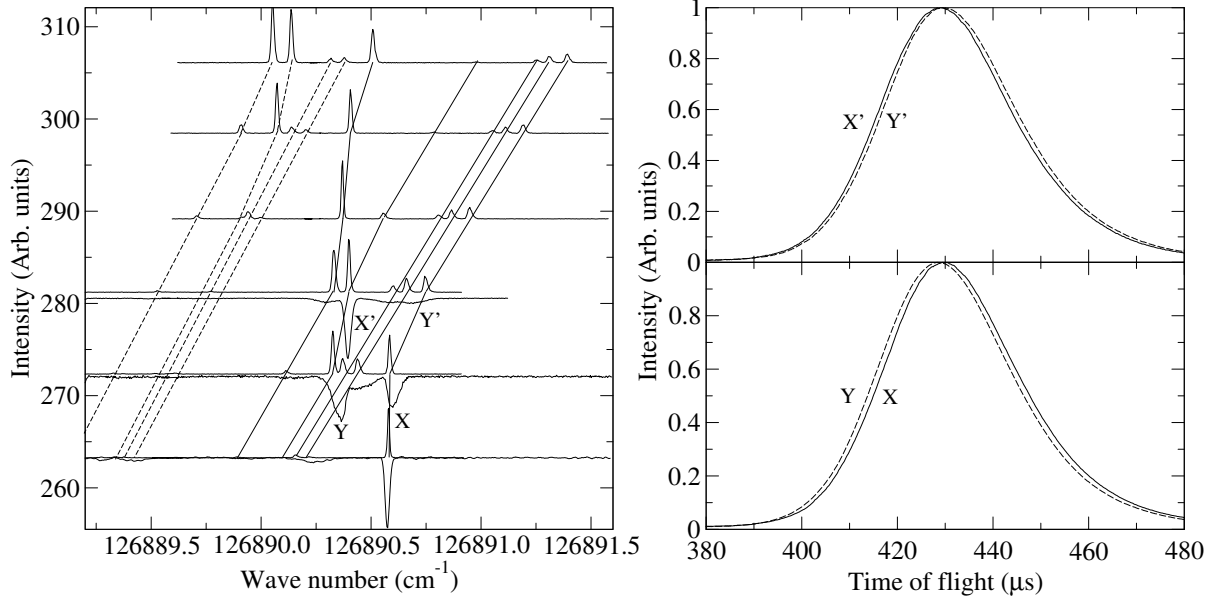


Figure 4.3: Left panel: Stark map of the avoided crossings of the $24p[1/2]_0$ state with the two most blue-shifted Stark states. The traces pointing upward were measured in homogeneous electric fields (point A in figure 4.1). The traces pointing downward were measured in inhomogeneous electric fields (point B in figure 4.1). The lines connect peaks which lie on the same adiabatic energy curve as a function of the field. X, Y, X', and Y' mark the states which were excited in the acceleration experiments. The spectra have been shifted along the y axis so that the origin of the intensity scale corresponds to the electric field strength in V/cm. Right panels: Time-of-flight traces of states excited below (X,Y, see lower panel) and above (X',Y', see upper panel) the first avoided crossing shown in the left panel.

above the avoided crossing (X' and Y'), see upper right panel in figure 4.3. In this case the atoms excited to the $24p[1/2]_0$ state are accelerated whereas the atoms excited to the most blue-shifted Stark state do not change their velocity. This behaviour indicates that the avoided crossing is traversed adiabatically when the atoms move toward regions of lower field strength.

Assuming a speed of ~ 580 m/s, a minimum distance between the energy curves of 0.1 cm^{-1} at the avoided crossing, determined from the spectroscopic measurements, and an electric field gradient of 310 V/cm^2 , we estimate from the Landau-Zener formula 2.21 that the probability of a diabatic passage is negligible. This result has profound implications for deceleration experiments: The most shifted Stark states, which in the H atom would undergo the largest acceleration/deceleration, are precisely those that undergo avoided crossings with low- ℓ states in all other atomic or molecular systems. The control of the translational motion of these states is correspondingly reduced. A similar explanation could be proposed for the less-than-expected deflection of the $n = 19$, $k = 10$ component of krypton observed in reference [120]. Indeed the reduced deflection is likely to have been caused by avoided crossings with the $22p$ states. It is essential to have a high-resolution Stark map such as figure 4.2 if one wants to determine which states will be decelerated efficiently.

4.3.3 Optimizing the deceleration

For a given Stark state the maximum deceleration can be achieved by maximizing the field strength and thus the field inhomogeneity. An upper limit to the field strength is given by the field F_{IT} at the Inglis-Teller limit, because avoided crossings between Stark states of neighbouring n -values above F_{IT} lead to rapid changes of k which are caused by adiabatic Landau-Zener dynamics. The most efficient way of influencing the velocity of the Rydberg particles therefore consists of keeping the field strength at their instantaneous position as close to F_{IT} as possible. One way how this can be achieved is by stepping up the voltage applied to the electrodes so as to compensate for the field changes along the trajectories of the Rydberg particles as shown in the right panel of figure 4.1. This method, the principle of which has been used extensively in the acceleration/deceleration experiments described in later chapters, is now presented in detail.

In the lower panel of figure 4.4 the Stark map is displayed around $F = 215$ V/cm in the energetic region where the $n = 24$ and the $n = 25$ manifolds start to overlap. The second most red-shifted Stark state of the $n = 25$ manifold and the third most blue-shifted Stark state of the $n = 24$ manifold (positions b and a in the lower panel of figure 4.4) were excited in the deceleration/acceleration experiments described below because 1) they have a larger intensity than the most blue-shifted and most red-shifted states and 2) the likelihood and effect of an avoided crossing with a low- ℓ state are reduced.

In the upper panel of figure 4.4 the dotted line represents the TOF spectra of atoms excited to a zero-field state which does neither decelerate nor accelerate and therefore serves as a reference. The inner dashed and solid lines are TOF measurements of state a and state b, respectively, recorded for a constant potential applied to the electrodes. The kinetic energy difference between the two sets of Rydberg atoms amounts to 6.6 cm^{-1} i.e. 54% of the combined Stark shift of the two states which is equal to 12.18 cm^{-1} . To increase the kinetic energy difference, the potential on the electrodes was stepped up in such a way that the homogenous field between the two electrodes increased from 217 V/cm at excitation to 515 V/cm after $12 \mu\text{s}$. The time-dependent potential resulted in a nearly constant electric field of 205 V/cm at the instantaneous position of the particles. The outer dashed and solid lines are the corresponding TOF spectra recorded for states a and b, respectively. In these measurements the kinetic energy difference is equal to 14.6 cm^{-1} or 120% of the combined Stark shift. Thus the kinetic energy difference could be increased by a factor of 2.2 by compensating for the field changes along the trajectories of the particles. Moreover, in this manner the change in kinetic energy could be made slightly larger than the Stark shift which shows that the kinetic energy differences that can be reached in experiments using time-dependent electric fields are not limited by the Stark shift of the excited Rydberg state.

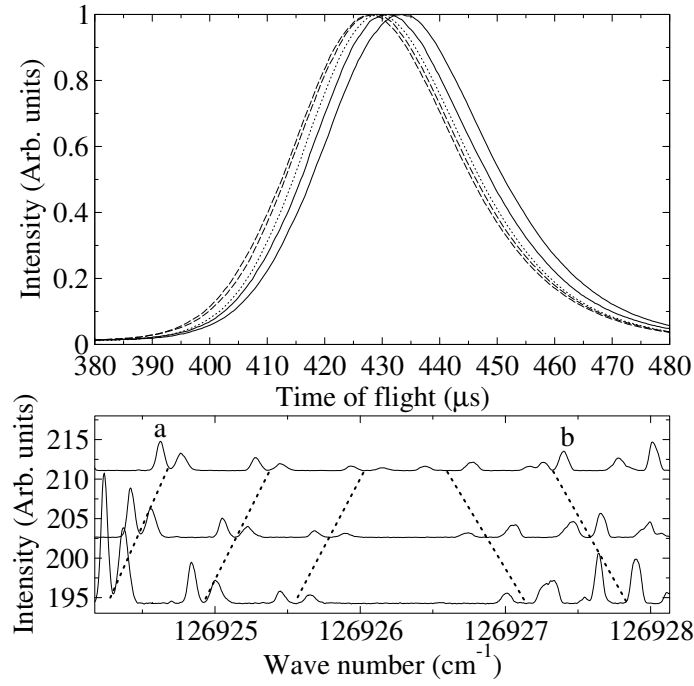


Figure 4.4: Lower panel: Spectrum of the energy region where the $n = 24$ and $n = 25$ manifold start to overlap. The dashed lines show the behaviour of the three outer groups of Stark states in the $n = 24$ manifold and the two outer groups of Stark states in the $n = 25$ manifold. Upper panel: The TOF traces of the blue-shifted state a (dashed lines) and the red-shifted state b (solid lines) compared to the TOF trace of a zero field state (dotted line). The outer dashed and solid lines correspond to measurements in which the potential was increased stepwise during deceleration whereas the inner dashed and solid lines correspond to measurements in a constant electric field.

4.3.4 Lifetimes of Rydberg states

The measured kinetic energy difference in time-independent deceleration experiments was at most 54% of the Stark shift of the excited state. The reason for this reduced kinetic energy difference most likely lies in the limited lifetimes of the excited states: If the particle makes a transition to a state which can still be detected but does not decelerate in inhomogeneous electric fields before it has traversed the whole region in which the field is inhomogeneous, the energy difference will be smaller than expected on the basis of equation 2.37. The lifetimes of the excited states are therefore important parameters in the deceleration experiments and the decay mechanisms, in particular radiative decay and transitions induced by black body radiation (see section 2.5) but also collisionally induced decay, must be established.

The spontaneous emission lifetimes of the zero field states in argon were measured by monitoring the fluorescence signal with the MCP-detector after excitation. This detection method is only sensitive to the VUV fluorescence of the Rydberg states to the 1S_0 ground state. Two problems arise when using this detection method:

- 1) The efficiency of the photon detection is low because the MCP detector is small (2 cm diameter) compared to the distance it is situated away from the excitation

Table 4.1: Measured fluorescence lifetimes of Rydberg states in argon. The wave number was taken from reference [146]. The uncertainties in the lifetime is given by the uncertainty in the fit procedure.

State	Wave number (cm^{-1})	Lifetime (μs)
16d[3/2] ₁	126672.0	0.61 ± 0.1
18s[3/2] ₁	126674.4	0.81 ± 0.05
8d'[3/2] ₁	126737.7	0.22 ± 0.04
10s'[1/2] ₁	126758.5	1.1 ± 0.2
20s[3/2] ₁	126768.3	0.16 ± 0.04
18d[3/2] ₁	126770.5	0.14 ± 0.04
19d[3/2] ₁	126803.2	0.37 ± 0.03
20d[3/2] ₁	126832.8	0.53 ± 0.05
21d[3/2] ₁	126858.8	0.72 ± 0.15
22d[3/2] ₁	126880.8	0.8 ± 0.2
30d[3/2] ₁	126987.0	1.3 ± 0.1

point (25 cm). The fraction of detectable photons is therefore reduced by a factor 1/2500. 2) The gas valve is open for $\pm 250 \mu\text{s}$ and, at excitation, the gas beam has a longitudinal spread of ~ 15 cm of which only ~ 0.5 mm overlaps with the VUV-laser beam. If the excitation region is situated in the middle of the gas beam, the emitted photons have to travel through approximately 7 cm of argon gas on their way to the MCP-detector. The photons can therefore be reabsorbed and reemitted during their flight through the argon gas. The measured fluorescence signal at the detector is thus not only a measure of how many photons were emitted as a function of time but also of how many photons were reabsorbed and reemitted on their way to the detector.

To perform reliable lifetime measurements by detection of the fluorescence the atoms were therefore excited at the front end of the gas beam so that less of the argon gas beam is situated between the photoexcitation point and the detector. The number of reabsorption/reemission events is then reduced, however at the expense of the total number of excited particles because the gas density is smaller at the front end of the gas beam than in the middle.

Both these problems can be circumvented partially by measuring the photons that are emitted perpendicular to the propagation direction of the gas beam. One can bring the detector much closer to the excitation point, which increases the number of detectable photons, and the lateral spread (FWHM) of the gas beam is only ~ 1 mm, which means that the probability of reabsorption is much smaller in this direction than in the direction of propagation of the beam. In the measurements presented here we did not implement this detection method.

We were able to measure lifetimes of several of the ns[3/2]₁ and nd[3/2]₁ Rydberg states in the range $n = 15$ to 30 together with two states which belong to series

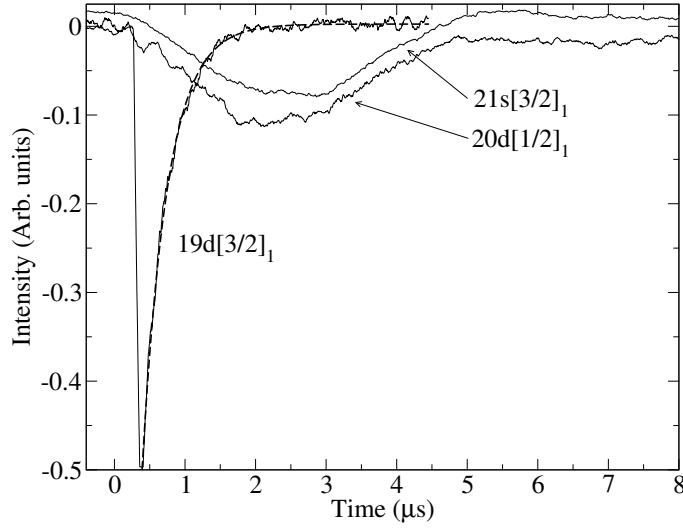


Figure 4.5: Measured VUV fluorescence signals after exciting the $19d[3/2]_1$, the $20d[1/2]_1$, and the $21s[3/2]_1$ state. The latter trace is shifted up by 0.01 for clarity. Also shown is a single-exponential fit to the fluorescence signal after exciting the $19d[3/2]_1$ state (dashed line).

converging on the $^2P_{1/2}$ ionic state which have a similar energy as the $20s[3/2]_1$ state, see table 4.1. Figure 4.5 shows the fluorescence signals measured after exciting the $19d[3/2]_1$, the $21s[3/2]_1$, and the $20d[1/2]_1$ states. For all three measurements, a background, recorded with the gas beam off but the VUV-laser beam on, was subtracted. The $19d[3/2]_1$ state was excited at the front edge of the gas beam and the other two states 3 cm more toward the middle. The fluorescence signal of the $19d[3/2]_1$ state is a single-exponential decay which can be simulated using a time constant of $0.37(3) \mu\text{s}$. The other two fluorescence signals show clearly a nonexponential decay which reflects the absorption/emission cycles discussed above. No fluorescence lifetime can be extracted from these measurements. The lifetimes that could be determined from single-exponential fits to the temporal profile of the fluorescence signals are listed in table 4.1 and lie in the range 0.14 to $1.3 \mu\text{s}$, in agreement with the qualitative discussion presented in section 2.5.

These spontaneous emission lifetimes stand in stark contrast with the fact that a strong signal of neutral Rydberg particles can be measured after more than $400 \mu\text{s}$ for states with principal quantum number as low as 9. The detected atoms must have changed to metastable states within or shortly after the decelerator. The states we excite in the range $n = 15$ to 30 are a superposition of $S = 0$ and $S = 1$ states. A mechanism for the production of metastable excited atoms is therefore the fluorescence to the lowest-lying state with pure $S = 1$ character. This state lives for longer than $400 \mu\text{s}$ because it cannot fluoresce to the 1S_0 ground state. The $4s \ ^3P_0$ and $4s \ ^3P_2$ both do not have any $S = 0$ character and can be reached from ns or nd Rydberg states via one of the $4p$ states by subsequent emission of two photons. Another mechanism is the m -changing processes as discussed in section 2.5.3.

Stark states are a superposition of all ℓ states, thus the transition intensity to these states is reduced by a factor $\sim n/2$ compared to the transition intensity to the s and d states. For the same reason, the fluorescence lifetimes of the Stark states increase by a factor $n/3$ to $n/2$ compared to that of the low- ℓ states, depending on whether the p-state lifetime is comparable or much longer than that of the s and d states. As a result, the fluorescence signals were too low for reliable measurements of the lifetimes of Stark states to be carried out. Because the rates of transitions induced by black body radiation is not affected by Stark mixing, the relative importance of black body radiation induced transitions compared to fluorescence strongly increases.

The decay of the Stark states was studied by switching the electric field off rapidly after a controllable delay τ_E following excitation and monitoring the integrated intensity of the neutral signal at the MCP detector as a function of τ_E . The rapid switching off of the electric field projects the Stark states onto all ℓ states of which the high- ℓ states live for much longer than $400 \mu\text{s}$. The loss of signal seen in the left panel of figure 4.6 for a Stark state at $n = 25$ as a function of τ_E is therefore an indirect measurement of the decay of the excited Stark state during the delay before switching off the electric field. A single-exponential fit to the data and to data recorded for other Stark states yields a lifetime of $\tau_{\text{Stark}} \approx 8.1 \mu\text{s}$ for Stark states at $n = 25$ which is consistent with the estimate of the lifetime of these states from the zero field fluorescence measurements: $\tau_{\text{Stark}} = \tau_{\text{nd}} \frac{n}{3}$ which is approximately equal to $10 \mu\text{s}$ for $n = 25$ Stark states. Approximately 25% of the total atom signal does not appear to be affected by the decay and corresponds to atoms that have gained metastability, possibly by m -changing processes.

To assess the importance of n -changing processes, such as transitions induced by black body radiation or collisions, selective field ionization (SFI) measurements were performed following excitation to specific Stark states. With this method one can exploit the strong n -dependence of the ionization field to monitor changes in the principal quantum number that occur because of black body radiation or collisions. In the right panel of figure 4.6 the result of such a SFI measurement is shown for a red-shifted $n = 30$ Stark state. Every circle/square represents the integrated signal of the TOF traces after background subtraction. The atoms were excited in a field of $\sim 70 \text{ V/cm}$ and field ionized $1 \mu\text{s}$ (solid circles) or $5 \mu\text{s}$ (open squares) after photoexcitation with a pulse of variable electric field strength. When the applied field strength exceeds the ionization field strength, the Rydberg atoms are ionized and the integrated atom signal is reduced. In the measurement in which the particles were ionized after $1 \mu\text{s}$, a decrease in signal of 90% is seen at a field strength of $\sim 450 \text{ V/cm}$ approximately equal to the adiabatic field ionization threshold of 397 V/cm for a $n = 30$ state. If the field ionization delay is increased to $5 \mu\text{s}$, the main decrease ($\sim 50\%$ of the total signal) is also seen at a field strength of $\sim 450 \text{ V/cm}$ but it is only above 1000 V/cm that the signal has decreased to less than 10%. The preservation of a neutral atom signal beyond 450 V/cm is probably caused by transitions induced by black body radiation to lower n states in the $5 \mu\text{s}$ before the ionization pulse. The

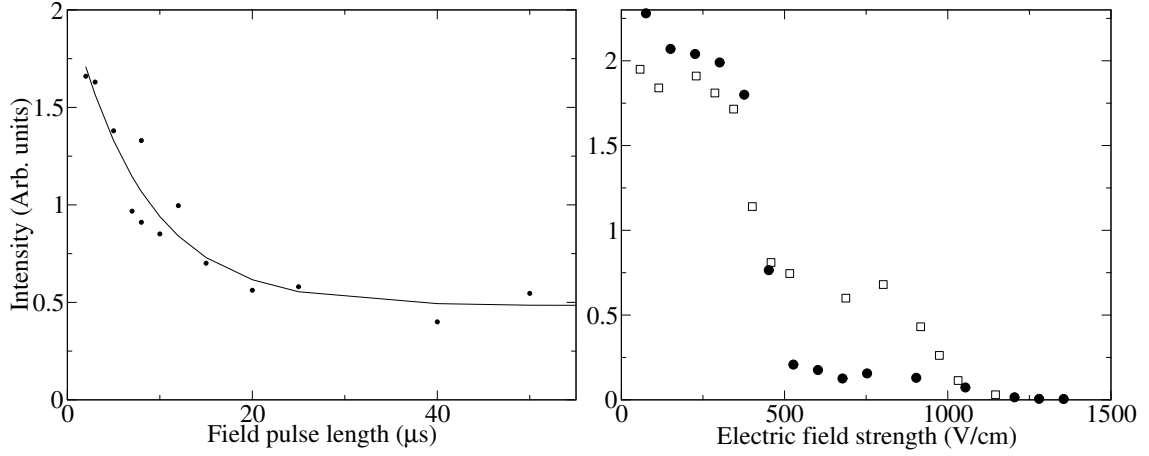


Figure 4.6: Left panel: Decay of a red-shifted $n = 25$ Stark state. The dots are the integrated intensities of the atom signal at the MCP. The solid line is a single-exponential fit to the data. Right panel: Results of SFI measurements after exciting a red-shifted $n = 30$ Stark state. The solid dots and the open squares are the integrated intensities of the atoms signal at the MCP after applying the ionization pulse after $1 \mu\text{s}$ and $5 \mu\text{s}$, respectively.

facts that 1) most atoms are ionized by a field strength of less than 1000 V/cm and 2) that only few atoms ionize at field strengths below 350 V/cm indicate that only a minor fraction of the initially prepared Stark states is subject to n -changing transitions during these first $5 \mu\text{s}$ and that these changes are small ($\Delta n < 5$).

This partial decay of the initially populated Stark state can also account for the fact that only $\sim 50\%$ of the Stark shift is converted into a kinetic energy difference. Indeed transitions to higher Rydberg states of the same k value induced by black body radiation inhibit the deceleration because the Inglis-Teller limit of the higher Rydberg state is reduced by $\left(\frac{n'}{n}\right)^5$ and the maximal useful Stark shift by $\left(\frac{n'}{n}\right)^3$. Transitions to lower n values also inhibit the deceleration because the Stark shift is proportional to n^2 . In either case a reduction of the kinetic energy on the order of 20% to 40% is expected for the changes of n of 1 to 4 observed on the timescale of the experiment, in agreement with the observations made in sections 4.3.2 and 4.3.3.

4.4 Multi-channel quantum defect theory

A better understanding of the structure of the Stark map depicted in figure 4.2 can be obtained by calculating the energy levels of the Rydberg Stark states as a function of the electric field strength F . In references [35, 149] the energy levels of Na, Li, and K [149] and Xe [35] were calculated by diagonalizing the Hamiltonian matrix

$$H = H_0 + V, \quad (4.1)$$

where H_0 is the matrix containing the zero-field energy levels and V is the electric

field interaction matrix. The disadvantage of calculating the energy levels by matrix diagonalization is that one has to take into account a large number of states to obtain accurate results, i.e. the matrix becomes large at high n and the diagonalization procedure time consuming.

An alternative way to calculate a Stark map is to incorporate interactions caused by the electric field in a multi-channel quantum defect theory (MQDT) calculation [36, 57, 58, 107, 108]. MQDT [110] is a scattering theory in which the bound Rydberg electron is treated in the same manner as an electron scattering off an ionic core, the main difference being the boundary conditions that are applied to the electron wave function.

In the remaining part of this section the MQDT calculation that incorporates the electric field is described and the results of the MQDT predictions for argon Rydberg Stark states are compared with the experimental results depicted in figure 4.2. The two main goals of these calculations are to obtain the wave functions of the fine-structure components that are most intense and to understand how the low- ℓ Stark states mix with the high- ℓ manifold. In particular, how the different fine-structure components interact with the low- ℓ states.

4.4.1 General outline of the theory

In an MQDT calculation for the rare gas atoms, which incorporates the electric field, the space in which the electron moves is divided into three regions:

- Region I: $0 < r < r_0$. In the short-range region, electrostatic and exchange interactions dominate and the eigenchannels can be approximated by LS -coupled channels. r_0 is chosen in such a way that the potential is purely Coulombic at $r > r_0$.
- Region II: $r_0 < r < r_F = F^{-1/2}$. In the middle-range region the Rydberg electron is nearly decoupled from the ionic core and the fine-structure of the ionic core dominates the energy level structure. The energy levels are most conveniently described by the $j_c K$ or $j_c J$ coupling scheme.
- Region III: $r_F < r$. For large r the pure $1/r$ Coulomb potential and the electrostatic potential dominate. It is most appropriate to use parabolic coordinates in this region and the wave functions are given by superpositions of the solutions of equations 2.9 and 2.10.

For $r \gg r_0$ the wave functions can thus be written as

$$H_i = \sum_j G(i, j) L_j, \quad (4.2)$$

where i and j are used to label the Stark states, L_j is the vector of superposition coefficients and $G(i, j)$ are the solutions to equations 2.9 and 2.10 which can be written

as

$$G(\gamma' \beta' m'; \gamma \beta m) = \Psi(F\epsilon \beta m) \delta_{\gamma' \gamma} \delta_{\beta' \beta} \delta_{m' m} + \bar{\Psi}(F\epsilon' \beta' m') R_{\gamma' \beta' m'; \gamma \beta m}, \quad (4.3)$$

in which γ is used to label the quantum state of the ionic core, β is the separation constant, denoted by Z_1 in equation 2.9, m is the magnetic quantum number, ϵ the binding energy of the electron with respect to the energy of the ionic core with quantum state γ , $\Psi(F\epsilon \beta m)$ and $\bar{\Psi}(F\epsilon \beta m)$ are the regular and the irregular solutions to equations 2.9 and 2.10 and $R_{\gamma' \beta' m'; \gamma \beta m}$ is the reactance matrix. $R_{\gamma' \beta' m'; \gamma \beta m}$ can be related to the usual reactance matrix R^0 used in field-free MQDT [76] by

$$R_{\gamma' \beta' m'; \gamma \beta m} = \sum_{\ell', \ell} U_{\beta' \ell'} R_{\gamma' \ell' m'; \gamma \ell m}^0 U_{\beta \ell}^t. \quad (4.4)$$

in which

$$R_{\gamma' \ell' m'; \gamma \ell m}^0 = \sum_{\alpha} Q_{i\alpha} \tan(\pi \mu_{\alpha}) Q_{j\alpha}^t. \quad (4.5)$$

The μ_{α} coefficients are the quantum defects of the LS -coupled channels and $Q_{i\alpha}$ are the transformation matrix elements between the LS -coupled channels and the $j_c J$ -coupled channels. The transformation matrix elements $Q_{i\alpha}$ are given by [147]

$$\begin{aligned} Q_{i\alpha} &= (-1)^{L-S-l-0.5+m_{j_c}} \sqrt{(2j_c+1)(2L+1)(2S+1)(2J+1)} \\ &\times \sum_{m_l^c m_s^c} \begin{pmatrix} \ell_c & s_c & j_c \\ m_l^c & m_s^c & -m_{j_c} \end{pmatrix} \begin{pmatrix} \ell_c & \ell & L \\ m_l^c & m_{\ell} & -M_L \end{pmatrix} \\ &\times \begin{pmatrix} s_c & s & S \\ m_s^c & m_s & -M_S \end{pmatrix} \begin{pmatrix} L & S & J \\ m_L & m_S & -M_J \end{pmatrix}. \end{aligned} \quad (4.6)$$

s-d and/or p-f interactions between the different LS -coupled channels can be taken into account by multiplying $Q_{i\alpha}$ with an interaction matrix $B_{\alpha\alpha'}$ which includes the mixing angles between the different LS -coupled channels [76].

The transformation elements $U_{\beta\ell}$ in equation 4.4 transform the regular and irregular Coulomb functions, $\psi^0(\epsilon\ell m)$ and $\bar{\psi}^0(\epsilon\ell m)$, respectively, into the regular and irregular parabolic functions

$$\Psi(F\epsilon \beta m) = \sum_{\ell} U_{\beta\ell}(F\epsilon m) \psi^0(\epsilon\ell m) \quad (4.7)$$

$$\bar{\Psi}(F\epsilon \beta m) = \sum_{\ell} U_{\beta\ell}(F\epsilon m) \bar{\psi}^0(\epsilon\ell m). \quad (4.8)$$

The effective potentials for the Schrödinger equations 2.9 and 2.10 in region III are

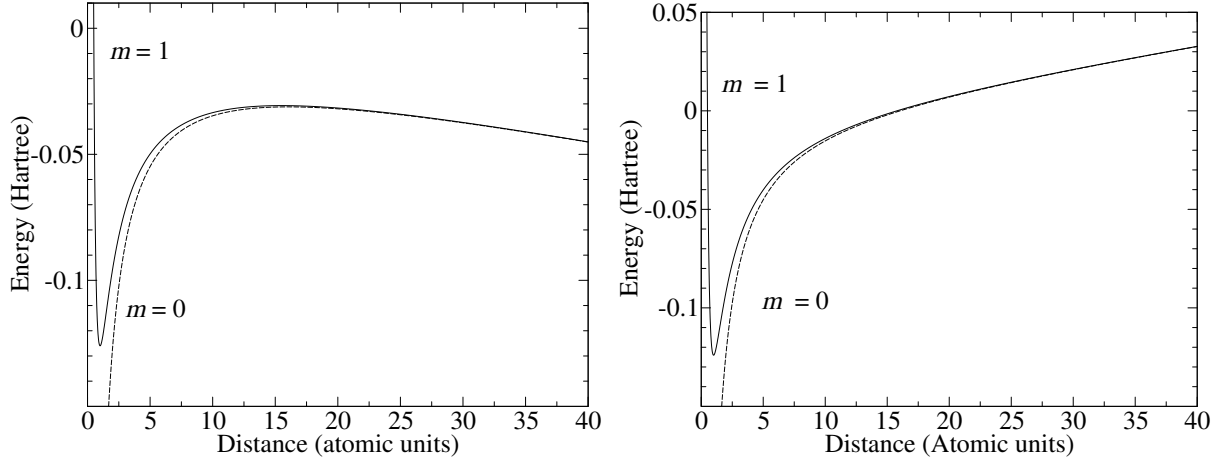


Figure 4.7: Effective potentials $V(\eta)$ (left panel) and $U(\xi)$ (right panel) as a function of the electron-core separation.

$$U(\xi) = \frac{m^2}{8\xi^2} - \frac{\beta}{2\xi} + \frac{F\xi}{8} \quad (4.9)$$

$$V(\eta) = \frac{m^2}{8\eta^2} - \frac{1-\beta}{2\eta} - \frac{F\eta}{8}. \quad (4.10)$$

For an electron with energy $\epsilon = -1/(2\nu^2)$, in which ν is the effective quantum number, we can define the corresponding momenta

$$p(\xi) = \left(\frac{\epsilon}{2} - 2U(\xi) \right)^{1/2} \quad (4.11)$$

$$q(\eta) = \left(\frac{\epsilon}{2} - 2V(\eta) \right)^{1/2}. \quad (4.12)$$

Figure 4.7 shows the effective potentials $V(\eta)$ (left panel) and $U(\xi)$ (right panel) for $m = 0$ (dashed lines) and $m = 1$ (solid lines), $\beta = 0.5$, and an electric field strength of $40 \cdot 10^6$ V/cm. The field was chosen so high to highlight the features of the two potentials. The main difference between these two potentials is that the motion in the ξ direction is always bound because the potential $U(\xi)$ *increases* with increasing ξ whereas the motion in the η direction is always quasi bound because the potential $V(\eta)$ *decreases* with increasing η for large η .

The parameter β can be determined for every electric field strength, m value, and energy by the Bohr-Sommerfeld quantization rule for the motion in the ξ direction

$$\int_{\xi_a}^{\xi_b} p(\xi) d\xi = \pi \left(n_1 + \frac{1}{2} \right), \quad (4.13)$$

in which ξ_a and ξ_b are the inner and outer classical turning points, respectively, for an electron with energy $\epsilon/4$ moving in the potential well $U(\xi)$. If $m = 0$, ξ_a is 0. In the computation of the energy levels, β can also be calculated using the power series described in reference [113], for which the leading term is

$$\beta^0 = \frac{1}{2}(2n_1 + |m_\ell| + 1)/\nu. \quad (4.14)$$

When β is known, the transformation elements $U_{\beta\ell}(F\epsilon m)$ can be calculated and are equal to [37, 107, 108]

$$U_{\beta\ell}(F\epsilon m) = (2\nu)^{1/2} C(F) X_{\beta\ell}(\epsilon m), \quad (4.15)$$

in which $X_{\beta\ell}(\epsilon m)$ is an angular momentum transformation matrix element and $C(F)$ is a field-dependent parameter that arises because of the normalization of the wave function in region II and region III. They are given by

$$X_{\beta\ell}(\epsilon m) = (-1)^{\ell+m} (2\ell + 1)^{1/2} \begin{pmatrix} \nu_{1/2} & \nu_{1/2} & l \\ m_+ & m_- & -m \end{pmatrix} \quad (4.16)$$

$$C(F) = \left(\frac{1}{\pi} \int_{\xi_a}^{\xi_b} \frac{d\xi}{p(\xi)\xi} \right)^{1/2}, \quad (4.17)$$

in which

$$\nu_{1/2} = \frac{1}{2}(\nu - 1) \quad (4.18)$$

$$m_\pm = \frac{1}{2}(m \pm (1 - 2\beta)\nu). \quad (4.19)$$

The wave functions for $r \gg r_0$ (see equation 4.2) are thus related, via the transformations $U_{\beta\ell}(F\epsilon m)$ and $Q_{i\alpha}$, to the phase shifts μ_α of the electron when it scatters off the positive nucleus in an LS -coupled channel α .

For an electron with an energy ϵ there are two classically allowed regions in the potential well $V(\eta)$, $\eta_a < \eta < \eta_b$ and $\eta_c < \eta$. If $m = 0$, η_a is 0. For a quasi-bound state, i.e. the energy of the electron is lower than the local maximum of the potential $V(\eta)$, the wave function in the region between η_b and η_c can be approximated by a WKB function [107]. This wave function depends on the accumulated phase between η_a and η_b

$$\Delta = \int_{\eta_a}^{\eta_b} q(\eta) d\eta. \quad (4.20)$$

The boundary condition that applies for $\eta_b < \eta < \eta_c$ is that terms in the wave function that grow exponentially with η have to vanish. This boundary condition is satisfied if

$$\det|\cot \Delta_i \delta_{ij} - R_{ij}| = 0, \quad (4.21)$$

in which i and j are used to label the Stark states. The phase Δ_i and the reactance matrix elements R_{ij} can be calculated at every field strength, m value, and energy using the formulae given above. By varying the energy and searching for the zeros of equation 4.21, the energy levels can be calculated as a function of the electric field strength.

The transition intensity from the ground state to a Stark state can be calculated by calculating the vector \vec{v} which solves the equation

$$(\cot \Delta_i \delta_{ij} - R_{ij}) \vec{v} = 0, \quad (4.22)$$

in which $(\cot \Delta_i \delta_{ij} - R_{ij})$ is evaluated at the energy of the Stark state. The vector \vec{v} is subsequently expressed in LS -coupled channels. The only two LS -coupled channels which can be excited from the ground state are to a good approximation the d 1P_1 and the s 1P_1 channels with a dipole transition moment of 2.1 and 1.4, respectively [76]. The transition intensity is thus proportional to

$$I \propto (2.1a_d + 1.4a_s)^2, \quad (4.23)$$

in which a_d and a_s are the expansion coefficients of the d 1P_1 channel and the s 1P_1 channel, respectively.

The parameters that are used in the MQDT calculation are

- The quantum defects of all LS -coupled eigenchannels. The $\ell > 3$ channels were assumed to have zero quantum defects, see table 4.2.
- The $B_{\alpha\alpha'}$ channel interaction parameters. These interaction elements are usually small. From the literature the s-d and d-d interactions are known for $J = 1$ [76], $J = 2$, and $J = 3$ [134] but not for $J = 0$. The p-p interaction for $J = 1$ and $J = 2$ are calculated in reference [93] but no p-f interaction was taken into account. Moreover, the p-p interaction for $J = 3$ was set to zero. The interaction matrices are given in appendix B.
- The energy interval between the $^2P_{3/2}$ and $^2P_{1/2}$ ionic levels which is equal to $\Delta E/hc = 1431.583 \text{ cm}^{-1}$ [18].

The quantum defects and the channel interaction parameters are assumed to be energy independent because the energy dependence is typically very small and in the present study the energy of the Stark states is calculated over only a narrow energy range. The studied energy range corresponds to $n^* = 21.5$ to 22.5, where n^* is the effective quantum number with respect to the $^2P_{3/2}$ ionic state.

Table 4.2: List of the quantum defects for the LS -coupled channels used in the MQDT calculation. For the channels marked by the asterisk no value for the quantum defect could be found in the literature but were assumed to be independent of J .

$\ell = 0$	1P_1	0.113 ³	$\ell = 2$	1P_1	0.074 ³	$\ell = 3$	1D_2	0.020 ²
	3P_0	0.148 ⁴		3P_0	0.534 ⁴		3D_1	0.022 ²
	3P_1	0.143 ³		3P_1	0.499 ³		3D_2	0.022 ²
	3P_2	0.146 ¹		3P_2	0.4973 ¹		3D_3	0.022 ^{2,*}
				1D_2	0.2454 ¹		1F_3	0.0 ⁶
$\ell = 1$	1S_0	0.533 ⁴		3D_1	0.2352 ³		3F_2	0.0 ²
	3S_1	0.754 ²		3D_2	0.2297 ¹		3F_3	0.0 ⁶
	1P_1	0.649 ²		3D_3	0.2325 ¹		3F_4	0.0 ⁶
	3P_0	0.65 ⁴		1F_3	0.2663 ¹		1G_4	0.0 ⁶
	3P_1	0.653 ²		3F_2	0.3888 ¹		3G_3	0.0 ⁶
	3P_2	0.649 ²		3F_3	0.3924 ¹		3G_4	0.0 ⁶
	1D_2	0.668 ²		3F_4	0.395 ⁵		3G_5	0.0 ⁶
	3D_1	0.695 ²						
	3D_2	0.694 ²						
	3D_3	0.694 ^{2,*}						

¹ Taken from reference [134]

² Taken from reference [93]

³ Taken from reference [143]

⁴ Calculated using data from reference [83]

⁵ Taken from reference [18]

⁶ Set to zero

4.4.2 Results of the calculation

Calculated Stark map

Figure 4.8 and figure 4.9 show the measured $M_J = 0$ Stark map of argon and the result of the $M_J = 0$ MQDT calculations, respectively. The wave number range in both Stark maps corresponds to an effective quantum number $n^* = 21.5$ to 22.5. The intensities of the transitions, the positions of the low- ℓ states as a function of field strength, and the fine-structure splittings of the Stark states in the two Stark maps are now compared in detail.

Intensities of the transitions

The intensities in the measured Stark map are a convolution of the transition intensity from the ground state to the Stark states and the probability that a particle

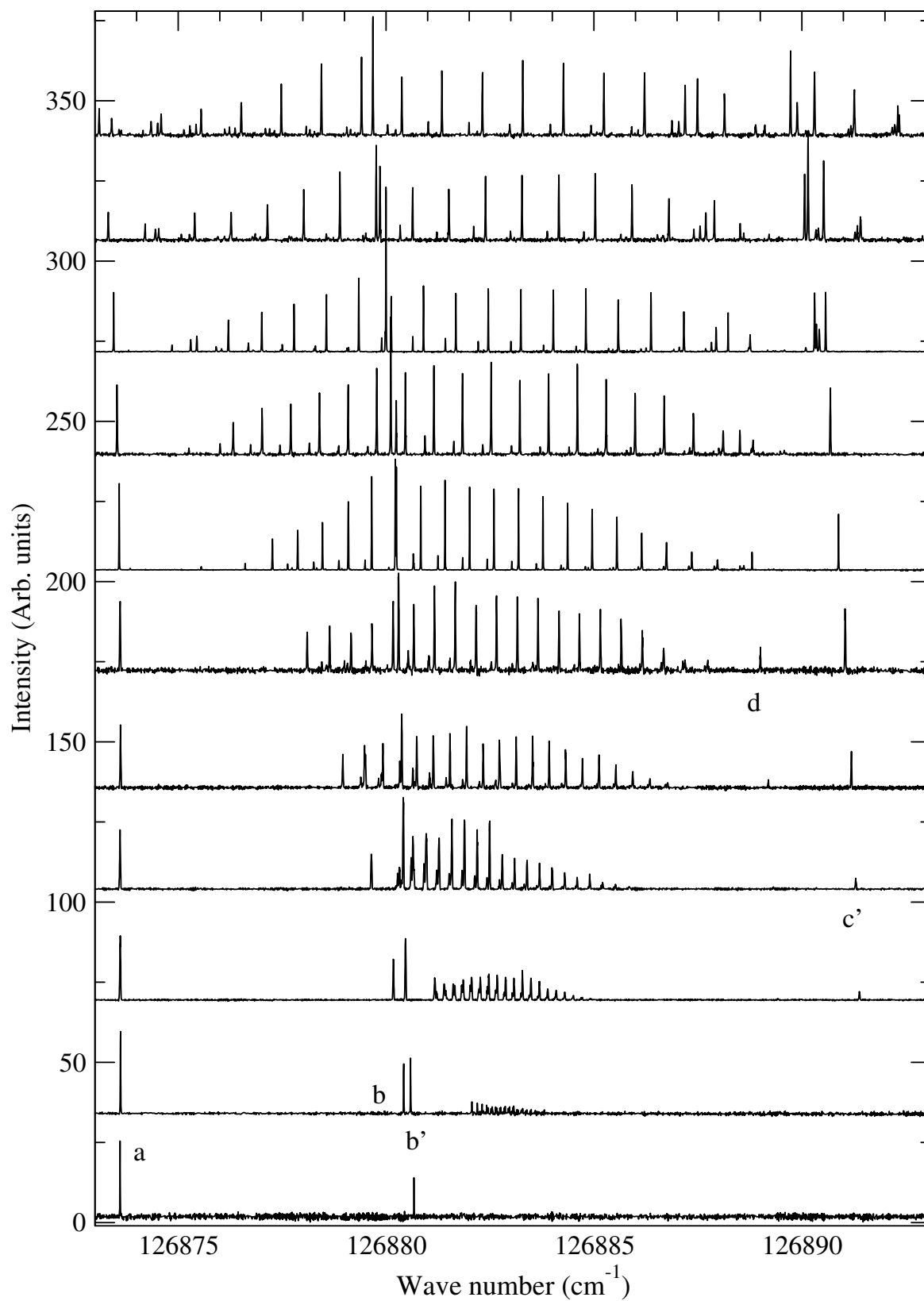


Figure 4.8: Measured Stark map of the $M_J = 0$ Rydberg states of argon in the region around $n = 22$. The spectra have been shifted along the y axis so that the origin of the intensity scale corresponds to the electric field strength in V/cm.

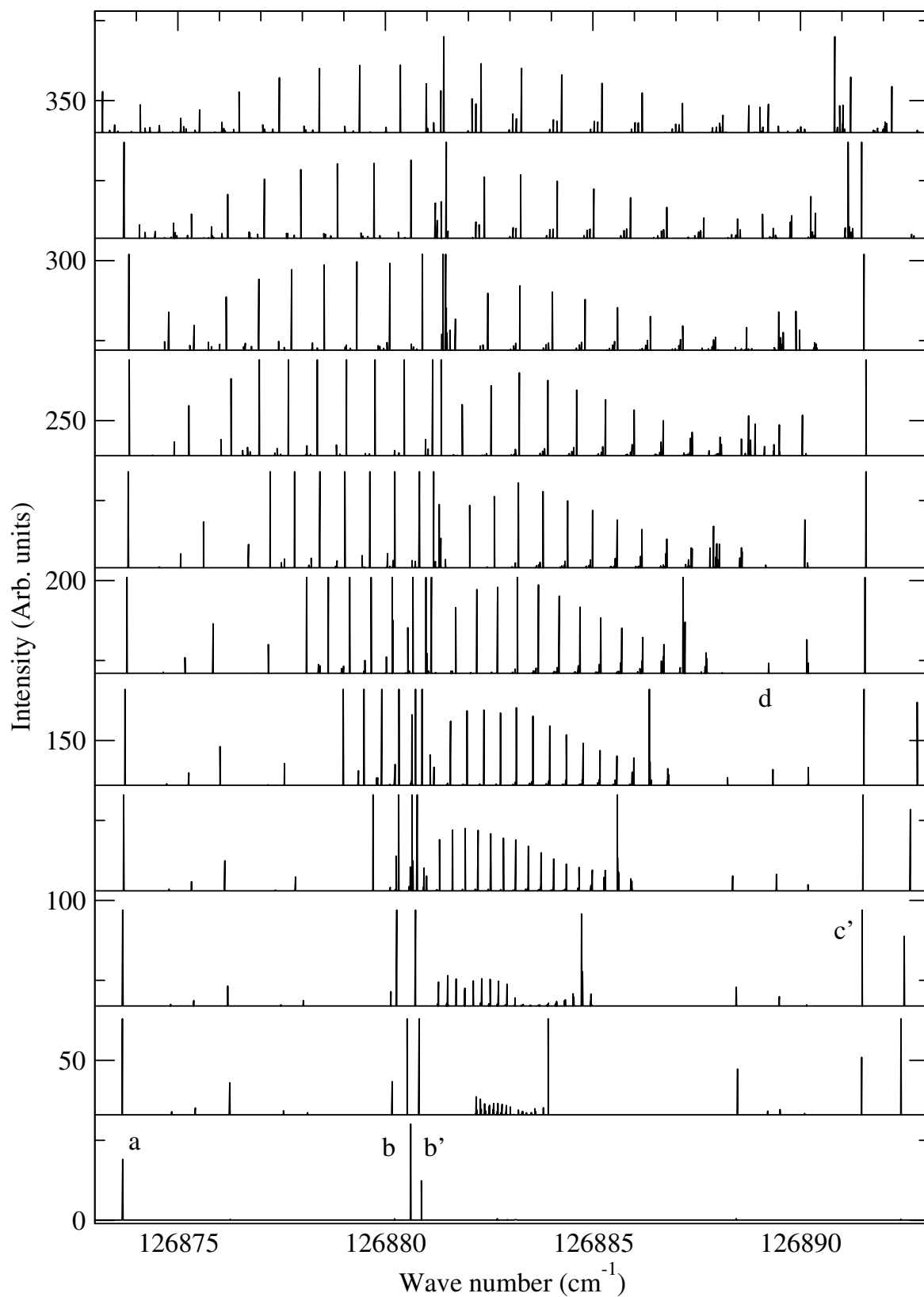


Figure 4.9: Calculated Stark map of the $M_J = 0$ Rydberg states of argon in the region around $n = 22$. The spectra have been shifted along the y axis so that the origin of the intensity scale corresponds to the electric field strength in V/cm.

excited to the Stark state reaches the detector in a detectable excited state. The s and d states indicated by the letters a, b, and b' mostly have large transition intensities but short lifetimes compared to the transition intensities and lifetimes of the high- ℓ Stark states. The shorter lifetimes reduce the measured intensities of these states and cause them to be quite similar to the measured intensities of the high- ℓ Stark states although the transition intensities differ significantly.

The intensities in the calculated Stark map directly correspond to the transition intensities from the ground state to the Stark states and are therefore much larger for the s and d states than for the high- ℓ Stark states. For clarity, the intensities in all spectra in figure 4.9 were multiplied so that the intensities of the Stark states in the central part of the manifold have equal intensity in the calculated and measured Stark map. Intensities exceeding 30 arbitrary units were truncated at 30 arbitrary units. The calculated intensity of the transition to the $d[3/2]_1$ state (labelled b) in a field of 67 V/cm is, without truncation, ~ 100 times larger than the intensity of the transition to the neighbouring Stark states in the high- ℓ manifold. In the measurements this ratio is only ~ 2 , see figure 4.8.

The modification of the intensities and the fact that the decay of the excited state is not taken into account, causes the transitions to the low- ℓ states that cannot be excited in zero electric field, to be clearly visible in the calculated Stark map even when they are not seen in the measured Stark map. The states at the zero-field position of the high- ℓ manifold in the zero electric field spectrum are f states [93], the states between 126875 cm^{-1} and 126880 cm^{-1} are the s and d states with $J \neq 1$ [94], and the states around 126890 cm^{-1} are p states [93].

Avoided crossings

The left panel of figure 4.10 shows a comparison between the calculated and measured Stark map in the energetic region of the $24p[1/2]_0$ state. At an electric field strength of 33 V/cm the calculated transition energy for the $24p[1/2]_0$ state and the measured value differ by less than 0.02 cm^{-1} . At higher fields, however, the measured transition energy is shifted toward *lower* energies whereas in the calculation it is shifted toward *higher* energies. The difference between calculated and measured transition energy is largest for $F = 272 \text{ V/cm}$ and is then equal to $\Delta E/hc = 0.9 \text{ cm}^{-1}$.

The dependence of the transition energy to the $24s[3/2]_1$ state (b') on the electric field strength shows a similar deviation between measured and calculated values. In this case the difference amounts to 1.7 cm^{-1} at $F = 340 \text{ V/cm}$. The $24s[3/2]_1$ perturbs the Stark manifold locally in both the calculations and the measurements, causing the two Stark maps to look qualitatively different in this energy region.

Because of this deviation between calculations and measurements at increasing field strengths, the low- ℓ states cross the high- ℓ manifold at a different electric field strength and energetic position in the measurements and the calculations. It is there-

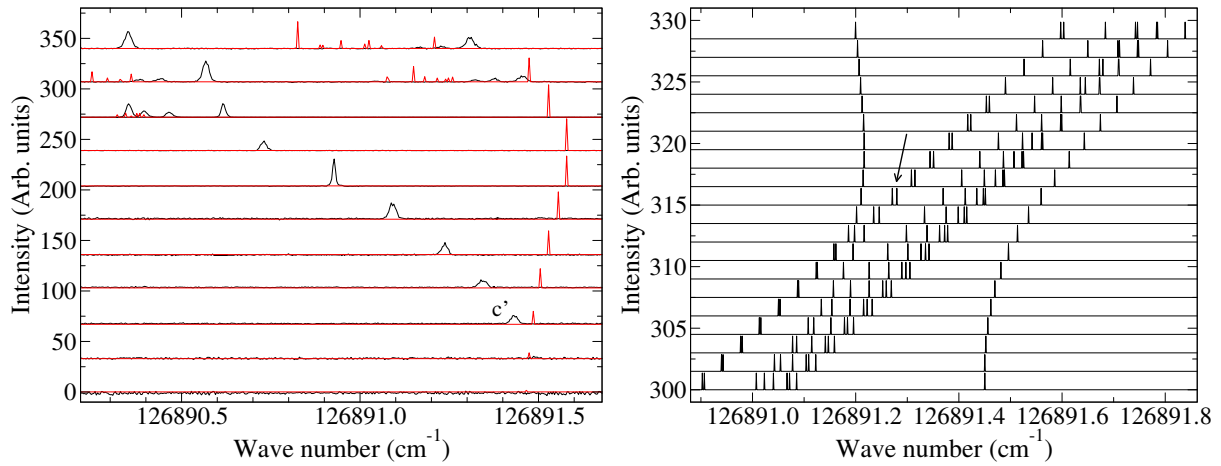


Figure 4.10: Left panel: Overview of the dependence of the energetic position of the $24p[1/2]_0$ state as a function of the electric field. The black curves are the experimental spectra and the red curves the calculated spectra. Right panel: Detailed view of the calculated avoided crossing between the $24p[1/2]_0$ state and the $n = 22$ $k = 19$ Stark state. All states were given the same transition intensity. The spectra in both panels have been shifted along the y axis so that the origin of the intensity scale corresponds to the electric field strength in V/cm.

fore not possible to quantitatively compare the measured spectra of avoided crossings such as displayed in the left panel of figure 4.3 with the corresponding calculated spectra.

In the calculation the energy of the transition to the $24p[1/2]_0$ state is shifted by approximately 0.8 cm^{-1} at an electric field of $\sim 300 \text{ V/cm}$. As a result, the first avoided crossing with a Stark state from the high- ℓ manifold does not occur around 275 V/cm (see figure 4.3) but at approximately 310 V/cm . A detailed view of the calculated Stark map around this avoided crossing is displayed in the right panel of figure 4.10. All states were given the same transition intensity to highlight the behaviour of all components of the Stark state. Going from low to high field through the avoided crossing, the $24p[1/2]_0$ state is converted adiabatically into the outer fine-structure component of the $n = 22$, $k = 19$ Stark state and the inner fine-structure component goes over into the $24p[1/2]_0$ state. All other components of the Stark state correlate at high electric fields to the next lower component of the Stark state. This can be most clearly seen for the state which at an electric field of 300 V/cm has an energy of 126891.0 cm^{-1} . This state correlates adiabatically to the higher energy component of the two states indicated by the arrow. This behaviour is similar to the behaviour seen in the measured spectra (see figure 4.3) for the lowest energy component of the group of three states at 126890.3 cm^{-1} .

The calculated spectra around the avoided crossing of the $24p[1/2]_0$ state with the $n = 22$, $k = 19$ Stark state indeed are in qualitative agreement with the corresponding experimental spectra displayed in figure 4.3. A direct comparison is hampered by the

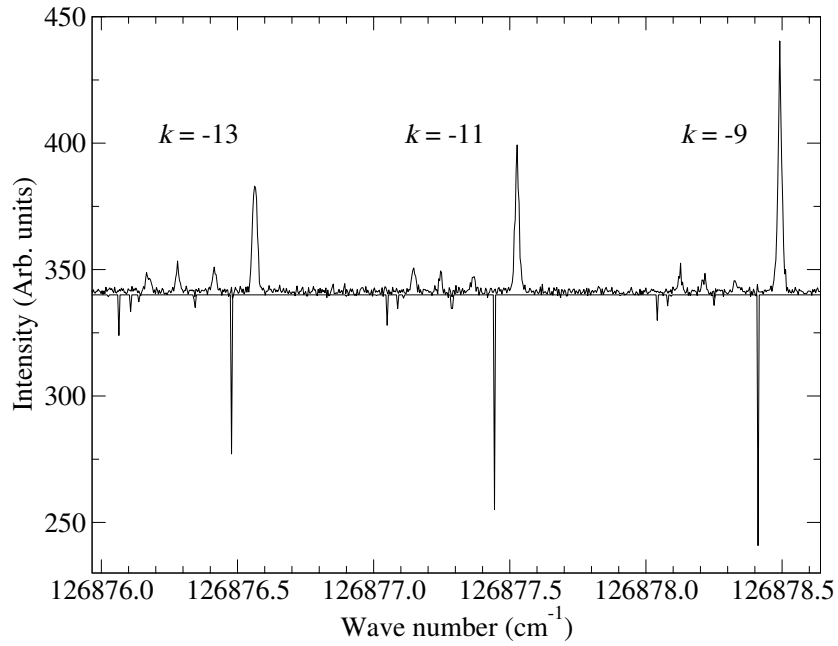


Figure 4.11: Detailed view of the $n = 22$, $k = -9$, -11 , and -13 Stark states of argon in an electric field of 340 V/cm. The experimental spectra point upward, the calculated spectra downward.

fact that the calculated quadratic Stark shift of the $24p[1/2]_0$ state deviates significantly from the measured Stark shift and that the intensities in the calculated spectra are transition intensities and do not take into account the decay of the excited states on their way to the detector. Therefore, the intensity of the $24p[1/2]_0$ state in the calculated spectra is much larger than in the experimental spectra when compared to the intensities of the Stark states.

Fine structure of the Stark states

The fine structure of each high- ℓ Stark state, as highlighted in the upper panel of figure 4.2, was also reproduced in the MQDT calculation. In figure 4.11, the $k = -9$, $k = -11$, and $k = -13$ Stark states are shown for an electric field of $F = 340$ V/cm. These three k states were selected for comparison because both in the simulation and in the measurement this energetic region is not perturbed by low- ℓ states. The intensities in the simulation were not modified and correspond directly to the transition intensities. The intensity scale of the simulated spectrum was chosen such that the intensity of the peak at ~ 126878.4 cm^{-1} was equal to the intensity of the corresponding peak in the measured spectrum at ~ 126878.5 cm^{-1} . The simulations reproduce the strong peak on the high energy side and the three smaller peaks at lower energies. The calculation also shows that each k state is split into eight components but that typically four, and at most five, carry most of the intensity. The simulated spectrum is displaced by ~ 0.1 cm^{-1} with respect to the measured spectrum. The origin of this

shift is not known but probably has its origin in the deviations of the quadratic Stark shifts of the low- ℓ states already noted above.

In the MQDT calculation the wave function of each state in the $nn_1m_{j_c}m_\ell m_s$ basis can be calculated. As expected from the discussion in section 4.3.1, the 8 fine-structure components differ in their m_{j_c} , m_ℓ , and m_s character. Moreover, the states that carry most of the intensity only differ in their n_1 character for states of different k and have the same m_{j_c} , m_ℓ , and m_s character. It was however not possible to deduce from the wave functions why specific components of a specific Stark state have larger transition intensities than others.

4.4.3 Discussion of the MQDT calculations

The MQDT formalism described above and developed in references [36, 57, 58, 107, 108] has not been used before to calculate a Stark map with such a high resolution as the Stark map displayed in figure 4.8. In references [37, 38, 113] the experimental resolution was less than 1 cm^{-1} whereas the resolution of the present XUV laser spectra amounts to 0.008 cm^{-1} . The overall agreement between the calculated and measured Stark maps is good. In particular the splitting of each Stark state in multiple fine-structure components is reproduced accurately and the Stark maps of avoided crossings between low- ℓ states and high- ℓ Stark states are qualitatively very similar to the corresponding measured Stark maps. However, the deviations of the energetic positions of the low- ℓ states at high electric fields are large when compared to the linewidth in the measured spectra and prevent a more quantitative comparison. Nevertheless, one should realize that a deviation of 1 cm^{-1} , though large compared with the experimental line widths, represents a deviation of 0.1% of the binding energy. Two main reasons may be put forward to explain the deviations between experimental and simulated Stark spectra.

First, the calculated Stark maps such as that displayed in figure 4.9 depends on all quantum defects of all low- ℓ states and on all interaction parameters between the s and d states and between the p and f states. Some of these quantities are not very well known:

- The quantum defects for all $J = 0$ states are extracted from the known energetic positions of only a small number of states [83].
- The s-d and p-f interaction parameters are often poorly known, guessed, or not known at all. The interaction element between the d 3D_2 and the s 3P_2 is given as 0.1008 in reference [134] but gave surprisingly large intensities at low electric fields for the $24s[3/2]_2$ state and was therefore set to zero.
- The quantum defects of the p 3D_3 and f 3D_3 states were assumed to be equal to the p 3D_2 and f 3D_2 quantum defects, respectively. No independent value was found in the literature for these two quantum defects.

Because the calculated Stark map depends on the quantum defects and interaction parameters of all low- ℓ states, an experimental Stark map over a large energetic region, i.e. a large number of n values, might be used to fit these parameters. The large number of channels that need to be taken into account in the calculation and the fact that spectra for a large number of electric field strengths need to be calculated complicates this task considerably.

The second source of potential deviations between experimental and simulated spectra is the MQDT theory itself. In a recent calculation of a Stark map of the $n = 25$ Stark states of neon [54], the low- ℓ states were also found to be shifted to higher energies compared to the experimental results. The Stark map was measured using a UV laser with a band width of 0.05 cm^{-1} . The deviations between the measured and calculated values at high electric field strength, $\sim 180 \text{ V/cm}$, were also on the order of 1 cm^{-1} . The calculations were done in the same manner as the calculation of the argon Stark map but using a different software code, making it improbable that the deviation comes from a software error. In the theory, but also in the calculations several approximations are made that may account for the remaining discrepancies between experimental and simulated spectra.

- The separation constant β is calculated using a power series in F up to third order [113]; terms of higher order in F are neglected. In the calculation, it was however checked that the Bohr-Sommerfeld quantization rule holds for the calculated value of β . The differences between the given value of n_1 and the calculated value of n_1 using equation 4.13 and β were never larger than $1 \cdot 10^{-4}$.
- The space the electron moves in is divided into three regions and the theory assumes that the effects of the electric field are only significant in region III. In the calculations presented above the electric field strength was at most equal to 340 V/cm . The assumption mentioned above is a good approximation when $r_0 \ll r_F = F^{-1/2}$. For $F = 340 \text{ V/cm}$, $r_F = 3900$ atomic units whereas r_0 is on the order of 100 atomic units. Nevertheless, at high electric field, the influence of the electric field on the wave function in region II may cause a deviation in the calculated energy levels, particularly when the theoretical spectra are compared with high-resolution spectra.
- The WKB approximation to the wave function in the region $\eta_b < \eta < \eta_c$ may also cause a deviation, although the approximation should be reasonably accurate in the investigated energy region.

4.5 Conclusions

Using high-resolution XUV spectroscopy and TOF spectroscopic measurements the nonhydrogenic effects in the deceleration of Rydberg atoms were studied. The adiabatic traversals of avoided crossings must be considered in the analysis of the

deceleration behaviour of the Rydberg states. To optimize the deceleration, the electric fields need to remain below the Inglis-Teller limit and one has to study the avoided crossings between low- ℓ states and the high- ℓ Stark manifold in detail by spectroscopy.

Insight into the dependence of the energy levels on the electric field can be obtained by calculating these energy levels using MQDT, taking the interactions caused by the electric field into account. The overall agreement between the measured and calculated Stark maps is good but the deviations of the energetic positions of the low- ℓ states of $\sim 1 \text{ cm}^{-1}$ render accurate predictions of the deceleration efficiencies of selected Stark states in the presence of avoided crossings with low- ℓ states difficult.

The importance of crossings between Stark states with $|m| > 2$ is much reduced compared to crossings between states with $|m| = 0$ and 1 as explained in chapter 2. A possible method to enforce hydrogenic behaviour and diabatical traversals of the avoided crossings is to excite these high- $|m|$ states in a multi-photon excitation process using circularly polarized radiation. The electric field may then well be increased above the Inglis-Teller limit.

The kinetic energy taken away in the deceleration process can be increased by a factor of more than two by compensating for the field changes along the trajectories of the particles during deceleration. Under optimal conditions, the kinetic energy losses/gains can even be made larger than the Stark shifts of the excited states.

The range of principal quantum numbers $n = 20$ to 30 selected for the experiments in this chapter is a compromise between a sufficiently large Stark shift at the Inglis-Teller limit, which favours low- n states, and sufficiently long lifetimes, which favours high- n states. The measurement of the decay of the Rydberg Stark states at $n = 25$ sets a limit of $\sim 10 \mu\text{s}$ to the time available for deceleration. Stopping the argon Rydberg atoms within $10 \mu\text{s}$ requires higher field inhomogeneities than used in the experiments described above at the same absolute field strength below the Inglis-Teller limit. This requirement can only be met by a different, more compact electrode design.

Chapter 5

Stark deceleration of hydrogen atoms

5.1 Introduction

The main restriction in the deceleration experiments using inhomogeneous electric fields, is the necessity to keep the electric field strength below the Inglis-Teller limit as explained in chapter 4. This restriction does not apply to acceleration/deceleration experiments on atomic hydrogen.

Atomic hydrogen offers the following advantages over other atoms and molecules when using Stark deceleration to manipulate the velocity of Rydberg particles:

- Atomic hydrogen has the smallest mass of all atoms and molecules. The force that can be exerted by a given field gradient thus leads to a stronger acceleration and therefore to a better control of the translational motion. This advantage becomes particularly apparent in experiments in which hydrogen is seeded in a supersonic beam of a heavier rare gas. In this case the initial kinetic energy is given by the velocity of the seed gas (~ 580 m/s for argon). If in the Stark deceleration experiments the kinetic energy is reduced by the same absolute amount as for argon, the relative kinetic energy reduction is higher by a factor $m_{\text{Ar}}/m_{\text{H}} = 40$ as long as the particle velocity is not reversed.
- The energy level structure of hydrogen is very regular and well understood. Particularly important for Stark deceleration are the facts that all ℓ states of a given n are almost degenerate and that no avoided crossings between the optically accessible low- ℓ states and the Stark manifold occur.
- If relativistic effects are ignored and the effects of magnetic fields can be neglected, the crossings between Stark states of different manifolds are exact and Stark states retain their k and n values above the Inglis-Teller field. The electric field strength can thus be increased up to the ionization field strength without inhibiting the deceleration mechanism. Because the field gradients are proportional to the field, larger forces can be applied.

The measurements presented in this chapter, which is based on reference [129], show that the crossings between the $n = 22$ and $n = 21$ Stark manifolds are traversed diabatically in the deceleration process, setting an upper bound of $1.7 \cdot 10^{-4} \text{ cm}^{-1}$ to the energy splitting at these crossings. As a result of the diabatic traversals of the crossings, the change in kinetic energy when an H atom in a Rydberg state moves in or out of a field is equal to the Stark shift of the Rydberg state, irrespective of whether the field is above or below the Inglis-Teller field. These advantages could be fully exploited and the kinetic energy of the hydrogen atoms could be quadrupled over a flight distance of only 3 mm and accelerations as high as $a = 2 \cdot 10^8 \text{ m/s}^2$ could be achieved. The experiments on hydrogen described here and in chapters 7 and 8 are also relevant in the context of research on antihydrogen ($\bar{\text{H}}$) conducted at CERN and indicate a possible route toward trapping $\bar{\text{H}}$.

5.2 The Runge-Lenz vector

The potential of an electron interacting with the proton by means of the coulomb potential and moving in a static external electric field which points in the z direction, is given by equation 2.4. Because the potential depends on the z coordinate, the Hamiltonian does not commute with the square of the orbital angular momentum operator $\hat{\mathbf{L}}^2$ and ℓ is not a good quantum number. However, in a nonrelativistic theory, the z component of the Runge-Lenz vector does commute with the Hamiltonian and represents a constant of motion with its associated good quantum number. The Runge-Lenz vector is given by [75]

$$\hat{\mathbf{A}} = \frac{\hat{\mathbf{r}}}{2} - \frac{1}{2} \left([\hat{\mathbf{p}}, \hat{\mathbf{L}}] - [\hat{\mathbf{L}}, \hat{\mathbf{p}}] \right), \quad (5.1)$$

where $\hat{\mathbf{r}}$ and $\hat{\mathbf{p}}$ are the position and impulse operators, respectively. The expectation values A_z for Stark states are given by (in atomic units) $A_z = (n_1 - n_2)/n$. Stark states with a different A_z value do not interact with each other and therefore cross exactly in a Stark map. At the Inglis-Teller limit, for instance, blue-shifted and red-shifted Stark states of neighbouring n values become exactly degenerate because they have an A_z value of opposite sign.

In nonhydrogenic systems the potential of the positive nucleus is not exactly Coulombic because of the finite structure of the core. In this case, \hat{A}_z does not commute with the Hamiltonian and the crossings between Stark states are avoided. The consequences of these avoided crossings on deceleration experiments on nonhydrogenic Rydberg states have been discussed in chapter 4. If relativistic effects, for instance LS coupling, are included in the Hamiltonian of the hydrogen atom, the Hamiltonian and \hat{A}_z do not commute either. In Rydberg states of the hydrogen atom these effects are very small; for $n = 25$, $\ell = 1$ the fine-structure splitting, which scales as n^{-3} , is equal to $0.366 \text{ cm}^{-1} \cdot \left(\frac{2}{25}\right)^3 = 1.87 \cdot 10^{-4} \text{ cm}^{-1}$. Consequently, the split-

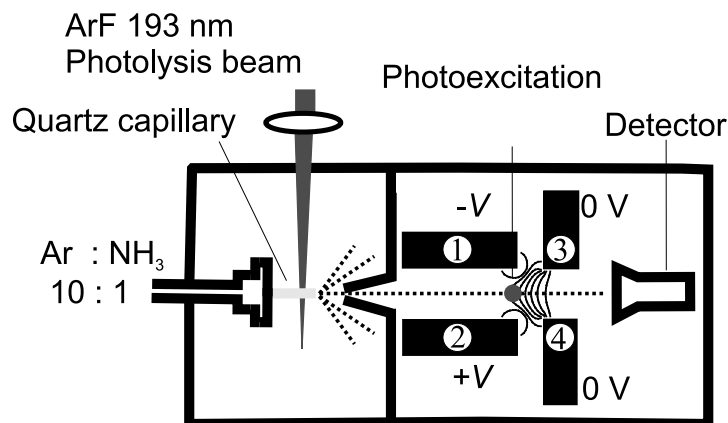


Figure 5.1: Schematic view of the experimental arrangement and the vacuum chamber. In the left part of the vacuum chamber a 10:1 Ar(He):NH₃ gas mixture was pulsed through a capillary mounted on a nozzle. The capillary was crossed by an ArF excimer photolysis laser operating at 193 nm to generate H atoms. The resulting skimmed supersonic beam containing H atoms propagated through a skimmer into the photoexcitation region which was surrounded by four metallic electrodes that were used to generate an inhomogeneous field. The anti collinear UV and VUV laser beams used to excite the H atoms to Rydberg states propagated parallel to the plate surfaces and perpendicular to the atomic beam. After flying through the inhomogeneous field region, the atoms reached a microchannel plate detector where they ionized and their time of flight was registered. The solid lines represent lines of constant electric field.

tings between different Stark states are typically much smaller than in nonhydrogenic systems at the same n values. At the slew rate of our experiment, the crossings of different Stark states are traversed diabatically as will be shown below.

5.3 Experimental setup

5.3.1 A supersonic beam of hydrogen atoms

The conventional way of producing an atomic beam of hydrogen atoms is by dissociating H₂ in a discharge and letting the hydrogen escape through a nozzle. In our lab a general method to generate radicals by photolyzing suitable precursors has been developed and extensively tested for studies of the radicals and their cations by pulsed-field-ionization zero-electron-kinetic-energy (PFI-ZEKE) photoelectron spectroscopy [136, 138, 139, 144]. This method was used to generate H atoms.

The radical source is depicted schematically in figure 5.1 and consists of a nozzle at the exit of which a quartz capillary with a length of approximately 2 cm and an inner diameter of 1 mm is mounted. The radical precursor is photolyzed in the capillary using an excimer laser beam with a wavelength that can be chosen to be 351 nm, 308 nm, 248 nm, or 193 nm, depending on the gas mixture. The essential characteristic of the radical source is that a supersonic expansion takes place at the

exit of the capillary, i.e. after the radicals have been produced. In this manner the radicals can cool down translationally and internally to temperatures of ~ 1 K, typical of supersonic expansions.

To generate hydrogen atoms, NH_3 seeded in a rare gas (argon or helium) in a 10 to 1 mixture, was photolyzed using a 193 nm excimer laser beam



This reaction was used in reference [137] to generate NH_2 radicals for high-resolution measurements by PFI-ZEKE photoelectron spectroscopy and it was estimated that 5% of the NH_3 was photolyzed into NH_2 , leading to a density in the photoexcitation region of $\sim 10^{12} \text{ cm}^{-3}$ [137, 139].

The NH_2 ground state only lies 37115 cm^{-1} above the NH_3 ground state [4] whereas the photolysis laser beam has a wave number of $51.7 \cdot 10^3 \text{ cm}^{-1}$. Therefore the H atoms can have a maximal kinetic energy of $E_{\text{kin}}/hc = 13.7 \cdot 10^3 \text{ cm}^{-1}$ or a velocity of $18.1 \cdot 10^3 \text{ m/s}$. Atoms travelling at such an initial velocity would be too fast to decelerate to zero velocity. However, collisions with the rare gas atoms within the capillary and during the supersonic expansion, decrease the velocity of the hydrogen atoms to approximately that of the rare gas atoms in the beam (580 m/s for argon, 1850 m/s for helium), reducing the kinetic energy of the H atoms in the supersonic beam to $E_{\text{kin}}/hc = 20$ to 25 cm^{-1} or $E_{\text{kin}}/hc = 140$ to 150 cm^{-1} depending on whether argon or helium is used as a seed gas. Before the hydrogen beam enters the excitation region, it is collimated by a 0.5 mm diameter skimmer placed 1 to 2 cm downstream from the capillary exit.

5.3.2 Electrode setup and excitation scheme

The excitation of the neutral hydrogen atoms to high-Rydberg states took place between the electrodes labelled 1 and 2 (see figure 5.1) which were set to an opposite voltage. The electrodes labelled 3 and 4 were held at zero potential so that the electric field between the two sets of electrodes was highly inhomogeneous. The distances between electrodes 1 and 2 and between electrodes 3 and 4 were 6 mm. The distance between electrodes 1 and 3 (2 and 4) amounted to 3 mm. The electrode setup could be translated along the z axis so that photoexcitation could take place in homogeneous or inhomogeneous electric fields.

The following two-colour, two-step photoexcitation sequence was used to excite the H atoms to the Rydberg Stark states:

$$1 \text{ } ^2\text{S}_{1/2} \xrightarrow{\text{VUV}} 2 \text{ } ^2\text{P}_{1/2,3/2} \xrightarrow{\text{UV}} |nn_1n_2m\rangle. \quad (5.3)$$

In the first excitation step the atoms were excited from the $1 \text{ } ^2\text{S}_{1/2}$ ground state to the two fine-structure components ($J = 1/2$ and $J = 3/2$) of the $2 \text{ } ^2\text{P}$ state. The VUV radiation at Lyman α was generated by resonance-enhanced difference-frequency mixing

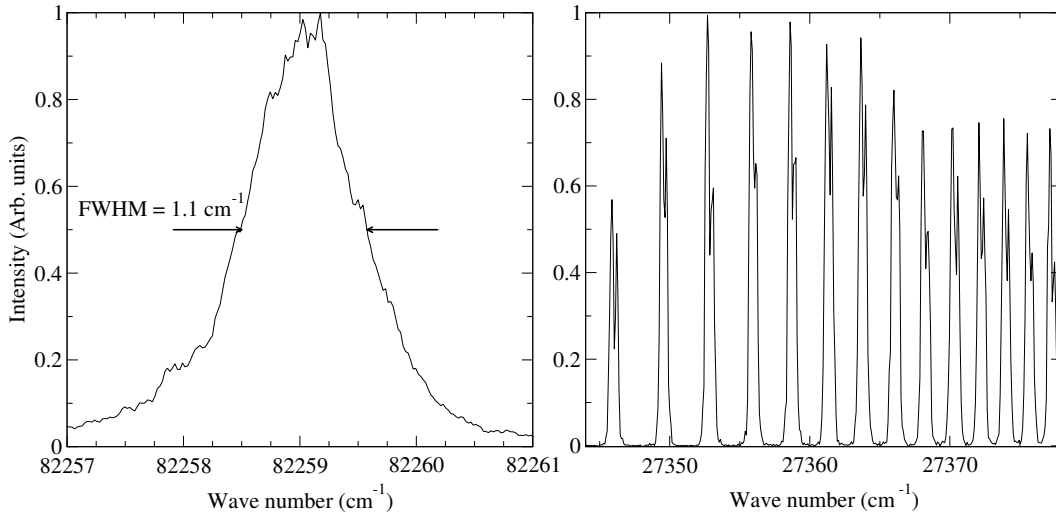


Figure 5.2: Left panel: Spectrum of the $1\ ^2S_{1/2} - 2\ ^2P$ resonance. The wave number of the second laser was held fixed above the ionization energy to ionize the hydrogen atoms. Right panel: Spectrum of the $n = 39$ to 52 Rydberg states in zero electric field. The VUV laser is kept fixed at the maximum of the $1\ ^2S_{1/2} - 2\ ^2P$ transition. The wave number scale in the left panel corresponds to the transition wave number from the ground state and in the right panel to the transition wave number from the intermediate state.

in a cell filled with krypton as described in section 3.1.2. In the second excitation step, the doubled output of a third Nd:YAG-pumped dye laser excited the atoms to Rydberg Stark states with $n \geq 20$. The polarizations of both laser beams could be chosen to lie either parallel or perpendicular to the static electric field vector at the point of excitation.

Depending on the Stark state they were excited to, the hydrogen atoms were decelerated or accelerated in the inhomogeneous electric field. After flying out of the electrode setup the atoms traversed a 20 cm long field-free region before they ionized at the MCP detector where their time of flight was registered.

5.4 Results

5.4.1 Zero-field spectroscopy

A measurement of the $1\ ^2S_{1/2} - 2\ ^2P$ resonance is displayed in the left panel of figure 5.2. In this measurement the excited hydrogen atoms were ionized by the second laser and the ion current detected at the MCP was measured as a function of the VUV laser wave number. The two fine-structure components of the $2\ ^2P$ state, which are separated by 0.366 cm^{-1} , are not resolved in this measurement. The observed full width at half maximum amounts to 1.1 cm^{-1} whereas the laser bandwidth is 0.7 cm^{-1} . The natural linewidth of these transitions is $3.3 \cdot 10^{-3}\text{ cm}^{-1}$ corresponding

to a natural lifetime of the 2^2P state of 1.6 ns [11]. Helium was used as seed gas and the hydrogen atoms moved with a velocity of approximately 1900 m/s. The end of the capillary and the tip of the skimmer were separated by a distance of ~ 1 cm so that after the skimmer the perpendicular velocity of the hydrogen atoms did not exceed 100 m/s. The velocity distribution along the laser propagation axis corresponds to a Doppler width of 0.046 cm^{-1} at 82259 cm^{-1} . Both the Doppler width and the natural linewidth of the transition are negligible compared to the bandwidth of the VUV laser which represents the main contribution to the width of the line shown in figure 5.2, taking into account the unresolved fine-structure interval.

To record the spectrum displayed in the right panel of figure 5.2, the second laser was scanned in the region $n = 39$ to 52 in zero electric field, while keeping the frequency of the VUV laser fixed at the maximum of the $1^2S_{1/2} - 2^2P$ transition. The MCP detector was at the limit of saturation for most of these transitions which explains the nearly constant peak intensity. The Rydberg states can be resolved up to $n \approx 65$ at which point the lines corresponding to adjacent n start to overlap. Because both fine structure components in the intermediate state are excited by the VUV laser, every line in this spectrum is split into two lines which are separated by $\sim 0.37 \text{ cm}^{-1}$. The linewidth of each component is approximately 0.35 cm^{-1} and corresponds to the bandwidth of the doubled output of the pulsed dye laser.

5.4.2 Polarization effects

The relative population of different magnetic sublevels of the excited Rydberg states of hydrogen depend on the relative polarizations of the two linearly polarized laser beams and of the static electric field. In the absence of a static electric field, it is convenient to choose the z axis of the laboratory frame to lie parallel to the electric field vector of one of the two lasers, e.g. the VUV laser. This choice implies the selection rule $\Delta M_J = 0$ for the first excitation step, and $\Delta M_J = 0$ or ± 1 for the second excitation step depending on whether the polarization vector of the second laser is parallel or perpendicular to that of the first laser, respectively. In the former case $M_J = \pm \frac{1}{2}$ magnetic sublevels are excited, in the latter $M_J = \pm \frac{1}{2}$ or $\pm \frac{3}{2}$ sublevels.

In the presence of a static electric field, the z axis of the laboratory frame is usually chosen to lie parallel to the static electric field vector and four independent situations can be realized with two linearly polarized lasers: Both lasers are polarized parallel to the static electric field vector (we call this configuration the $\pi - \pi$ configuration), both lasers are polarized perpendicularly to the static electric field vector ($\sigma - \sigma$ configuration) or one laser is polarized parallel and one perpendicularly to the static electric field vector ($\sigma - \pi$ or $\pi - \sigma$ configurations). The magnetic sublevels of the Rydberg Stark states that are excited from the $2S_{1/2}$ ground state in these cases are: $M_J = \pm \frac{1}{2}$ ($\pi - \pi$), $M_J = \pm \frac{1}{2}, \pm \frac{3}{2}, \pm \frac{5}{2}$ ($\sigma - \sigma$) and $M_J = \pm \frac{1}{2}, \pm \frac{3}{2}$ ($\sigma - \pi$ and $\pi - \sigma$). Because of the spin-orbit coupling neither m'_ℓ nor m'_s are good quantum numbers in the $2P_J$ intermediate level and both $m'_\ell = 0$ and ± 1 components are excited in a coherent

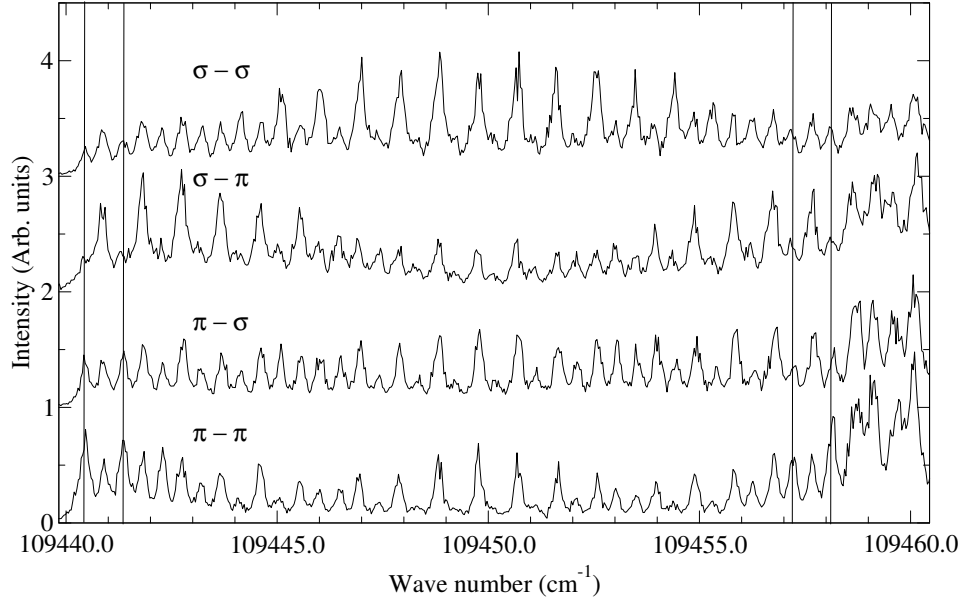


Figure 5.3: Four scans around the zero field position of the $n = 22$ state in a field of 333 V/cm. The polarizations of the VUV and the second laser with respect to the electric field vector are (from bottom to top): $\pi - \pi$, $\pi - \sigma$, $\sigma - \pi$, $\sigma - \sigma$. The vertical lines connect states with $k = -21, -19, 17$ and 19 (from left to right).

superposition.

The spin-orbit splitting of higher Rydberg states of hydrogen scales as n^{-3} and rapidly becomes negligible (it amounts to $\sim 3.7 \cdot 10^{-4} \text{ cm}^{-1}$ at $n = 10$). The Rydberg electron spin can thus be regarded as being completely decoupled from the orbital motion. The final states are therefore more conveniently labelled by $m_\ell = m$ than by M_J . In the second excitation step of equation 5.3, $|m'_\ell - m| = 0$ for π polarization and $|m'_\ell - m| = 1$ for σ polarization of the second laser, and $|m| = 0, 1, 2$ Stark states are excited in the $\sigma - \pi$ and $\pi - \pi$ configurations whereas $|m| = 0, 1, 2$ Stark states are accessed in the $\sigma - \sigma$ and $\pi - \sigma$ configurations. Consequently, the Stark spectra recorded with the two-photon excitation sequence 5.3 are expected to exhibit transitions to Stark states of both even and odd k values, see equation 2.11.

The relative intensities of the transitions to the Stark states, however, depends on the polarization configuration as was shown in reference [29], and is illustrated in figure 5.3. Four two-photon spectra of the Stark states of $n = 22$ are displayed in this figure corresponding to the four polarization configurations described above. The spectra were recorded in the region of the electrode setup between plates 1 and 2 where the electric field is homogeneous at a field strength of 333 V/cm.

The strong dependence of the intensity distribution on the polarization configuration enables one to optimize the production of selected Stark states. The $\sigma - \sigma$ configuration is best suited to excite Stark states of low- $|k|$ values at the centre of the Stark manifold. Even- $|k|$ Stark states at both edges of the Stark manifold are pro-

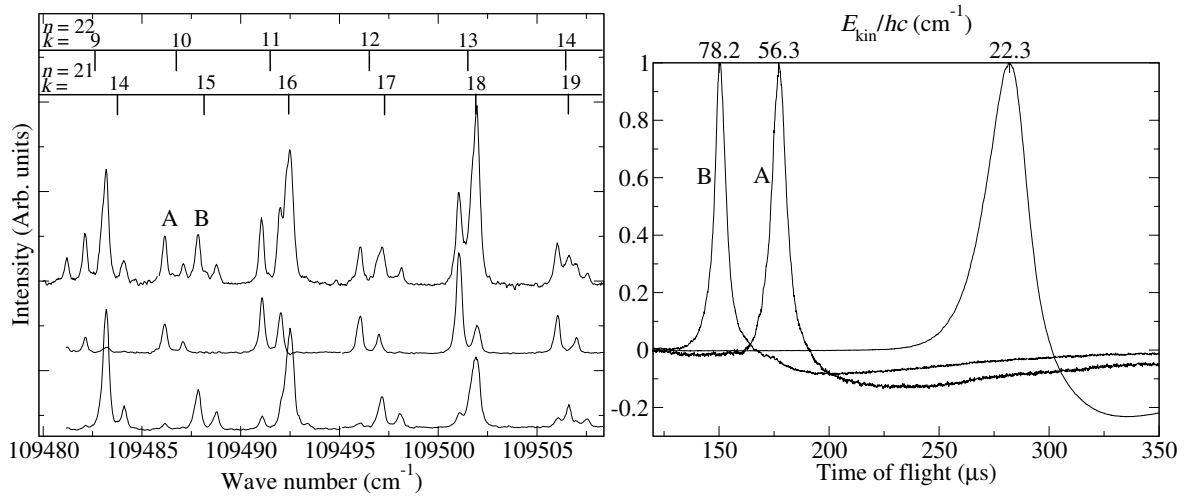


Figure 5.4: Left panel: Upper trace: Stark spectrum around $n^* = 23.5$ to 25.5 in a homogeneous electric field of 3333 V/cm. The electric field is switched off after excitation. Middle (Lower) trace: Same as the upper trace without switching off the electric field. The detection window is placed at the expected time of flight for blue-shifted $n = 22$ ($n = 21$) states. Right panel: TOF traces of atoms excited to a zero-field state (outer right trace) and to the states A and B in the spectrum displayed in the left panel.

duced efficiently with the $\sigma - \pi$ configuration. Both odd- and even- $|k|$ Stark states gain intensity at the edge of the manifold for π polarization of the VUV laser and the intensity of the outermost Stark states is optimal in the $\pi - \pi$ configuration. Because the acceleration/deceleration forces are largest for the outer components of the Stark manifold, the $\pi - \pi$ polarization configuration was selected to carry out the acceleration/deceleration experiments described in the next subsection and in the mirroring and trapping experiments described in chapters 7 and 8.

5.4.3 Acceleration after excitation in homogeneous electric fields

The left panel of figure 5.4 shows the spectrum of hydrogen in the region of effective principal quantum number $n^* = 23.5$ to 25.5 recorded in a homogeneous electric field of 3333 V/cm. In the measurement corresponding to the upper trace, the electric field was switched off immediately after excitation to avoid any acceleration/deceleration and all the atoms reached the MCP $\sim 280 \mu\text{s}$ after photoexcitation.

In the right panel, a TOF trace for a beam of hydrogen atoms excited in zero electric field to the $n = 22$ Rydberg state is displayed. Because the inhomogeneous field is off in this measurement, the atoms neither accelerate nor decelerate and the TOF trace serves as a reference. From this measurement, the initial velocity and kinetic energy are determined to be 730 m/s and 22.3 cm^{-1} , respectively. The initial velocity depends on the exact delay between the excimer laser pulse and the excitation laser pulses. Therefore, reference measurements were taken regularly to establish the ini-

tial kinetic energy. The FWHM of the TOF trace corresponds to a velocity distribution with a FWHM of 40 m/s or a translational temperature of 0.1 K.

The traces labelled A and B in the right panel of figure 5.4 represent TOF traces of atoms excited to the states labelled A and B in the left panel of the same figure, respectively. In these measurements, the electric field was not switched off, and the Rydberg atoms accelerated in the inhomogeneous electric field. The accelerated atom beams have a mean final velocity of 1350 m/s (B) and 1150 m/s (A). In the acceleration process a constant amount of energy is added, irrespective of the initial position or velocity of the Rydberg atoms in the beam. Hence, the energy spread of the atomic beam does not change. The observed reduction in width of the TOF traces merely reflects the fact that the time of flight is inversely proportional to the velocity. The TOF trace of a decelerated atomic beam would thus become wider than that of the reference measurement.

The kinetic energy differences compared to the zero-field measurement amount to 34 cm^{-1} and 55.9 cm^{-1} for the hydrogen atoms of trace A and trace B, respectively. The Stark shift of state A with respect to the $n = 22$ zero-field position is $E_{\text{Stark}}/hc = 35.7 \text{ cm}^{-1}$ and that of state B with respect to the $n = 21$ zero field position $E_{\text{Stark}}/hc = 59.5 \text{ cm}^{-1}$. State A is therefore identified to be a blue-shifted Stark state in the $n = 22$ manifold and state B to be a blue-shifted Stark state in the $n = 21$ manifold. Indeed, if we do not switch off the electric field and record the integrated MCP-detector signal over the expected time-of-flight window for the $n = 22$ and $n = 21$ states separately as a function of the laser wave number, the Stark spectrum gets simplified: The upper trace in the left panel gets disentangled into the Stark spectra for $n = 22$ (middle trace) and $n = 21$ (lower trace). The k value for each transition can be calculated using the known formula for the Stark shift up to third order. For every k value two lines are observed because of the fine-structure splitting in the intermediate state, which has increased to almost 1 cm^{-1} [102] in an electric field of 3333 V/cm.

The Inglis-Teller fields for $n = 21$ and $n = 22$ are $F_{\text{IT}} = 420 \text{ V/cm}$ and $F_{\text{IT}} = 333 \text{ V/cm}$, respectively. Even though the applied electric field in the measurements in figure 5.4 is a factor 8 (10) higher than F_{IT} for $n = 22$ ($n = 21$), the measured kinetic energy differences are equal to the Stark shifts of the excited states. Moreover, when state B is excited, no signal is measured at the time of flight corresponding to a kinetic energy difference equal to the Stark shift of the excited state with respect to the $n = 22$ zero-field position. Such a time of flight would approximately correspond to the time of flight, t_A^{max} , at which trace A has its maximum.

The $n = 21$, $k = 15$, $|m| = 1$ state crosses 16 Stark states with $n = 22$ and $|m| = 1$ when the electric field changes from 3333 V/cm to 0. If any of these crossings would be traversed adiabatically, a signal would arise at a time of flight approximately equal to t_A^{max} . The lack of signal at a signal-to-noise ratio of 1:70 means that the probability of an adiabatic traversal of an avoided crossing is smaller than $\frac{1}{70 \cdot 16} = 8.9 \cdot 10^{-4}$. In argon this probability was found to be unity. To first order $\frac{dE}{dF} = \frac{3}{2}nk$ and the electric

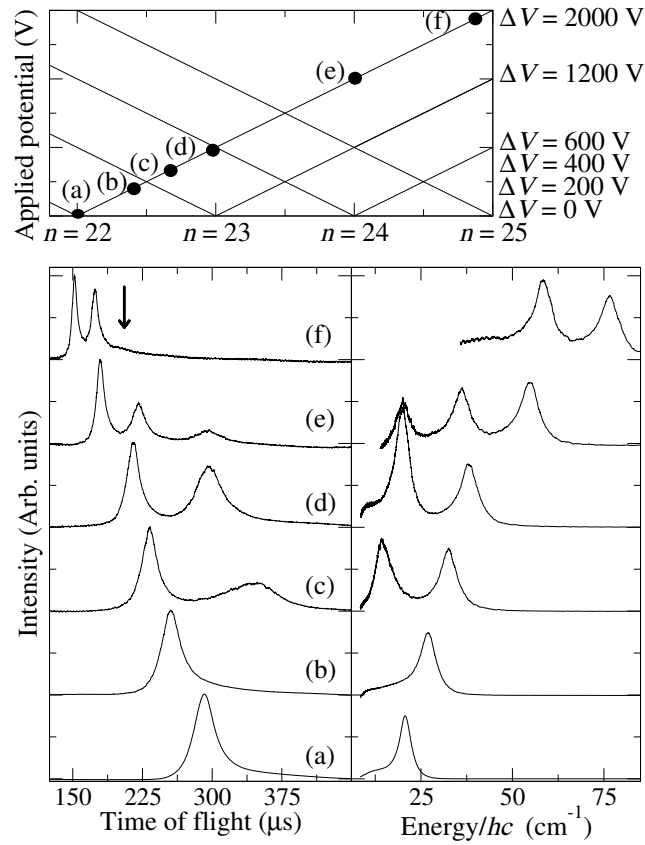


Figure 5.5: Upper panel: Schematic map of the Stark states of H in the range of principal quantum number $n = 22$ to 25. The dots in this panel correspond to the positions where the acceleration/deceleration experiments shown in the lower panel were performed. Lower left panel: TOF spectra of the H atoms recorded at the positions indicated in the top panel. Lower right panel: Kinetic energy distribution extracted from the experimental TOF spectra.

field slew rate can be approximated by

$$\frac{dF}{dt} = \frac{v_{\text{av}} \Delta F}{l} \approx 1 \cdot 10^9 \text{ V}/(\text{cm s}), \quad (5.4)$$

where v_{av} is the average velocity of the atomic beam and $l = 3 \text{ mm}$ the path length over which the electric field changes from 3333 V/cm to 0. A probability of an adiabatic crossing of $8.9 \cdot 10^{-4}$ implies that the minimal distance between the adiabatic energy curves of the $n = 21$, $k = 15$ state and the Stark states of the $n = 22$ manifold is less than $1.7 \cdot 10^{-4} \text{ cm}^{-1}$, see equation 2.21.

5.4.4 Acceleration after excitation in inhomogeneous electric fields

Figure 5.5 summarizes a set of TOF measurements of the Rydberg atoms carried out after photoexcitation to the blue-shifted Stark states of $n = 22$ at several inhomogeneous electric fields, which are indicated as dots in the schematic Stark map displayed

in the upper panel. To change the excitation point from a region where the field is homogeneous to one where it is inhomogeneous, the electrodes were shifted 5.5 mm away from the MCP detector so that excitation approximately took place at the height of the edges of electrodes one and two, facing electrodes three and four.

The TOF scale of the lower left-hand-side panel of the figure was converted into an energy scale in the right-hand-side panel. As a result the intensity axis was scaled by multiplying the intensity scale of the right-hand-side panel with the Jacobian element $(dE_{\text{kin}}/dt) \propto E^{-3/2}$.

The bottom trace (trace (a)) in the lower panels corresponds to the zero-field reference measurement. The initial velocity determined from this measurement is 702 m/s. The H atoms in the beam thus have a kinetic energy $E_{\text{kin}}/hc = 20.8 \text{ cm}^{-1}$ when they enter the decelerator. At an applied voltage of $\pm 100 \text{ V}$ (trace (b)), the times of flight are shifted by $\sim 50 \mu\text{s}$ to earlier times as expected for a low-field seeking state. The peak in the distribution corresponds to a final kinetic energy of $E_{\text{kin}}/hc = 27.1 \text{ cm}^{-1}$. At $\pm 200 \text{ V}$, above the Inglis-Teller field of $n = 22$ (trace (c)), the outer red-shifted Stark states of the $n = 23$ manifold are also excited by the laser because the strongly inhomogeneously broadened lines overlap. The atoms in the red-shifted states are decelerated and their times of flight increase by about $60 \mu\text{s}$, corresponding to a final kinetic energy of $E_{\text{kin}}/hc = 14.6 \text{ cm}^{-1}$, whereas the atoms in the blue-shifted Stark states are accelerated to a final kinetic energy of $E_{\text{kin}}/hc = 32.7 \text{ cm}^{-1}$. The late peak in the TOF spectrum (c) shows how efficiently atoms can be decelerated but also illustrates the problems that arise when detecting the atoms that are slowed down to close to zero velocity: The TOF distribution becomes very broad and rapidly shifts toward long times of flight so that very slow atoms can no longer be detected in TOF measurements.

The TOF spectrum recorded at $\pm 300 \text{ V}$ shows two peaks at final kinetic energies of 38.2 cm^{-1} and 20.1 cm^{-1} , corresponding to a blue-shifted Stark state with $n = 22$, and a $k \approx 0$ state of $n = 23$, respectively. The position of the latter of these two TOF peaks is almost the same as for the reference measurement, as expected for $k \approx 0$ states. At an applied voltage of $\pm 600 \text{ V}$, the blue-shifted Stark states of the $n = 22$ manifold overlap spectrally with less blue-shifted Stark states of $n = 23$ and with $n = 24$, $k \approx 0$ Stark states. Consequently, three peaks are observed in the TOF spectrum at positions corresponding to final kinetic energies of 55 cm^{-1} , 36.2 cm^{-1} , and 20.3 cm^{-1} for the Stark states with $n = 22$, 23 , and 24 , respectively. The top trace (f) in figure 5.5 represents a measurement recorded at $\pm 1000 \text{ V}$, above the field-free position of the $n = 25$ states. Here, only two maxima are observed in the TOF spectra corresponding to the acceleration of the blue-shifted states with $n = 22$ and $n = 23$ to final kinetic energies of 76.7 cm^{-1} and 58.5 cm^{-1} , respectively. At the corresponding field strength of more than 3000 V/cm , the $n \geq 24$ Stark states within the laser bandwidth are all field ionized and do not contribute to the TOF spectrum.

Converting the TOF scale in the lower left-hand-side panel of figure 5.5 into a kinetic energy scale (see lower right-hand-side panel of figure 5.5) demonstrates that

Table 5.1: Summary of acceleration/deceleration experiments on H atoms in time-independent inhomogeneous electric fields. The Stark shift was calculated as the difference between the laser excitation energy and the zero-field position of the Rydberg states. The change in kinetic energy ΔE_{kin} was determined from the maxima of the energy distributions displayed in figure 5.5.

Applied voltage (V)	n	Stark shift (cm^{-1})	$\Delta E_{\text{kin}}/hc$ (cm^{-1})
0		0	0
± 100	22	6.4	6.3
± 200	22	12	11.9
	23	-7	-6.2
± 300	22	17.6	17.4
	23	-1.4	-0.7
± 600	22	34.5	34.2
	23	15.6	15.4
	24	-1.5	-0.5
± 1000	22	57	55.9
	23	38.1	37.7
	24	21.1	—

the Rydberg atoms can be as efficiently decelerated as they can be accelerated. Indeed, the two peaks in trace (c) have the same integrated intensity. Unfortunately, the stopping of the Rydberg atoms cannot be demonstrated directly in the experimental configuration used in these experiments because stopped atoms cannot reach the detector.

Table 5.1 summarizes the results of the quantitative analysis of the TOF spectra shown in figure 5.5 and compares the measured changes in kinetic energy with the Stark shift. The Stark shift is calculated by taking the difference between the excitation energy of the laser and the well-known zero-field position of the corresponding n state. All the measured kinetic energy differences are equal to the Stark shift of the excited state within 1 cm^{-1} , which represents the uncertainty of the measurements.

5.5 Conclusions

The following conclusions can be drawn from the results summarized in figures 5.4 and 5.5 and table 5.1:

1. Individual Stark states can be excited selectively and accelerated or decelerated, depending on their k value. No change in quantum state is observed in the 3 to 8 μs between excitation and exiting the electrode setup. Consequently, beams of hydrogen atoms with freely adjustable kinetic energy can be produced that could be used in scattering experiments.

2. Changes in kinetic energy of up to three times the initial kinetic energy of the H atoms can be readily achieved. This observation directly implies that H atoms can be stopped using our 3 mm long decelerator provided that their initial kinetic energy is less than $E_{\text{kin}}/hc = 55 \text{ cm}^{-1}$ (or $E_{\text{kin}} = 1.1 \cdot 10^{-21} \text{ J}$, corresponding to an initial velocity of 1150 m/s). This very large improvement over previous experiments, in which the initial kinetic energy could only be modified by a few percent (see chapter 4 and references [95, 126, 127, 131, 145]), results from the small mass of the H atoms and from the fact that the crossings of the Stark states are traversed diabatically which enables one to use electric fields several times larger than the Inglis-Teller field.
3. Upper bounds of 0.089 % for the probability of adiabatic traversals of the crossings between Stark states at a slew rate of $1 \cdot 10^9 \text{ V}/(\text{cm s})$ and of $1.7 \cdot 10^{-4} \text{ cm}^{-1}$ for the magnitude of the avoided crossings at $n = 22$ were derived. In our experiments on argon this probability was found to be 100%.
4. The average acceleration over the length of the decelerator can be as high as $(600 \text{ m/s})/(3 \mu\text{s}) = 2 \cdot 10^8 \text{ m/s}^2$. By expressing the acceleration in terms of the average field gradient $\overline{\nabla F}$, the mass m of the decelerated atoms and the quantum numbers n and k of the Stark state

$$\frac{a}{(\text{m/s}^2)} = \frac{3a_0^3 e m_e E_h}{2\hbar^2} \frac{\overline{\nabla F}}{\text{V/m}^2} \frac{1}{m/\text{kg}} nk, \quad (5.5)$$

one sees that a field gradient of only $350 \mu\text{V}/\text{cm}^2$ is sufficient to accelerate a hydrogen (or an antihydrogen) atom in a blue- or red-shifted Stark state with $n \geq 20$ as efficiently as the earth gravitational field. Potential future experiments to determine the sign of the gravitational force on antihydrogen atoms may thus have to consider the effects of the gradients of stray electric fields if such experiments are to be carried out on the excited Rydberg antihydrogen atoms which are currently being produced at CERN [1, 43].

Chapter 6

Deceleration of argon using time-dependent inhomogeneous electric fields

6.1 Introduction

In this chapter, which is based on references [126] and [127], the deceleration of argon Rydberg atoms in time-dependent electric fields is studied. As was already shown in chapter 4, the deceleration of Rydberg particles can be increased considerably by using time-dependent potentials. By using appropriate voltage pulses the kinetic energy loss can be made three times larger than the Stark shift of the excited state. The kinetic energy loss for an $n = 15$ state can thus be as high as 60 cm^{-1} . This result opens up the possibility to slow down supersonic beams of light atoms and molecules ($m \leq 14 \text{ u}$) seeded in xenon (beam velocity 320 m/s) to zero velocity.

To quantify the acceleration in the dimension perpendicular to the beam propagation axis, images of the transverse distribution of the atom beam were measured and analyzed. These images were recorded using an MCP detector connected to a phosphor screen and a CCD camera. From these measurements, the three-dimensional velocity distribution of the Rydberg atoms in the slowed down atomic beam could be extracted with the aid of particle trajectory calculations.

6.2 The electrode setup

The narrow bandwidth vacuum ultraviolet laser system described in section 3.1.1 was used to excite argon atoms from the 1S_0 ground state to $n = 15$ to 30 Rydberg states located below the $^2P_{3/2}$ ionization threshold in a single-photon excitation process. The VUV laser beam intersected the skimmed supersonic expansion of argon gas at right angles halfway between the two parallel plates labelled 1 and 2 of the electrode setup represented in figure 6.1. These two electrodes, referred to below as the front

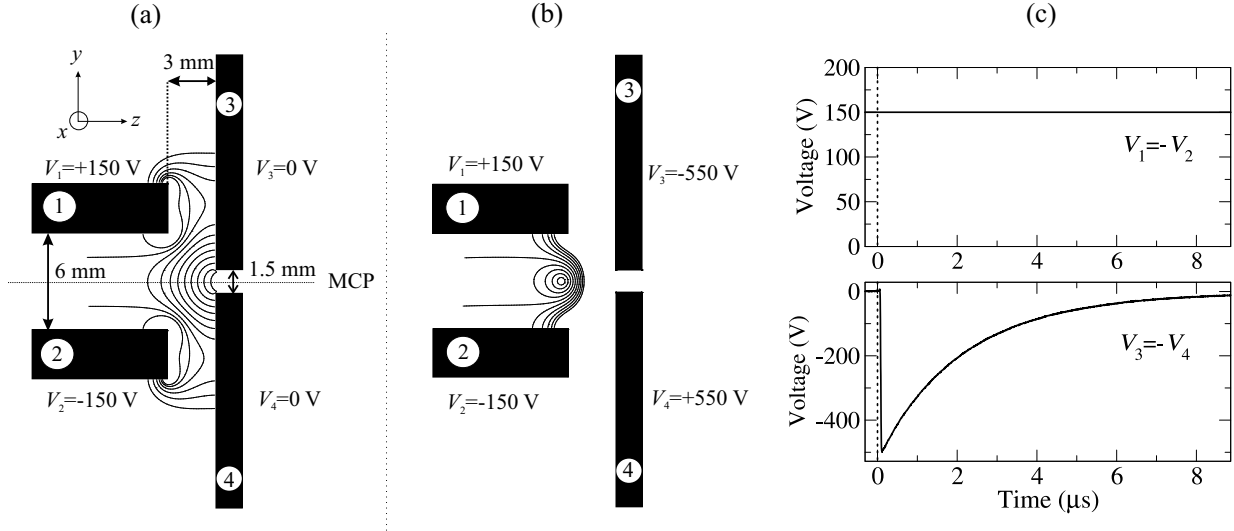


Figure 6.1: Panel (a) and (b): Schematic overview of the electrode setup. The skimmed supersonic beam of the sample gas (argon) propagated in the z direction halfway between the metallic electrodes. The VUV laser beam propagated in the x direction parallel to the plate surfaces and perpendicular to the atomic beam. The photoexcitation point could be shifted by translating the electrode setup in the z direction. For the voltages indicated in the figure, the solid lines represent lines of constant electric field ranging from 50 V/cm to 550 V/cm in steps of 50 V/cm (panel (a)) and from 100 V/cm to 1000 V/cm in steps of 100 V/cm (panel (b)). Panel (c): Time dependence of the electrode potentials in the deceleration experiments in time-dependent electric fields. The excitation time is indicated at $t = 0$ by the dashed line. The electric field vectors between the front plates and between the back plates pointed in opposite directions.

plates, were on the upstream side of the gas expansion and were 15 mm long and 6 mm apart. The other two electrodes, the back plates (3 and 4 in figure 6.1), were placed at a distance of 3 mm from the edge of the front plates and were separated by 1.5 mm. All four electrodes were 20 mm long in the x direction and could be independently set to any voltage between 0 and 5000 V.

Two types of deceleration experiments were performed with this electrode setup. In the first type of experiments the back plates were kept at zero volt and the front plates at a constant but opposite voltage of magnitude V_{FP} , i.e., $V_1 = -V_2 = V_{\text{FP}}$, chosen such that the argon atoms were photoexcited in an electric field $F = 2V_{\text{FP}}/(6 \text{ mm})$ approximately equal to the Inglis-Teller field. In this configuration, the electric field difference between the excitation region and the field-free region beyond the back plates amounted to $2V_{\text{FP}}/l_1$ with $l_1 = 6 \text{ mm}$ and the maximum gain/loss of kinetic energy was $\Delta E = \frac{3}{2}nk(2V_{\text{FP}}/l_1)$. For example, $\Delta E/hc = -10.8 \text{ cm}^{-1}$ for the most red-shifted Stark state ($k = -21$) of the $n = 22$ Stark manifold when $V_{\text{FP}} = 110 \text{ V}$.

In the second type of experiments (see panel (b) in figure 6.1) the front plates were kept at a constant voltage, such that the electric field at excitation lay only slightly below the Inglis-Teller field. 50 ns after photoexcitation, the back plates were switched from zero volt to a high voltage of opposite polarity and of magnitude V_{BP} , so that the electric field generated by the front plates had the opposite sign to that generated by

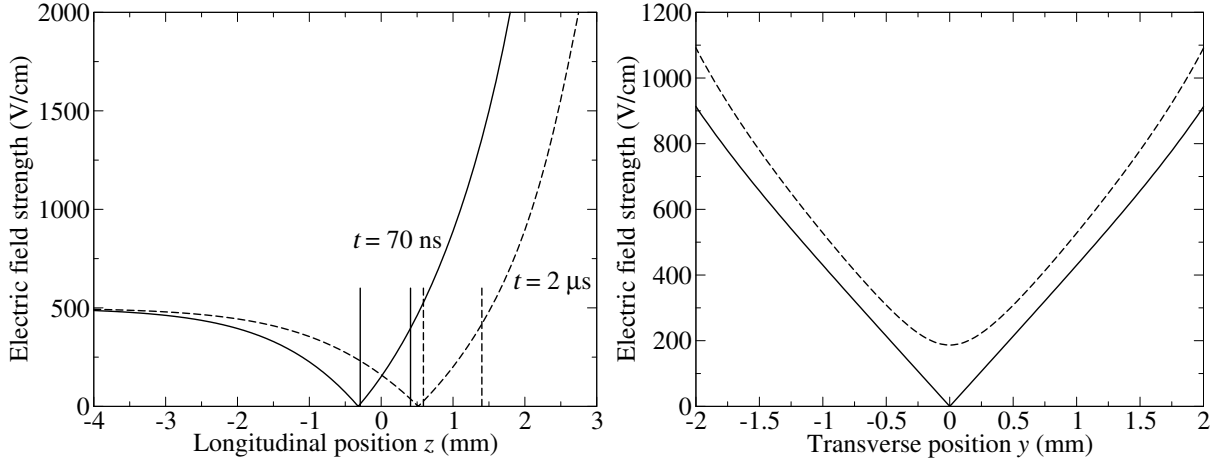


Figure 6.2: Left panel: Electric field strength along the z axis 70 ns (solid line) and 2 μ s (dashed line) after photoexcitation calculated for the following sets of potentials: $t = 70$ ns: $V_1 = -V_2 = 150$ V, $V_3 = -V_4 = -550$ V and $t = 2$ μ s: $V_1 = -V_2 = 150$ V, $V_3 = -V_4 = -222$ V. $z = 0$ corresponds to the edge of plates 1 and 2 facing plates 3 and 4, as shown in figure 6.1a. The full and dotted vertical lines limit the regions where the electric field strength lies between 0 V/cm and the Inglis-Teller field at $n = 22$. On lines parallel to the z axis in the yz plane, the distribution of electric field strengths has a similar shape but the minimum is slightly above 0 V/cm. Right panel: Electric field strength along the y axis on the lines $z = -0.4$ mm (solid line) and $z = 0$ (dashed line). The potentials that were applied are $V_1 = -V_2 = 150$ V and $V_3 = -V_4 = -550$ V.

the back plates. This voltage pulse reversed the sign of the z component of the electric field vector in the electrodes. During the sign reversal the electric field strength returned to exactly zero in the $y = 0$ plane, potentially causing a loss of the low-field seeking character of the Rydberg atoms located in this plane. At positions above or below this plane, the field experienced by the Rydberg atoms did not return to zero at any time during the voltage rise because of the residual component of the field along the z axis. Instead, the direction of the field vector made an (anti)clockwise rotation for $y > 0$ ($y < 0$). Only a very small fraction of the initially prepared Rydberg atoms were located close enough to the $z = 0$ plane to lose their low-field seeking character.

The sign reversal of the electric field that took place along the gas propagation direction (z axis) led to much higher electric field gradients than in the first type of experiments, as can be seen from the lines of constant electric field depicted in figure 6.1. The solid line in the left panel of figure 6.2 describes the change in electric field along the gas expansion direction when the pulsed voltages on the back plates have reached their maximum value. A simple RC circuit made the voltages on the back plates decay exponentially as illustrated in the lower half of panel (c) of figure 6.1. The time constant of the exponential function was chosen such that 1) the particles did not experience a field larger than the Inglis-Teller field at any point of their trajectories and 2) the field gradients remained maximal during the whole tra-

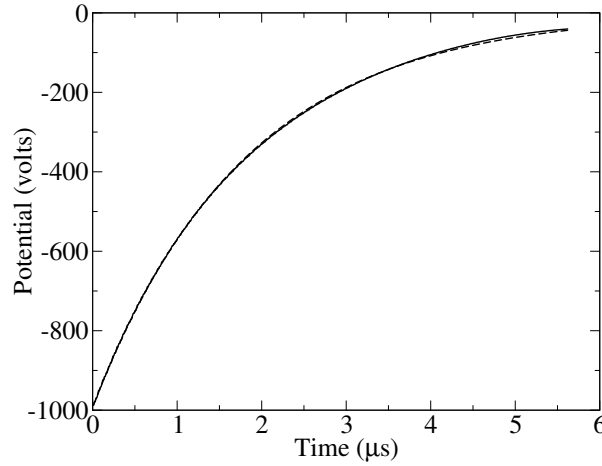


Figure 6.3: Calculated values of the optimal $V_3 = -V_4$ value for $n = 22$ and $V_1 = -V_2 = 150$ V (solid line) and a single exponential fit to these values (dashed line). The decay constant has a value of $1.80 \mu\text{s}$ and the peak voltage a value of -993 V. The time $t = 0$ corresponds to the photoexcitation pulse, and the photoexcitation took place 0.25 mm away from the edge of the front plates in the direction of the homogeneous part of the field distribution.

jectory. For example, the dashed line in the left panel of figure 6.2 represents the field distribution along the z axis $2 \mu\text{s}$ after photoexcitation using a time constant of $1.9 \mu\text{s}$. The RC circuit used to generate the exponential decay could not be operated at voltages higher than 2750 V.

In the left panel of figure 6.2, the vertical lines mark the edges of the spatial region where the particles experience an electric field between 0 V/cm and the Inglis-Teller field. This region moved along the z -axis as the voltages decayed and, for a suitable time constant, closely followed the motion of the Rydberg particles. This time constant can be estimated, by calculating at every time step and for given initial values of the front plate voltages (e.g. ± 150 V for $n = 22$), the values of the back plate voltages such that the particles in the front part of the excited beam, where the field is highest, experience a field equal to the Inglis-Teller field. The result of such a calculation for the $n = 22$, $k = 20$ Stark state is displayed as a solid line in figure 6.3. The peak voltage and the time constant of a single exponential decay curve were then fitted to the calculated points, yielding the dashed curve in figure 6.3. A set of similar calculations for different Stark states demonstrated that the overall optimal voltage decay closely corresponds to a single exponential with a time constant of about $2 \mu\text{s}$, whereby the exact value depends on n and k and whether a small DC offset voltage is included or not.

To assess the changes in velocity in the direction perpendicular to the VUV beam, the y dependence of the electric field strength in the xy plane must be considered. In the direction parallel to the VUV laser beam (the x axis in figure 6.1a), the electric field was homogeneous because the electrodes were much longer (2 cm) in this direction than the spread of the atomic cloud (~ 1.1 mm). The particles therefore neither

decelerated nor accelerated in this direction and the corresponding velocity and spatial distributions of the Rydberg atoms were independent of the n and k quantum numbers of the excited state. The distributions along the y axis are drawn in the right panel of figure 6.2 for the longitudinal positions $z = -0.4$ mm (solid line) and $z = 0$ (dashed line). The photoexcitation region was located between these two points. From the distribution of equi-field lines in figure 6.1b and the field distribution in the xy planes depicted in the right panel of figure 6.2, one can see that the electrode setup acts as a concave cylindrical lens for high-field seeking states ($k < 0$) which are accelerated along the z axis and as a convex lens for the low-field seeking states that are decelerated. This behaviour will be discussed in more detail in section 6.4.

The electrode setup could be translated along the z axis so that photoexcitation could be carried out at any point on the gas expansion axis. After photoexcitation, the Rydberg particles flew out of the deceleration/acceleration stage and entered a field-free region at the end of which they impinged on a MCP detector where an ionization signal was detected at a time corresponding to their time of flight. For selected n values, the time-of-flight measurements were complemented by imaging measurements using the imaging detector as described in section 3.3, to assess the changes in velocities in the transverse directions.

6.3 Deceleration results

Figure 6.4 displays Stark spectra of the Rydberg states of argon between $n^* = 21.2$ and $n^* = 22.1$ recorded in inhomogeneous electric fields, with the centre of the field distribution at about 380 V/cm (lower trace) and 450 V/cm (upper trace) as determined from the spacings between adjacent Stark states. The spectra are characterized by very sharp lines near the centre of the Stark manifold of states and a progressive broadening of the lines as one moves to the edges of the Stark manifold. As discussed in chapter 4, this behaviour is a consequence of the field inhomogeneities which lead to a pronounced inhomogeneous broadening of the outer Stark states. The sharp spectral structures on the low wave number side of the figure correspond to transitions to Rydberg states of dominant p character which are not fully integrated in the linear Stark manifold and only undergo a quadratic Stark effect. Particularly sharp lines arise at the positions of avoided crossings between these states and the extreme blue-shifted members of the $n = 21$ Stark manifold where the field dependence of the Stark energies is strongly reduced.

Day-to-day alignment of the VUV laser beam caused small changes in the exact position of the photoexcitation point. Consequently, Stark spectra such as those shown in figure 6.4 had to be recorded prior to each set of measurements to determine the excitation position. Given the large inhomogeneous broadening, the fine structure of the outer Stark states that is well resolvable in experiments carried out in homogeneous fields (see figure 4.2 in chapter 4) cannot be observed. Photoexcitation to the

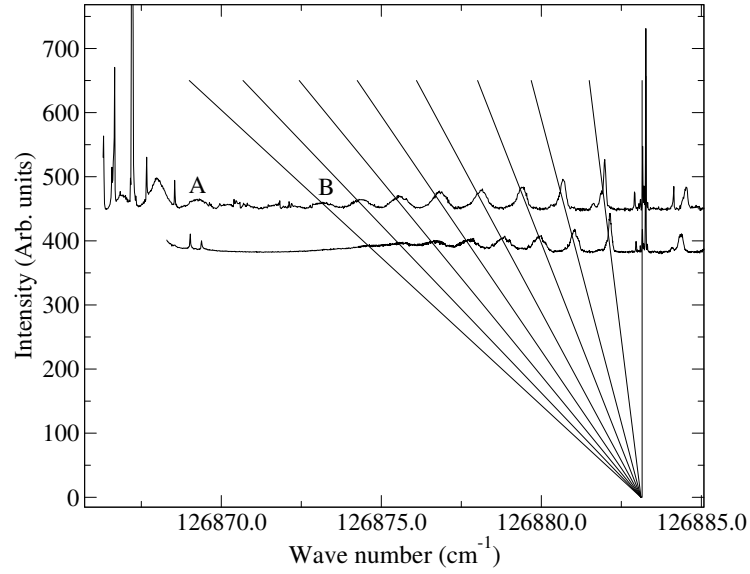


Figure 6.4: Stark spectra of the $n = 22$, $M_J = 1$ argon Rydberg states. The origin of the intensity scale of each spectrum has been shifted along the vertical axis so that it corresponds to the electric field strength in V/cm, i.e. 380 V/cm and 450 V/cm. The straight lines correspond to the position of the Stark states ranging from $k = -16$ to $k = 0$ from left to right. The states that were excited in the deceleration experiments are labelled A and B.

positions of the outer Stark states of the manifold thus leads to the preparation of several m_ℓ components simultaneously. These components display an almost identical field dependence and, unless some components are subject to avoided crossings with low- ℓ states, display an identical deceleration behaviour. As a consequence of the adiabatic traversals of the avoided crossings, the fine-structure components of the extreme Stark states that undergo avoided crossings with low- ℓ states display a different deceleration behaviour which can be identified from an analysis of the TOF distributions (see below).

Deceleration experiments were performed by exciting selected Stark states using various sets of time-independent and dependent voltages. The largest accelerations and decelerations were obtained for the outer members of the Stark manifolds, as expected from equation 2.16. At $n = 22$, the excitation positions correspond to the spectral features labelled A and B in figure 6.4. Figure 6.5 summarizes the results obtained at $n^* \approx 21.5$ (panel (a)), $n^* \approx 18.5$ (panel (b)), and $n^* \approx 15.5$ (panel (c)) and compares the observed and simulated time-of-flight distributions of the neutral Rydberg states to the MCP detector. In each panel the solid and dashed lines correspond to experiments carried out following excitation to one of the outer red- and blue-shifted Stark states of each manifold, respectively, and the dotted line to a reference experiment for Rydberg atoms in $k = 0$ Stark states which are neither accelerated nor decelerated. The TOF spectra showing the smaller shifts from the reference TOF spectra correspond to experiments carried out using the voltage configuration of panel (a)

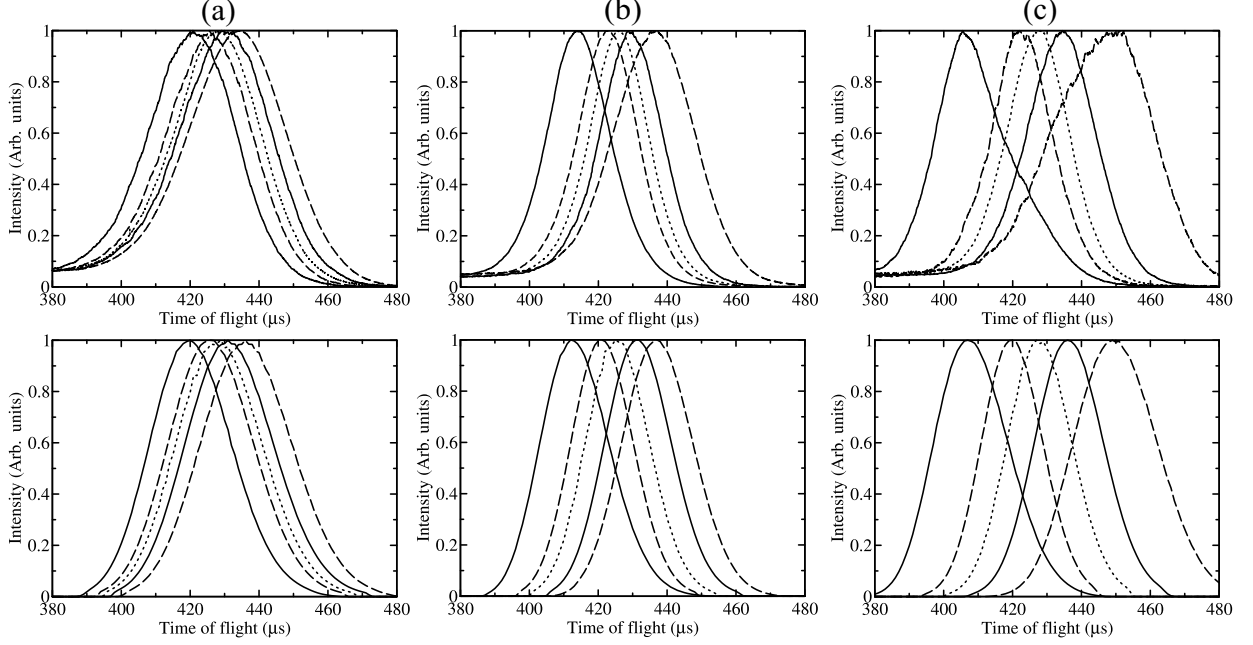


Figure 6.5: Deceleration results for states with $n^* \approx 21.5$ (panel (a)), $n^* \approx 18.5$ (panel (b)) and $n^* \approx 15.5$ (panel (c)). In all three panels, the solid lines are the TOF traces of the red-shifted states (designated by n_B^* in table 6.1) and the dashed lines the TOF traces of the blue-shifted states (designated by n_A^* in table 6.1). The dotted lines represent the TOF traces of atoms excited to $k = 0$ states which do not decelerate nor accelerate. In each panel the simulation results are presented below the experimental results.

of figure 6.1, and those showing the larger shifts to experiments carried out using the voltage configuration of panel (b) of figure 6.1 with time-dependent fields. From these results, one can immediately see that the TOF shifts can be increased by a factor of ~ 3 using time-dependent fields and that the shifts decrease with increasing n values, primarily reflecting the decrease of Stark energy at the corresponding Inglis-Teller field. The two sets of measurements are now described in more detail.

6.3.1 Experiments using time-independent fields

Table 6.1 summarizes the results of deceleration/acceleration experiments carried out on outer members of the Stark manifold which correspond, at $n^* = 22.5$, to the states labelled A and B in figure 6.4. Photoexcitation was carried out in a field lower than the Inglis-Teller field to avoid complications arising from multiple avoided crossings as explained in chapter 4, see also reference [131]. Consequently, the effective quantum numbers n_A^* and n_B^* of the Stark states slightly deviate from half-integer values, being smaller for the blue-shifted Stark states and larger for the red-shifted Stark states. The values of the voltages applied to the front plates are listed in the third column; the back plates were kept at zero volt. In all experiments, the absolute value of V_2 was chosen to be smaller than that of V_1 to compensate for a slight displacement of the photoexcitation point from the central plane between the front

Table 6.1: Summary of deceleration/acceleration experiments in time-independent electric fields. n_A^* and n_B^* represent the effective principal quantum numbers of the outer blue-shifted and outer red-shifted Stark states used in the experiment. Δt and ΔE_{kin} are the differences in the time of flight and the kinetic energy, respectively, and E_{Stark} designates the kinetic energy changes expected solely on account of the Stark energy of the Rydberg states. The back plates were kept at zero volt in these experiments.

n_A^*	n_B^*	$V_1(\text{V})/V_2(\text{V})$	Δt (μs)	ΔE_{kin} ($hc \text{ cm}^{-1}$)	E_{Stark} ($hc \text{ cm}^{-1}$)	$\frac{\Delta E_{\text{kin}}}{E_{\text{Stark}}}$
21.36	21.61	150/-140	4.7	12.5	16.6	0.75 ± 0.06
18.32	18.62	343/-267	6.5	17.5	24.3	0.72 ± 0.04
15.32	15.56	950/-800	12.0	32	44.6	0.71 ± 0.02

plates. In this voltage configuration, the Rydberg atoms fly out of a high-field region, and the red-shifted states that are high-field seeking are decelerated and have a longer TOF to the detector than the blue-shifted Stark states, as can be seen in figure 6.5. The TOF difference Δt between the outer red- and blue-shifted states corresponds to the difference between the maximal points of the respective TOF distributions and decreases from 12 μs at $n^* \approx 15.5$ to 4.7 μs at $n^* \approx 21.5$. These TOF differences can be converted into kinetic energy differences $\Delta E_{\text{kin}}/hc$ ranging from 32 cm^{-1} at $n^* \approx 15.5$ to 12.5 cm^{-1} at $n^* \approx 21.5$, representing approximately 70% to 75% of the available Stark energy. Similar experiments carried out at different electric fields and with different path lengths showed a variation of the ratio $\eta = \frac{\Delta E_{\text{kin}}}{E_{\text{Stark}}}$ in the ranges 60% to 75% at $n^* \approx 15.5$ and 75% to 95% at $n^* \approx 21.5$. Overall, the ratio increases with increasing n value and this increase supports the conclusion drawn in subsection 4.3.4 that the deviation from 100% primarily lies in the limited lifetimes of the Stark states and a partial decay during the $\sim 5 \mu\text{s}$ time needed to traverse the deceleration stage. The ratio is also affected, to a lesser extent, by avoided crossings with low- ℓ states. In the measurements carried out with the deceleration stage described in chapter 4, the field inhomogeneities were smaller and the deceleration path longer than in the present experiment, and the largest ratio amounted to 54% at $n^* \approx 24.5$ and dropped at lower principal quantum numbers, see section 4.3.3. These observations clearly illustrate the necessity of minimizing the deceleration path length and maximizing the field gradients.

6.3.2 Experiments using time-dependent fields

The second voltage configuration (see panel (b) of figure 6.1) enables the optimization of the field gradient along the deceleration path as discussed in section 2.6. In this configuration, the atoms move from low to high electric fields and therefore the high-field seeking states are accelerated and the low-field seeking states decelerated,

Table 6.2: Summary of deceleration/acceleration experiments in time-dependent electric fields using a decay constant of $2.1 \mu\text{s}$. n_A^* , n_B^* , Δt , ΔE_{kin} and E_{Stark} have the same meanings as in table 6.1.

n_A^*	n_B^*	$V_3(\text{V})/V_4(\text{V})$	$\Delta t (\mu\text{s})$	$\Delta E_{\text{kin}}/(hc \text{ cm}^{-1})$	$E_{\text{Stark}}/(hc \text{ cm}^{-1})$	$\frac{\Delta E_{\text{kin}}}{E_{\text{Stark}}}$
21.29	21.61	-550/550	13.5	36	14.9	2.4 ± 0.1
18.32	18.62	-605/1320	23	64	24.3	2.7 ± 0.1
15.32	15.56	-1925/1925	45	118	44.6	2.7 ± 0.1

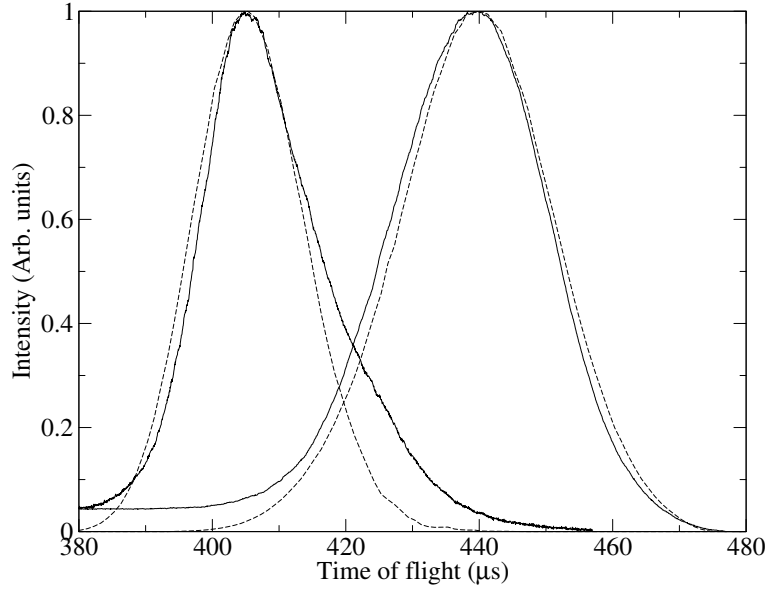


Figure 6.6: Time-of-flight spectra corresponding to experiments carried out using optimized time-dependent fields on an outer red- and an outer blue-shifted Stark state of argon around $n^* = 18.5$ (solid lines). The dashed lines represent the results of numerical simulations.

a behaviour opposite to that observed in the experiments with constant electric fields (see figure 6.5). Table 6.2 summarizes the results obtained with this configuration and a time constant of $2.1 \mu\text{s}$ for the exponential decay. The kinetic energy difference between the outer Stark states is about 2.5 times larger than the available Stark energy, i.e. $\eta = \frac{\Delta E_{\text{kin}}}{E_{\text{Stark}}} \approx 2.5$, and amounts to $\sim 120 \text{ cm}^{-1}$ at $n^* \approx 15.5$. This value is approximately eight times larger than reached in the experiments described in chapter 4.

An even larger kinetic energy difference was reached by reducing the time constant of the exponential decay of the back plate voltages to $1.9 \mu\text{s}$ and separately optimizing the potentials of the third and fourth electrodes. The optimal deceleration/acceleration conditions for several n values are listed in table 6.3. In the range $n^* = 15$ to 17 the kinetic energy differences are larger than 100 cm^{-1} and the TOF differences amount to $\sim 40 \mu\text{s}$, i.e. approximately 10% of the total time of flight. The largest deceleration was achieved for the most blue-shifted Stark state of the $n = 15$

Table 6.3: Characterization of the optimal deceleration/acceleration behaviour at selected n^* values.

n^*	Δt (μs)	$\Delta E_{\text{kin}}/(hc \text{ cm}^{-1})$	$E_{\text{Stark}}/(hc \text{ cm}^{-1})$	$\frac{\Delta E_{\text{kin}}}{E_{\text{Stark}}}$
21.5	17	50	18.0	2.8 ± 0.1
18.5	35	97	26.7	3.6 ± 0.1
17.5	38.5	108	33.4	3.2 ± 0.1
15.5	43	122	43.1	2.8 ± 0.1

Stark manifold for which a kinetic energy $\Delta E_{\text{kin}}/hc = 60 \text{ cm}^{-1}$ was taken away in a single deceleration stage. According to the simulations, an even larger value of 90 cm^{-1} could have been reached for a time constant of $1.75 \mu\text{s}$ and a peak voltage of 4.5 kV that unfortunately is too high for the RC circuit we used to generate the exponentially decaying voltage functions. A comparison of the experimental (solid line) and simulated (dashed line) TOF spectra corresponding to the measurements at $n^* \approx 18.5$ is presented in figure 6.6. Given that no adjustable parameters were used in the simulations the agreement is good. A similar level of agreement was reached for all other measurements using time-dependent fields, the largest deviation amounting to 15% of the difference in the TOF of the outer Stark states at $n^* \approx 17.5$. The simulations even reproduced the increased width and the asymmetry of the TOF distribution, both of which have their origin in the distribution of positions and velocities of the photoexcited particles, as a result of which they experience slightly different forces and follow slightly different trajectories. Our estimate of the absolute accuracy of the trajectory simulations based on the experimental uncertainties in the location of the exact photoexcitation point, in the size of the laser spot and in the lifetimes of the Stark states suggests that an agreement better than 20% in the TOF differences is fortuitous.

The large time-of-flight differences offer the possibility of carrying out efficient spectral searches for the Stark states most suitable for acceleration/deceleration experiments. Indeed, at the maximum of the TOF distribution of the low-field seeking Stark state ($\sim 440 \mu\text{s}$, see figure 6.6), the TOF distribution of the high-field seeking state has almost returned to zero. By setting suitable time gates on the digital oscilloscope and recording the integrated signal as a function of the VUV wave number, one can therefore record spectra of accelerating and decelerating Rydberg states separately in a manner similar to that used in the experiments on hydrogen, see section 5.4.3. As an illustration, figure 6.7 compares Stark spectra obtained in the region $n^* = 18$ to 19 by collecting the integrated TOF signal over three detection windows centred at $415 \mu\text{s}$ (top trace), $425 \mu\text{s}$ (middle trace) and $440 \mu\text{s}$ (bottom trace). In general, the low-field seeking blue-shifted Stark states do not contribute to the spectra recorded by collecting the signal in the early window and the high-field seeking red-

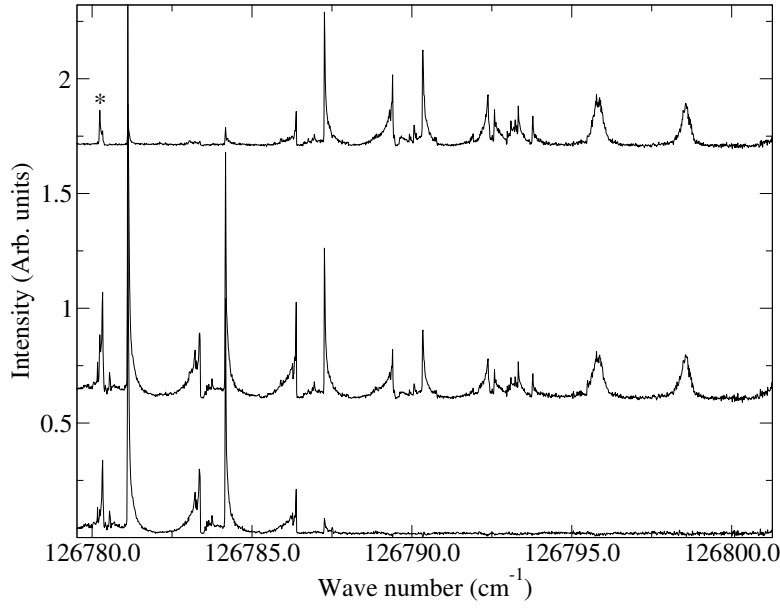


Figure 6.7: Stark spectra of argon in the range $n^* = 18$ to 19 recorded with $V_1 = -V_2 = 450$ V, $V_3 = -2300$ V and $V_4 = 1800$ V. The top, middle, and bottom traces correspond to spectra recorded by integrating the intensity over time-of-flight regions centred around $t = 410$ μ s, 425 μ s, and 440 μ s, respectively.

shifted Stark states do not contribute to the spectra corresponding to the late window. However, avoided crossings of selected fine-structure components with the penetrating low- ℓ states or with other Stark states can affect the deceleration behaviour and even cause an overall acceleration of atoms initially prepared in a blue-shifted state. An example of such a situation is the Stark state marked by an asterisk in figure 6.7. The different deceleration behaviour thus enables the disentanglement of unresolved spectral structures associated with different fine-structure components. Figure 6.7 illustrates a form of two-dimensional spectroscopy which provides more information than that contained in a conventional Stark spectrum.

6.4 Imaging results

To measure the three-dimensional Rydberg atom distribution in the supersonic beam the MCP setup as described in section 3.3 was used with which we can record CCD-camera images and perform time-of-flight measurements simultaneously. The distance from the laser-excitation point to the surface of the detector was smaller in this configuration (250 mm for the measurements carried out without the CCD camera vs. 205 mm here). Consequently, all the times of flight are shorter than those discussed in the previous section.

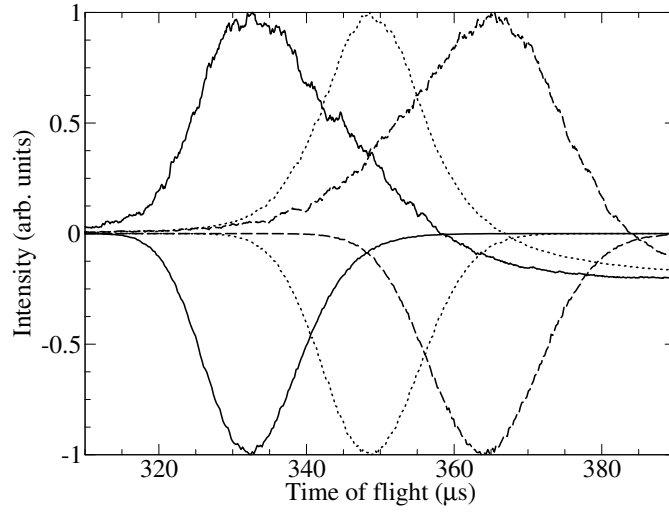


Figure 6.8: TOF spectra of atoms in $n = 18$, $k = 0$ (dotted line), $n = 18$, $k = -12$ (solid line) and $n = 17$, $k = 11$ (dashed line) corresponding to measurements carried out using time-dependent fields. The experimental spectra point upward, the simulated spectra point downward.

6.4.1 Experimental results

Figure 6.8 shows the TOF spectra measured for the $n = 18$, $k = 0$, $n = 18$, $k = -12$ and $n = 17$, $k = 11$ states of argon as dotted, solid and dashed lines, respectively. The kinetic energy differences of the $k = -12$ and $k = 11$ atoms relative to the $k = 0$ atoms are 55 cm^{-1} and -51 cm^{-1} , respectively, and are identical to the kinetic energy differences obtained in the previous section for the same states within the experimental uncertainty.

The corresponding images of the Rydberg atom beam on the MCP-detector are displayed in the upper half of figure 6.9, and the intensity distributions along the $x = 0$ and $y = 0$ lines are shown in figure 6.10, where the $y = 0$ line corresponds to the dimension parallel, and the $x = 0$ line to the dimension perpendicular to the VUV beam. All three images in the upper half of figure 6.9 have the same intensity distribution along the x axis (see also figure 6.10b). This observation is in agreement with the fact that no forces act on the particles in this dimension because of the homogeneous nature of the electric field distribution.

The image obtained for the particles in the $k = 0$ state (panel (a) in figure 6.9) directly reflects the experimental geometry because these particles are not subject to any forces. This measurement enables the characterization of the spatial and velocity distributions of the beam in the absence of any field effects. The image has an elliptical shape with the long axis along the x dimension (full width at half maximum FWHM = 4.6 mm) and the short axis along the y dimension (FWHM = 2.1 mm). Assuming that the effective nozzle opening is equal to the actual nozzle opening and that the skimmer rejects all particles that have too large a transverse velocity, but has no effect on the velocity distribution of the particles that pass through it, the

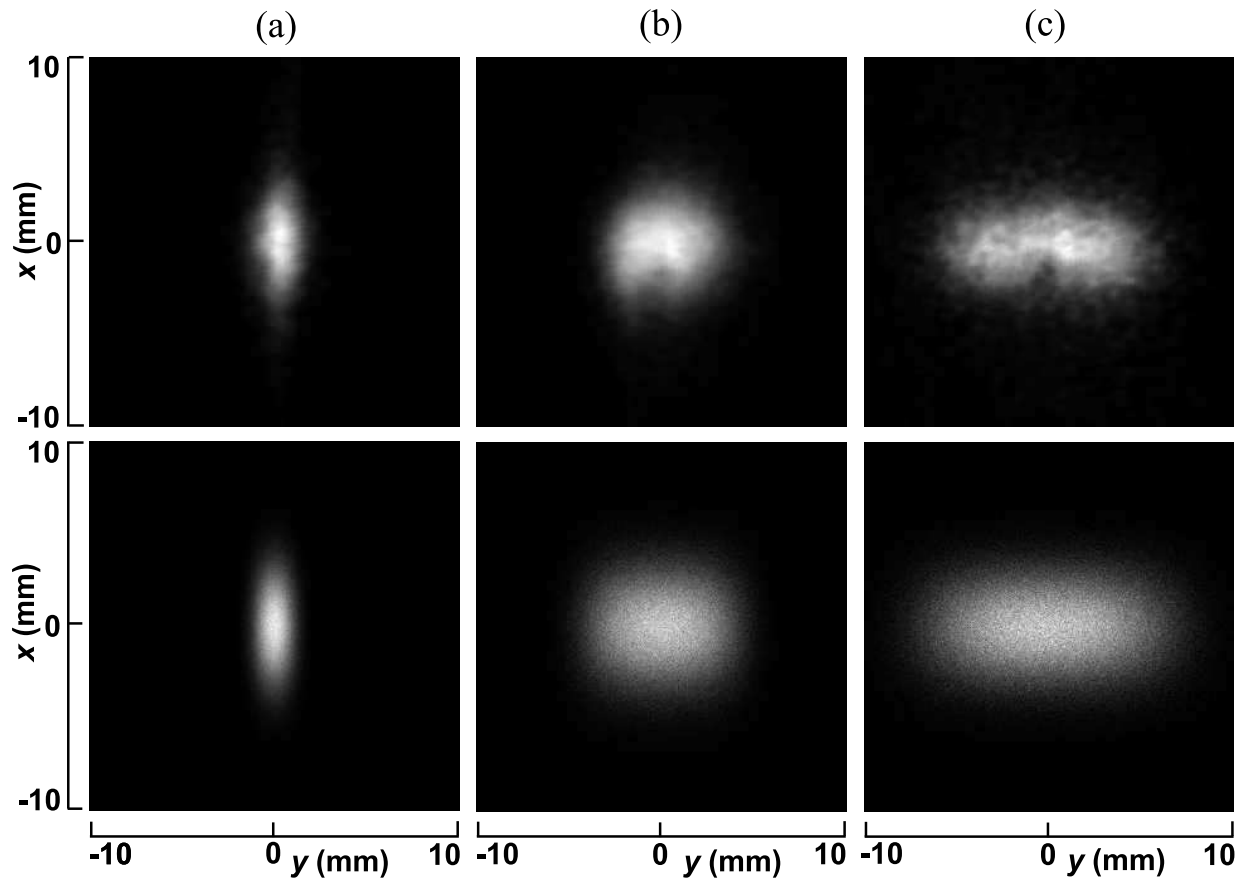


Figure 6.9: CCD-camera images of the three excited Stark states. Left: $n = 18, k = 0$, middle $n = 17, k = 11$, right $n = 18, k = -12$. The simulations are shown below the CCD camera images.

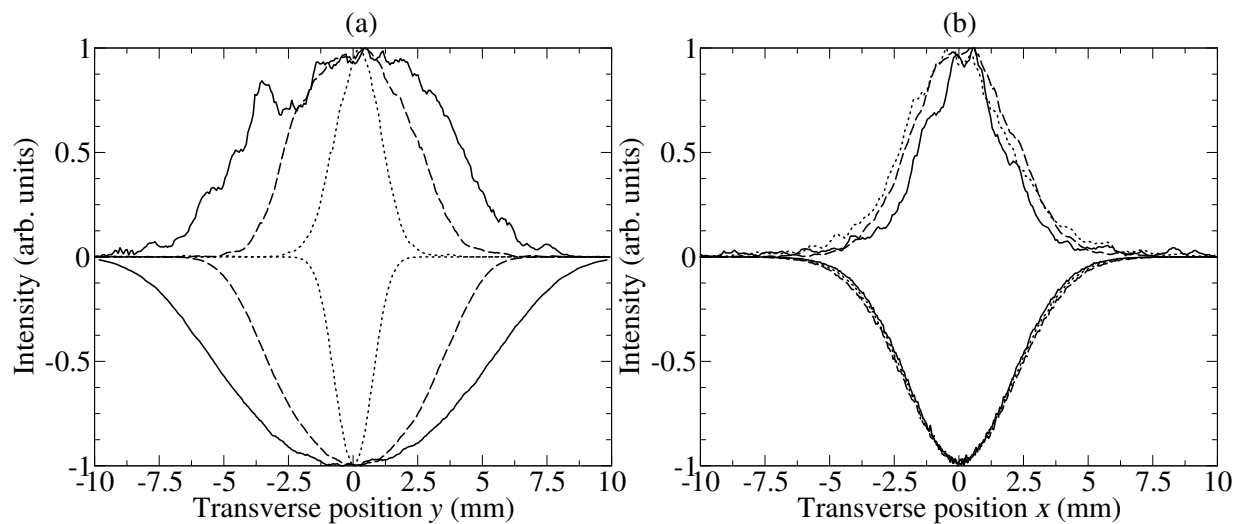


Figure 6.10: Line profiles taken from the CCD-camera images (pointing upward) and taken from the simulations (pointing downward) for $n = 18, k = 0$ (dotted line), $n = 18, k = -12$ (solid line) and $n = 17, k = 11$ (dashed line). (a) Line profiles in the direction perpendicular to the VUV beam (y direction). (b) Line profiles in the direction parallel to the VUV beam (x direction).

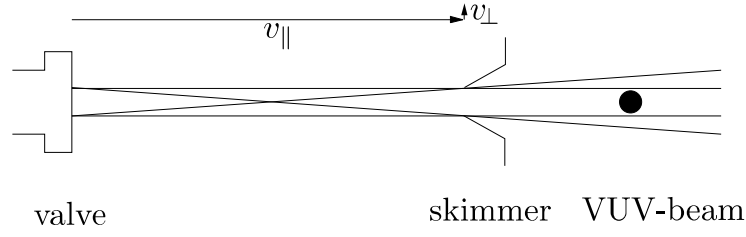


Figure 6.11: Valve and skimmer geometry to estimate the maximum transverse velocity in the absence of beam-skimmer interactions. Shown are the trajectories that have maximum transverse velocity and the outer trajectories for which the transverse velocity is zero.

image can be constructed geometrically from the known nozzle and skimmer orifice diameters (0.5 mm) and the known nozzle-skimmer and skimmer-detector distances (see table 6.4 and figure 6.11). Under these conditions, a circular image of radius 1.7 mm with a flat intensity distribution is expected. The actual image, however, is significantly broader in the x dimension. Because the VUV beam crosses the supersonic beam along the x axis, it probes the complete spatial and velocity distribution along this axis. From the unexpectedly large width of the distribution along the x axis, one can therefore conclude that, either the effective nozzle opening is much larger than the actual nozzle opening, or that the skimmer perturbs the particles during their flight through the orifice and broadens the velocity distribution as already observed in previous studies [47]. The broadening of the velocity distribution by the skimmer was observed independently in the same apparatus as a Doppler broadening in a high-resolution spectroscopic measurement of the hyperfine structure of the $(5p)^6\ ^1S_0 \rightarrow (5p)^5 7d[3/2](J = 1)$ transition of xenon [91]. As will be discussed in section 6.4.2, this broadening can be quantitatively reproduced if one assumes that a rethermalization of the beam in the transverse dimensions to a temperature $T_t = 100$ mK takes place at the skimmer. Under these conditions, the waist of the supersonic beam at the point of intersection with the VUV laser beam is predicted to be ~ 1.1 mm (FWHM). The reduced size of the image in the y dimension compared to that in the x dimension is a consequence of the fact that the size of the VUV laser beam (0.3 mm) is smaller than that of the molecular beam and selects the low transverse velocity components in that dimension, leading to a distribution approximately described by a temperature of 15 mK.

The images in figures 6.9(b) and (c) for the low-field seeking $k = 11$ and the high-field seeking $k = -12$ Rydberg levels can be qualitatively understood by considering the electric field distribution in the deceleration stage. Both images show a broader distribution along the y axis than that corresponding to the $k = 0$ Stark state (panel (a)). In the case of the $k = -12$ state, the inhomogeneity of the electric field in the y direction leads to an acceleration *away* from the z axis over the whole deceleration stage and thus to the widest image on the detector. In contrast, the particles excited

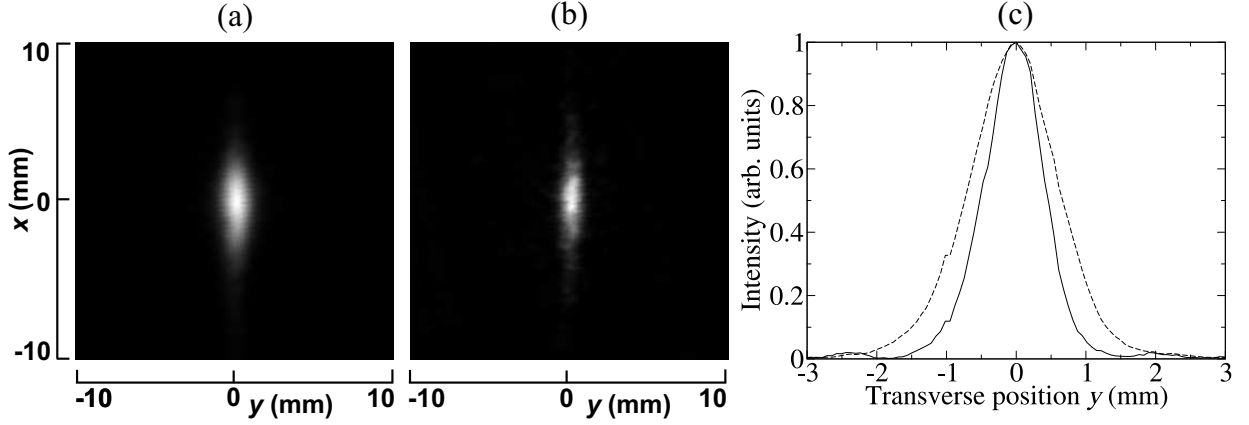


Figure 6.12: CCD-camera images of the Rydberg atom cloud in $n = 16, k = 0$ state (panel (a)) and in the $n = 15, k = 9$ state (panel (b)) obtained by operating the deceleration stage with time-independent voltages $V_1 = -V_2 = 880$ V and $V_3 = V_4 = 0$ V. The dashed (full) line in panel (c) represents the measured intensity distribution along the y dimension at $x = 0$ for the $k = 0$ ($k = 9$) state.

to the $k = 11$ state are first accelerated *toward* the z axis so that the Rydberg atom beam, which initially diverges away from the z axis, is refocussed. After crossing the z axis, the beam diverges again on its way to the detector. The path to the detector after the crossing is long enough so that the image size along the y axis is larger than for the $k = 0$ particles. The image size along the y axis thus indirectly demonstrates the possibility of focussing a Rydberg atom beam with inhomogeneous fields.

A similar behaviour was observed in measurements made with Rydberg Stark states with $n = 15$ to 16, 18 to 19 and 21 to 22. The effects, however, become less pronounced at increasing n , primarily as a result of the reduced maximal field strength imposed by the necessity of carrying out the experiments below the Inglis-Teller field.

The focussing of the Rydberg atom beam could be demonstrated directly in experiments with time-independent fields. In this case, the forces acting on the particles are reduced and the focal point can be brought close enough to the detector so that the size of the image in the y dimension is reduced. This behaviour is demonstrated in figure 6.12 which compares CCD-camera images recorded for atoms in $n = 16, k = 0$ (panel (a)) and $n = 15, k = 9$ (panel (b)) states, respectively, using $V_1 = -V_2 = 880$ V and $V_3 = V_4 = 0$. In this voltage configuration, the atoms in $k > 0$ states are accelerated toward the z axis. Because the focal point for the beam of $k = 9$ atoms now lies close to the detector, the width of the particle distribution in the y dimension is narrower (FWHM = 0.9 mm) than in the case of the $k = 0$ atoms (FWHM = 1.4 mm). Figure 6.12 thus represents a direct demonstration of the operational principle of a Rydberg atom convex cylindrical lense.

Table 6.4: Parameters used in the particle trajectory simulations.

parameter	value	source
longitudinal velocity	590 m/s	TOF spectrum
longitudinal temperature	0.6 K	TOF spectrum
valve orifice diameter	0.5 mm	specified by supplier
skimmer orifice diameter	0.5 mm	specified by supplier
valve-skimmer distance	12 cm	directly measurable
skimmer-laser beam distance	7 cm	directly measurable
laser beam-detector distance	20.5 cm	directly measurable
VUV-laser beam width	0.3 mm	inferred from the beam widths of the input lasers

6.4.2 Simulations

The parameters listed in table 6.4 and the potentials applied to the four electrodes of the deceleration stage determine the experimental setup completely and form the input of the particle trajectory calculations presented above for comparison with the experimental results. The width of the VUV-laser beam was estimated by measuring the widths of the input beams to the four-wave-mixing process. This measurement gives only a rough estimate of the beam width but optimizing this parameter in the simulations gave the same result, i.e. 0.3 mm, for the beam width. Because of the elongated shape of the image of the $k = 0$ particles discussed in the previous subsection, an additional parameter describing the transverse velocity distribution of the particles leaving the skimmer had to be introduced and optimized to obtain a satisfactory agreement with the experimental results. An optimal value of 100 mK was found and led to the simulated images shown in the lower half of figure 6.9 and the calculated TOF and spatial distributions displayed as inverted traces in figure 6.8 and figure 6.10. Each simulated image was constructed from 1 000 000 trajectories sampling the whole space of initial velocities and positions, taking into account the Maxwell-Boltzmann velocity distributions and assuming a Gaussian profile with a width of 0.3 mm for the laser beam. The good agreement between the experimental and the simulated images obtained using a single adjustable parameter for which no second, independent measurement was available, clearly indicates that the deceleration stage is well characterized.

The simulations can be used to highlight features not directly accessible from the raw experimental data. Firstly, the simulations of the trajectories of the high-field seeking Rydberg particles show that these particles are brought back to the xz plane in a narrow range of positions approximately 1 cm after leaving the deceleration stage. The analysis of the trajectories together with the results displayed in figure 6.12 make us confident that the electrode setup can be easily modified to achieve a perfect focus of the Rydberg particles. Secondly, the simulations enable the deter-

mination of the velocity distributions in all three dimensions and of the changes in these distributions occurring during the deceleration/acceleration process. Effective translational temperatures can then be estimated by fitting Maxwell-Boltzmann distributions to these velocity distributions. The initial effective temperature along the x axis amounts to 100 mK and remains unaffected during the acceleration/deceleration. The initial effective temperature along the y axis is only ~ 15 mK immediately after the Rydberg states have been generated by the VUV laser pulse. This temperature does not change for the $k = 0$ states but increases to 300 mK and 700 mK for the $k = 11$ and $k = -12$ Stark states, respectively.

Because of the refocussing effect of the deceleration stage, the translational temperature along the y dimension will always be smaller for the decelerated particles than for the accelerated particles. Adjustments of the electrode separation and voltages can lead to a significant reduction of this temperature, however, at the cost of the effectiveness of the overall deceleration, as illustrated by the time-independent deceleration measurements displayed in figure 6.12.

6.5 Conclusions

The results presented in this chapter enabled us to characterize the Rydberg Stark decelerator fully. From the measurements, aided by particle trajectory simulations, the size of the VUV beam and the initial size of, and velocity distribution in the supersonic atomic beam after passing through the skimmer, could be determined. The combination of TOF and imaging measurements with numerical simulations enabled us to determine the full three-dimensional velocity distribution of the Rydberg particles after deceleration/acceleration.

The kinetic energy could be decreased or increased by more than three times the Stark shift of the excited Stark state using time-dependent fields, reaching $\Delta E_{\text{kin}}/hc = 60 \text{ cm}^{-1}$ around $n = 16$. The use of time-dependent electric fields as opposed to time-independent fields greatly enhances the efficiency of the deceleration/acceleration process. In experiments using time-independent fields, the kinetic energy differences were 95% of the Stark shift, as opposed to typically 50% in the setup described in chapter 4. Moreover, because the deceleration/acceleration takes place within a distance of 3.5 mm or within a time of 6 μs , constraints imposed by the limited lifetimes of Rydberg states are considerably reduced compared to the measurements carried out in the setup described in chapter 4.

From the CCD-camera images we found that although the transverse velocity distribution is broadened by acceleration perpendicular to the beam propagation axis, the increase is typically much smaller, up to 100 times smaller, than the decrease in kinetic energy in the longitudinal direction in the same experiment. The temperatures in the transverse dimensions of 100 mK (x dimension) and 300 mK (y dimension) for these particles are sufficiently low that trapping can be envisaged.

For argon atoms the maximal change in kinetic energy represents only $\sim 10\%$ of the total kinetic energy but enables the complete separation of the TOF distributions of atoms in low-field seeking states from those of the atoms in high-field seeking states. A kinetic energy of 60 cm^{-1} corresponds to that of a hydrogen molecule moving at 800 m/s , a mean velocity that can easily be achieved in a supersonic expansion of H_2 seeded in xenon or argon. The maximal mass of a particle which has a initial kinetic energy of 60 cm^{-1} when seeded in xenon, and can therefore be decelerated to zero velocity, is $m = 14 \text{ u}$.

Chapter 7

Normal-incidence Rydberg atom mirror

7.1 Introduction

The convex cylindrical lense presented in chapter 6 is one example of how the large dipole moments of Rydberg Stark states can be used to build elements that have an analogue in the optical domain such as, for instance, lenses, beam splitters, and mirrors. The first example of an atom-optics experiment using Rydberg Stark states is the krypton deflection experiment described in reference [120].

In this chapter, which is based on reference [128], the operational principle of a normal incidence mirror for particles excited to Rydberg Stark states is presented and its experimental realization is described. A cloud of hydrogen atoms, photoexcited to $n = 27$ Rydberg Stark states and initially moving at a velocity of 720 m/s, was stopped in $4.8 \mu\text{s}$ only 1.9 mm away from the excitation spot, and was then reflected back. The mirroring process was studied by ion-time-of-flight and ion-imaging techniques following pulsed-field ionization. The chapter begins with a brief review of the literature on atom and molecule mirrors.

7.2 Mirrors for atoms and molecules

Experiments which use electromagnetic radiation to reflect beams of neutral atoms and molecules can be divided into three categories:

- Experiments using resonant laser radiation
- Experiments using nonresonant laser radiation
- Experiments using static electric and/or magnetic fields

The experiments that use resonant laser radiation are based on the momentum change in many absorption and emission cycles of the photons of the resonant laser fields and can thus only be applied to atoms which have a closed two-level system.

Nonresonant laser radiation was used in references [8] and [72] to reflect atoms from an optical evanescent wave. The reflection of the atoms is based on the dipole induced by the electric field of the laser beam. The magnitude of the induced dipole, and thus the applied force, depends on the polarizability of the particle. In similar experiments Cs_2 [116] and I_2 [106] molecules were deflected near the focus of a high intensity ($\sim 10^{12} \text{ W/cm}^2$) infra-red (IR) laser beam. By overlapping the IR laser beam and the atomic beam, the laser focus can also function as a lense [45] as was shown for a beam of xenon atoms [42].

When an atom or a molecule exhibits a first-order Stark or Zeeman shift in its ground state, static electric or magnetic fields can be used to exert a force on the neutral particle [86]. The resulting forces are small, so that high electric or magnetic fields are needed to change the velocity.

In reference [109] a microstructured element was used to retro reflect a beam of ND_3 molecules which was first decelerated to 30 m/s using a Stark decelerator. Because of the small distances between the electrodes of the mirror, only small potentials ($\sim 300 \text{ V}$) were needed to induce a Stark shift which was larger than the kinetic energy of the molecules. Using the same principle but larger electrodes, an undecelerated beam of CH_3Cl molecules was deflected by an angle of $\sim 5 \text{ mrad}$ [133].

A microstructured element was also used in reference [69] to deflect a beam of metastable helium atoms using the Zeeman effect. Because the beam was unpolarized, all three M_J values were present in the beam. The magnitude of the Zeeman shift depends on the value of M_J and thus particles with different M_J are deflected by a different angle. The deflection therefore also polarizes the atomic beam, like in the famous Stern-Gerlach experiment [48].

The Zeeman shift can also be used to reflect laser-cooled atoms from the recording tracks of a magnetic tape. In reference [105], for instance, a cloud of Rb atoms with a temperature of $18 \mu\text{K}$ was bounced off a concave mirror more than 14 times.

7.3 Experimental methods and techniques

In the experiments described in this chapter, the electrode setup and the photoexcitation scheme was the same as for the experiments described in chapter 5. In the deceleration experiments on atomic hydrogen described in chapter 5, the stopping of the Rydberg hydrogen beam could not be shown directly because stopped atoms cannot reach the MCP detector. A field-ionization detection method for the experiments presented here was therefore implemented. Instead of using time-independent fields, as in chapter 5, the electric field in the electrode region was switched on and off to facilitate excitation and detection.

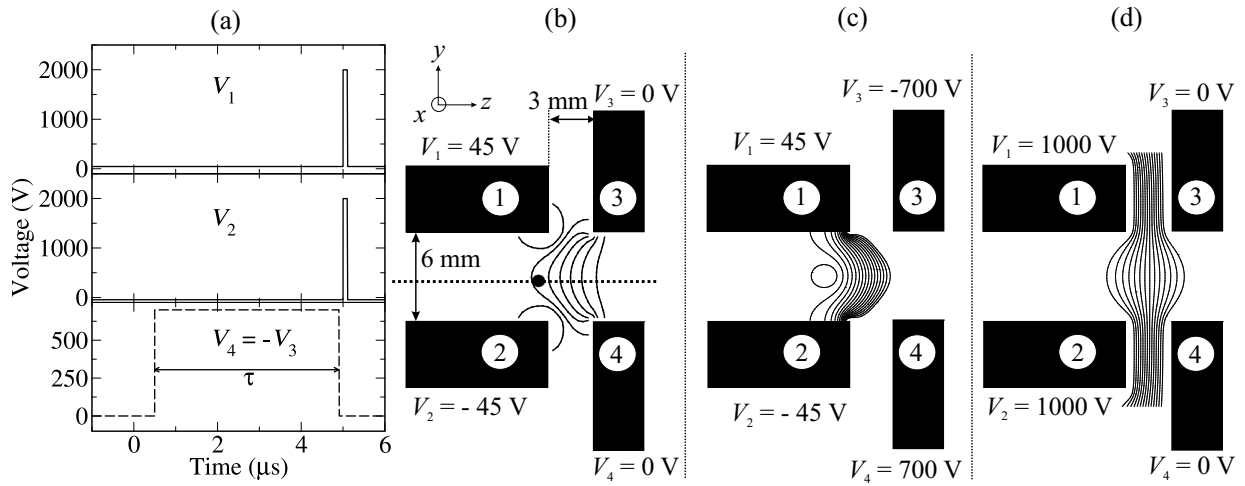


Figure 7.1: Panel (a): Voltage sequence used in the mirroring process. Panels (b), (c), and (d): Voltage configurations used to (b) prepare the H atoms in Rydberg Stark states, (c) to reflect the H atoms, and (d) to field ionize the reflected atoms. The width of the electrodes in the x dimension is 2 cm. The solid lines in panels (b) and (c) are lines of constant electric field in steps of 25 V/cm (b) and 100 V/cm (c). In panel (d) equipotential lines between 850 V and 200 V in steps of 50 V are shown. The dot in panel (b) marks the photoexcitation point.

7.3.1 Detection of Rydberg atoms by pulsed field ionization

Field ionization is a convenient way to detect Rydberg particles because the required field strengths for n values above 20 are easily generated in the laboratory, and because the resulting ions can be detected with a high efficiency.

To field ionize Rydberg particles in our setup, a large electric field pulse was applied to electrodes 1 and 2, see panel (d) in figure 7.1. The field also extracted the ions toward the MCP detector where the TOF distribution of the ions was monitored. The spatial distribution of the ions on the detector was measured with a CCD camera by taking images of the fluorescence of the phosphor screen connected to the anode of the MCP detector. Both the times of flight and the images of the ions strongly depended on the positions of the parent Rydberg atoms in the electrode setup at the time of field ionization. Ion clouds produced close to electrodes 3 and 4 were subject to a smaller acceleration and had longer times of flight than those produced close to electrodes 1 and 2. Moreover, the field distribution (figure 7.1d) was such that the former ion clouds expanded more than the latter on their way to the detector and formed larger images. The images and TOF distributions could therefore be used to reconstruct the position and shape of the Rydberg atom cloud during deceleration, mirroring, or trapping.

7.3.2 Atom mirror pulse sequence

Photoexcitation took place in the middle of the four metallic electrodes of the electrostatic mirror depicted in figure 7.1b. The figure also shows (panel (a)) the voltage pulse sequence used to reflect and field ionize the H Rydberg atoms. This sequence consisted of three phases: photoexcitation ($t = 0$, voltage configuration in panel (b)), mirroring ($500 \text{ ns} < t < t_{\text{ion}}$, panel (c)), and field ionization ($t = t_{\text{ion}}$, panel (d)).

The atoms were excited to the $n = 27$, $k = 18$, $|m| = 0$ or 2 Stark states in the field generated by applying voltages $V_1 = -V_2 = 45 \text{ V}$ to the two electrodes on the nozzle side of the mirror (1 and 2 in figure 7.1b). 500 ns after photoexcitation, a first voltage pulse $V_4 = -V_3 = 700 \text{ V}$ of adjustable duration τ and of 50 ns rise time was applied to the electrodes on the detector side of the mirror (3 and 4 in figure 7.1c). The electric field at which the Stark shift is as large as the initial kinetic energy of the H atoms, i.e. $E_{\text{kin}} = E_{\text{Stark}} = 21.8 \text{ cm}^{-1}$, amounts to 750 V/cm. Because the electric field strength difference between the excitation region and the region between electrodes 3 and 4 was more than 2000 V/cm, the H atoms could be stopped and reflected. The potentials on the third and fourth electrodes were switched back to zero after the variable delay τ , just before field ionization. A large field-ionization pulse $V_1 = V_2 = 2000 \text{ V}$ was then applied to electrodes 1 and 2 to field ionize all Rydberg atoms and extract the ions. The minimal electric field required to ionize a low-field seeking $n = 27$ Stark state is $\sim 2100 \text{ V/cm}$ [44].

7.4 Results

7.4.1 Ion TOF measurements

Figure 7.2a shows the TOF distributions obtained after various delays τ between $0.6 \mu\text{s}$ and $8.6 \mu\text{s}$ during which $V_4 = -V_3 = 700 \text{ V}$ (solid lines, “mirror on” configuration) and $V_4 = -V_3 = 0 \text{ V}$ (dashed lines, “mirror off” configuration). In the latter case the particles fly through the electrodes with constant velocity and leave the field ionization region at $\sim 6 \mu\text{s}$. The ion times of flight shift to longer times with increasing τ because the voltage difference the ions experience when the field ionization pulse is applied becomes smaller. When the mirror is on ($V_4 = -V_3 = 700 \text{ V}$) the ion times of flight first increase (by up to 62 ns at $\tau = 3.6 \mu\text{s}$) because the particles move in the forward direction to lower potential. At $\tau = 4.6 \mu\text{s}$, the ion times of flight decrease again, indicating that the Rydberg particles have been reflected and are moving in the backward direction to higher potentials.

Panel (b) of figure 7.2 shows a set of simulated ion TOF spectra using the particle trajectory simulation method described in chapter 6. The simulation procedure does not involve any adjustable parameters but rely on independent measurements of the initial velocity (720 m/s), longitudinal temperature (100 mK), and size of the cloud (FWHM = 0.8 mm). The main deviations between experiment and simulation

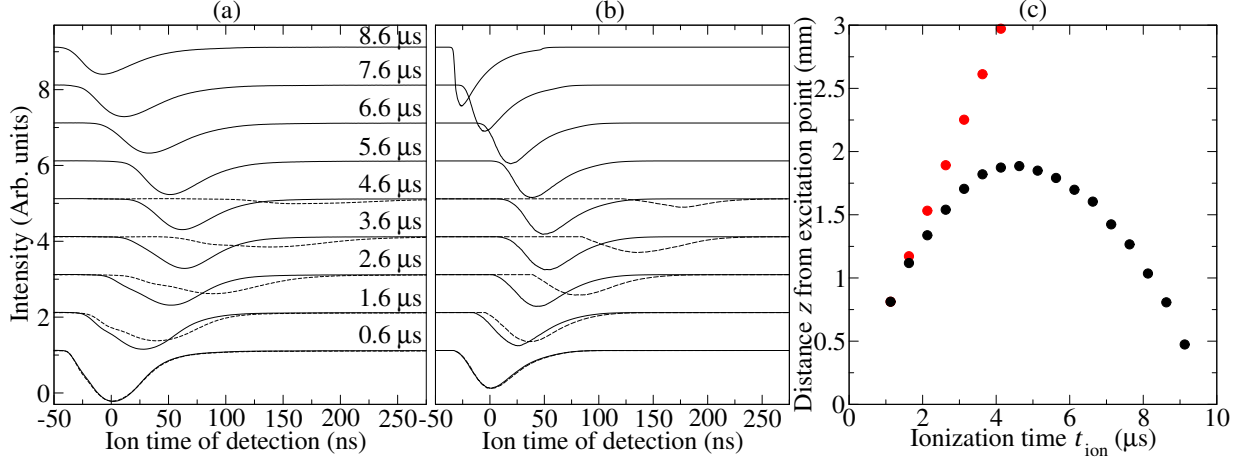


Figure 7.2: Panel (a) and panel (b): TOF distributions of the H^+ ions after deceleration periods τ of (from bottom to top) 0.6 μs , 1.6 μs , 2.6 μs , 3.6 μs , 4.6 μs , 5.6 μs , 6.6 μs , 7.6 μs , and 8.6 μs . The solid lines are measurements with $V_4 = -V_3 = 700$ V (“mirror on”) and the dashed lines are measurements with $V_4 = -V_3 = 0$ V (“mirror off”). Panel (a) shows the experimental spectra and panel (b) the simulations. The origin of the time scale is chosen to be at the maximum of the TOF distribution of the $\tau = 0.6$ μs measurement. Panel (c): Comparison between the mirror on and mirror off trajectories of the central part of the atomic cloud. The (red) upper dots show the calculated trajectory of a cloud that moves with a constant velocity of 720 m/s. The (black) lower dots show the measured trajectory of the atomic cloud in the “mirror on” experiments. The dot size is larger than the experimental uncertainty.

in figure 7.2 occur at $\tau > 6.6$ μs because in the simulations the particles return to the photoexcitation point slightly earlier than in the experiment. The otherwise good agreement indicates that the simulations capture the essential features of the mirror action.

Because the centre of the Rydberg cloud at the field ionization times in the “mirror off” experiments can be calculated from the known initial velocity, the TOF spectra can be used to determine where the particles were in the “mirror on” experiment at the time of field ionization. Figure 7.2c compares the position of the centre of the atomic cloud at $t_{\text{ion}} = \tau + 500$ ns in the “mirror off” and the “mirror on” measurements. The measurements show that the atomic cloud has come to rest in 4.8 μs only 1.9 mm away from the photoexcitation point and that it has returned to this point after ~ 9.8 μs .

In an additional measurement the mirror was switched off at the moment when the particles have come to rest, i.e. 4.8 μs after excitation, see figure 7.3. The potentials on the first two electrodes were still at $V_1 = -V_2 = 45$ V, so that the atoms were subject to a small force directed toward the MCP detector, out of the decelerator. Within the first 3 μs after switching the mirror off, the time at which the ion TOF distribution has its maximum shifts by only 2 ns. By comparing these ion TOF distributions with the ion TOF distributions of a cloud of atoms which moves at a

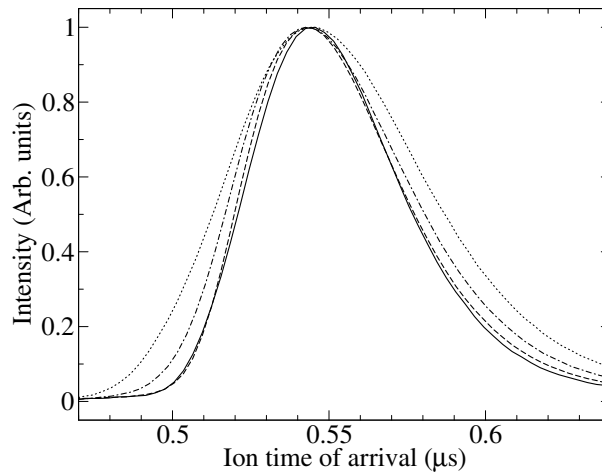


Figure 7.3: Ion TOF distributions recorded after switching the mirror off after $4.8 \mu\text{s}$ and field ionizing the particles after $t_{\text{ion}} = 5.1 \mu\text{s}$ (solid line), $t_{\text{ion}} = 6.1 \mu\text{s}$ (dashed line), $t_{\text{ion}} = 7.1 \mu\text{s}$ (dashed-dotted line), and $t_{\text{ion}} = 8.1 \mu\text{s}$ (dotted line). To overlay the TOF traces, t_{ion} was subtracted from all times of flight for each trace. The TOF traces were normalized in such a way that the maximum of the intensity scale is at one.

constant velocity, one concludes that the central part of the cloud has moved by no more than 0.03 mm during these $3 \mu\text{s}$. This corresponds to a mean velocity of less than 10 m/s . During the same period, the FWHM of the ion TOF distribution increases from 56 ns to 74 ns . From this increase one can estimate that the velocity distribution has a FWHM of 90 m/s , corresponding to a longitudinal temperature of 180 mK .

Instead of switching the mirror from on to off after $4.8 \mu\text{s}$, one can also lower the potentials on the third and fourth electrodes so that the atom cloud is trapped. A disadvantage of this trapping sequence compared to the sequence described in chapter 8 is that the temperature in the y dimension is relatively high at the moment the trap is switched on, see section 7.4.2. Because the number of trapped atoms did not appear to be higher and the trapping times were not longer than in the experiments based on the trapping sequence presented in chapter 8 we did not pursue this trapping method further.

To verify that the differences in time of flight of the ions can be correlated directly to a difference in z position at the time of ionization, it was necessary to consider the following potential sources of systematic errors:

- Errors caused by the finite velocity of the H atoms at the moment of ionization. The difference in times of flight between ions coming from H atoms moving with 720 m/s in the forward or in the backward direction is less than 0.1 ns . This time of flight difference is negligible compared to the shifts in times of flight in the measurements depicted in figure 7.2.
- Errors caused by the finite spread of the atomic cloud in the y dimension. The spread of the atomic cloud in the y dimension causes a spread in the ion TOF

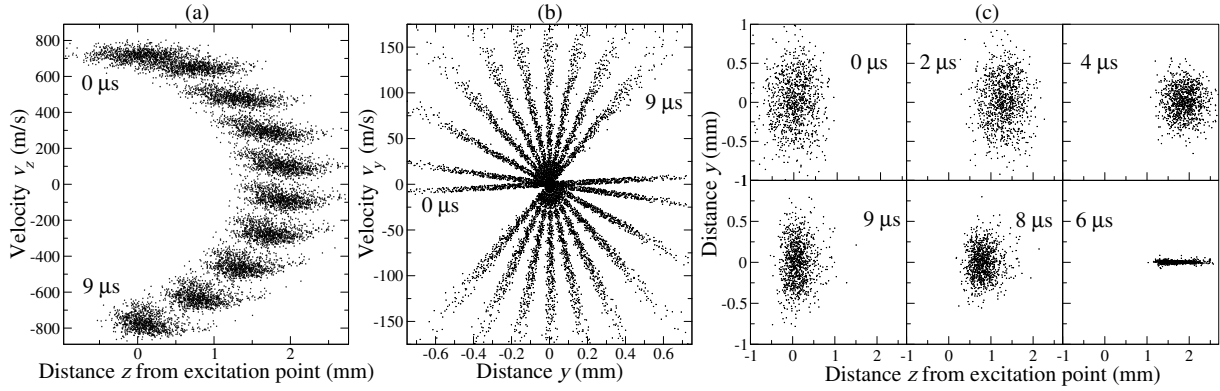


Figure 7.4: Panel (a): Simulated phase-space diagrams of the distribution of the Rydberg atom cloud in the z dimension between $t = 0$ (top left corner) and $t = 9 \mu s$ (lower left corner) in steps of $1 \mu s$. Panel (b): Simulated phase-space diagrams in the y dimension at the same times. Panel (c): Simulated distribution of the particles within the electrodes at $t = 0, 2 \mu s, 4 \mu s, 6 \mu s, 8 \mu s,$ and $9 \mu s$. In all these graphs $z = 0$ is the excitation point of the particles.

of less than 1 ns, whereas the FWHM of the TOF distributions are 50 to 70 ns.

- Errors caused by the delay between the trigger of the field ionization pulse and the actual rise of the potential on the electrodes. The delay between triggering the high-voltage switch and the actual application of the PFI pulse to the electrodes was measured with an absolute accuracy of 10 ns, to be able to make a correct correlation between the ion times of flight and the instantaneous position of the atomic cloud at ionization.

7.4.2 Calculations of phase-space distributions

To visualize the mirroring process, the phase-space distributions of the atom cloud were calculated using the particle trajectory simulation program. In panel (a) of figure 7.4, the phase-space distributions in the z dimension are drawn for t_{ion} between 0 and $9 \mu s$. The size of the atomic cloud in the z dimension remains almost constant (FWHM ≈ 0.8 mm) during the mirroring process. In the y dimension (panel (b)) the initial particle spread is also 0.8 mm, but the initial velocity is 0 with an effective temperature of only 2.3 mK, leading to a narrow, elongated distribution. The low effective temperature results from skimming the supersonic expansion and from the small VUV spot size, see chapter 6. During the mirroring process the particles are accelerated toward the central axis, leading to a narrower particle distribution but a wider velocity spread. In phase space this corresponds to a clockwise rotation of the distribution.

If the external potential in which the particles move were perfectly harmonic, the period of rotation would be the same for all particles in the atomic cloud, irrespective of their initial distance away from the z axis. The reason for the apparent harmonic-

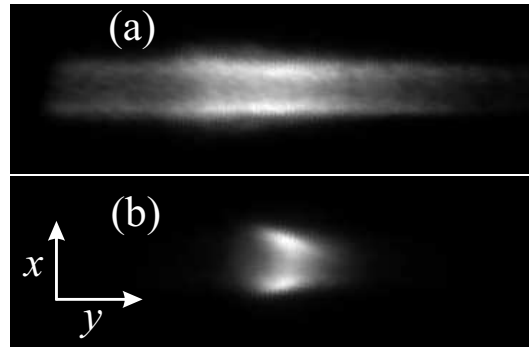


Figure 7.5: CCD-camera images of the ions after field ionizing the Rydberg particles in the mirror after (a) $\tau = 2.6 \mu\text{s}$ and (b) $\tau = 5.6 \mu\text{s}$. Each image is 25 mm long and 8 mm high. The VUV and UV laser beams propagate along the x axis.

ity in the y dimension lies in the quadratic dependence of the electric field strength on y for small displacements of the cloud from the central axis at $z \neq 0$, see dashed line in figure 6.2. Because the potential energy of the Stark states depends to first order linearly on the electric field strength, the resulting dependence of the potential energy on the displacement y is quadratic for small y . When, after $\sim 11 \mu\text{s}$, the particles come near to the point where $F(y = 0, z) = 0$, the dependence of the electric field strength on y becomes linear, see solid line in figure 6.2, and a clearly nonharmonic behaviour is expected and was also reproduced in the simulations of the phase-space distributions (not shown).

At $\sim 6 \mu\text{s}$ the beam of Rydberg atoms is focussed onto the central axis and the temperature in the y dimension has risen to 1.2 K. This focussing can also be seen in the simulated particle distributions in the yz plane displayed in figure 7.4c: After $6 \mu\text{s}$ the particle density has reached its maximum and after $9 \mu\text{s}$ the Rydberg atom cloud has approximately regained its original distribution. To exactly reach the original particle distribution, the mirroring time ($9.8 \mu\text{s}$ here) must be equal to half the period of rotation in phase space in the y dimension. In our electrode setup the full period is $24 \mu\text{s}$ and therefore, although we are close to perfect mirroring, the spatial spread in the y dimension is slightly smaller, and the velocity spread slightly wider after reflection.

7.4.3 Imaging measurements

To verify the predictions of the simulations shown in figure 7.4, CCD-camera images were recorded at different delays τ . Figure 7.5 displays the observation of the focussing in the y dimension predicted at $t_{\text{ion}} = 6 \mu\text{s}$ in panel (c) of figure 7.4. The figure compares images of the Rydberg atom cloud at $\tau = 2.6 \mu\text{s}$ ($t_{\text{ion}} = 3.1 \mu\text{s}$), i.e. before focussing (panel (a)) and at $\tau = 5.6 \mu\text{s}$ ($t_{\text{ion}} = 6.1 \mu\text{s}$), when the cloud is fo-

cussed (panel (b)). The size of the atom cloud is reduced in the y dimension by a factor of more than four at $\tau = 5.6 \mu\text{s}$, as expected from figure 7.4c. At these two times the centre of the atom cloud is located at the same point, 1.7 mm away from the photoexcitation spot. One can therefore rule out the possibility that the differences in the images are caused by the dependence of the ion beam divergence on the position of the cloud along the z axis. Both images in figure 7.5 reveal a minimum in the intensity distribution along the $x = 0$ axis. This behaviour, which was also observed in images recorded in control experiments carried out in the “mirror off” configuration, results from the well-known effect that light gases seeded in heavy gases have the highest density close to the edge of the gas expansion cone [47]. A control measurement in the “mirror off” configuration at $\tau = 2.1 \mu\text{s}$ ($t_{\text{ion}} = 2.6 \mu\text{s}$), when the centre of the cloud is also located 1.7 mm away from the photoexcitation point, yielded images almost identical to that shown in panel (a).

7.5 Conclusions

The mirroring of a Rydberg atom beam at normal incidence has been demonstrated for the first time. At the end of the mirroring process the atomic cloud has returned to its initial position almost unchanged. Moreover, the phase-space density has remained nearly constant because the decay of the Rydberg Stark states is not significant on the experimental time scale. Using time-of-flight and CCD-camera imaging techniques, we also found that the atomic beam can be focussed strongly, leading to a more than fourfold increase in the particle density, however at the expense of a wider velocity distribution. These results reveal an unprecedented control over the spatial and velocity distributions of a Rydberg atom cloud. This control is achieved using only small ($\leq 2000 \text{ V/cm}$) electric fields and a very compact electrode setup. Halfway through the mirroring process, the atoms are brought back to zero velocity in the laboratory frame after only $4.8 \mu\text{s}$ and 1.9 mm of flight. The mirroring measurements described above thus also represent the first direct demonstration that a Rydberg atom beam can be stopped in a single deceleration stage.

Chapter 8

Trapping Rydberg atoms

8.1 Introduction

The study of the properties of atoms and molecules and the manipulation of their internal state over extended periods of time necessitate trapping the atoms and molecules. In this chapter a new method to trap atoms and molecules excited to Rydberg Stark states is described and its application to trap state-selected hydrogen Rydberg atoms is demonstrated. Hydrogen atoms in blue-shifted Stark states were trapped in two dimensions and the number of trapped atoms decayed approximately exponentially with a decay time of $50 \mu\text{s}$. The motion of the cloud of atoms within the trap was studied by pulsed field ionization aided by simulations of the neutral particle trajectories in the trap and of the trajectories of the ions in the time-of-flight tube.

Although the atoms were excited to a well-defined quantum state, black body radiation induced transitions and collisions can redistribute the initial population of hydrogen Rydberg atoms over states of several n and k values. This process was studied using selective field ionization as a function of the time between photoexcitation and pulsed field ionization.

8.2 Trapping atoms and molecules using electromagnetic fields

The coldest and most dense samples of atoms were obtained to date by trapping laser cooled atoms magnetically using the Zeeman shift [81], in the overlap region of 6 nearly resonant laser beams in so-called optical molasses [25, 77], by combining a magnetic trap with nearly resonant laser beams in so-called magneto-optical traps [98], or in a tightly focussed laser beam using the induced dipole of the atoms in the strong electric field of the laser beam [24, 82]. The temperatures in these samples were low enough ($\sim \mu\text{K}$) and the densities high enough ($\sim 10^{15} \text{ cm}^{-3}$) that Bose-Einstein conden-

sation could be observed for magnetically [2, 20, 28] and optically [52, 115] trapped atoms. Bose-Einstein condensation was also observed in magnetically trapped atomic hydrogen [40] but the hydrogen atoms were cooled by cryogenic means followed by evaporative cooling.

The trapping of atoms and molecules in electric fields using the Stark effect was first described in references [141] and [142] in which the idea of trapping polar molecules and atoms and molecules in Rydberg Stark states was introduced. These ideas and trap designs were used to trap NH_3 , ND_3 [15, 124] and OH [121] molecules in their electronic ground state, see also section 1.2.2. The results presented in this chapter are the first demonstration of electrostatic trapping of atoms in Rydberg Stark states.

Magnetic trapping of atoms excited to Rydberg states has been shown in reference [23] which describes how rubidium Rydberg atoms were trapped in permanent magnetic fields of approximately 2.9 T. The trapping times were long, on the order of 25 ms, but the quantum state of the trapped atoms could not be controlled; the rubidium atoms, initially in the 5P state, were excited to states with $n \approx 130$ after which they spontaneously evolved to high- n states ($n \approx 300$) with high m ($m \approx 300$). These high- m states can be trapped in inhomogeneous magnetic fields.

8.3 Experimental methods and techniques

In the experiments described in this chapter, the electrode setup and the photoexcitation scheme were the same as for the experiments in chapters 5 and 7. However, instead of decelerating the atoms with time-independent electric fields, the experiments made use of time-dependent fields as described in chapter 6 for the deceleration experiments on argon Rydberg states. The trapped hydrogen atoms were detected by pulsed-field ionization as described in chapter 7.

8.3.1 Atom trap pulse sequence

Panel (a) of figure 8.1 shows the voltage pulse sequence used in the trapping experiments. The voltage sequence consisted of four phases: photoexcitation ($t = 0$), deceleration ($0 < t < 10 \mu\text{s}$, voltage configuration in panel (b)), trapping ($10 \mu\text{s} < t < t_{\text{ion}}$, panel (c)) and field ionization ($t = t_{\text{ion}}$).

The hydrogen atoms were excited to $n = 27$ Stark states in the field generated by applying voltages $V_1 = -V_2 = V_{\text{DC}} = 45 \text{ V}$ on the electrodes 1 and 2. Depending on whether the trap was “off” or “on” after deceleration (see below), the potentials on electrodes 3 and 4 at excitation were at zero volt or at $V_4 = -V_3 = 25 \text{ V}$, respectively. In the latter case the additional nonzero voltages lowered the electric field strength slightly at the excitation point and increased the inhomogeneity of the electric field distribution, and thus the inhomogeneous line widths of the transitions to the Stark

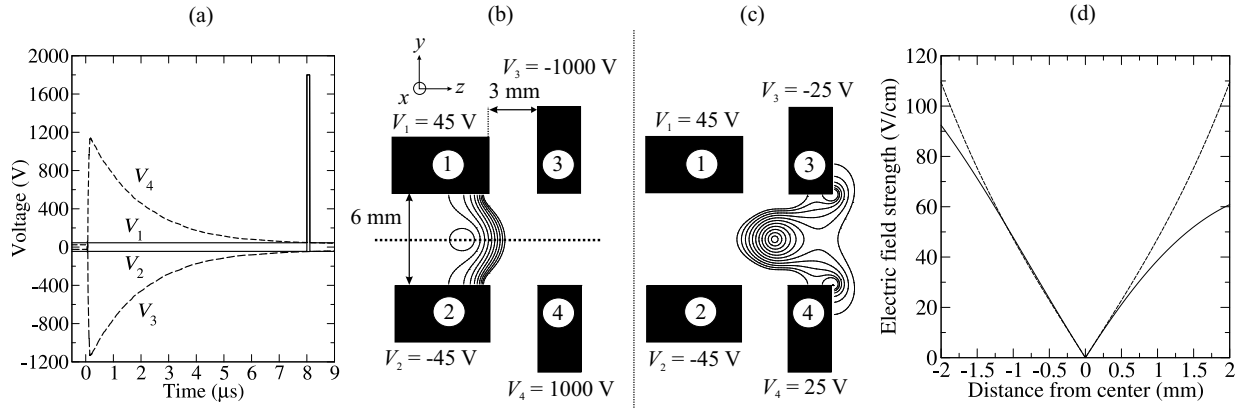


Figure 8.1: Panel (a): Voltage sequence used in the trapping process. Panels (b) and (c): Voltage configurations used to decelerate (b) and trap (c) the H atoms in low-field seeking states. The solid lines in panels (b) and (c) are lines of constant electric field in steps of 100 V/cm (b) and 10 V/cm (c). In panel (d) the electric field strength is shown on lines parallel to the z axis (solid line) and the y axis (dashed line) through the point where $F = 0$ for the potential configuration shown in panel (c).

states so that more than one k state was excited.

Immediately after excitation, the potentials on the third and fourth electrodes were switched to a high potential which decayed exponentially, as described in chapter 6. The atoms were excited to low-field seeking states and they therefore decelerated, see panel (b) of figure 8.1. The peak value of the potential, V_{decel} , and the time constant of the exponential decay were chosen such that (1) the atoms decelerated to zero velocity at the end of the decay and (2) they were located close to the centre of the trap at that time. After $10\text{ }\mu\text{s}$ the time-dependent part of the potentials on the third and fourth electrodes had decayed to less than 1% of the initial value because the $1/e$ decay time was $1.9\text{ }\mu\text{s}$. The potentials decayed either to 0 or to a constant potential $-V_3 = V_4 = 25\text{ V} = V_{\text{trap}}$. In the former case the resulting electric field distribution is equal to the one shown in panel (b) of figure 7.1 and the low-field seeking atoms were slowly accelerated out of the electrode setup. This final potential configuration is referred to as the “trap off” configuration. When the potential decayed to a constant potential, the electric field distribution corresponds to that displayed in panel (c) of figure 8.1. This final potential configuration is referred to as the “trap on” configuration.

After a controllable delay t_{ion} the Rydberg atoms were field ionized and the ions collected on the MCP. When the potentials on electrodes 3 and 4 decayed to a nonzero potential, the ions were accelerated slightly toward electrode 3. As long as the potentials on electrodes 3 and 4 were small compared to the potential used for field ionization, this lateral acceleration was small compared to the acceleration in the z dimension and most ions reached the MCP detector. However, in the time before $t \approx 10\text{ }\mu\text{s}$, the time-dependent part of the potentials on electrodes 3 and 4 has not decayed yet to zero and most ions are deflected away from the MCP detector. There-

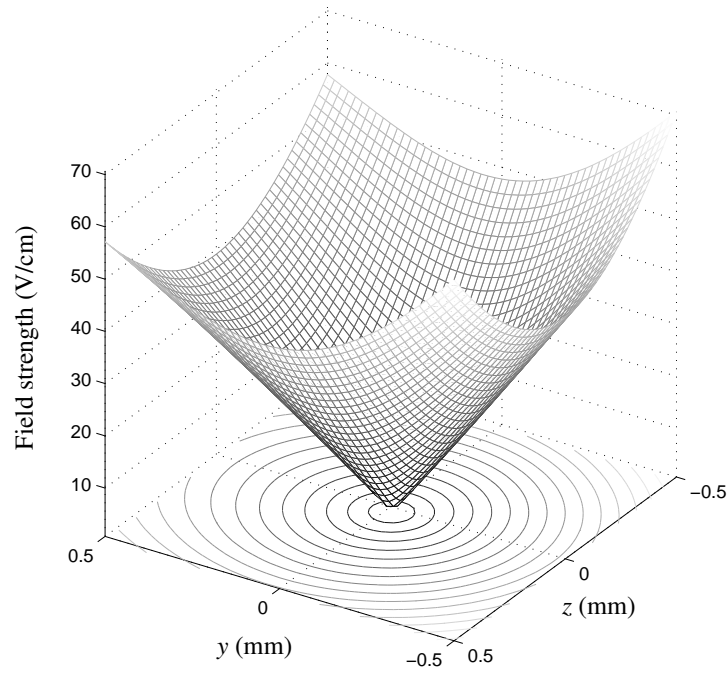


Figure 8.2: Three-dimensional view of the trap for the same potentials as in figures 8.1c and 8.1d. The origin of the y and z axis is the point in the trap where $F = 0$.

fore, within the first $10 \mu\text{s}$ we cannot monitor the motion of the Rydberg atoms in the decelerator using pulsed-field ionization.

8.3.2 The Rydberg atom trap

Panel (d) of figure 8.1 displays the electric field strength on the lines parallel to the z axis (solid line) and the y axis (dashed line), through the point where $F = 0$ for the “trap on” potential configuration. From panels (c) and (d) it is clear that for this voltage configuration the electrode setup constitutes a trap in two dimensions for low-field seeking states because the electric field strength increases in all direction in the yz plane around the point where $F = 0$. In the x dimension the electric field is homogeneous and no forces are exerted on the Rydberg atoms. A three-dimensional view of the electrostatic trap is shown in figure 8.2 in which the electric field strength is drawn as a function of y and z .

Atoms which are situated away from the centre of the trap experience a restoring force toward the centre equal to

$$\vec{f} = -\frac{3}{2}nk\nabla F. \quad (8.1)$$

Panel (d) of figure 8.1 shows that in the middle of the trap the electric field strength depends linearly on the distance away from the centre of the trap, as is expected for an electric quadrupole configuration. Because equation 8.1 depends linearly on the gradient of the electric field strength, the restoring force is independent on the distance away from the centre of the quadrupole. The motion of a cloud of Rydberg atoms within the trap is therefore anharmonic.

For the potentials used in panel (d) of figure 8.1 the electric field gradient is equal to $\sim 450 \text{ V/cm}^2$. Using equation 5.5 one sees that the hydrogen atoms experience an acceleration of $1.75 \cdot 10^7 \text{ m/s}^2$ toward the centre of the trap. A particle at rest situated 0.5 mm away from the centre of the trap thus travels through the middle of the trap to 0.5 away from the centre of the trap in $\sim 11 \mu\text{s}$.

The lowest saddle point in the electric field strength distribution is situated between electrodes 3 and 4 and has a value of $F = 65 \text{ V/cm}$. For a hydrogen atom in a $n = 27, k = 19$ state this corresponds to a potential energy difference $E_{\text{Stark}} = 2.1 \text{ cm}^{-1}$ relative to the point where $F = 0$ or to a temperature of 3 K and, for atomic hydrogen, to a maximal velocity of 225 m/s. The trap depth can be raised or lowered by raising or lowering the potentials on all the electrodes. Moreover, the position of the trap can be shifted by changing either the potentials of electrodes 3 and 4, or the potentials of electrodes 1 and 2.

8.4 Results

In this section the results of the trapping experiments and the conclusions that could be drawn from these experiments are discussed. It consists of four parts: In the first part, the trapping of hydrogen Rydberg atoms is demonstrated for a large number of n values. In the second part, the dynamics of the atom cloud in the trap is discussed and the results of the SFI measurements in the trap are presented in the third section. In the last part the processes that can limit the trapping times are discussed.

8.4.1 Trapping Rydberg hydrogen atoms

Generic trapping experiment

In figure 8.3 the result of a typical trapping measurement is shown. In this measurement the hydrogen atoms were excited to the $n = 27, k \approx 20$ Stark state, decelerated using $V_{\text{decel}} = 1155 \text{ V}$, and subsequently trapped using a trapping potential $V_{\text{trap}} = 25 \text{ V}$. The atoms were field ionized using an ionization pulse with an amplitude of 1800 V after a controllable delay t_{ion} and the ions were collected on the MCP detector where the ion TOF spectra were recorded.

From figure 8.3 it is clear that, although the intensity of the ionization signal decreases with increasing ionization delay, a significant fraction of the atoms remains trapped for more than $100 \mu\text{s}$. The integrated intensity of the ion TOF traces decays

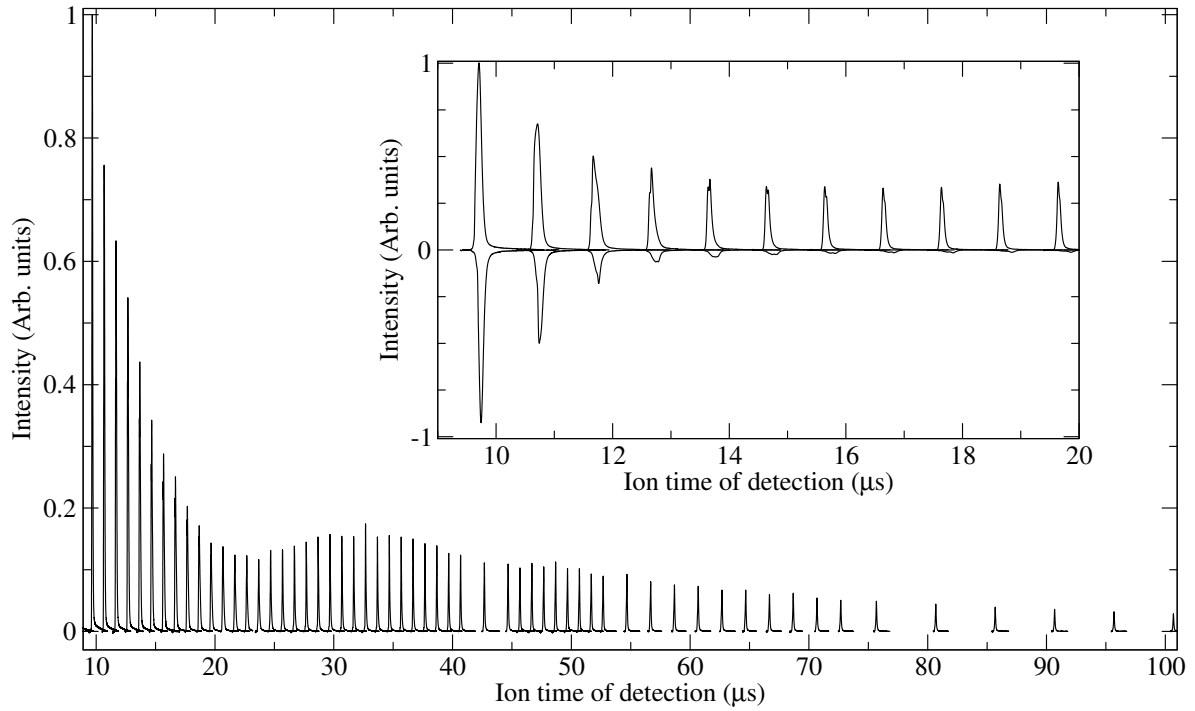


Figure 8.3: Sequence of ion TOF profiles after trapping the hydrogen atoms for a variable delay. In the inset a comparison is shown between ion TOF profiles with the trap on (traces pointing upward) and with the trap off (inverted traces). The potentials that were used in the trap on experiment are: $V_{DC} = 45$ V, $V_{decel} = 1155$ V, and $V_{trap} = 25$ V.

rapidly between $t_{ion} = 10 \mu s$ and $t_{ion} = 22 \mu s$, but after this rapid initial decay, the integrated intensity decreases approximately exponentially with a $1/e$ time of $50 \mu s$. Moreover, the comparison of the integrated intensities of the TOF signals with that of a single ion enables one to estimate that more than 10 000 atoms are initially trapped. Given that the trap volume is less than 1 mm^3 one can calculate that the density of Rydberg atoms in the trap is in excess of 10^7 cm^{-3} .

In the inset in figure 8.3 a comparison is shown between the ion TOF traces with the trap on (traces pointing upward) and with the trap off (inverted traces). In the latter case, the intensities of the ion TOF spectra for $t_{ion} > 15.1 \mu s$ were more than an order of magnitude smaller than in the case where the trap was on. This observation indicates that the ion signals come from the field ionization of Rydberg hydrogen atoms that are trapped in two dimensions.

In figure 8.4 five ion TOF profiles are shown for which $t_{ion} = 50.1 \mu s$ and the trapping potential V_{trap} was equal to 50 V, 40 V, 30 V, 20 V, and 10 V. The time at which the TOF profile has its maximum shifts to shorter times of flight with increasing trapping potential. This shift can be explained by the fact that the zero of the trap, and thus the region where most of the atoms are situated, lies closer to electrodes 1 and 2 with increasing V_{trap} . Ions resulting from Rydberg atoms which were ionized closer

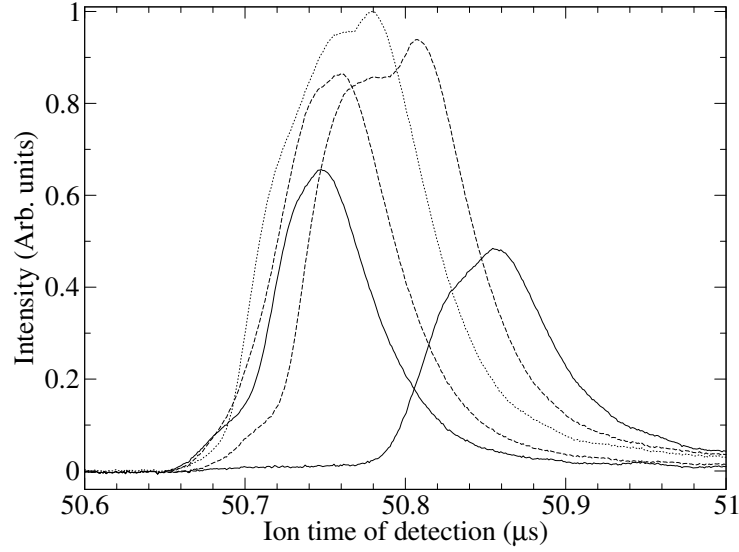


Figure 8.4: Dependence of the time-of-flight profile on the trapping potential. In all measurements the trapped Rydberg atoms were field ionized at $t_{\text{ion}} = 50.1 \mu\text{s}$. The trapping potentials were 50 V (left solid line), 40 V (left dashed line), 30 V (dotted line), 20 V (right dashed line), and 10 V (right solid line).

to electrodes 1 and 2 have shorter times of flight than ions resulting from Rydberg atoms which were ionized further away from electrodes 1 and 2 as explained in chapter 7.

The integrated intensity of the TOF profile is maximal for $V_{\text{trap}} = 30 \text{ V}$. The decrease in integrated intensity for higher and lower trapping potentials is probably caused by a poorer spatial overlap between the cloud of decelerated atoms and the location of the trap.

Phase-space calculations

The phase-space distributions of the atom cloud in the trapping experiment calculated for the potentials indicated in figure 8.3 are given in figure 8.5. In the left panel the phase-space distributions in the z dimension are drawn for $t_{\text{ion}} = 0, 2 \mu\text{s}$, and $10 \mu\text{s}$. At $t_{\text{ion}} = 0$ the atom cloud has a size (FWHM) of 0.8 mm and a velocity of 720 m/s with a temperature of 0.1 K . During the first $10 \mu\text{s}$, the deceleration phase, the centre of the atom cloud moves toward $z \approx 2.5 \text{ mm}$, where the centre of the trap is situated, and the mean longitudinal velocity of the atom cloud is reduced to zero. After this deceleration phase the trapping phase starts. In the inset of the left panel, the phase-space distribution $50 \mu\text{s}$ after excitation is drawn. The atoms have spread out in the z dimension over $\sim 1 \text{ mm}$ in the trap and have an effective temperature of 320 mK in this dimension.

In the right panel of figure 8.5 the phase-space distributions in the y dimension

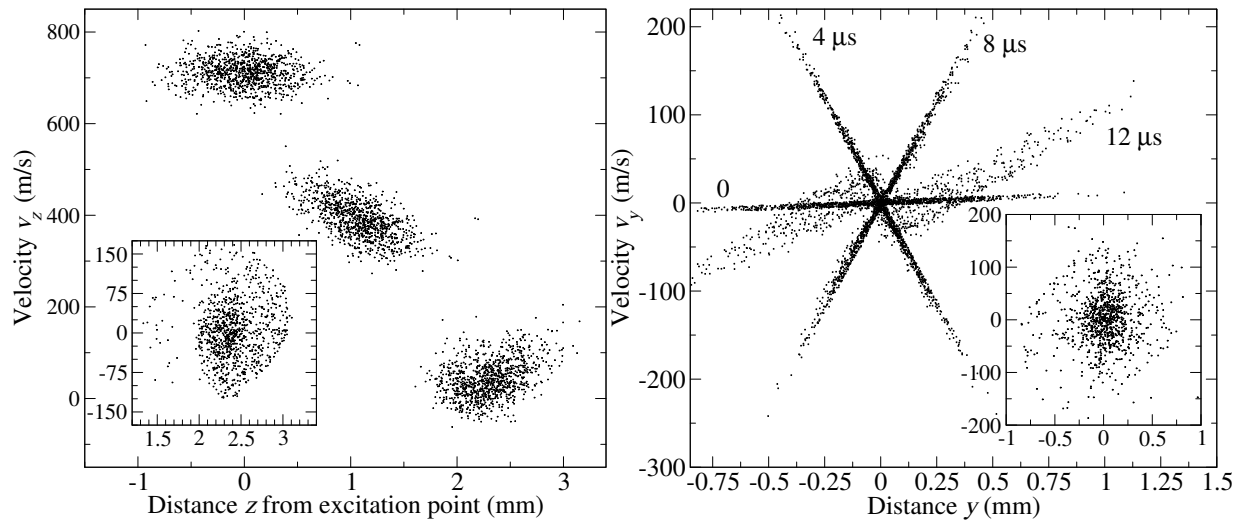


Figure 8.5: Calculated phase-space distributions of the hydrogen atom cloud in the trapping experiment. Left panel: Phase-space distributions in the z dimension at $t_{\text{ion}} = 0, 2 \mu\text{s}$, and $10 \mu\text{s}$. Right panel: Phase-space distributions in the y dimension at $t_{\text{ion}} = 0, 4 \mu\text{s}$, $8 \mu\text{s}$, and $12 \mu\text{s}$. In both panels the inset shows the phase-space distribution of the atom cloud after $50 \mu\text{s}$. The axis labels are the same for the insets as for the main plots. The potentials that were used in the simulations are: $V_{\text{DC}} = 45 \text{ V}$, $V_{\text{decel}} = 1155 \text{ V}$, and $V_{\text{trap}} = 25 \text{ V}$.

are shown for $t_{\text{ion}} = 0, 4 \mu\text{s}$, $8 \mu\text{s}$, and $12 \mu\text{s}$. In this dimension the initial mean velocity is 0 with an effective temperature of 2.3 mK. The evolution of the phase-space distribution in this dimension is similar to the evolution of the phase-space distribution in the mirroring experiment: The atoms are accelerated toward the central axis, leading to a wider velocity distribution and a narrower spatial distribution. In phase space this corresponds to a clockwise rotation. After $12 \mu\text{s}$ the anharmonicity of the trapping potential can be seen as a spiraling in phase space: Not all atoms rotate in phase-space with the same angular velocity as would be the case for a harmonic trap. The inset in the right panel shows the phase-space distribution $50 \mu\text{s}$ after excitation. Because of the anharmonicity the atoms have spread out evenly over the whole phase-space in the y dimension and are spread out over $\sim 1 \text{ mm}$ and have an effective temperature of 220 mK in this dimension.

Trapping at different n values

Although most of the experiments described in this chapter were performed with hydrogen atoms excited to the $n = 27$, $k \approx 20$ state, trapping was observed for a wide range of n values. In figure 8.6 three spectra are shown which together span the energetic region from the zero electric field positions of $n = 20$ to 60. In all three measurements the atoms were decelerated, trapped, and subsequently ionized $50.1 \mu\text{s}$ after excitation. Because the deceleration and trapping behaviour changes

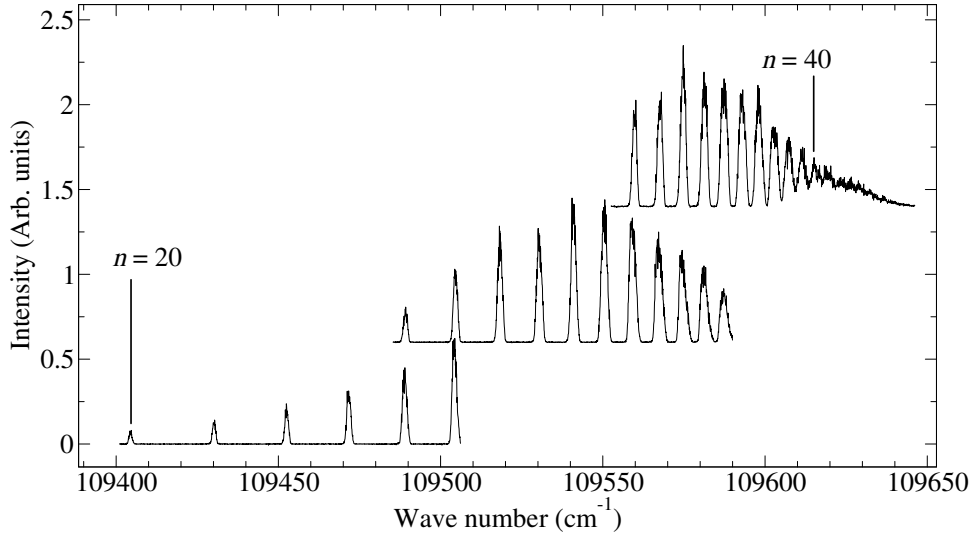


Figure 8.6: Spectra of the trapping efficiency over the first 50 μs for $n = 20$ to 40. The middle and top spectra are offset for clarity. The potentials that were used in the experiments are: Top spectrum: $V_{\text{DC}} = 35$ V, $V_{\text{decel}} = 715$ V, and $V_{\text{trap}} = 20$ V. Middle spectrum: $V_{\text{DC}} = 45$ V, $V_{\text{decel}} = 1155$ V, and $V_{\text{trap}} = 25$ V. Bottom spectrum: $V_{\text{DC}} = 47.5$ V, $V_{\text{decel}} = 1760$ V, and $V_{\text{trap}} = 25$ V.

with n , the three spectra were recorded with different potential configurations: bottom spectrum: $V_1 = -V_2 = 47.5$ V, $V_{\text{trap}} = 25$ V, and $V_{\text{decel}} = 1760$ V, middle spectrum $V_1 = -V_2 = 45$ V, $V_{\text{trap}} = 25$ V, and $V_{\text{decel}} = 1155$ V, top spectrum: $V_1 = -V_2 = 35$ V, $V_{\text{trap}} = 20$ V, and $V_{\text{decel}} = 715$ V. To record the bottom spectrum the potential applied to electrodes 1 and 2 to field ionize the Rydberg atoms was equal to 2 kV and it amounted to 1.8 kV for the upper two spectra. For the low- n states the ionization probability for a given electric field strength goes to zero rapidly and below $n = 20$ the Rydberg atoms cannot be ionized anymore in this setup. Above $n = 40$ the different blue-shifted manifolds are no longer resolved, leading to the broad shoulder above this n value.

The intensity distributions in figure 8.6 are a convolution of the transition intensity, the deceleration and the trapping efficiency, the ionization probability, and the ion collection efficiency. Because the potentials were in each case optimized for one n value, the deceleration and trapping efficiencies are lower for the other n values. Nevertheless, the results depicted in figure 8.6 show that with one set of potentials, Rydberg Stark states with a wide range of n and k values can be trapped for more than 50 μs , indicating that the trap is versatile and not selective in n or k .

8.4.2 Dynamics in the trap

To obtain more insight into the dynamics of the Rydberg atoms within the trap, different series of experiments were performed in which V_{decel} was varied. In the measurements shown in figure 8.7 the hydrogen atoms were excited to the $n = 27$,

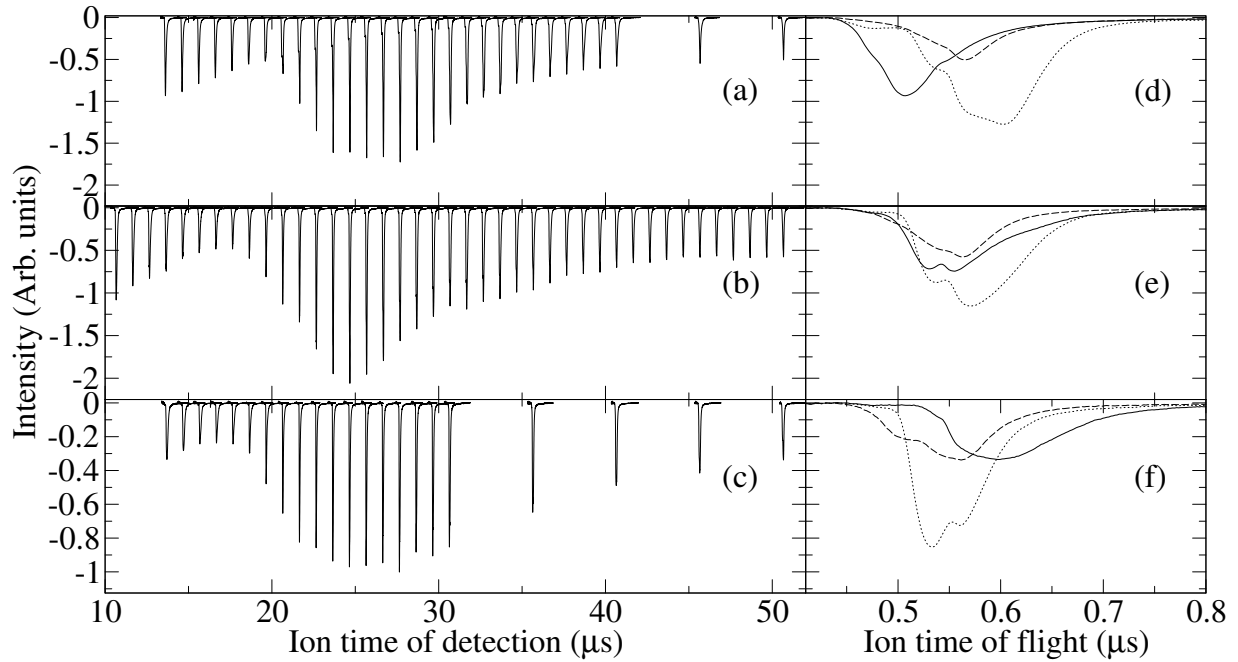


Figure 8.7: Trapping experiments for different deceleration potentials. In the left panels (a) to (c) the ion times of flight are shown as a function of t_{ion} and in the right panels (d) to (f) the ion times of flight for $t_{\text{ion}} = 13.1 \mu\text{s}$ (solid line), $t_{\text{ion}} = 30.1 \mu\text{s}$ (dotted line), and $t_{\text{ion}} = 50.1 \mu\text{s}$ (dashed line) are overlapped by subtracting t_{ion} from the ion time of detection. The deceleration potentials were equal to $V_{\text{decel}} = 1375 \text{ V}$ (upper panels), $V_{\text{decel}} = 1155 \text{ V}$ (middle panels), and $V_{\text{decel}} = 935 \text{ V}$ (lower panels). The intensity scale for the two lower panels is twice smaller than the intensity scale for the upper panels.

$k \approx 20$ Stark state using $V_{\text{DC}} = 45 \text{ V}$ and $V_{\text{trap}} = 25 \text{ V}$. The atoms were ionized after a controllable delay using an ionization potential $V_{\text{ion}} = 1800 \text{ V}$. In the upper two panels the deceleration potential V_{decel} was equal to 1375 V , in the middle two panels $V_{\text{decel}} = 1155 \text{ V}$, and in the lower two panels $V_{\text{decel}} = 935 \text{ V}$. The three left panels (a) to (c) show a series of ion TOF spectra as a function of t_{ion} for these three deceleration potentials. A striking feature in these three series of measurements are the large oscillations in peak intensity as a function of t_{ion} . The fact that the integrated intensity after $t_{\text{ion}} \approx 25 \mu\text{s}$ is *larger* than after $t_{\text{ion}} \approx 18 \mu\text{s}$ proves that the reduction of intensity is not caused by a loss of atoms from the trap but rather by a reduced ionization probability or by a reduced ion collection efficiency. Because these efficiencies depend on the location and spatial spread of the Rydberg atoms in the trap, the oscillations in intensity are a signature of the dynamics of the cloud of decelerated Rydberg atoms in the trap. The $\sim 10 \mu\text{s}$ time scale of the oscillations is in agreement with the calculation in section 8.3.2 of the time of oscillation ($\sim 11 \mu\text{s}$) of a single particle within the trap.

The main difference in the three series of measurements shown in the left panels of figure 8.7 is the spatial position of the cloud of decelerated hydrogen atoms after

the $\sim 10 \mu\text{s}$ long deceleration period. In the experiments depicted in the middle panel, for which $V_{\text{decel}} = 1155 \text{ V}$, the centres of the decelerated atom cloud and of the trap coincide. Shown in panel (e) in figure 8.7 are the measurements at $t_{\text{ion}} = 13.1 \mu\text{s}$ (solid line), $t_{\text{ion}} = 30.1 \mu\text{s}$ (dotted line), and $t_{\text{ion}} = 50.1 \mu\text{s}$ (dashed line). In each case, t_{ion} was subtracted from the ion time of detection for direct comparison of the times of flight. The three ion TOF traces, and also all the other TOF traces derived from panel (b), nearly overlap, indicating that the spatial distribution of the parent Rydberg atoms in the z dimension remains nearly constant with time.

In the other two measurements, on the contrary, the ion TOF spectra recorded at $t_{\text{ion}} = 13.1 \mu\text{s}$ (solid lines), differ significantly from the ion TOF spectra recorded at $t_{\text{ion}} = 50.1 \mu\text{s}$ (dashed line), see panel (d) and (f) in figure 8.7. In the measurements with $V_{\text{decel}} = 1375 \text{ V}$, the gradients of the electric field, and therefore also the forces on the atoms, are larger during the deceleration phase than in the measurements with $V_{\text{decel}} = 1155 \text{ V}$, and the atom cloud reaches zero mean velocity at a spatial position closer to electrodes 1 and 2, i.e. before the centre of the trap. This leads to shorter ion times of flight for $t_{\text{ion}} = 13.1 \mu\text{s}$ than in the measurements where $V_{\text{decel}} = 1155 \text{ V}$. After $50.1 \mu\text{s}$ the atoms have moved toward the centre of the trap, the ion times of flight have increased and the ion TOF spectrum resembles the ion TOF spectra of the $V_{\text{decel}} = 1155 \text{ V}$ measurements closely.

In the measurements with $V_{\text{decel}} = 935 \text{ V}$ (panels (a) and (d) in figure 8.7), the electric field gradients are smaller during the deceleration phase and the atom cloud reaches zero mean velocity closer to electrodes 3 and 4, i.e. behind the centre of the trap. The ion TOF peak recorded after ionizing the atoms $13.1 \mu\text{s}$ after excitation is thus shifted toward later times and then shifts to shorter times of flight for increasing ionization times until the atoms have moved back toward the centre of the trap.

In the three series of measurements shown in figure 8.7 the dynamics of the cloud of atoms in the z dimension is complementary. Therefore, the intensity oscillations which are very similar for all three measurement series cannot be the consequence of an oscillatory behaviour in the z dimension. Instead, the intensity oscillations are likely to originate from an oscillation of the atom cloud in the y dimension resulting from a slight displacement of the initially prepared Rydberg atom cloud from the $y = 0$ plane. Although the electrodes themselves are symmetric with respect to the $y = 0$ plane, the potentials applied to the electrodes during ionization are not; the potentials on electrodes 3 and 4 are equal to $V_4 = -V_3 = 25 \text{ V}$. This potential is small compared to the ionization pulse on electrodes 1 and 2, $V_{\text{ion}} = 1800 \text{ V}$, and does not cause a spatial difference in the ionization probability for $y < 0$ and $y > 0$. The ion collection efficiency, on the other hand, is sensitive to this small asymmetry because the positive ions are accelerated toward electrode 3 and deflected from electrode 4. Therefore ions generated at $y > 0$ are collected less efficiently than ions generated at $y < 0$. Unfortunately it is not possible to calibrate the collection efficiency as a function of the y position of the Rydberg atom cloud. The particle trajectory simulation program was therefore used to calculate how the intensities of the ion TOF traces

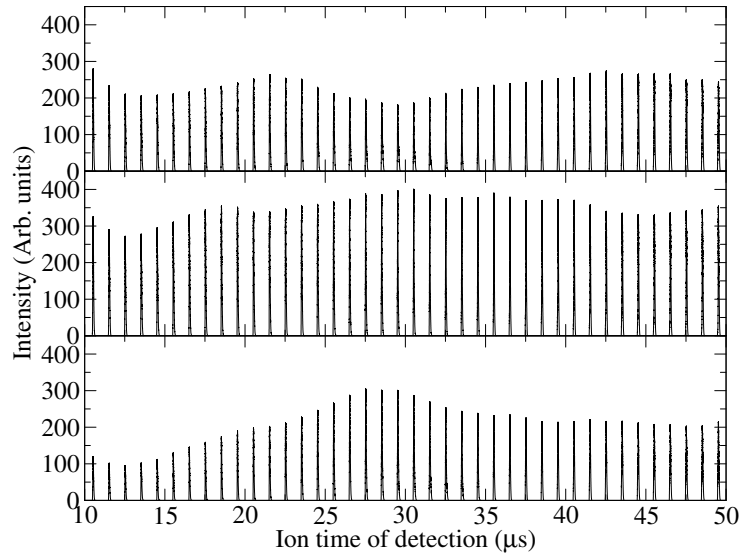


Figure 8.8: Simulated ion TOF traces as a function of t_{ion} . In the bottom (top) trace the atomic beam is offset by 0.5 mm in the negative (positive) y direction. In the middle trace the atom cloud is on axis. All other parameters were the same as used for the recording of the traces in the middle panels of figure 8.7.

change when the atomic beam is slightly displaced in the y dimension to induce a spatial oscillation in this dimension.

In figure 8.8 the simulated ion TOF traces are shown in which the same parameters were used as in the experiment with $V_{\text{decel}} = 1155$ V. In the simulations depicted in the upper trace, the centre of the hydrogen atomic beam was offset by 0.5 mm in the positive y direction, i.e. closer to electrodes 1 and 3, in the middle trace the centre of the atomic beam was set to lie in the middle between electrodes 1 and 2, and in the bottom trace the centre of the atomic beam was offset by 0.5 mm toward electrodes 2 and 4. A clear intensity oscillation is observed in the bottom trace similar to the oscillations shown in figure 8.7. The simulations provide the explanation for the intensity oscillations: The central position of the atom cloud moves from negative to positive y values in the first 10 μs . Because in the region with $y > 0$ the ion collection efficiency is lower than in the region with $y < 0$ (see above), the measured ion current is also lower. From ~ 15 μs onward the atom cloud moves toward negative y values again and the ion intensity increases.

When the atom cloud is on axis at excitation (see middle panel of figure 8.8), hardly any intensity oscillations are observed because the centre of the atom cloud does not oscillate in the y direction. Although care was taken to align the atomic beam, skimmer, and VUV-laser beam with the central axis of the electrode setup, a deviation of 0.5 mm is well within the alignment error margin of approximately 1 mm.

In figure 8.3 the ion TOF peak intensities as a function of time look qualitatively different from the data displayed in figure 8.7: In figure 8.3 the ion TOF peak intensity

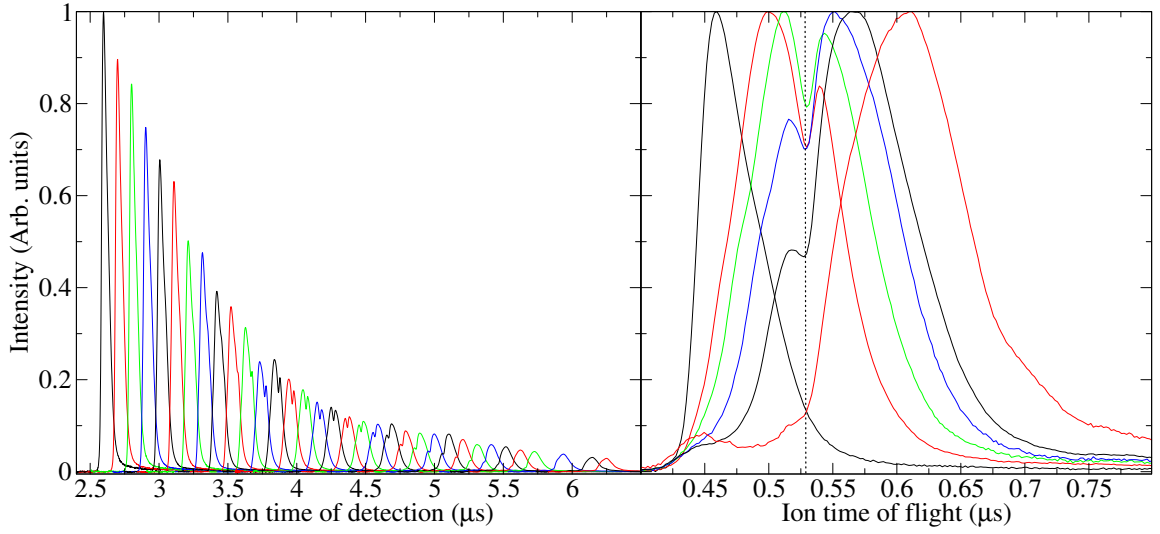


Figure 8.9: Ion TOF profiles measured after exciting the hydrogen atoms to the $n = 27$, $k = 20$ Stark state with $V_1 = -V_2 = 45$ V and $V_4 = -V_3 = 25$ V. The left panel shows the measurements with t_{ion} between $2.1 \mu\text{s}$ and $5.6 \mu\text{s}$ with steps of $0.1 \mu\text{s}$. In the right panel the measurements with t_{ion} equal to $2.1 \mu\text{s}$ (left black line), $3.3 \mu\text{s}$ (left red line), $3.7 \mu\text{s}$ (green line), $4.1 \mu\text{s}$ (blue line), $4.5 \mu\text{s}$ (right black line), $5.1 \mu\text{s}$ (right red line) are shown. The TOF traces are overlapped by subtracting t_{ion} from the ion time of flight. The maxima of all these measurements are normalized to one.

drops significantly as a function of t_{ion} and hardly increases at later ionization times. This is another illustration of the importance of the early time dynamics in the trap.

Many ion TOF profiles measured in the trapping experiment have a double peak structure as can be seen in the right-hand-side panels of figure 8.7 for instance. This double peak structure is also present in the ion TOF profiles recorded after letting an undecelerated beam of hydrogen atoms excited to the $n = 27$, $k \approx 20$ state fly through the trap, i.e. $V_1 = -V_2 = 45$ V and $V_4 = -V_3 = 25$ V, and ionizing the atoms after a variable delay. The results of such a measurement series are depicted in the left panel of figure 8.9. In these measurements t_{ion} was increased from $2.1 \mu\text{s}$ (outer left trace) to $5.6 \mu\text{s}$ (outer right trace) in steps of $0.1 \mu\text{s}$. In principle such a series of measurements could be used to study the dynamics in the z dimension in more detail because the ion times of flight depend on the z value of the parent Rydberg atom which can be calculated as a function of time for an undecelerated beam of hydrogen atoms with a known velocity. To draw the correct conclusions about the dynamics in the trapping experiments, these ion TOF profiles need to be understood in detail.

When t_{ion} is subtracted from the ion time of detection the local minima between the two peaks are at the same ion times of flight for all t_{ion} as indicated by the dotted vertical line in the right panel of figure 8.9. This observation is a strong indication that the double-peak structure has a spatial origin. The two peaks have a nearly equal intensity in the measurement in which the atoms were ionized $3.7 \mu\text{s}$ after excitation. At this time, the Rydberg atoms have travelled 2.7 mm from the excitation point, and

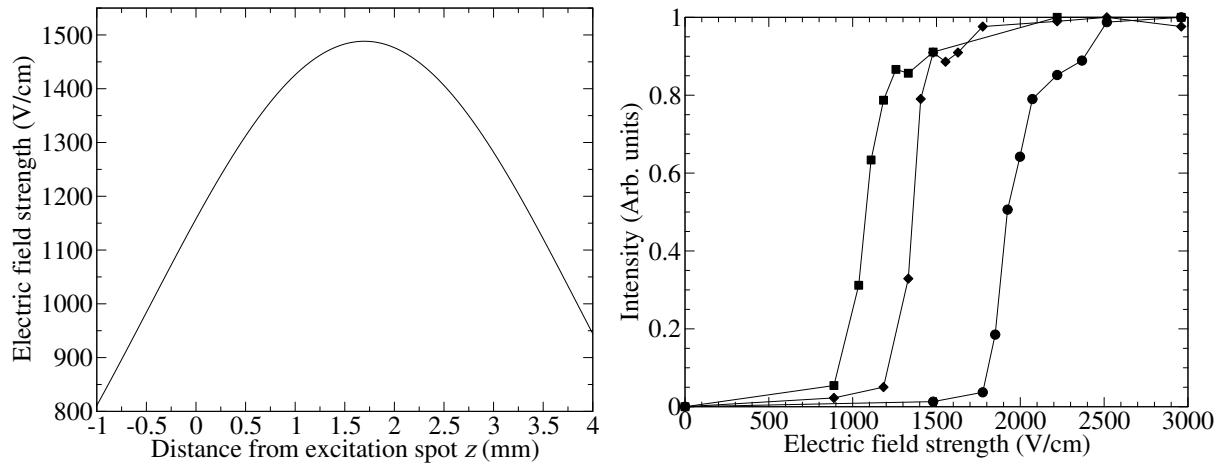


Figure 8.10: Left panel: Electric field strength on the z axis for the following potentials: $V_1 = V_2 = 1000$ V, $V_3 = V_4 = 0$ V. $z = 0$ corresponds to the centre of the excitation spot. Right panel: Results of SFI measurements for $n = 25$ (circles), $n = 27$ (diamonds), and $n = 29$ (squares). The Rydberg atoms were ionized $2.1 \mu\text{s}$ after excitation. The solid lines connect the data points.

the centre of the atom cloud nearly overlaps with the zero of the electric field distribution which is approximately situated 2.5 mm away from the excitation point. In similar measurements in which $V_3 = V_4 = 0$, no double-peak structure was observed which also suggests that the origin of the minimum in the TOF distribution is linked with the zero field position of the trap.

Simulations of the experiments with $V_4 = -V_3 = 25$ V did not reproduce a double peak structure in the ion TOF profile. Therefore this structure must be caused by a process, such as a k -changing process, which is not implemented in the simulations. To investigate the possibility of k -changing processes, SFI measurements were performed.

8.4.3 SFI measurements

As mentioned in chapter 2, selective field ionization (SFI) is a convenient method to study the distribution of quantum states in a cloud of Rydberg atoms. In particular the threshold field for ionization of Stark states of a given n value increases rapidly from the most red-shifted Stark state to the most blue-shifted Stark state, see section 2.4. In SFI measurements it is important that the electric field strength does not vary significantly over the cloud of atoms so that all atoms experience the same electric field strength. In our deceleration device this requirement is not completely fulfilled as can be seen from the equipotential lines in panel (d) of figure 7.1 and from the left panel of figure 8.10 in which the electric field strength on the z axis is drawn for $V_1 = V_2 = 1000$ V and $V_3 = V_4 = 0$ V as a function of z . The VUV spot size is estimated

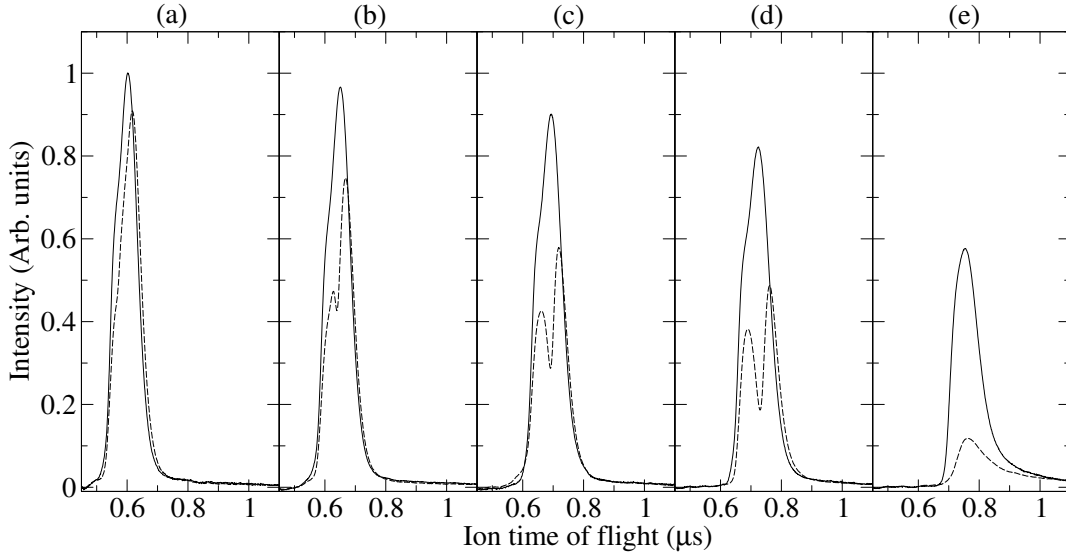


Figure 8.11: Ion TOF profiles measured after exciting the hydrogen atoms to a red-shifted $n = 27$ Stark state with $V_1 = -V_2 = 45$ V and $V_4 = -V_3 = 25$ V (dashed lines) or $V_4 = -V_3 = 0$ (solid lines). The potentials that were applied to electrodes 1 and 2 to ionize the hydrogen atoms were equal to $V_{\text{ion}} = 1500$ V (panel (a)), $V_{\text{ion}} = 1200$ V (panel (b)), $V_{\text{ion}} = 1000$ V (panel (c)), $V_{\text{ion}} = 900$ V (panel (d)), $V_{\text{ion}} = 800$ V (panel (e)). The Rydberg atoms were field ionized $3.6 \mu\text{s}$ after excitation.

to be 0.8 mm and the electric field strength thus varies between 1190 V/cm and 1390 V/cm for a cloud of atoms centred around $z = 0.5$ mm and between 1470 V/cm and 1490 V/cm for a cloud of atoms centred around $z = 1.7$ mm which corresponds to the maximum of the electric field strength distribution.

With this electrode setup it is nevertheless possible to measure the ionization field strength of Rydberg states of neighbouring n values selectively. In the right panel of figure 8.10 results of SFI measurements are shown for $n = 25$ (circles), $n = 27$ (diamonds), and $n = 29$ (squares) Rydberg states. The atoms were excited in an electric field to excite the $k = 0$ Stark states selectively and were ionized $2.1 \mu\text{s}$ after excitation. The potentials on electrodes 3 and 4 were kept at zero. For all three measurements a clear step is seen at an electric field strength of 1080 V/cm ($n = 29$), 1360 V/cm ($n = 27$), and 1920 V/cm ($n = 25$). The diabatic ionization thresholds for red-shifted Stark states are 807 V/cm ($n = 29$), 1075 V/cm ($n = 27$), and 1462 V/cm ($n = 25$). The measured ionization thresholds lie somewhat higher because these states are $k = 0$ states for which the probability that the electron is near the saddle point is lower than for a red-shifted Stark state. These measurements demonstrate the possibility to perform SFI measurements in our setup to establish the value of n . They also indicate that n -changing processes are negligible on a time scale of $2.1 \mu\text{s}$.

The situation becomes more complicated when the field ionization is carried out with $V_4 = -V_3 = 25$ V, i.e. with the trap on. These trapping potentials were not switched off during ionization and their effect needs to be taken into account to

correctly interpret the SFI measurements with trapped hydrogen Rydberg atoms. In figure 8.11 the result of an SFI measurements is shown in which an undecelerated beam of hydrogen atoms excited to a red-shifted $n = 27$ state were field ionized $3.6 \mu\text{s}$ after photoexcitation. Red-shifted Stark states cannot be trapped in our setup but their ionization field is approximately twice smaller than that of blue-shifted states of the same n value, making it possible to apply electric fields with a strength significantly above the ionization field strength. The full lines represent measurements for which $V_3 = V_4 = 0 \text{ V}$, i.e. for which the trap was off, and the dashed lines represent measurements in which the trap was on. The atoms move through the electrode setup with an almost constant velocity of approximately 720 m/s . In both the trap on and the trap off measurements, hardly any ion signal was observed for ionization potentials below 800 V . In the measurements in which the trap was off, the integrated intensity increases only slightly for potentials above 800 V and thus the field ionization yield sharply increases at $V_{\text{ion}} \approx 800 \text{ V}$, corresponding to an ionization field of 1120 V/cm .

In the trap on measurements a local minimum, similar to the local minimum described in the previous section, is seen in the measurements with $V_{\text{ion}} = 900 \text{ V}$, $V_{\text{ion}} = 1000 \text{ V}$, and $V_{\text{ion}} = 1200 \text{ V}$ but not in the measurement with $V_{\text{ion}} = 1500 \text{ V}$, for which the intensity is almost the same as for the trap off measurement. One can therefore conclude that, the local minima in the TOF distributions are not caused by a loss of excited atoms but by a reduced ionization probability or by a reduced collection efficiency. The electric field distribution at the end of the ionization pulse is almost identical in the trap on and the trap off situation as long as the ionization pulse is sufficiently large. It is therefore unlikely that the ionization probability is much lower for the trap off situation than for the trap on situation for hydrogen atoms in the same quantum state. A possible explanation for the observed ionization behaviour is the following.

Some of the Rydberg atoms change quantum state, i.e. k or m , so that these atoms can only be ionized by a large electric field strength, corresponding to the measurement with $V_{\text{ion}} = 1500 \text{ V}$, but not by a lower electric field strength, corresponding to the other measurements in figure 8.11. To explain the local minimum in the TOF distribution this change in quantum state has to occur at a specific spatial position, as explained in the previous section. The most likely mechanism is a change of k value taking place around the point where the electric field is zero. In this region, all k states are almost degenerate, the quantization axis is lost, and the atoms might make a transition from a red-shifted state to a blue-shifted state. Because the ionization field of blue-shifted states is higher than that of red-shifted states, the local minimum at low ionization fields and the disappearance of this local minimum at higher ionization potentials are readily explained. From the measurements it cannot be derived if the change in k value occurs already before the ionization pulse is applied, or occurs only during the initial rise of the ionization pulse when the electric field vector rotates rapidly.

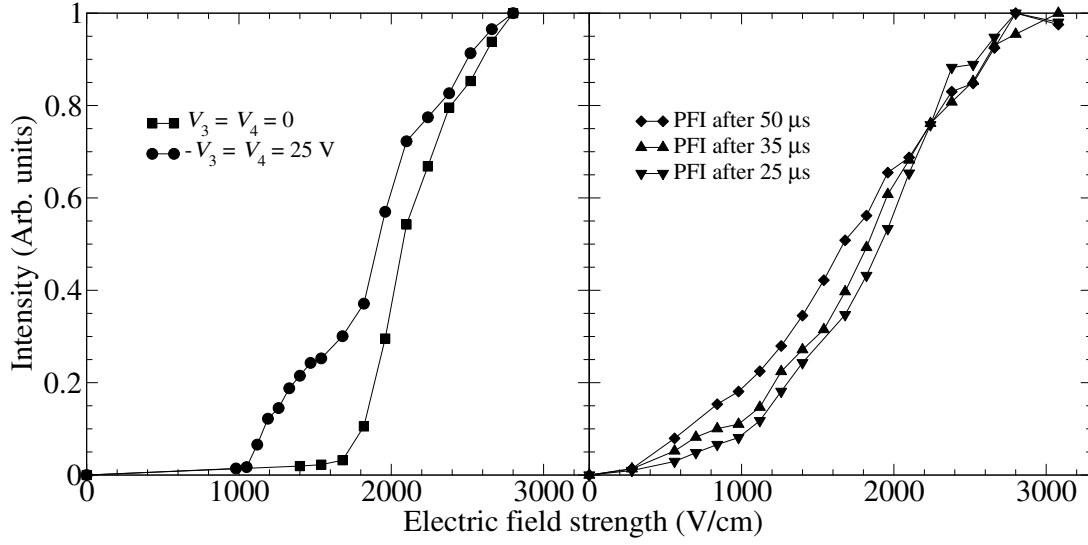


Figure 8.12: Results of SFI measurements after initially exciting the $n = 27$, $k \approx 20$ state. Left panel: The data represented by the squares and the circles correspond to measurements of the field ionization yield of an undecelerated beam of hydrogen $3 \mu\text{s}$ after excitation in the trap off and the trap on configuration, respectively. Right panel: The hydrogen atoms are decelerated and trapped, and field ionized $25 \mu\text{s}$ (triangles pointing down), $35 \mu\text{s}$ (triangles pointing up), and $50 \mu\text{s}$ (diamonds) after excitation.

The opposite behaviour is expected for blue-shifted Stark states: When the atoms excited to blue-shifted Stark states approach the centre of the trap and undergo a change of k , the change can only be to states of lower k values that ionize at a lower electric field. This expectation is confirmed by the comparison of field ionization measurements carried out on an undecelerated beam of hydrogen atoms excited to the $n = 27$, $k = 20$, blue-shifted Stark states in the trap on (data points represented by the circles) and trap off (data points represented by the squares) configurations as displayed in the left panel of figure 8.12. In the trap off configuration, a sharp increase in intensity is observed around 2000 V/cm which corresponds closely to the estimated ionization field strength for blue-shifted, $n = 27$ Stark states: $F_{\text{ion}}^{\text{blue}} = 2F_{\text{ion}}^{\text{red}} = \frac{2}{9n^4} \cdot 5.142 \cdot 10^9 \text{ V/cm} = 2150 \text{ V/cm}$. In the trap on configuration, instead of a clear step, a gradual increase in intensity is seen from $F \approx 1000 \text{ V/cm}$ onward. This is in accordance with k -changing processes taking place around the zero electric field point in the trap. Such a change in k state is not implemented in the trajectory simulations program at present.

The local minima in the ion TOF distributions following field ionization of the $n = 27$, $k \approx 20$ blue-shifted Stark state observed in figure 8.9 cannot be interpreted in the same way as for the red-shifted Stark states because the threshold ionization field of the atoms that undergo a k change to a more red-shifted state is *lowered* in this case. However, these atoms ionize at an earlier time during the rise of the electric field and their TOF is shifted toward later times resulting in a dip in the TOF distri-

bution at the position corresponding to the zero-field position in the trap.

SFI can also be used to follow the changes in the Stark state distribution of the trapped atoms over longer times, as illustrated in the right panel of figure 8.12 for a trapped cloud of Rydberg atoms excited to the $n = 27$, $k \approx 20$ Stark state. The measurements represented by the triangles pointing down, the triangles pointing up, and the diamonds were taken after decelerating and trapping the hydrogen atoms, and ionizing them $25 \mu\text{s}$, $35 \mu\text{s}$, and $50 \mu\text{s}$ after excitation, respectively. For the comparison the maxima of the integrated intensities were normalized to 1 for all measurements depicted in figure 8.12. Ionization is seen to occur for lower electric field strengths with increasing ionization delay, which is an indication that not only k but also n -changing processes to higher n values take place in the trap on the time scale of tens of μs , probably caused by black body radiation. Unfortunately, the electric field strength could not be increased far enough above the ionization field strength for blue-shifted Stark states with $n = 27$ so that n -changing processes to lower n values could be observed.

8.4.4 Factors limiting the trapping time

After the initial oscillations of the Rydberg atoms in the y dimension discussed in section 8.4.2, the Rydberg atom cloud fills the trap homogeneously. The subsequent exponential decay of the signal intensity with a $1/e$ time of $\sim 50 \mu\text{s}$ can be interpreted as a loss of Rydberg atoms from the trap. The following loss mechanisms have been considered to explain the decay of signal:

- Losses because the atoms are not trapped in the x dimension. In the x dimension, the electric field is homogeneous and the atoms are not trapped in this dimension. The perpendicular temperature in the atomic beam is approximately equal to 100 mK and the initial velocities in the x dimension are on the order of 50 m/s. The electrodes in this dimension are 2 cm long. Consequently, it takes an atom moving at a velocity of 50 m/s approximately $200 \mu\text{s}$ to travel from the middle to the edge of the electrodes where it cannot be field ionized anymore. The trapping time of $50 \mu\text{s}$ is much smaller, and the losses are probably negligible for the present measurements.
- Losses at the zero electric field point. At zero electric field the dipole of the Rydberg state is not directed anymore; all Stark states are degenerate at this point. Therefore, when a particle travels from a nonzero electric field through the centre of the trap to nonzero electric field again, the k value of the Rydberg atom may change from a trapable blue-shifted Stark state to a red-shifted Stark state that is accelerated out of the trap. The zero electric field point can therefore lead to losses in the number of trapped atoms. This process is analogous to losses in magnetic traps caused by Majorana transitions.

The chance that such a transition from a blue-shifted to a red-shifted Stark

state takes place can be calculated using Landau-Zener theory, see section 2.3. For a trapped Rydberg atom in a blue-shifted $n = 27$ state, the probability of a transition to a red-shifted Stark state becomes larger than 1% if the minimum electric field strength on the atoms trajectory through the trap is smaller than 0.1 V/cm. The atom then has to pass through the trap centre less than $2 \mu\text{m}$ away from the point in the trap where the electric field is zero. From these considerations it seems unlikely that the zero electric field point plays a significant role in the loss of atoms from the trap on the time scale of $50 \mu\text{s}$ because the atoms pass the centre of the trap only approximately 3 times on this time scale.

- Losses because of spontaneous emission to low-lying states. The trapped Stark states can fluoresce to, for instance, the $1^2S_{1/2}$ ground state or to the $2^2P_{1/2,3/2}$ states. The rates of these decay processes can be calculated for all ℓ components of the Stark state using equations 2.27 and 2.28 and, from these decay rates, the lifetime of the Stark state can be calculated [11]. The $n = 27$, $k = 20$, $m = 0$ Stark state has a fluorescence lifetime approximately equal to $50 \mu\text{s}$, which is dominated by the decay of the $\ell = 1$ component to the ground state. The $n = 27$, $k = 20$, $|m| = 2$ Stark state does not have any p character and therefore lives much longer, approximately $130 \mu\text{s}$. In the experiment, most excited states have $|m| = 0$ character and the trapping lifetime is likely to be dominated by the spontaneous emission rate of the Stark state back to the ground state.
- Losses because of transitions induced by black body radiation to states which are not trapped. The black body radiation rate can be calculated using equation 2.33 and yields an effective lifetime of $\tau_{n\ell}^{\text{BB}} = 35.8 \mu\text{s}$ for $n = 27$ Stark states. As already discussed in chapter 2, black body radiation induces transitions to states with similar n and k values. From figure 8.6 it is clear that if a hydrogen atom makes such a transition, it will remain trapped. Although black body radiation certainly leads to a redistribution of the quantum numbers of the trapped atoms, it is unlikely to be an important cause of the loss of signal on a time scale of $50 \mu\text{s}$.
- Losses from collisions with the background gas or with the unexcited atoms in the gas beam. The background pressure in our experimental setup is on the order of 10^{-7} mbar, making collisions between hydrogen atoms in Rydberg states and background gas unlikely. The local pressure in the gas beam, on the other hand, is much higher, on the order of 10^{-2} to 10^{-3} mbar. The hydrogen atoms that are excited to Rydberg Stark states represent only a small fraction (~ 1 mm) of the total gas beam (~ 20 cm). The gas beam mostly consists of undecelerated ground state argon atoms with a kinetic energy of $\sim 600 \text{ cm}^{-1}$ and when the hydrogen atoms lose velocity, the collision probability increases. In a collision the total energy is large enough to ionize the Rydberg particle leading to a reduction in the number of atoms. The modeling of collisional losses would necessitate

elastic and inelastic cross sections for collisions between Rydberg Stark states and argon at low energies that are not available at present.

Although fluorescence decay alone suffices to explain the observed trap losses it would be desirable to devise experiments that enable one to distinguish between these different loss mechanisms, in particular between losses from collisions with the background gas and losses because of spontaneous emission to low-lying states.

8.5 Conclusions

The electrostatic trapping of hydrogen atoms in Rydberg Stark states in a two-dimensional trap has been shown for the first time and was studied in detail. After an initial nonexponential behaviour, the number of particles in the trap decays approximately exponentially as a function of time with a $1/e$ trapping time of $\sim 50 \mu\text{s}$. The electrostatic trap is versatile in the sense that Rydberg atoms in very different Stark states can be trapped by applying the same potentials to the electrodes of the trap.

The spatial dynamics of the cloud of atoms in the trap was studied by field ionizing the Rydberg atoms and detecting the subsequent ions. Oscillatory movements in both the z and y dimensions were observed. The oscillations have a period of $\sim 20 \mu\text{s}$, as expected from the calculations of the movement of individual particles in the trap.

The evolution of the distribution of quantum states of the Rydberg atoms in the trap, was studied using selective field ionization. The results of these measurements indicate that n -changing processes occur on the time scale of tens of μs but transitions to lower n values could not be observed because of the limited ionization field that could be applied. Moreover, the interpretation of the measurements was complicated by k -changing processes that seem to occur around the point in the trap where the electric field is zero.

The dominant loss mechanism within the trap is likely to be the decay of the excited Stark states to low-lying states by fluorescence. Nevertheless the trapping experiments described in this chapter show that it is possible to contain Rydberg particles within a small volume for long times, enabling longer interaction times between the Rydberg atoms and, for instance, millimeter-wave radiation, than in a standard molecular beam experiment.

Chapter 9

Outlook

9.1 High-resolution spectroscopic experiments on slow decelerated Rydberg atoms and molecules

The results presented in this thesis show that it is possible to change the velocity of atoms in Rydberg states continuously over a wide range. For instance, a cloud of hydrogen atoms excited to $n = 20$ Stark states, initially moving at a velocity of 700 m/s can be decelerated to zero velocity or accelerated to 1400 m/s using time-independent electric fields. The possibility to accelerate or decelerate the atoms to a wide range of velocities, with a narrow velocity distribution corresponding to a temperature $T < 1$ K, opens up the possibility to study the dependence of the line width of millimeter-wave (mmw) transitions between Rydberg states on the measurement time. Most importantly, at very low velocities the contribution to the line width because of the finite measurement time becomes negligible and the natural lifetime of the Rydberg Stark states becomes accessible.

The Doppler contribution to the line width in these measurements is independent of the final longitudinal velocity because the mmw radiation can be directed in the transversal dimension in which the electric field is homogeneous, the x dimension in this thesis. The velocity in this dimension remains constant during the deceleration/acceleration of the atoms in the longitudinal direction.

The measurement time can be extended even further when the mmw radiation is applied to atoms that are trapped in the electrostatic trap presented in chapter 8. In such an experiment, however, the effects of the electric fields on the transition energies, on the line widths, and on the line shapes need to be taken into account. Alternatively, the electrostatic trap can be switched off just before applying the mmw radiation. In this case, the atoms slowly drift out of the mmw excitation region but the measurement time can be long if the atoms are very cold and move only slowly.

A current important application of mmw spectroscopy of transitions between Rydberg states is the determination of the hyperfine structure of molecular cations from the hyperfine structure of the Rydberg states by extrapolation. In this way the first

measurements of the hyperfine structure of the $X^2\Sigma_g^+ v^+ = 0, N^+ = 1$ ground state of ortho H_2^+ has been carried out recently [89]. Hyperfine structure intervals in molecular ions and in high Rydberg states typically lie in the range 1 kHz to 1 MHz. In the latest measurements by mmw spectroscopy the transit-time-limited resolution of 200 kHz [89] sufficed to observe the main hyperfine intervals but was insufficient to resolve the structure originating from the coupling of the Rydberg electron spin with the core angular momentum. Improving the resolution beyond the current limit will necessitate an improvement of the measurement time to more than 10 μ s and ideally up to 1 ms. Only then will it be possible to observe the finest details of the energy level structure of electronically highly excited atoms and molecules. From such experiments one will not only obtain new spectroscopic information on molecular cations but also on the dynamics of the Rydberg states and on the photoionization dynamics, for instance, in the form of coupling constants for the interaction between channels associated with different orbital angular momenta (s-d and p-f interactions) or interactions between singlet and triplet channels. Such measurements are not only of fundamental interest in molecular physics, but are also of importance to understand and model basic astrophysical processes such as recombination or to provide the reference laboratory data to facilitate the searches of molecular species in space by radioastronomy.

Measuring mmw transitions between Rydberg states is also an alternative method to the usual Doppler-free two-photon $1^2S_{1/2} - 2^2S_{1/2}$ transition to measure the Rydberg constant. The Stark deceleration method presented here thus might be applied to slow down the fast antihydrogen atoms which are planned to be produced in Rydberg states with $n = 25$ to 45 at CERN for the first measurement of the Rydberg constant in antimatter. The measurement of a transition between Rydberg states of slowed down antihydrogen atoms circumvents the problem of having to bring the antihydrogen atoms down from the Rydberg states to the ground state to be able to perform the $1^2S_{1/2} - 2^2S_{1/2}$ laser spectroscopic experiment. However, it is questionable whether a measurement of a transition between Rydberg states would reach the desired accuracy to test fundamental physics.

Other spectroscopic experiments that can be performed on slowed down or trapped atoms and molecules are, for instance,

- Natural lifetime measurements. If the collection efficiency of the fluorescence photons can be improved then the lifetime of Rydberg states can be measured in a range extending beyond 50 μ s.
- n -changing processes such as collisions and black body radiation induced transitions can be studied on a very long time scale for a wide range of n values.
- The slow relaxation dynamics by predissociation, autoionization, or a sequence of radiative processes of a highly excited Rydberg atom or molecule can be studied at an unprecedented level of detail.

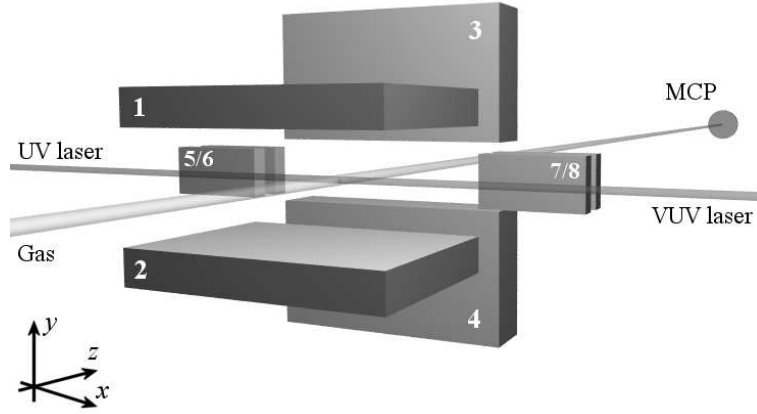


Figure 9.1: Three dimensional view of the trap with which the particles can be contained in all three dimensions. The electrodes 1, 2, 3, and 4 are at the same distance from each other as in the trap presented in chapter 8 and are 1.5 cm long in the x dimension. Electrodes 5, 6, 7, and 8 are each 1 mm wide in the z dimension and the distance between electrodes 5 and 6 (7 and 8) is 1 mm. Electrodes 5 and 6 and electrodes 7 and 8 are 1.5 cm apart in the x dimension. The UV and the VUV laser beams cross the trap approximately 1 mm away from the surface of electrodes 5 and 7.

9.2 Three-dimensional trapping of Rydberg atoms

The electrostatic trap described in chapter 8 traps the hydrogen atoms in two dimensions; the electric field is homogeneous in the third dimension so that the velocity of the particles in this dimension cannot be manipulated. By adding two sets of electrodes to the two-dimensional trap, the particles can also be contained in the third dimension as is shown in figure 9.1. With this setup the minimum of the electric field strength in the three dimensional trap can be either zero, $V_5 = V_6 = V_7 = V_8 = V_{\text{trap}}^{3D}$, or nonzero, $V_5 = V_6 = -V_7 = -V_8 = V_{\text{trap}}^{3D}$, and it is thus possible to study the loss mechanisms in the trap in more detail:

- The trap can either operate as a two-dimensional trap or as a three-dimensional trap and it is possible to measure on which timescale losses because the particles are only trapped in two dimensions play a role.
- In the three-dimensional trapping configuration the minimum can either be set to zero or to a nonzero value, so that one can study the role of the zero electric field point in the loss processes and in the ion TOF profiles in more detail than was possible in the experiments described in chapter 8.
- Furthermore, the decay of the number of particles in the three-dimensional trap can be studied as a function of time at different n values to study the role of spontaneous emission and black body radiation induced transitions. These two processes depend differently on n and thus from the dependence of the trapping time on n it can be determined which process dominates at which n .

9.3 Deceleration and trapping of molecules in Rydberg Stark states

Using time-dependent electric fields, atoms and molecules with mass $m = 14$ u or smaller can be decelerated to zero velocity when they are initially seeded in a supersonic beam of xenon. Therefore molecules such as, for instance, H_2 , D_2 , H_3 , HeH , He_2 , BH , BeH , BH_3 , CH , CH_2 and possibly CH_4 , CH_3 , NH , NH_2 , NH_3 , and OH can be decelerated to zero velocity and subsequently trapped using the techniques described in chapters 6 and 8. In such experiments it will be imperative to study the avoided crossings between Rydberg Stark states which converge on different rovibrational energy levels of the ion because the rotational splitting between such levels can be much smaller than the zero-field splittings between the high- ℓ manifolds of the Rydberg states that are used in the deceleration experiments.

H_2 offers the following advantages when extending the deceleration method to molecules:

- A small but significant deceleration has already been measured for H_2 [95, 130].
- The mass of H_2 is small so that the initial kinetic energy of H_2 seeded in xenon ($E_{\text{kin}}/hc = 9 \text{ cm}^{-1}$) or argon ($E_{\text{kin}}/hc = 29 \text{ cm}^{-1}$) is much smaller than the maximal kinetic energy change that has been obtained for argon ($\Delta E_{\text{kin}}/hc = 60 \text{ cm}^{-1}$).
- From the experimental results in references [88] and [89] it is known that many Rydberg states are long lived.
- The rotational constant of the H_2^+ ion is larger than the zero-field splittings between the Rydberg states that are used in the deceleration experiments so that in specific energetic regions the energy level structure of the Rydberg Stark states is not heavily perturbed by the rotational energy level structure of the ion.

In figure 9.2 the result of a preliminary deceleration experiment on H_2 is displayed that was carried out using the time-dependent field and the wedge-shaped decelerator described in chapter 4. The kinetic energy difference between the red-shifted $n = 26$ Stark state (dashed line) and the blue-shifted $n = 25$ Stark state (solid line), both belonging to a series converging on the $\text{X}^+ \text{}^2\Sigma_g^+ v^+ = 0, N^+ = 1$ ground state of ortho H_2^+ , amounts to 8.3 cm^{-1} which corresponds to 85% of the combined Stark shift of the two states. Given that the wedge-shaped deceleration device is far less efficient than the quadrupolar deceleration device, these preliminary results are encouraging and show that trapping Rydberg molecules will be possible.

Autoionization of the molecules can be avoided by exciting Rydberg Stark states lying energetically below the lowest ionization threshold. The importance of predissociation can be reduced significantly by exciting an $|m| > 2$ state in a multi-photon

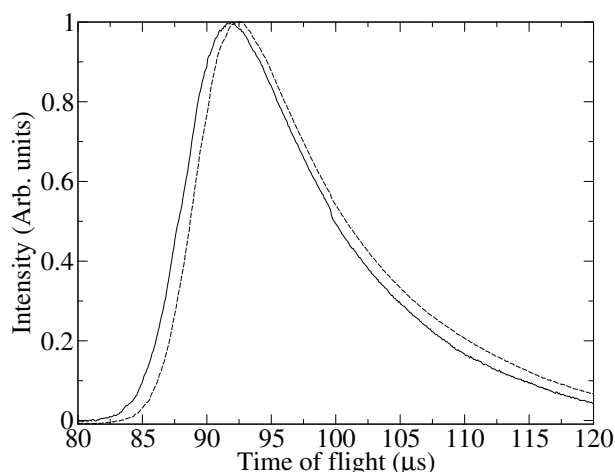


Figure 9.2: Results of deceleration/acceleration experiments on H_2 . The solid line is the TOF trace of a blue-shifted $n = 25$ Stark state and the dashed line is the TOF trace of a red-shifted $n = 26$ state. Both states belong to a series converging on the $X^+ \ ^2\Sigma_g^+ \ v^+ = 0, N^+ = 1$ ground state of ortho H_2^+ .

excitation process, see also chapter 2. By using such high- $|m|$ states, limitations arising because of the adiabatic traversal of avoided crossings between different Stark states (see chapter 4) might also be overcome, so that the maximum electric field strength that can be applied in the deceleration experiments may be increased from the Inglis-Teller limit to the ionization limit and molecules with a much larger mass can be stopped and trapped.

Appendix A

Units and Constant

Constants

Table A.1: List of frequently used constants [84]

Quantity	Symbol	Value	Unit
Speed of light	c	299 792 458	m/s
Electric field constant	ϵ_0	$8.854\,187\,817 \dots \times 10^{-12}$	A s/(V m)
Planck constant	h	$6.626\,069\,3(11) \times 10^{-34}$	J s
	$\hbar = \frac{h}{2\pi}$	$1.054\,571\,68(18) \times 10^{-34}$	J s
Elementry charge	e	$1.602\,176\,53(14) \times 10^{-19}$	C
Rydberg constant	$R_\infty = \frac{\alpha^2 m_e c}{2h}$	109 737.315 685 25(73)	cm ⁻¹
Bohr radius	$a_0 = \frac{4\pi\epsilon_0\hbar^2}{m_e e^2}$	$0.529\,177\,210\,8(18) \times 10^{-10}$	m
Mass of the electron	m_e	$9.109\,382\,6(16) \times 10^{-31}$	kg
Constant of Avagadro	N_A	$6.022\,141\,5(10) \times 10^{23}$	mol ⁻¹
Boltzmann constant	k	$1.380\,650\,5(24) \times 10^{-23}$	J/K

Atomic units

Table A.2: List of atomic units [84]

Quantity	Symbol	Value	Unit
Electric charge	e	$1.602\,176\,53(14) \times 10^{-19}$	C
Mass	m_e	$9.109\,382\,6(16) \times 10^{-31}$	kg
Action	\hbar	$1.054\,571\,68(18) \times 10^{-34}$	J/s
Length	a_0	$0.529\,177\,210\,8(18) \times 10^{-10}$	m
Energy	E_h	$4.359\,744\,17(75) \times 10^{-18}$	J
Time	$\frac{\hbar}{E_h}$	$2.418\,884\,326\,505(16) \times 10^{-17}$	s
Force	$\frac{E_h}{a_0}$	$8.238\,722\,5(14) \times 10^{-8}$	N
Velocity	$\frac{a_0 E_h}{\hbar}$	$2.187\,691\,263\,3(73) \times 10^6$	m/s
Electric potential	$\frac{E_h}{e}$	27.211 384 5(23)	V
Electric field	$\frac{E_h}{a_0 e}$	$5.142\,206\,42(44) \times 10^{11}$	V/m

In this unit system

$$\begin{aligned}
 \hbar &= 1 \\
 e &= 1 \\
 c &= 137.036 = \frac{1}{\alpha} \\
 \epsilon_0 &= \frac{1}{4\pi} \\
 R_\infty &= \frac{1}{2}
 \end{aligned}$$

Energy equivalents

Table A.3: List of energy equivalents [84]

	$\frac{E}{hc} / \text{cm}^{-1}$	$\frac{E}{h} / \text{GHz}$
$E = 1 \text{ J}$	$5.034\,117\,20(86) \times 10^{22}$	$1.509\,190\,37(26) \times 10^{24}$
$\frac{E}{hc} = 1 \text{ cm}^{-1}$	1	29.979 245 8
$\frac{E}{h} = 1 \text{ GHz}$	0.033 356 409 ...	1
$E = 1 \text{ eV}$	8 065.544 45(69)	$2.417\,989\,40(21) \times 10^5$
$E = 1 E_h$	$2.194\,746\,313\,705(15) \times 10^5$	$6.579\,683\,920\,721(44) \times 10^6$

Appendix B

s-d and p-p interaction elements for argon

Odd parity channels

	d ³ D ₁	d ¹ P ₁	d ³ P ₁	s ³ P ₁	s ¹ P ₁
d ³ D ₁	1	0.009	0	0	0.006
d ¹ P ₁	-0.009	0.999	-0.041	0	-0.001
d ³ P ₁	0	0.041	1	0	0.027
s ³ P ₁	0	0	0	1	-0.001
s ¹ P ₁	-0.006	0	-0.027	0	1

	d ³ P ₂	d ³ F ₂	d ¹ D ₂	d ³ D ₂	s ³ P ₂
d ³ P ₂	0.9927	0.05558	0.0369	-0.0037	-0.1006
d ³ F ₂	-0.0556	0.9962	0.0021	-0.0668	0.0056
d ¹ D ₂	0.0368	0	0.9993	0	-0.0037
d ³ D ₂	0	0.0669	0	0.9978	0
s ³ P ₂	0.1008	0	0	0	0.9949

	d ¹ F ₃	d ³ F ₃	d ³ D ₃
d ¹ F ₃	0.9975	0.0033	0.0709
d ³ F ₃	0	0.9989	-0.0470
d ³ D ₃	-0.0709	0.04686	0.9964

Even parity channels

	p^3S_1	p^1P_1	p^3P_1	p^3D_1
p^3S_1	1	0.0030	0	0.0026
p^1P_1	-0.0027	1	0.0102	0
p^3P_1	0	-0.0103	1	-0.006
p^3D_1	0.0023	0	0.00679	1

	p^3P_2	p^1D_2	p^3D_2
p^3P_2	0.9985	-0.0600	0
p^1D_2	0.0604	0.9982	0
p^3D_2	0	0	1

List of Figures

2.1	Charge density distributions for all $n = 8$, $m = 0$ Stark states.	10
2.2	Calculated Stark map of the $m = 0$ Stark states of the hydrogen atom with $n = 8$ to 14.	11
2.3	$ m = 1$ Stark map of Na around $n = 15$	12
2.4	Schematic view of an (avoided) crossing in a two-level system.	13
2.5	Potential energy $\tilde{V}(z)$ felt by a Rydberg electron along the z axis for different electric field strengths.	15
2.6	Two possible electrode configurations to decelerate Rydberg particles. .	21
2.7	Phase-space plot of a cold ($T = 1$ K) cloud of argon atoms moving with a constant mean velocity of 600 m/s.	23
3.1	Schematic overview of VUV generation using four-wave mixing.	25
3.2	Experimental setup used in the experiments on argon.	27
3.3	Experimental setup used in the experiments on atomic hydrogen.	28
3.4	Schematic drawing of the electronic circuit used to apply potentials to the MCP detector.	31
3.5	TOF spectrum recorded after exciting argon atoms to a 24d state in zero electric field.	33
3.6	TOF spectra of molecular hydrogen and argon excited to Rydberg states. .	34
3.7	Images on the MCP detector of a cloud of Rydberg argon atoms.	35
3.8	Magnified view of the images obtained at the MCP detector for particles arriving after different times of flight.	36
4.1	Schematic overview of the electrode setup and time dependence of the potential applied to the electrodes.	40
4.2	Stark map of the $M_J = 0$ Rydberg states of argon in the region around $n = 22$	42
4.3	Stark map and TOF spectra recorded near an avoided crossing in argon. .	45
4.4	Stark map and deceleration results around $n = 24$ and $n = 25$	47
4.5	Measured VUV fluorescence signal recorded after exciting several Rydberg states in argon.	49
4.6	Measurement of the decay of a red-shifted $n = 25$ Stark state of argon and SFI measurements after exciting a red-shifted $n = 30$ Stark state. . .	51

4.7	Effective potentials $V(\eta)$ and $U(\xi)$ as a function of the electron-core separation.	54
4.8	Measured Stark map of the $M_J = 0$ Rydberg states of argon in the region around $n = 22$	58
4.9	Calculated Stark map of the $M_J = 0$ Rydberg states of argon in the region around $n = 22$	59
4.10	Detailed view of the dependence of the energetic position of the $24p[1/2]_0$ state of argon as a function of the electric field.	61
4.11	Detailed view of the $n = 22$, $k = -9$, $k = -11$, and $k = -13$ Stark states of argon in an electric field of 340 V/cm.	62
5.1	Schematic view of the experimental arrangement used in the experiments on atomic hydrogen.	69
5.2	Spectrum of the $1\ ^2S_{1/2} - 2\ ^2P$ resonance of hydrogen and spectrum of the $n = 39$ to 52 Rydberg states in zero electric field.	71
5.3	Four scans around the zero field position of the $n = 22$ state of hydrogen in a field of 333 V/cm for different polarizations of the VUV and UV laser.	73
5.4	Deceleration results for hydrogen after excitation in homogeneous electric fields.	74
5.5	Deceleration results for hydrogen after excitation in inhomogeneous electric fields.	76
6.1	Schematic overview of the electrode setup and potentials used in the experiments with time-dependent electric fields.	82
6.2	Electric field strengths along the z and the y axes for different sets of potentials applied to the electrodes.	83
6.3	Calculated values of the optimal $V_3 = -V_4$ value for decelerating argon with $n = 22$ and $V_1 = -V_2 = 150$ V.	84
6.4	Stark spectra of the $n = 22$, $M_J = 1$ argon Rydberg states.	86
6.5	Deceleration results for argon for different n values in time-dependent and time-independent electric fields.	87
6.6	TOF spectra corresponding to experiments carried out on argon using optimized time-dependent fields for Stark states around $n^* = 18.5$	89
6.7	Stark spectra of argon in the range $n^* = 18$ to 19 recorded by integrating the intensity over different time windows.	91
6.8	TOF spectra of argon atoms in Stark states with $n = 17$ and $n = 18$	92
6.9	CCD-camera images of the argon beam obtained after exciting several Stark states with $n = 17$ and $n = 18$	93
6.10	Line profiles in the x and y dimensions taken from the CCD-camera images.	93
6.11	Valve and skimmer geometry to estimate the maximum transverse velocity in the absence of beam-skimmer interactions.	94

6.12	CCD-camera images of the Rydberg atom cloud showing focussing. . . .	95
7.1	Atom mirror voltage pulse sequence and voltage configurations.	101
7.2	Ion TOF traces recorded in the mirror experiment.	103
7.3	Ion TOF traces recorded in the mirror experiment after switching the mirror off after $4.8 \mu\text{s}$	104
7.4	Calculations of the phase-space distributions of the atomic cloud in the mirror experiment.	105
7.5	CCD-camera images of the ions after field ionizing the hydrogen Rydberg atoms in the mirror.	106
8.1	Atom trap voltage pulse sequence and voltage configurations.	111
8.2	Three-dimensional view of the Rydberg atom trap.	112
8.3	Sequence of ion TOF profiles after trapping the hydrogen atoms for a variable delay.	114
8.4	Dependence of the ion TOF profiles on the trapping potential.	115
8.5	Calculated phase-space distributions of the hydrogen atom cloud in the trap.	116
8.6	Spectra of the trapping efficiency over the first $50 \mu\text{s}$ for $n = 20$ to 40 . .	117
8.7	Sequence of ion TOF profiles in the trapping experiment for different deceleration potentials.	118
8.8	Simulated ion TOF traces as a function of t_{ion} for different y offsets of the atom beam.	120
8.9	Ion TOF profiles for a cloud of undecelerated hydrogen atoms excited to a blue-shifted $n = 27$ Stark state in the trapping configuration.	121
8.10	Electric field strength along the z axis during ionization and results of SFI experiments for different n states.	122
8.11	Ion TOF profiles measured for hydrogen atom excited to a red-shifted $n = 27$ Stark state in the trap on and trap off potential configurations. .	123
8.12	Results of SFI measurements of trapped hydrogen atoms as a function of t_{ion}	125
9.1	Three-dimensional view of the trap with which the particles can be con- tained in all three dimensions	131
9.2	Results of deceleration/acceleration experiments on H_2	133

List of Tables

4.1	Measured fluorescence lifetimes of Rydberg states in argon.	48
4.2	List of the quantum defects for the <i>LS</i> -coupled channels used in the MQDT calculation.	57
5.1	Summary of acceleration/deceleration experiments on H atoms in time-independent inhomogeneous electric fields.	78
6.1	Summary of deceleration/acceleration experiments on argon in time-independent electric fields.	88
6.2	Summary of deceleration/acceleration experiments on argon in time-dependent electric fields using a decay constant of $2.1 \mu\text{s}$	89
6.3	Characterization of the optimal deceleration/acceleration behaviour for argon at selected n^* values.	90
6.4	Parameters used in the particle trajectory simulations.	96
A.1	List of frequently used constants [84]	135
A.2	List of atomic units [84]	136
A.3	List of energy equivalents [84]	136

Bibliography

- [1] M. Amoretti et al. (ATHENA collaboration), Production and detection of cold antihydrogen atoms, *Nature* **419**(6906), 456 (2002).
- [2] M. H. Anderson, J. R. Ensher, M. R. Matthews, C. E. Wieman, and E. A. Cornell, Observation of Bose-Einstein Condensation in a Dilute Atomic Vapor, *Science* **269**(5521), 198 (1995).
- [3] M. Andrews, C. G. Townsend, H. J. Miesner, D. S. Durfee, D. M. Kurn, and W. Ketterle, Observation of interference between two Bose condensates, *Science* **275**(5300), 637 (1997).
- [4] A. Bach, J. M. Hutchison, R. J. Holiday, and F. F. Crim, Competition between Adiabatic and Nonadiabatic Pathways in the Photodissociation of Vibrationally Excited Ammonia, *J. Phys. Chem. A* **107**(49), 10490 (2003).
- [5] N. Balakrishnan, On the role of van der Waals interaction in chemical reactions at low temperatures, *J. Chem. Phys.* **121**(12), 5563 (2004).
- [6] N. Balakrishnan and A. Dalgarno, Chemistry at ultracold temperature, *Chem. Phys. Lett.* **341**(5-6), 652 (2001).
- [7] J. J. Balmer, Notiz über die Spectrallinien des Wasserstoffs, *Ann. der Phys. und Chem.* **261**(5), 80 (1885).
- [8] V. I. Balykin, V. S. Letokhov, Yu. B. Ovchinnikov, and A. I. Sidorov, Quantum-State-Selective Mirror Reflection of Atoms by Laser Light, *Phys. Rev. Lett.* **60**(21), 2137 (1988).
- [9] L. Y. Baranov, A. Held, H. L. Selze, and E. W. Schlag, Long lived Rydberg ZEKE states using fast programmed electric pulses. I. The basic method, *Chem. Phys. Lett.* **291**(3-4), 311 (1998).
- [10] R. Berger, G. Laubender, M. Quack, A. Sieben, J. Stohner, and M. Willeke, Isotopic chirality and molecular parity violation, *Angew. chem. int. ed.* **44**(23), 3623 (2005).
- [11] H. A. Bethe and E. E. Salpeter, *Quantum Mechanics of One- and Two-Electron Atoms*, Springer, Berlin, 1957.

- [12] H. L. Bethlem, G. Berden, and G. Meijer, Decelerating Neutral Dipolar Molecules, *Phys. Rev. Lett.* **83**(8), 1558 (1999).
- [13] H. L. Bethlem, F. M. H. Crompvoets, R. T. Jongma, S. Y. T. van de Meerakker, and G. Meijer, Deceleration and trapping of ammonia using time-varying electric fields, *Phys. Rev. A* **65**(5), 053416 (2002).
- [14] H. L. Bethlem and G. Meijer, Production and application of translationally cold molecules, *Int. Rev. Phys. Chem.* **22**(1), 73 (2003).
- [15] H. L. Bethlem, G. Berden, F. M. H. Crompvoets, R. T. Jongma, A. J. A. van Roij, and G. Meijer, Electrostatic trapping of ammonia molecules, *Nature* **406**, 491 (2000).
- [16] I. Bloch, T. W. Hänsch, and T. Esslinger, Atom Laser with a cw Output Coupler, *Phys. Rev. Lett.* **82**(15), 3008 (1999).
- [17] J. R. Bochinski, E. R. Hudson, H. J. Lewandowski, G. Meijer, and J. Ye, Phase Space Manipulation of Cold Free Radical OH Molecules, *Phys. Rev. Lett.* **91**(24), 243001 (2003).
- [18] J. Bömmels, J. M. Weber, A. Gopalan, N. Herschbach, E. Leber, A. Schramm, K. Ueda, M.-W. Ruf, and H. Hotop, Odd Rydberg spectrum of $^{40}\text{Ar}(\text{I})$: High-resolution laser spectroscopy and MQDT analyses of the $nd, J=4$ levels and the $ng', J=4$ resonances, *J. Phys. B: At. Mol. Opt. Phys.* **32**(10), 2399 (1999).
- [19] T. Bourdel, L. Khaykovich, J. Cubizolles, J. Zhang, F. Chevy, M. Teichmann, L. Tarruell, S. J. J. M. F. Kokkelmans, and C. Salomon, Experimental Study of the BEC-BCS Crossover Region in Lithium 6, *Phys. Rev. Lett.* **93**(5), 050401 (2004).
- [20] C. C. Bradley, C. A. Sackett, J. J. Tollett, and R. G. Hulet, Evidence of Bose-Einstein Condensation in an Atomic Gas with Attractive Interactions, *Phys. Rev. Lett.* **75**(9), 1687 (1995).
- [21] T. Breeden and H. Metcalf, Stark Acceleration of Rydberg Atoms in Inhomogeneous Electric Fields, *Phys. Rev. Lett.* **47**(24), 1726 (1981).
- [22] P. F. Brevet, M. Pellarin, and J. L. Vialle, Stark effect in argon Rydberg states, *Phys. Rev. A* **42**(3), 1460 (1990).
- [23] J. H. Choi, J. R. Guest, A. P. Povilus, E. Hansis, and G. Raithel, Magnetic Trapping of Long-Lived Cold Rydberg Atoms, *Phys. Rev. Lett.* **95**(24), 243001 (2005).
- [24] S. Chu, J. E. Bjorkholm, A. Ashkin, and A. Cable, Experimental Observation of Optically Trapped Atoms, *Phys. Rev. Lett.* **57**(3), 314 (1986).

- [25] S. Chu, L. Hollberg, J. E. Bjorkholm, A. Cable, and A. Ashkin, Three-dimensional viscous confinement and cooling of atoms by resonance radiation pressure, *Phys. Rev. Lett.* **55**(1), 48 (1985).
- [26] W. A. Chupka, Factors affecting lifetimes and resolution of Rydberg states observed in zero-electron-kinetic-energy spectroscopy, *J. Chem. Phys.* **98**(6), 4520 (1993).
- [27] F. M. H. Crompvoets, H. L. Bethlem, R. T. Jongma, and G. Meijer, A prototype storage ring for neutral molecules, *Nature* **411**(6834), 174 (2001).
- [28] K. B. Davis, M. O. Mewes, M. R. Andrews, N. J. van Druten, D. S. Durfee, D. M. Kurn, and W. Ketterle, Bose-Einstein Condensation in a Gas of Sodium Atoms, *Phys. Rev. Lett.* **75**(22), 3969 (1995).
- [29] C. Delsart, L. Cabaret, C. Blondel, and R.-J. Champeau, Two-step high-resolution laser spectroscopy of the Stark substates of the $n = 33$ level in atomic-hydrogen, *J. Phys. B: At. Mol. Opt. Phys.* **20**(18), 4699 (1987).
- [30] M. D. Di Rosa, Laser-cooling molecules - Concept, candidates, and supporting hyperfine-resolved measurements of rotational lines in the A-X(0,0) band of CaH, *Eur. Phys. J. D* **31**(2), 395 (2004).
- [31] J. Doyle, B. Friedrich, R. V. Krems, and F. Masnou-Seeuws, Quo vadis, cold molecules?, *Eur. Phys. J. D* **31**(2), 149 (2004).
- [32] F. B. Dunning and R. F. Stebbings, *Rydberg states of atoms and molecules*, Cambridge University Press, Cambridge, 1983.
- [33] D. Egorov, W. C. Campbell, B. Friedrich, S. Maxwell, E. Tsikata, L. D. van Buuren, and J. M. Doyle, Buffer-gas cooling of NH via the beam loaded buffer-gas method, *Eur. Phys. J. D* **31**(2), 307 (2004).
- [34] M. S. Elioﬀ, J. J. Valentini, and D. W. Chandler, Subkelvin Cooling NO Molecules via "Billiard-like" Collisions with Argon, *Science* **302**(5652), 1940 (2003).
- [35] W. E. Ernst, T. P. Softley, and R. N. Zare, Stark-effect studies in xenon autoionizing Rydberg states using a tunable extreme-ultraviolet laser source, *Phys. Rev. A* **37**(11), 4172 (1988).
- [36] U. Fano, Stark effect of nonhydrogenic Rydberg spectra, *Phys. Rev. A* **24**(1), 619 (1981).
- [37] H. H. Fielding and T. P. Softley, Observation of the Stark effect in autoionizing Rydberg states of Ar with a multichannel quantum-defect analysis, *J. Phys. B: At. Mol. Opt. Phys.* **25**(20), 4125 (1992).

- [38] H. H. Fielding and T. P. Softley, Multichannel-quantum-defect-theory analysis of the Stark effect in autoionizing Rydberg states of H_2 , *Phys. Rev. A* **49**(2), 969 (1994).
- [39] A. Fioretti, J. Lozielle, C. A. Massa, M. Mazzoni, and C. Gabbanini, An optical trap for cold rubidium molecules, *Opt. Comm.* **243**(1-6), 203 (2004).
- [40] D. G. Fried, T. C. Killian, L. Willmann, D. Landhuis, S. C. Moss, D. Kleppner, and T. J. Greytak, Bose-Einstein Condensation of Atomic Hydrogen, *Phys. Rev. Lett.* **81**(18), 3811 (1998).
- [41] R. Fulton, A. I. Bishop, and P. F. Barker, Optical Stark Decelerator for Molecules, *Phys. Rev. Lett.* **93**(24), 243004 (2004).
- [42] R. Fulton, A. I. Bishop, and P. F. Barker, Focussing ground-state xenon in a pulsed optical field, *Phys. Rev. A* **71**(4), 043404 (2005).
- [43] G. Gabrielse et al. (ATRAP collaboration), Background-free observation of cold antihydrogen with field-ionization analysis of its states, *Phys. Rev. Lett.* **89**(21), 213401 (2002).
- [44] T. F. Gallagher, *Rydberg Atoms*, Cambridge University Press, Cambridge, 1994.
- [45] G. M. Gallatin and P. L. Gould, Laser focusing of atomic beams, *J. Opt. Soc. Am. B* **8**(3), 502 (1991).
- [46] E. J. Galvez, C. W. MacGregor, B. Chaudhuri, S. Gupta, E. Massoni, and F. De Zela, Blackbody-radiation-induced resonances between Rydberg-Stark states of Na, *Phys. Rev. A* **55**(4), 3002 (1997).
- [47] W. R. Gentry, *Atomic and Molecular Beam Methods*, Ed. by G. Scoles, Oxford University Press, Oxford, 1988.
- [48] W. Gerlach and O. Stern, The experimental proof of magnetic moment of silver atoms, *Z. Phys.* **8**, 110 (1921).
- [49] A. L. Goodgame and T. P. Softley, Control of atomic and molecular motion via the Stark effect in Rydberg states, *J. Phys. B: At. Mol. Opt. Phys.* **32**(10), 4839 (1999).
- [50] M. Gottselig, M. Quack, J. Stohner, and M. Willeke, Mode-selective stereomutation tunneling and parity violation in $HOClH^+$ and H_2Te_2 isotopomers, *Int. J. Mass. Spec.* **233**(1-3), 373 (2004).
- [51] M. Greiner, O. Mandel, T. Esslinger, T. W. Hänsch, and I. Bloch, Quantum phase transition from a superfluid to a Mott insulator in a gas of ultracold atoms, *Nature* **415**(6867), 39 (2002).

- [52] M. Greiner, I. Bloch, O. Mandel, T. W. Hänsch, and T. Esslinger, Exploring Phase Coherence in a 2D Lattice of Bose-Einstein Condensates, *Phys. Rev. Lett.* **87**(16), 160405 (2001).
- [53] M. Greiner, C. A. Regall, and D. S. Jin, Emergence of a molecular Bose-Einstein condensate from a Fermi gas, *Nature* **426**(6966), 537 (2003).
- [54] M. Grütter, O. Zehnder, T. P. Softley, and F. Merkt, unpublished results.
- [55] M. Gupta and D. Herschbach, A mechanical means to produce intense beams of slow molecules, *J. Phys. Chem. A* **103**(9), 10670 (1999).
- [56] M. Gupta and D. Herschbach, Slowing and speeding molecular beams by means of a rapidly rotating source, *J. Phys. Chem. A* **105**(50), 1626 (2001).
- [57] D. A. Harmin, Theory of the Stark effect, *Phys. Rev. A* **26**(5), 2656 (1982).
- [58] D. A. Harmin, Analytical study of quasidiscrete Stark levels in Rydberg atoms, *Phys. Rev. A* **30**(5), 2413 (1984).
- [59] A. Held, L. Y. Baranov, H. L. Selzle, and E. W. Schlag, Lifetime control in Rydberg states using fast switching DC electric field II. Enhancement for nitric oxide, *Chem. Phys. Lett.* **291**(3-4), 318 (1998).
- [60] R. Hilbig and R. Wallenstein, Enhanced Production of Tunable VUV Radiation by Phase-Matched Frequency Tripling in Krypton and Xenon, *IEEE J. Quantum Electr.* **17**(8), 1566 (1981).
- [61] R. Hilbig and R. Wallenstein, Resonant sum- and difference-frequency mixing in Hg, *IEEE J. Quantum Electr.* **19**(12), 1759 (1983).
- [62] U. Hollenstein, *Erzeugung und spektroskopische Anwendungen von schmalbandiger, kohärenter, vakuum-ultravioletter Strahlung*, PhD thesis, Eidgenössische Technische Hochschule Zürich, 2003, Diss. ETH Nr. 15237.
- [63] U. Hollenstein, H. Palm, and F. Merkt, A broadly tunable extreme ultraviolet laser source with a 0.008 cm^{-1} bandwidth, *Rev. Sci. Instr.* **71**(11), 4023 (2000).
- [64] E. R. Hudson, C. Ticknor, B. C. Sawyer, C. A. Taatjes, H. J. Lewandowski, J. R. Bochinski, J. L. Bohn, and J. Ye, Production of cold formaldehyde molecules for study and control of chemical reaction dynamics with hydroxyl radicals, *Phys. Rev. A* **73**(6), 063404 (2006).
- [65] J. J. Hudson, B. Sauer, M. R. Tarbutt, and E. A. Hinds, Measurement of the electron electric dipole moment using YbF molecules, *Phys. Rev. Lett.* **89**(2), 023003 (2002).

- [66] D. R. Inglis and E. Teller, Ionic depression of series limits in one-electron spectra, *Astrophys. J.* **90**, 439 (1939).
- [67] T. H. Jeys, G. W. Foltz, A. Smith, E. J. Beiting, F. G. Kellert, F. B. Dunning, and R. F. Stebbibgs, Diabatic Field Ionization of Highly Excited Sodium Atoms, *Phys. Rev. Lett.* **44**(6), 390 (1980).
- [68] S. Jochim, M. Bartenstein, A. Altmeyer, G. Hendl, S. Riedl, C. Chin, J. H. Denschlag, and R. Grimm, Bose-Einstein Condensation of Molecules, *Science* **302**(5653), 2101 (2003).
- [69] K. S. Johnson, M. Drndic, J. H. Thywissen, G. Zabow, R. M. Westervelt, and M. Prentiss, Atomic Deflection Using an Adaptive Microelectromagnet Mirror, *Phys. Rev. Lett.* **81**(6), 1137 (1998).
- [70] R. T. Jongma, T. Rasing, and G. Meijer, Two-dimensional imaging of metastable CO molecules, *J. Chem. Phys.* **102**(5), 1925 (1994).
- [71] T. Junglen, T. Rieger, S. A. Rangwala, P. W. H. Pinkse, and G. Rempe, Slow ammonia molecules in an electrostatic quadrupole guide, *Eur. Phys. J. D* **31**(2), 365 (2004).
- [72] M. A. Kasevich, D. S. Weiss, and S. Chu, Normal-incidence reflection of slow atoms from an optical evanescent wave, *Optics Letters* **15**(11), 607 (1990).
- [73] R. V. Krems, Controlling collisions of ultracold atoms with dc electric fields, *Phys. Rev. Lett.* **96**(12), 123202 (2006).
- [74] L. D. Landau, Zur Theorie der Energieübertragung II, *Phys. Z. Sowjetunion* **2**, 46 (1932).
- [75] L. D. Landau and E. M. Lifschitz, *Quantum Mechanics (Non Relativistic Theory)*, Pergamon, Oxford, 1976.
- [76] C.-M. Lee and K. T. Lu, Spectroscopy and Collision Theory. II. The Ar Absorption Spectrum, *Phys. Rev. A* **8**(3), 1241 (1973).
- [77] P. D. Lett, R. N. Watts, C. I. Westbrook, W. D. Phillips, P. L. Gould, and H. J. Metcalf, Observation of Atoms Laser Cooled below the Doppler Limit, *Phys. Rev. Lett.* **61**(2), 169 (1988).
- [78] K. W. Madison, F. Chevy, W. Wohlleben, and J. Dalibard, Vortex Formation in a Stirred Bose-Einstein Condensate, *Phys. Rev. Lett.* **84**(5), 806 (2000).
- [79] F. Merkt, Collisional and electric field effects in the delayed pulsed field ionization zero-kinetic-energy photoelectron spectrum of argon, *J. Chem. Phys.* **100**(4), 2623 (1994).

- [80] F. Merkt, Molecules in high Rydberg states, *Ann. Rev. Phys. Chem.* **48**, 675 (1997).
- [81] A. L. Migdall, J. V. Prodan, W. D. Phillips, T. H. Bergeman, and H. J. Metcalf, First Observation of Magnetically Trapped Neutral Atoms, *Phys. Rev. Lett.* **54**(24), 2596 (1985).
- [82] J. D. Miller, R. A. Cline, and D. J. Heinzen, Far-off-resonance optical trapping of atoms, *Phys. Rev. A* **47**(6), R4567 (1993).
- [83] L. Minnhagen, Spectrum and the energy levels of neutral argon, *J. Opt. Soc. Am.* **63**(10), 1185 (1973).
- [84] P. J. Mohr and B. N. Taylor, CODATA recommended values of the fundamental physical constants: 2002, *Rev. Mod. Phys.* **77**(1), 1 (2005).
- [85] J. Oberheide, M. Wilhelms, and M. Zimmer, New results on the absolute ion detection efficiencies of a microchannel plate, *Mass. Sci. Techn.* **8**(4), 351 (1997).
- [86] G. I. Opat, S. J. Wark, and A. Cimmino, Electric and Magnetic Mirrors and Gratings for Slowly Moving Neutral Atoms and Molecules, *Appl. Phys. B* **54**(5), 396 (1992).
- [87] A. Osterwalder and F. Merkt, Using High Rydberg States as Electric Field Sensors, *Phys. Rev. Lett.* **82**(9), 1831 (1999).
- [88] A. Osterwalder, R. Seiler, and F. Merkt, Measurement of the hyperfine structure in low- l , high- n Rydberg states of ortho H_2 by millimeter wave spectroscopy, *J. Chem. Phys.* **113**(18), 7939 (2000).
- [89] A. Osterwalder, A. Wüest, F. Merkt, and Ch. Jungen, High-resolution millimeter wave spectroscopy and multichannel quantum defect theory of the hyperfine structure in high Rydberg states of molecular hydrogen H_2 , *J. Chem. Phys.* **121**(23), 11810 (2004).
- [90] H. Palm and F. Merkt, Ion Density Effects in the Pulsed Field Ionization of High Rydberg States, *Chem. Phys. Lett.* **270**(1-2), 1 (1997).
- [91] T. A. Paul and F. Merkt, High-resolution spectroscopy of xenon using a tunable Fourier-transform-limited all-solid-state vacuum-ultraviolet laser system, *J. Phys. B: At. Mol. Phys.* **38**(22), 4145 (2005).
- [92] B. L. Peko and T. M. Stephen, Absolute detection efficiencies of low energy H , H^- , H^+ , H_2^+ and H_3^+ incident on a multichannel plate detector, *Nucl. Inst. Meth. in Phys. Res. B* **171**(4), 597 (2000).

- [93] M. Pellarin, J. L. Viale, M. Carré, J. Lermé, and M. Aymar, Even parity series of argon Rydberg states studied by fast-beam collinear laser spectroscopy, *J. Phys. B: At. Mol. Opt. Phys.* **21**(23), 3833 (1988).
- [94] N. K. Piracha, M. A. Baig, S. H. Khan, and B. Suleman, Two-photon optogalvanic spectra of argon: Odd parity Rydberg states, *J. Phys. B: At. Mol. Opt. Phys.* **30**(5), 1151 (1997).
- [95] S. R. Procter, Y. Yamakita, F. Merkt, and T. P. Softley, Controlling the motion of hydrogen molecules, *Chem. Phys. Lett.* **374**(5-6), 667 (2003).
- [96] M. Quack, On the measurement of the parity violating energy difference between enantiomers, *Chem. Phys. Lett.* **132**(2), 147 (1986).
- [97] M. Quack, Structure and dynamics of chiral molecules, *Angew. chem. int. ed.* **28**(5), 571 (1989).
- [98] E. L. Raab, M. Prentiss, A. Cable, S. Chu, and D. E. Pritchard, Trapping of Neutral Sodium Atoms with Radiation Pressure, *Phys. Rev. Lett.* **59**(23), 2631 (1987).
- [99] S. A. Rangwala, T. Junglen, T. Rieger, P. W. H. Pinkse, and G. Rempe, Continuous source of translationally cold dipolar molecules, *Phys. Rev. A* **67**(4), 043406 (2003).
- [100] G. Reiser, W. Habenicht, K. Müller-Dethlefs, and E. W. Schlag, The ionization energy of nitric oxide, *Chem. Phys. Lett.* **152**(2-3), 119 (1988).
- [101] T. Rieger, T. Junglen, S. A. Rangwala, P. W. H. Pinkse, , and G. Rempe, Continuous Loading of an Electrostatic Trap for Polar Molecules, *Phys. Rev. Lett.* **95**(17), 173002 (2005).
- [102] H. Rottke and K. H. Welge, Photoionization of the hydrogen atom near the ionization limit in strong electric fields, *Phys. Rev. A* **33**(1), 301 (1986).
- [103] J. R. Rubbmark, M. M. Kash, M. G. Littman, and D. Kleppner, Dynamical effects at avoided level crossings: A study of the Landau-Zener effect using Rydberg atoms, *Phys. Rev. A* **23**(6), 3107 (1981).
- [104] J. R. Rydberg, Über den Bau der Linienspektren der chemischen Grundstoffe, *Z. Phys. Chem.* **5**, 227 (1890).
- [105] C. V. Saba, P. A. Barton, M. G. Boshier, I. G. Hughes, P. Rosenbusch, B. E. Sauer, and E. A. Hinds, Reconstruction of a Cold Atom Cloud by Magnetic Focusing, *Phys. Rev. Lett.* **82**(3), 468 (1999).
- [106] H. Sakai, A. Tarasevitch, J. Danilov, H. Stapelfeldt, R. W. Yip, C. Ellert, E. Contant, and P. B. Corkum, Optical deflection of molecules, *Phys. Rev. A* **57**(4), 2794 (1998).

- [107] K. Sakimoto, Multichannel quantum-defect theory of the Stark effect, *J. Phys. B: At. Mol. Opt. Phys.* **19**(19), 3011 (1986).
- [108] K. Sakimoto, Influence of electric fields on highly excited states of H_2 : quantum-defect-theory approach, *J. Phys. B: At. Mol. Opt. Phys.* **22**(17), 2727 (1989).
- [109] S. A. Schulz, H. L. Bethlem, J. van Veldhoven, J. Küpper, H. Conrad, and G. Meijer, Microstructured switchable mirror for polar molecules, *Phys. Rev. Lett.* **93**(2), 020406 (2004).
- [110] M. J. Seaton, Quantum defect theory, *Rep. Prog. Phys.* **46**(2), 167 (1983).
- [111] H. J. Silverstone, Perturbation theory of the Stark effect in hydrogen to arbitrarily high order, *Phys. Rev. A* **18**(5), 1853 (1978).
- [112] T. P. Softley, Applications of molecular Rydberg states in chemical dynamics and spectroscopy, *Int. Rev. Phys. Chem.* **23**(1), 1 (2004).
- [113] T. P. Softley, A. J. Hudson, and R. Watson, Multichannel quantum defect theory Stark effect calculation of autoionization lifetimes in high- n Rydberg states of Ar, N_2 and H_2 , *J. Chem. Phys.* **106**(3), 1041 (1996).
- [114] M. Sommovilla, U. Hollenstein, G. M. Greetham, and F. Merkt, High-Resolution Laser Absorption Spectroscopy in the Extreme Ultraviolet, *J. Phys. B: At. Mol. Opt. Phys.* **35**(18), 3901 (2002).
- [115] D. M. Stamper-Kurn, M. R. Andrews, A. P. Chikkatur, S. Inouye, H.-J. Miesner, J. Stenger, and W. Ketterle, Optical Confinement of a Bose-Einstein Condensate, *Phys. Rev. Lett.* **80**(10), 2027 (1998).
- [116] H. Stapelfeldt, H. Sakai, E. Constant, and P. B. Corkum, Deflection of Neutral Molecules using the Nonresonant Dipole Force, *Phys. Rev. Lett.* **79**(15), 2787 (1997).
- [117] J. Stark, Beobachtungen über den Effekt des elektrischen Feldes auf Spektrallinien. V. Feinzerlegung der Wasserstoffserie, *Annalen der Physik* **48**, 193 (1913).
- [118] T. Takekoshi, B. M. Patterson, and R. J. Knize, Observation of Optically Trapped Cold Cesium Molecules, *Phys. Rev. Lett.* **81**(23), 5105 (1998).
- [119] M. R. Tarbutt, H. L. Bethlem, J. J. Hudson, V. L. Ryabov, V. A. Ryzhov, B. E. Sauer, G. Meijer, and E. A. Hinds, Slowing Heavy, Ground-State Molecules using an Alternating Gradient Decelerator, *Phys. Rev. Lett.* **92**(17), 173002 (2004).
- [120] D. Townsend, A. L. Goodgame, S. R. Procter, S. R. Mackenzie, and T. P. Softley, Deflection of krypton Rydberg atoms in the field of an electric dipole, *J. Phys. B: At. Mol. Phys.* **34**(3), 439 (2001).

- [121] S. Y. T. van de Meerakker, P. H. M. Smeets, N. Vanhaecke, R. T. Jongma, and G. Meijer, Deceleration and Electrostatic trapping of OH Radicals, *Phys. Rev. Lett.* **94**(2), 023004 (2005).
- [122] S. Y. T. van de Meerakker, N. Vanhaecke, M. P. J. van der Loo, G. C. Groenenboom, and G. Meijer, Direct Measurement of the Radiative Lifetime of Vibrationally Excited OH Radicals, *Phys. Rev. Lett.* **95**(1), 013003 (2005).
- [123] J. van Veldhoven, J. Küpper, H. L. Bethlem, B. Sartakov, A. J. A. van Roij, and G. Meijer, Decelerated molecular beams for high-resolution spectroscopy, *Eur. Phys. J. D* **31**(2), 337 (2004).
- [124] J. van Veldhoven, H. L. Bethlem, M. Schnell, and G. Meijer, Versatile electrostatic trap, *Phys. Rev. A* **73**(6), 063408 (2006).
- [125] N. Vanhaecke, W. de Souza Melo, B. L. Tolra, D. Comparat, and P. Pillet, Accumulation of Cold Cesium Molecules via Photoassociation in a Mixed Atomic and Molecular Trap, *Phys. Rev. Lett.* **89**(6), 063001 (2002).
- [126] E. Vliegen, P. A. Limacher, and F. Merkt, Measurement of the three-dimensional velocity distribution of Stark-decelerated Rydberg atoms, *Eur. Phys. J. D* **40**(1), 73 (2006).
- [127] E. Vliegen and F. Merkt, On the electrostatic deceleration of argon atoms in high Rydberg states by time-dependent inhomogeneous electric fields, *J. Phys. B: At. Mol. Opt. Phys.* **38**(11), 1623 (2005).
- [128] E. Vliegen and F. Merkt, Normal-Incidence Electrostatic Rydberg Atom Mirror, *Phys. Rev. Lett.* **97**(3), 033002 (2006).
- [129] E. Vliegen and F. Merkt, Stark deceleration of hydrogen atoms, *J. Phys. B: At. Mol. Opt. Phys.* **39**(11), L241 (2006).
- [130] E. Vliegen, H. J. Wörner, and F. Merkt, unpublished results.
- [131] E. Vliegen, H. J. Wörner, T. P. Softley, and F. Merkt, Nonhydrogenic Effects in the Deceleration of Rydberg Atoms in Inhomogeneous Electric Fields, *Phys. Rev. Lett.* **92**(3), 033005 (2004).
- [132] D. Wang, J. Qi, M. F. Stone, O. Nikolayeva, B. Hattaway, S. Gensemer, H. Wang, W. T. Zemke, P. L. Gould, E. E. Eyler, and W. C. Stwalley, The photoassociative spectroscopy, photoassociative molecule formation, and trapping of ultracold $^{39}\text{K}^{85}\text{Rb}$, *Eur. Phys. J. D* **31**(2), 165 (2004).
- [133] S. J. Wark and G. I. Opat, An electrostatic mirror for neutral polar molecules, *J. Phys. B: At. Mol. Opt. Phys.* **25**(20), 4229 (1992).

- [134] J. M. Weber, K. Ueda, D. Klar, J. Kreil, M. W. Ruf, and H. Hotop, Odd Rydberg spectrum of $^{40}\text{Ar}(\text{I})$: high-resolution laser spectroscopy and multichannel quantum defect analysis of the $J = 2$ and 3 levels, *J. Phys. B: At. Mol. Opt. Phys.* **32**(10), 2381 (1999).
- [135] J. D. Weinstein, R. deCarvalho, T. Guillet, B. Friedrich, and J. M. Doyle, Magnetic trapping of calcium monohydride molecules at millikelvin temperatures, *Nature* **395**(6698), 148 (1998).
- [136] S. Willitsch, J. M. Dyke, and F. Merkt, Generation and High-Resolution Photoelectron Spectroscopy of Small Organic Radicals in Cold Supersonic Expansions, *Helv. Chim. Acta* **86**(4), 1152 (2003).
- [137] S. Willitsch, J. M. Dyke, and F. Merkt, Rotationally resolved photoelectron spectrum of the lowest singlet electronic state of NH_2^+ and ND_2^+ : photoionization dynamics and rovibrational energy level structure of the $\tilde{a}^+ \ ^1\text{A}_1$ state, *Mol. Phys.* **102**(14-15), 1543 (2004).
- [138] S. Willitsch, F. Innocenti, J. M. Dyke, and F. Merkt, High-resolution pulsed-field-ionization zero-kinetic-energy photoelectron spectroscopic study of the two lowest electronic states of the ozone cation O_3^+ , *J. Chem. Phys.* **122**(2), 024311 (2005).
- [139] S. Willitsch, Ch. Jungen, and F. Merkt, Bending energy level structure and quasi-linearity of the $\tilde{X}^+ \ ^3\text{B}_1$ ground electronic state of NH_2^+ , *J. Chem. Phys.* **124**(20), 204312 (2006).
- [140] S. Willitsch, *Photoionisation asymmetrischer Kreisel: Struktur und Dynamik molekularer Radikale und Kationen*, PhD thesis, Eidgenössische Technische Hochschule Zürich, 2004, Diss. ETH Nr. 15713.
- [141] W. H. Wing, Electrostatic Trapping of Neutral Atomic Particles, *Phys. Rev. Lett.* **45**(8), 631 (1980).
- [142] W. H. Wing, On neutral particle trapping in quasistatic electromagnetic fields, *Prog. in Quant. Elec.* **8**(3-4), 181 (1984).
- [143] H. J. Wörner, Verlangsamung und Beschleunigung von Argon-Rydbergatomen in inhomogenen elektrischen Feldern, Diploma thesis, Eidgenössische Technische Hochschule Zürich, ETH Zentrum, CH-8092 Zürich, Switzerland, 2003.
- [144] H. J. Wörner and F. Merkt, Photoelectron Spectroscopic Study of the First Singlet and Triplet States of the Cyclopentadienyl Cation, *Angew. Chem. (int. ed. engl.)* **45**(2), 293 (2006).

-
- [145] Y. Yamakita, S. R. Procter, A. L. Goodgame, T. P. Softley, and F. Merkt, Deflection and deceleration of hydrogen Rydberg molecules in inhomogeneous electric fields, *J. Chem. Phys.* **121**(3), 1419 (2004).
- [146] K. Yoshino, Absorption Spectrum of the Argon Atom in the Vacuum-Ultraviolet Region, *J. Opt. Soc. Am.* **60**(9), 1220 (1970).
- [147] R. N. Zare, *Angular Momentum: Understanding spatial aspects in chemistry and physics*, John Wiley & Sons, New York, 1988.
- [148] C. Zener, Non-Adiabatic Crossing of Energy Levels, *Proc. R. Soc. London Ser. A* **137**(833), 696 (1932).
- [149] M. L. Zimmerman, M. G. Littman, M. M. Kash, and D. Kleppner, Stark structure of the Rydberg states of alkali-metal atoms, *Phys. Rev. A* **20**(6), 2251 (1979).
- [150] M. W. Zwierlein, C. A. Stan, C. H. Schunck, S. M. F. Raupach, S. Gupta, Z. Hadzibabic, and W. Ketterle, Observation of Bose-Einstein Condensation of Molecules, *Phys. Rev. Lett.* **91**, 250401 (2003).

Curriculum Vitae

Name	Edward Vliegen
Date of birth	4 November 1976
Place of birth	Loon op Zand, The Netherlands
Nationality	Dutch

Education

1989-1995	Secondary education (VWO) Phillips van Horne SG, Weert, The Netherlands
1995-2001	Studies of physics and mathematics at the University of Utrecht Utrecht, The Netherlands
2000-2001	Master thesis in the group of Prof. P. van der Straaten on "Photoassociation in a metastable-helium MOT"
2001	Master thesis in the group of Prof. H.T.C. Stoof on "Topological excitations in a spinor BEC"
1998-1999	Studies of physics and mathematics at the University of Wisconsin Madison, Wisconsin, USA
2002-2006	PhD thesis in the group of Prof. F. Merkt at the Laboratory of Physical Chemistry of the ETH Zurich Zurich, Switzerland

Other activities

1998-2001	Teaching assistant in several lectures at the University of Utrecht
2002	Teaching physics at grammar school "College de Klop" Utrecht, The Netherlands
2002-2006	Teaching assistant in several lectures at the Laboratory of Physical Chemistry, ETH Zurich
2003-2006	Administration of the local computer system
2003	Supervising the master thesis of H. J. Wörner
2005	Supervising the master thesis of P. A. Limacher

Languages

Dutch, English, German

Publications

Publications

1. "Faraday rotation density measurements of optically thick alkali metal vapors"
E. Vliegen, S. Kadlecěk, L.W. Anderson, T.G. Walker, C.J. Erickson, and W. Happer
Nucl. Instr. and Meth. Phys. Res. A, **460**(2-3), 444-450 (2001)
2. "Monopoles in an antiferromagnetic Bose-Einstein condensate"
H.T.C. Stoof, E. Vliegen, and U. Al Khawaja
Phys. Rev. Lett, **87**(12), 120407 (2001)
3. "Nonhydrogenic effects in the deceleration of Rydberg atoms in inhomogeneous electric fields"
E. Vliegen, H.J. Wörner, T.P. Softley, and F. Merkt
Phys Rev. Lett, **92**(3), 033005 (2004)
4. "Role of nuclear spin in photoionization: Hyperfine-resolved photoionization of Xe and multichannel quantum defect theory analysis"
H.J. Wörner, M. Grütter, E. Vliegen, and F. Merkt
Phys. Rev. A, **71**(5), 052504 (2005)
5. "On the electrostatic deceleration of argon atoms in high Rydberg states by time-dependent inhomogeneous electric fields"
E. Vliegen and F. Merkt
J. Phys. B **38**(11), 1623-1636 (2005)
6. "Stark deceleration of hydrogen atoms "
E. Vliegen and F. Merkt
J. Phys. B **39**(11), L241-L247 (2006)
7. "Measurement of the three-dimensional velocity distribution of Stark-decelerated Rydberg atoms"
E. Vliegen, P. Limacher and F. Merkt
Eur. Phys. J. D **40**(1), 73-80 (2006)
8. "A normal-incidence electrostatic Rydberg atom mirror"
E. Vliegen and F. Merkt
Phys. Rev. Lett, **97**(3), 033002 (2006)

Talks

1. "Controlling the motion of Rydberg atoms and molecules in selected Stark states"
Quantum systems in information technology meeting, Flums, March 6th 2004
2. "Stark deceleration of Rydberg atoms: A possible contribution to anti-hydrogen research"
AEGIS meeting on anti-hydrogen research, CERN, Geneva, November 28th 2005
3. "Rydberg particle optics: Decelerators, mirrors, and traps"
Quantum systems in information technology meeting, Arosa, January 4th 2006
4. "Of Rydberg particle decelerators, lenses, mirrors, and traps"
Colloquium of the Laboratory of Physical Chemistry, ETH Zürich, Zürich, April 18th 2006
5. "Hydrogen Rydberg atom optics: Lenses, mirrors, and traps"
AEGIS meeting on anti-hydrogen research, CERN, Geneva, June 14th 2006

Poster presentations

1. "High-resolution spectroscopy and deceleration of high Rydberg states of argon"
GRC conference on Photoions, Photoionization and Photodetachment
Oxford, England, September 21-26, 2003
2. "Non-hydrogenic effects in the deceleration of Rydberg atoms in inhomogeneous electric fields"
39th Symposium on Theoretical Chemistry
Gwatt, Switzerland, 28 September-2 October, 2003
3. "High-resolution spectroscopy and deceleration of high Rydberg states of argon"
International Workshop and Seminar on Rydberg Physics
Dresden, Germany, May 2-7, 2004
4. "Deceleration of high Rydberg states of argon using time-dependent electric fields"
Workshop on Ultracold Plasmas and Rydberg Systems
Gif-sur-Yvette, France, March 14-16, 2005
5. "Motional control of high Rydberg states of argon using time-dependent electric fields"
Swiss Chemical Society Fall Meeting, Lausanne, Switzerland, October 13th, 2005
6. "Motional control of high Rydberg states of argon using time-dependent electric fields"
Workshop on Cold Polar Molecules
Ringberg Castle, Germany, October 19-22, 2005

Dankwoord

Frédéric, ich bin sehr dankbar für alles was du mir beigebracht hast und für alle Chancen und Möglichkeiten die du mir gegeben hast, aber auch dafür, dass du dafür gesorgt hast, dass die Arbeit vier Jahr lang **Spass** gemacht hat.

Tilman, ich danke dir nicht nur für die Übernahme des Korreferats, aber auch für dein kontinuierliches Interesse, das du an meiner Arbeit gezeigt hast.

Hansjürg und René, euch möchte ich danke für eure Fähigkeit, meine bisweilen erst halbwegs ausgereiften Ideen in einer funktionierender Aufbau umzuwandeln. Mit euch zusammen arbeiten zu dürfen war wirklich ein Vergnügen.

Markus, ich danke dir speziell für deine Arbeit an dem Imaging-Aufbau, die uns so viele neue Kenntnisse über den Bremsvorgang gebracht hat. Peter, dass die Bilder so schön waren und dass uns deren Interpretation gelungen ist, ist dir zu verdanken. Marco, vielen Dank für deine Hilfe bei der Konstruktion der Abkühl-Installation.

Natürlich möchte ich auch der ganzen Merkt Gruppe danken für die ausgezeichnete Arbeitsstimmung, die viele Kuchen und die Gruppefilme von zweifelhafter Qualität.

Hans Jakob, dir möchte ich danke sagen für die schöne Zusammenarbeit während der letzten vier Jahre, für deine Versuche, mein Deutsch zumindestens ein bisschen zu verbessern und für das Fussballspielen im Gang während der letzten Wochenenden vor der Abgabe.

Stefan, danke für das H dass du mir geschenkt hast, für deine blöde Witze und für deine Freundschaft.

Anna und Oli! Was gibt es da noch zu sagen? Ihr wart traumhafte Bürokollegen und ich werde unsere Unterhaltungen sehr vermissen. Anna, Poster 64 war das interessanteste Poster, das ich je gesehen habe. Oli, ich hoffe wir haben deine Klatsch und Tratsch Fähigkeiten ein bisschen fördern können.

Schlussendlich möchte ich noch allen danken, die mit mir zu Fuss, auf Schneeschuhen oder auf Skis die Schweizer Alpen durchquert haben. Wie schön und besonders das für einen Holländer war (höchster "Berg" der Niederlande: Vaalserberg 322 m!) werdet ihr wahrscheinlich nie wirklich verstehen, aber glaubt mir einfach: es war fabelhaft!